Metamaterials and Extraordinary Transmission structures applied to microwave, millimeter and terahertz waves devices

Pablo Rodríguez Ulibarri

Supervisor: **Dr. Miguel Beruete Díaz**

Dr. Andriy E. Serebryannikov

Departmento de Ingeniería Eléctrica y Electrónica

Universidad Pública de Navarra

This dissertation is submitted for the degree of

Doctor of Philosophy in Telecommunication Engineering

September 2017

Acknowledgements

First of all I would like to express my most sincere gratitude to my supervisors Dr. Miguel Beruete and Dr. Andriy Serebryannikov. Miguel, you taught me most of the concepts and phenomena that I have learned during this Thesis period. I am grateful for having the opportunity of working with you not only from a scientific context, but more importantly, from the human point of view. You have been always supportive, committed and positive, and that is something valuable when pursuing a PhD. Andriy, I also have learned a myriad of physic concepts from you. I admire your great dedication and passion for the electromagnetism in particular and physics in general. In the human aspect, only good adjectives come into my mind if I had to describe you.

I would like to write some lines in memoriam of Prof. Mario Sorolla with whom my scientific career started. Although we could not spent much time together I could learn first hand about his quality as scientist and what is more, as human being.

In addition, I would like to acknowledge the support received by the whole Antennas Group of the Public University of Navarra. I should mention those colleagues (and friends), Alicia, Adur, Baha, Jose, Pacheco, Torres and Unai, with whom I had the pleasure to share great work-related moments but also had the chance to enjoy happy personal events. Thanks to everyone.

I would like to acknowledge the warm welcome received by the Microwaves Group of the University of Seville under supervision of Professor Francisco Medina. I kept good memories from my office mates Alejandro, Armando y Carlos.

Last but not least, I thank my whole family, especially parents and brothers, and in-laws, their great support in many aspects of my life surely non-related with this Thesis, and surely way more important. I also have some special memories for those relatives who left us during this three year period, my aunts Isabel and Carmela and my uncle Javi. Finally, I have to thank to the two most important people in my life, Maite and Xabi. Maite, thanks for your patience, support and unconditional love, for teaching me techniques to deal with this process, for being my partner, my friend and my wife. Xabi, thanks for making me smile every single day.

Agradecimientos

En primer lugar me gustaría expresar mi más sincera gratitud a mis dos supervisores, los doctores Miguel Beruete y Andriy Serebryannikov. Miguel, gracias por haberme enseñado muchos de los conceptos y fenómenos que he aprendido durante estos años de tesis. Me siento afortunado de haber trabajado contigo no sólo desde el punto de vista científico, sino también y más importante, desde el de las relaciones humanas. Has sido comprensivo, comprometido y siempre has mostrado una actitud positiva, condiciones muy valiosas cuando alguien realiza una tesis doctoral. Andriy, también he aprendido infinidad de conceptos físicos contigo. Admiro tu gran dedicación y pasión por la física en general y el electromagnetismo en particular. En el aspecto humano, sólo se me ocurren buenos adjetivos para describirte como persona.

Quisiera dedicar unas líneas al profesor Mario Sorolla con el que tuve el placer de empezar mi carrera científica. Aunque coincidimos poco tiempo, pude constatar de primera mano su calidad como científico pero sobre todo, como persona.

Por supuesto quiero agradecer el apoyo recibido por el Grupo de Antenas de la Universidad Pública de Navarra. Debo mencionar especialmente aquellos colegas (en todas sus acepciones), Alicia, Adur, Baha, Jose, Pacheco, Torres y Unai, con los que he tenido el placer de compartir grandes momentos de trabajo y de disfrutar también de momentos personales muy felices. Gracias a todos.

Agradezco también la acogida recibida en la estancia que he realizado en el Grupo de Microondas de la Universidad de Sevilla bajo la supervisión de Francisco Medina. Guardo un especial recuerdo de mis compañeros de despacho, Armando, Alejandro y Carlos.

Por último pero no por ello menos importante, agradezco a mi familia al completo, mención especial para mis padres y hermanos, su apoyo en muchos aspectos de la vida que, probablemente no están relacionados con el desarrollo de la tesis, pero sin duda son mucho más importantes. También quiero recordar a los familiares que nos han dejado durante este período de tiempo y a quienes llevo siempre muy dentro, mis tías Isabel y Carmela y mi tío Javi. Finalmente, agradezco a las dos personas que me acompañan, soportan, alegran, ayudan en el día a día. Maite, gracias por tu paciencia, apoyo y amor incondicional, por enseñarme

técnicas para lidiar con este proceso, por ser mi compañera, mi amiga, y mi mujer. Xabi, gracias por arrancarme una sonrisa todos los días del año.

Abstract

Metamaterials emerged in the early 2000's as manmade materials that exhibit exotic electromagnetic properties. At the same time, a new phenomenon termed as the extraordinary transmission was discovered. These two topics entailed a profound review of the electromagnetism theory bringing together the microwave and optical communities. In addition, metamaterials and extraordinary transmission were exploited to develop new and advanced devices for a broad range of applications such as security, communications, spectroscopy, to name a few. In this Thesis the use of metamaterials and extraordinary transmission inspired devices working at frequencies ranging from microwaves and millimeter waves to terahertz waves is investigated. The content of the Thesis can be divided in three different yet related topics dealing with each frequency regime, namely *microwaves, millimeter* and *terahertz* waves. The first part is devoted to investigation of metamaterials use for enhancing the performance of an antenna system intended for radar applications in the microwave regime. The second part deals with theoretical and experimental implementations of two-dimensional periodic structures working at millimeter waves to study the limits between extraordinary transmission and ordinary transmission regimes, design of unidirectional and tunable devices and metasurfaces with non-conventional angular response. Finally the third part of the Thesis, extends the use of two-dimensional periodic structures to sensing applications within the terahertz regime.

Resumen

Los metamateriales aparecen en los primeros años del siglo XXI como materiales artificiales que presentan un comportamiento electromagnético de alguna manera exótico. Al mismo tiempo, se descubre un nuevo fenómeno denominado transmisión extraordinaria. Ambas disciplinas conllevaron a una revisión profunda del electromagnetismo básico aunando dos comunidades científicas que últimamente permanecían desligadas, las microondas y la óptica. Además, tanto los metamateriales como la transmisión extraordinaria fueron explotados para desarrollar nuevos dispositivos para un amplio abanico de aplicaciones tales como seguridad, comunicaciones o espectroscopía. En esta Tesis se investiga el uso de dispositivos inspirados en estructuras metamaterial y el fenómeno de transmisión extraordinaria operando a frecuencias de microondas, ondas milimétricas y terahercios. El contenido de la Tesis se puede dividir en tres partes diferenciadas que se relacionan con cada uno de los rangos frecuenciales estudiados, es decir, *microondas, ondas milimétricas* y *terahercios*. La primera parte de la Tesis está dedicada a investigar cómo los metamateriales pueden mejorar las prestaciones de un sistema de antenas para aplicaciones radar en el rango de las microondas. La segunda parte trata de forma teórica y experimental diferentes estructuras periódicas bidimensionales que trabajan en el rango de las ondas milimétricas con el fin de estudiar los límites entre el fenómeno de transmisión extraordinaria y regímenes ordinarios, diseñar dispositivos unidireccionales y sintonizables y metasuperficies con una respuesta angular no convencional. Finalmente, la tercera parte de la Tesis, hace extensible el uso de estructuras periódicas bidimensionales para aplicaciones de sensado a frecuencias de terahercio.

Table of contents

List of figures

List of tables

Acronyms, Abbreviations and Constants

Acronyms / Abbreviations

CAD	Computer Aided Design
CSRR	Complementary Split Ring Resonator
DNG	Double-Negative
DPS	Double-Positive
ECA	Equivalent Circuit Approach
EM	Electromagnetic
ENG	Epsilon-Negative
ENMZ	Epsilon-and-Mu-Near-Zero
ENZ	Epsilon-Near-Zero
ET	Extraordinary Transmission
FB	Floquet-Bloch
MNG	Mu-Negative
MNZ	Mu-Near-Zero
RCS	Radar Cross Section
RWA	Rayleigh-Wood Anomaly
SHA	Stacked Hole Array
SPP	Surface Plasmon Polariton

SRR Split Ring Resonator

TDS Time Domain Spectroscopy

WAIM Wide Angular Impedance Matching

Physic Constants

c_0 Speed of light in vacuum, $c_0 = 1/\sqrt{\varepsilon_0\mu_0/} = 2.9986\ldots\cdot 10^8$ (m/s)

η_0 Vacuum wave impedance, $\eta_0 = \sqrt{\mu_0/\varepsilon_0} \approx 120\pi$ (Ω)

ε_0 Vacuum permittivity, $\varepsilon_0 = 8.85\cdot 10^{-12}$ (F/m)

μ_0 Vacuum permeability, $\mu_0 = 4\pi\cdot 10^{-7}$ (H/m)

Chapter 1

Introduction

Nowadays electromagnetic (EM) waves are ubiquitous in everyday life. During the last 150 years, the human being has been capable of developing a complete theory; generating and detecting and adding information into them making point to point communications possible. Continuous progress in electromagnetics has given birth to a myriad of applications of EM waves. Telecommunications is perhaps the most evident one, but the scope of EM waves is much wider, encompassing security, medicine or defense applications to name a few. Thus, finding and exploiting advanced physical scenarios is a major task and its understanding and continuous research is carried out the scientific community to develop new devices and applications.

The term *wave* itself is rather general and sometimes its physical meaning is somehow misunderstood. A very accurate wave definition is given by D. J. Griffith: "a wave is a disturbance of a continuous medium that propagates with a fixed shape at a constant velocity" [Gri15]. This definition is still very general and applicable to mechanics; waves propagating through water or a string; sound waves; etc. Generally, waves result from the interchange of two forms of energy at the presence of time varying rate. In the particular case of EM waves, these two forms of energy are electric and magnetic. A change in the magnetic field produces variations of the electric field both in time and space. The subsequent electric field variations generate a change of the magnetic field and so on and so forth. So, EM waves carry energy that is interchanged between electric and magnetic components as they travel. EM waves do not need a medium to propagate since they do it in vacuum at a constant velocity which is the speed of light in vacuum, $c_0 \approx 2.997925 \cdot 10^8$ m/s. When propagating through media EM waves travels at the speed of light, c (which is always $c < c_0$). The c_0 constant relates the main parameters of an EM wave, namely, its frequency, f, and wavelength, λ. The frequency, f, determines the number of oscillations per unit time (it is measured in Hertz, Hz [s^{-1}]) and the wavelength, λ, is the spatial period of the wave and it is measured in meters, m.

Therefore, EM waves are classified by their frequency (or equivalently wavelength) within the so called EM spectrum. There are EM waves as long as kilometers (radio waves) and as short as picometers (gamma rays). Between these two examples located at the bottom and top spectrum limits all the remaining bands are located. Amongst them are *microwaves, millimeter and terahertz* waves, which will be treated intensely in this Thesis.

Controlling EM waves has been a recurrent goal for scientists along the past one hundred and fifty years since Maxwell's equations came out. This event ignited the spark for the development of modern electromagnetics and brought about the great advances and EM based devices available nowadays. However, the human being has desired to control EM waves long before than Maxwell formulation came true. Think for instance about mirrors and lenses as keybone parts of devices such microscopes, telescopes, or the optical telegraph that have been known for centuries. The genius of Maxwell was in reconciling different electromagnetic results in a single formulation and, more strikingly, recognizing that light was an EM wave. Maxwell theory was corroborated in the laboratory by H. Hertz eight yeara after Maxwell's decease. Hertz proved the existence of EM waves and compiled these results in a book [Her93]. These findings led to the invention of radio in the closing years of the 19^{th} century. By that time, the electrical engineer was already considered a distinct profession and the first worldwide companies dealing with communications came out.

In the 20^{th} century the communication systems were rapidly developed and usually tragic events such World Wars acted as catalysts. In particular, during second World War, radar systems enabled a rapid evolution of the so called microwave technology. This research was kept and extended during the cold war and eventually transferred to civil applications especially after the fall of Berlin wall. As an example, the satellite Global Positioning System (GPS) was opened to civil use in 1995. By the end of 20^{th}, many of the most used communication systems nowadays were invented. Although the 20^{th} was rather technological, the foundations of electromagnetism settled by Maxwell were always present.

At the beginning of the 21^{th} century a new class of artificial materials termed *metamaterials* were born. The most appealing property of these manmade materials was that the EM response could be engineered to obtain exotic and unexplored behaviors that cannot be observed in nature. The emergence of metamaterials and the intensive research that brought along, unveiled many unknown physical phenomena and revisited many others that could be considered classical. In this context, the discovery of the so called extraordinary transmission (ET) phenomenon made by T. W. Ebbesen can be considered a real scientific breakthrough [Ebb98]. This phenomenon was firstly observed in the optical regime and replicated later at millimeter waves [Ber04]. At first, plasmon theory was used to explain the ET phenomenon. All the research that came along refueled plasmonics research leading to

an effective *plasmonic resurrection* [Edi12]. On the other hand, the microwave community found that the plasmon theory was a particular case of a rather general theory, namely, complex waves [Ber04]. Another approach to study plasmons was developed in microwave using equivalent circuit approach (ECA) techniques.

In this chapter the aforementioned concepts are contextualized and their particularities and main features are discussed. First of all, a brief introduction of the three frequency regimes that are studied in this thesis is provided. Then, the basics of metamaterials and ET are given with a special attention of those examples put on some cases that will be treated in detail in the subsequent chapters of this Thesis. Furthermore, some words regarding ECA technique for periodic array of elements are given. Finally, an outline of the thesis is provided.

1.1 Microwaves, Millimeter and Terahertz Waves

The EM spectrum is divided in different regimes depending on their frequency (or wavelength) (see Fig. 1.1). Each of the frequency regimes within the EM spectrum owns different features which made them more appropriate to certain applications than others. For instance, radio waves are the best candidate for commercial radio broadcast. If we think in terms of Friis attenuation, low frequency EM waves are allowed to travel longer distances at the same conditions of signal intensity, absorption losses, etc. Moreover, due to the natural response of materials at these frequencies, they are able to penetrate and overcome big obstacles such as buildings and mountains. Furthermore, according to Planck's equation their associated photon energy is low so under low intensities they are harmless to the human being despite some thermal effects. On the other hand, ultrahigh frequency waves, such as X-rays, which are useful for radiography in medical diagnosis are waves with very high photon energy. In fact, they can break the molecular bonds of the human body tissues and are harmful even for short-term exposures.

In this thesis, the frequency regions targeted *microwaves, millimeter and terahertz waves* are located between the above mentioned examples. However, the boundaries between these regimes sometimes lack of a general consensus between the scientific community. In the following this issue and the particularities of each frequency regime will be addressed.

1.1.1 Microwaves

Microwaves is a quite mature technology which frequency limits are 300 MHz and 300 GHz (corresponding to electrical wavelengths of 1 m and 1 mm respectively). The fundamental

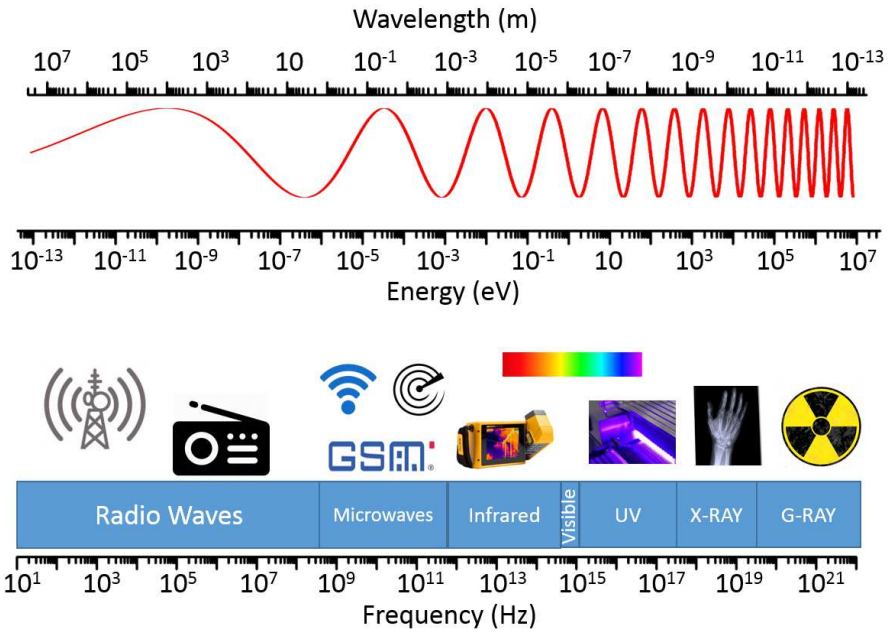

Fig. 1.1 Full Electromagnetic Spectrum covering from radio waves to gamma rays frequencies.

concepts of EM that underlay the microwaves discipline were discovered more than 150 years ago with the treatise of J. C. Maxwell that provided the Maxwell's equations [Max81]. Since then, microwaves technology has been widely used both in the past and in our present days. During the World War II, the intense activity on radar technology accelerated its development [Oli84]. Nowadays microwaves are ubiquitous. Most of the recent communication applications such Global System Mobile (GSM), its advanced version, Universal Mobile Telecommunication System (UMTS) for cellular technology, Wireless Local Area Networks (WLANS) for high-speed and short range communications between computers and the Global Positioning System (GPS) to name a few, operate in this band. The selection of microwaves for these purposes is not arbitrary. The trade-off between the radio-frequency (RF) components features such as antennas, filters, detectors and generators and their cost has been the main propeller of microwaves when compared with alternative technologies.

1.1.2 Millimeter Waves

Millimeter waves have wavelengths of the order of millimeters. They are considered a subfamily of microwaves and are located between 30 and 300 GHz (see Fig. 1.2). As the frequency increases, the classical guided-wave techniques used in microwaves can be prohibitively lossy. Quasi-optical techniques are the free space alternative to guided-wave

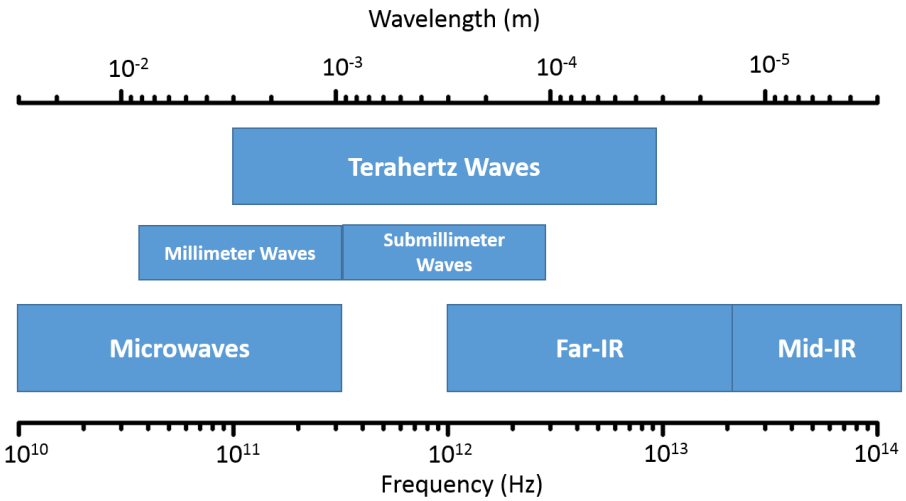

Fig. 1.2 Portion of the electromagnetic spectrum ranging from microwave to infrared frequencies.

technology wherein propagation relies on fairly well collimated beams. The quasi-optical components, in contrast with mirrors and lenses used in optics, are only a few times larger than the wavelength of operation. In fact, many of the first experiments dealing with EM waves conducted by H. Hertz and J. C. Bose were performed with quasi-optical systems.

The first millimeter waves experiments trace back to the 19^{th} century. More than one hundred years ago J. C. Bose developed the first millimeter wave communication system [Eme97]. He was able to ring a bell remotely and detonate a small amount of gunpowder. To achieve this goal, he had to develop a transmitter, a detector, a dielectric lens, a polarizer a horn antenna and a cylindrical diffraction grating. All these components are nowadays crucial in every millimeter wave communication and despite the early work of Bose, there is still room for improvement and therefore, for further research investigations.

As frequency increases the size of the RF components becomes smaller. In fact, this was also a reason that encouraged Bose to perform his experiments at millimeter waves. His small laboratory facilities were more suitable for quasi-optical devices. Indeed, the smaller size of millimeter wavelengths is an advantage with respect to microwaves since, in principle, the same antenna gain and eventually performance can be obtained in a reduced space. However, the drawback is that the complexity of the fabrication of the components also increases as the frequency is raised. Although it is true that Bose could demonstrate a millimeter wave system back in the 19^{th} century, it was rather rudimentary compared to the ones available today. In any case, his results were outstanding and remarkable and in fact, the next millimeter-wave works came out about 50 years later, putting in value Bose's findings.

In the framework of communications, working at higher frequency is beneficial as it increases data capacity (or equivalently data rate) according to Shannon's theorem. The capacity of the channel is proportional to the operational bandwidth. Then, under good conditions in terms of signal to noise ratio, increasing the operation frequency and therefore the bandwidth leads to a parallel increment of the data rate. For this reason, millimeter waves are very appealing for future communications wherein the amount of data to be handled grows day by day due to the ubiquity of multimedia applications. Nevertheless, millimeter waves have also hurdles that need to be overcome. For instance, they suffer from high attenuation due to absorption bands related to the atmosphere components like oxygen or water limiting its application range to short distance communications.

Another field of application of millimeter waves is radar technology. Specifically, automotive radar systems for collision avoidance find their needs in this kind of use this technology due to the reduced size of the RF components that enable an easy integration on car's front face bumper. The research community is doing a great effort towards lowering the cost for this kind of technology solutions. In this way, new fabrication techniques as well as new EM concepts raised by metamaterials appearance may contribute to the improvement of last generation radar systems.

Summing up, the millimeter wave regime is very appealing for the development of communications and radar applications. All in all, the technology it is not yet as mature as microwaves and hence, a continuous effort by scientific community should be done towards this direction. To this end, in this Thesis several devices working at millimeter waves are treated with remarkable EM properties such as unidirectional transmission devices based on fishnet configurations and angular selectivity using a special case of complementary split ring resonators (CSRR) among others.

1.1.3 Terahertz Waves

The terahertz (THz) band lies between millimeter waves and far-infrared. Although the THz limits are generally accepted to be from 0.1 to 10 THz [Lee09], the exact boundaries are still under debate. For instance, from a microwave engineering point of view, the millimeter wave regime spans from 30 to 300 GHz overlapping with the lower region of the THz band. Likewise, for the upper limit, classical optics set the far-infrared limit in 1 THz. This lack of consensus comes from the multidisciplinary character of the THz band, wherein scientists and technologists of diverse disciplines came together in this relatively new band. In any case, we pragmatically set here the THz band limits from 0.1 and 10 THz being aware that there exists certain overlapping with millimeter (sub-millimeter) and far infrared regimes.

The THz band has been known for years as the "THz gap". The lack of efficient and cost-effective generators and detectors at these frequencies hindered the development of applications leaving this portion of spectrum unexploited. For a long time, the THz band applications was reduced to two main niches: astronomy and spectroscopy. The classical THz sources were based on bulky, expensive and low efficiency solutions such as tubes (carcinotrons, klynstrons and backward wave oscillators) and free electron lasers (FEL). In a similar way THz detection usually relied on bolometers wherein cryogenic cooling is required for attaining good sensitivities. The emergence of new THz generation and detection techniques changed drastically the THz panorama. On the generation side, the appearance of optical rectification and photomixing techniques and new THz sources like quantum cascade lasers (QCLs) combined with the improvement of classical microwave up-converters based on solid state multipliers gave rise to a tremendous advance. In addition, cheaper receivers such as those based on photomixing or microwave heterodyne detection contributed to improve the THz systems. These discoveries were fundamental for the development of complete and affordable THz systems and for "bridging the THz gap" with running applications. A paradigm of this new kind of THz system is the Time Domain Spectroscopy (TDS-THz) that was crucial for the the popularization of THz research in the field of spectroscopy. Extensive review articles and books treating this revolutionary way of generating and detecting THz waves can be found in the literature [Lee09, Sie02, Sae13].

These technological advances paved the way for many potential applications. In fact, applications and technology had a symbiotic relationship wherein the former pushed the latter leading to a continuous improvement of both, applications and technology. As an example, space applications where the research on THz technology was under intense development, transferred the outcomes in the form of detector, sources and other THz components to ground applications [Gai00]. As in the case of millimeter waves, THz waves have very appealing characteristics for communications. On the one hand, the potential data rates are much higher. On the other hand, the absorption loss and the intrinsic short wavelength of THz waves are more restrictive than in the millimeter wave regime. In any case, THz waves can be very good candidates for certain scenarios such as short range and indoor communications [Pie07, Aky14].

As mentioned aboved, the TDS-THz system was a breakthrough in the field of spectroscopy. In this field, the research interests are focused on gathering information of large-size molecules for biological and biomedical applications. For instance, amino-acids have special fingerprints, namely, absorption bands that are related with the vibrational modes of bending, stretching or torsion of these molecules. Since THz wavelengths are comparable to these vibrations they are postulated as the ideal candidates for characterizing substances

in these terms. Then, a myriad of possibilities arise in a wide range of sectors such as security for detecting explosives and concealed weapons [Liu07], pharmaceutical industry for studying the cristallinity of pharmaceutical materials [Str04] and for tissue and disease identification in biomedical applications [Sie04]. In particular, security and public health THz applications have recently become of great importance for obvious reasons. Nowadays, security in crowded public areas such as airports and railway stations needs to be ensured and therefore early detection of any threat in terms of concealed weapons and explosive materials has become fundamental. At the same time, these security scanner systems must preserve the privacy and must be innocuous for the health. THz waves fulfill these requirements as non-invasive and non-ionizing radiation [Liu07]. In connection with this topic, THz imaging is the backbone in multiple applications in security and health care [Mit96].

Strongly related with THz spectroscopy, THz sensing is one of the most popular among THz applications. As stated before, due to the use of wavelengths of THz waves, valuable information (such as absorption bands caused by molecular bonds and concentration of a certain component) can be extracted from transmittance/reflectance and absorbance measurements. This information can be directly gathered from the target sample that often requires an exhaustive post-processing data analysis. Or, as an alternative, engineered devices can be employed to enhance the response of the material to be analyzed. In addition, depending on the sample form (solid, fluid, liquid or gaseous), suitable measurement platforms can be designed in order to minimize the amount of sample to be analyzed. THz sensors based on different technologies such as fiber optics, resonant structures and waveguiding structures can be found within the literature [RU17b]. In this thesis, resonant structures based on metasurfaces and frequency selective surfaces will be proposed as ultrasensitive THz sensors for thin-film and microorganisms detection.

1.2 Metamaterials: Beyond the natural

The term metamaterials it is a compound word formed by the prefix meta and materials. The former derives from Greek and means “Beyond”, so the term “Metamaterials” refers to something beyond ordinary materials [Sol09]. Indeed, metamaterials stand for those structures whose electromagnetic properties cannot be found in nature and whose electromagnetic parameters can be engineered in order to obtain arbitrary responses. It should be pointed out that photonic crystals (PCs) do also represent structures whose electromagnetic properties cannot be found in nature. However, metamaterials are composed of subwavelength unit cells while PCs use unit cells comparable to the wavelength.

Rodger M. Walser gave a definition of metamaterials in 1999 which is still valid nowadays: *"Macroscopic composites having a synthetic, three-dimensional, periodic cellular architecture designed to produce an optimized combination, not available in nature, of two or more responses to specific excitation"* [Wal03]. However, there are authors that find this definition incomplete. Tie Jun Cui and D. R. Smith literally stated: "A metamaterial is a macroscopic composite of periodic or non-periodic structure, whose function is due to both the cellular architecture and the chemical composition" [Cui14]. As seen, there is not a steady definition but it depends on the level of generality assumed. Another important feature regarding metamaterials is that their macroscopic behaviour does not depend directly on the composition of the material, but on how the microscopic atoms (i.e. unit cell of the periodic lattice) are spatially distributed and structured. Therefore, exotic electromagnetic parameters can be artificially achieved while maintaining the chemical composition unperturbed.

The constitutive parameters (CP) ε and μ are used to characterize materials in EM terms. In addition, the index of refraction n and impedance Z which are derived quantities from the CP are frequently used. The EM waves behavior is given by the Maxwell's equations:

$$\begin{aligned} \nabla \times \mathbf{E} &= -\frac{\partial \mathbf{B}}{\partial t}, \\ \nabla \times \mathbf{H} &= \frac{\partial \mathbf{D}}{\partial t} + \mathbf{J}, \\ \nabla \cdot \mathbf{D} &= \rho, \\ \nabla \cdot \mathbf{B} &= 0. \end{aligned} \tag{1.1}$$

where $\mathbf{E}$ is the electric field, $\mathbf{H}$ is the magnetic field, $\mathbf{D}$ the electric flux density, $\mathbf{B}$ is the magnetic flux density, $\mathbf{J}$ is the electric current density and ρ is the electric charge density (vector quantities are shown in bold font). These equations are valid for vacuum conditions, for charge and current free scenarios (i.e. $\rho = 0$ and $\mathbf{J} = 0$) and also for propagation through matter media. In the latter case, for instance, an electric field $\mathbf{E}$ applied to a dielectric material causes the polarization of the atoms or molecules of the material creating electric dipole moments that lead to an increment of the total electric flux density, $\mathbf{D}$. The situation for an applied magnetic field $\mathbf{H}$ and its magnetization effect in $\mathbf{B}$ is analogous. These features are implied within the CP ε and μ. Under linear conditions, i.e. ε and μ do not depend on $\mathbf{E}$ or $\mathbf{H}$, $\mathbf{D}$ and $\mathbf{B}$ can be written as:

$$\begin{aligned} \mathbf{D} &= \varepsilon \varepsilon_0 \mathbf{E}, \\ \mathbf{B} &= \mu \mu_0 \mathbf{H}, \end{aligned} \tag{1.2}$$

where ε_0 and μ_0 are the vacuum permittivity and permeability respectively. In the presence of loss due to damping of the vibrating dipole moments, ε and μ are complex quantities: $\varepsilon = \varepsilon' - j\varepsilon''$ and $\mu = \mu' - j\mu''$. The imaginary parts ε'' and μ'' must be positive in order to comply with the passivity principle. In addition, both ε and μ may depend on the orientation vector of the external field. In other words, the creation of electric and/or magnetic dipole moments is not the same for different directions. Materials having this property are called anisotropic whereas materials wherein the polarization vector is identical for all the directions are called isotropic. Thus, more general relations between **D**, **B**, **E** and **H** for three dimensional coordinate system may be written taking ε and μ as tensors (dyads) as follows:

$$\begin{pmatrix} D_x \\ D_y \\ D_z \end{pmatrix} = \begin{pmatrix} \varepsilon_{xx} & \varepsilon_{xy} & \varepsilon_{xz} \\ \varepsilon_{yx} & \varepsilon_{yy} & \varepsilon_{yz} \\ \varepsilon_{zx} & \varepsilon_{zy} & \varepsilon_{zz} \end{pmatrix} \begin{pmatrix} E_x \\ E_y \\ E_z \end{pmatrix} = (\bar{\bar{\varepsilon}}) \begin{pmatrix} E_x \\ E_y \\ E_z \end{pmatrix},$$
$$\begin{pmatrix} B_x \\ B_y \\ B_z \end{pmatrix} = \begin{pmatrix} \mu_{xx} & \mu_{xy} & \mu_{xz} \\ \mu_{yx} & \mu_{yy} & \mu_{yz} \\ \mu_{zx} & \mu_{zy} & \mu_{zz} \end{pmatrix} \begin{pmatrix} H_x \\ H_y \\ H_z \end{pmatrix} = (\bar{\mu}) \begin{pmatrix} H_x \\ H_y \\ H_z \end{pmatrix}. \tag{1.3}$$

For isotropic materials $\bar{\bar{\varepsilon}}$ and $\bar{\mu}$ tensors are diagonal and with all the three elements identical (i.e. they can be represented in a scalar form ε and μ). In the case of anisotropic materials, the diagonal elements may be or not equal and non-diagonal elements can have non-zero values. There are special cases of anisotropy. For instance, if all the non-diagonal elements are zero and those on the diagonal are two equal and one different, the material is called uniaxial (the principal axis that is different is called the optical axis). If all the diagonal elements are different the material is called biaxial.

Another interesting property of materials is the bi-anisotropy. It is said that a medium is bi-anisotropic when there exists coupling between electric and magnetic fields. Then, the Eqs. 1.3 can be re-written as:

$$\begin{aligned} \mathbf{D} &= \bar{\bar{\varepsilon}}\mathbf{E} + \bar{\bar{\xi}}\mathbf{H}, \\ \mathbf{B} &= \bar{\bar{\zeta}}\mathbf{E} + \bar{\mu}\mathbf{H}, \end{aligned} \tag{1.4}$$

where tensors $\bar{\bar{\xi}}$ and $\bar{\bar{\zeta}}$ are the magnetoelectric and electromagnetic coupling constants. These relations imply that a bianisotropic medium is both polarized and magnetized at the presence of an electric or magnetic field. Finally, a chiral media which is actually a subclass of bi-anisotropic media deserve some attention. Chiral media are able to rotate the plane of EM

plane waves. They can be expressed in terms of CP as follows [Lin92]:

$$\begin{aligned} \mathbf{D} &= \varepsilon\mathbf{E} - j\varsigma\sqrt{\varepsilon_0\mu_0}\mathbf{H}, \\ \mathbf{B} &= \mu\mathbf{H} + j\varsigma\sqrt{\varepsilon_0\mu_0}\mathbf{E}, \end{aligned} \tag{1.5}$$

where ς accounts for the magneto-electric coupling and furthermore, contains the degree of chirality. Chiral materials are also referred as bi-isotropic materials since the constitutive parameters ε and μ are scalar quantities.

All these equations are useful to characterize the EM response of natural materials. Identically, under certain conditions wherein homogenization is ensured, metamaterials can be also characterized by the CP ε and μ.[1] Now, the particularity is that these CP can be, in principle, engineered and selected at will. Then, metamaterials can exhibit exotic EM behaviors depending on the selected CP values. As mentioned before, the index of refraction, n, is also frequently used for EM characterization and it can be written as:

$$n = \sqrt{\varepsilon\varepsilon_0\mu\mu_0} = \frac{\sqrt{\varepsilon\mu}}{c_0}. \tag{1.6}$$

When losses are taken into account a complex index of refraction can be defined as $\tilde{n} = n - j\kappa$ where κ is known as the extinction ratio. A material classification in terms of the values of the real part of ε and μ domain is displayed in Fig. 1.3. Four groups can be distinguished: double-positive (DPS), epsilon-negative (ENG), double-negative (DNG) and mu-negative (MNG) media.

Most of natural materials have ε and μ greater than 0 and therefore belong to DPS media. This is, in a way, the conventional EM behavior. To fully describe the four different media shown in Fig. 1.3, let us introduce first, the basic quantities involved in wave propagation of

[1] For the sake of simplicity scalar notation of ε and μ is taken from now on. When dealing with anisotropy, bianisotropy or chirality it will be explicitly said.

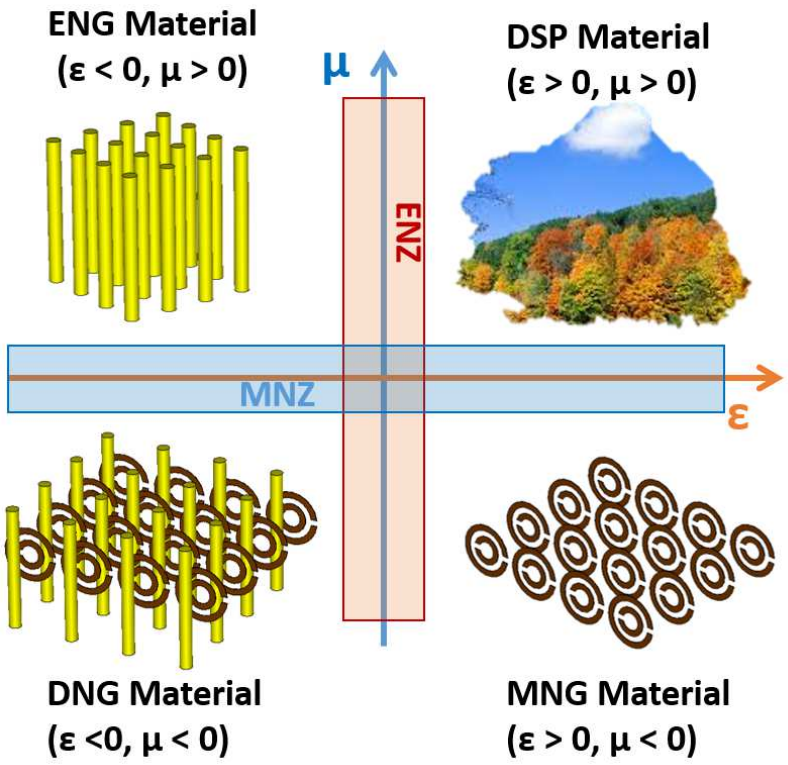

Fig. 1.3 Material classification in the ε, μ domain

monochromatic plane-waves that arise when solving Maxwell's equations.

$$\begin{aligned}
\mathbf{k} &= k\hat{k} = \omega\sqrt{\varepsilon\varepsilon_0\mu\mu_0} = \frac{\omega n}{c_0}, \\
\eta &= \frac{\mathbf{E}}{\mathbf{H}} = \sqrt{\frac{\mu\mu_0}{\varepsilon\varepsilon_0}} = \eta_0\sqrt{\frac{\mu}{\varepsilon}}, \\
v_p &= \frac{\omega}{k}, \\
v_g &= \frac{\partial\omega}{\partial k}, \\
\mathbf{S} &= \frac{1}{\mu}\mathbf{E}\times\mathbf{H},
\end{aligned} \tag{1.7}$$

where $\mathbf{k}$ is the wavevector (with k denoting the wavenumber (or phase constant) and $\hat{k}$ its unit vector giving the direction of phase variation), ω is the angular frequency ($\omega = 2\pi f$), η is the wave impedance defined as the $\mathbf{E}/\mathbf{H}$ ratio (being η_0 the free-space impedance), v_p is the phase velocity that is the velocity at which a fixed phase point of the wave travels, v_g is the group velocity which is generally the velocity at which the energy carried by the wave travels[2] and $\mathbf{S}$ is the Poynting vector which represents the energy flux density. In the case of monochromatic plane-waves propagating through DPS media, $\mathbf{k}$ and $\mathbf{S}$ are parallel and the triplet formed by $\mathbf{E}$, $\mathbf{H}$ and $\mathbf{k}$ is right-handed [Gri15]. In other words, the energy flux travels in the same direction as the wavevector. Usually, this kind of media are called right-handed media (RHM). Most of the conventional dielectrics available in nature belong to this category.

In 1968, V. G. Veselago [Ves68] theoretically investigated the opposite scenario. He predicted the implications of plane-wave propagation in a medium with simultaneously negative values of ε and μ (labeled in Fig. 1.3 as DNG). He demonstrated that such a medium presents also a negative n leading to antiparallel $\mathbf{S}$ and $\mathbf{k}$, and hence, to a left-handed $\mathbf{E}$, $\mathbf{H}$ and $\mathbf{k}$ triplet. In this case, the energy carried by the wave travels in the opposite direction as the wave propagates. This kind of media receives the name of left-handed media (LHM). Probably, the most evident and fascinating consequence is negative refraction that can be visualized when applying Snell's law to the interface between RHM and LHM slabs. Thus,

$$n_1 \sin\theta_1 = n_2 \sin\theta_2 \tag{1.8}$$

[2]This is not the case for anomalous dispersion cases.

where n_1 is the refractive index in the first medium (considered as RHM), θ_1 is the angle of incidence, n_2 is the refractive index of the second medium (assumed to be LHM) and θ_2 is the refracted angle of the wave propagating in that medium. In this scenario, the wave bents over into the opposite direction when passing from medium 1 to medium 2 compared to a conventional RHM medium. Thus, θ_2 gets a negative value. On the contrary, in conventional RHM materials θ_2 is always positive. A schematic picturing the above described situations is displayed in Fig. 1.4.

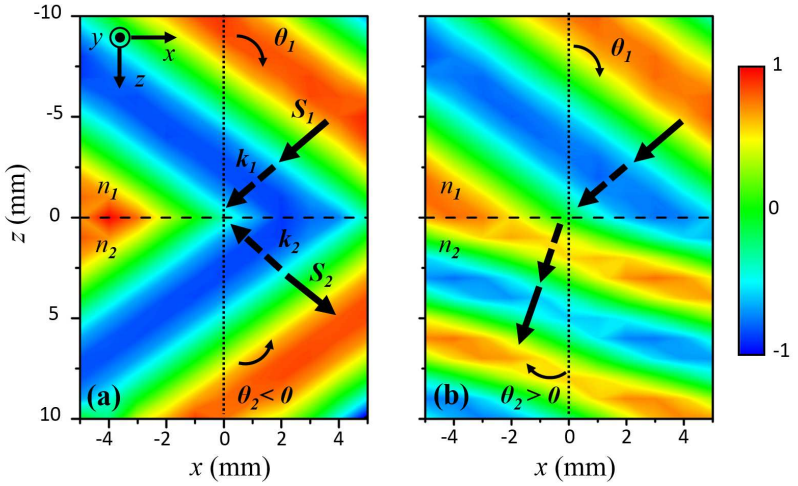

Fig. 1.4 Snell's law on LHM and RHM media. (a) LHM behavior; $n_1 = 1$, $\theta_1 = 45°$, $n_2 = -1$, $\theta_2 = -45°$. (b) RHM behavior; $n_1 = 1$, $\theta_1 = 45°$, $n_2 = 1.73$, $\theta_2 = 24°$. The horizontal dashed-black line delimits the interface between media 1 and 2. The vertical dotted-black line accounts for the normal incidence axis.

Veselago's theory did not attract the atention of the scientific community at the time it was proposed. In fact, the experimental proof of such theory was performed thirty years after Veselago's work. It is true that in the framework of the classical discipline "Artificial Dielectrics Materials", exotic EM phenomenons were studied by Jagadis Chandra Bose and Karl F. Lindman such as chirality in twisted structures [Bos98] and in a host medium loaded with helicoidal wires randomly oriented [Lin92]. However, it took some time until these man-made materials started to be deeply considered by the scientific community. In the 1940s, structures of this kind were used in the field of antenna engineering. Concretely, in 1946, Kock developed a metal-lens antenna becoming a breakthrough within the antenna community. He was able to demonstrate how EM waves could be focused by using conducting plates [Koc46]. This metal-lens provided a variable n from 0 to 1 where the tuning was done by controlling the separation distance between the parallel plates leading to a tuning of the effective ε. This n variation provided the required phase distribution at the ouptut of

the metal-lens in order to get a focus. This work by Kock inspired researchers to explore this field of artificial dielectrics [Col60, Bro53, Rot62] which can be considered the initial version of the current metamaterials.

In the quest for the LHM material proposed by Veselago, the first step was to emulate a media with $\varepsilon < 0$, i.e. ENG materials in Fig 1.3. Certain natural materials such as semiconductor compounds show ENG feature at THz frequencies due to covalent bonds from elements situated in columns 13 to 17 of the periodic table that correspond to poor metalic and non-metallic elements. These materials are usually called polar dielectrics and the frequency region where the ENG behavior occurs is termed as the polaritonic gap [Kit05]. In the context of artificial materials with ENG properties, Rotman already treated this issue in his early works where he proved the plasma behavior of a wire medium in the microwave regime [Rot62]. This theory was later revisited by Pendry *et al.* from another perspective [Pen96] setting the wire medium as the paradigm of ENG artificial materials.

It was a matter of time that Pendry and coworkers managed to achieve an artificial MNG material. In 1999, they proposed the split-ring resonator (SRR) and since then, it has become the most evident and probably studied metamaterial particle with MNG response [Pen99]. Among natural materials, certain ferrites and gyrotropic materials can exhibit MNG response. However, usually ferrites require an applied external magnetic field to excite the ferromagnetic resonance. For this reason, the SRR element has been the preferred option when synthesizing materials with MNG response.

The first artificial DNG (i.e. LHM) material was developed by D. R. Smith *et al.* in 2000 by combining a wire medium and arrays of SRR elements [Smi00]. Soon after, the first experimental demonstration of a negative index of refraction was reported at microwaves by R. A. Shelby *et al.* [She01]. These experiments were the spark that lighted up the growing interest in LHM and in a way marked the beginning of the metamaterials discipline. From then on, multiple theoretical and experimental works were reported. Among the multiple examples it is worth remarking the proposal of the novel concept of perfect lens introduced by Pendry [Pen00] which evolved lately to the development of "superlenses" [Zha08] and the invisibility cloak that envisages the possibility of hiding objects by guiding the EM waves around the object. In this context, the experimental realization of a cloaking device working in the microwave regime was another breakthrough in the metamaterials scientific community [Sch06, Liu09]. More recently, carpet cloaking devices have been proposed [Li08, Zha10, Est14, Ora15, Ora17].

In Fig. 1.3 the regimes where ε and μ are vanishingly small are termed as epsilon-near-zero (ENZ) and mu-near-zero (MNZ) regimes, respectively. Specifically, ENZ regime has attracted scientific community attention during the last decade. This kind of materials present

very interesting properties such as propagation constant and group velocity close to zero enabling fascinating electromagnetic effects such as tunneling, supercoupling and squeezing of electromagnetic waves [Sil06, Sil07, Alù07, Edw08]. Recently, graded-index lenses based on ENZ behavior have been proposed for millimeter and THz regime [Tor13, PP14, Tor15]. The combination of both regimes ENZ and MNZ lead to the epsilon-and-mu-near-zero (EMNZ), i.e. refractive index close to zero, which also shows very interesting properties in terms of guiding and scattering of EM waves. A extensive review of this topic can be found in [Lib17].

In summary, metamaterials are presented as composite materials that present extraordinary electromagnetic behavior opening many possibilities for scientific community to develop very exciting potential applications. In fact, this kind of revolution that accompanied the metamaterials advent has been very useful for revisiting the whole EM theory besides providing new concepts and fascinating ideas for future EM devices. In addition, it has been a commonplace for disciplines that have been working well apart for years as optics and microwaves.

1.2.1 Metamaterials Homogenization

In the previous section a historical review on metamaterials has been given. Therein, it has been stated that metamaterials are able to emulate any arbitrary CP, ε and μ and therefore, be treated as an effective medium. One of the intrinsic characteristic of metamaterials is that their elementary units are sub-wavelength. This may raise two important concerns regarding metamaterials homogenization. First, the effective medium approximation of a sub-wavelength unit cell periodic structure must be tested. Second, if this is finally accepted one should find the way of determining the effective medium parameters for a given periodic structure.

Among the scientific community there was some controversy regarding the effective medium consideration for metamaterials. In the end, it was finally accepted that a necessary condition for a correct homogenization was having a sufficiently large number of unit cells per wavelength. When the scale of the unit cell is much smaller than the wavelength the homogenization at the macroscopic level is valid [Smi06]. One of the most used numerical tool for effective medium theory was the inversion scattering parameter technique termed as retrieval [Smi05]). This retrieval technique must be fed by numerical (or experimental) data, namely the S-parameters (reflection and transmission), in order to obtain the effective parameters ε and μ of a generic slab. Despite giving quite accurate results, retrieval techniques experience some limitations. For instance, dealing with small reflection and transmission magnitudes may be troublesome and eventually lead to inaccurate results. In addition, some

considerations must be carefully taken. For instance, it must be assured that the sign of the root of the retrieved impedance as well as the branch of the real part of the refractive index do not violate causality laws [Che04]. The first retrieval techniques were applied to simple particles and only to their principal axes. However, the constant evolution of metamaterials required more sophisticated homogenization models able to retrieve the CP of metamaterials showing properties such as anisotropy for instance [Jia11]. In this thesis, a retrieval technique is used for synthesizing a metamaterial for radar applications in Chapter 2.

1.2.2 Metasurfaces: 2D Metamaterials

Metamaterials have recently evolved to their two-dimensional version. Thus, thin substrate slabs with an array of subwavelength elements patterned on the surface are used instead of the three-dimensional arrangements of sub-wavelength particles proposed at the beginning of the metamaterials era. In this way, more compact devices with full control over EM waves are attainable [Hol12, Kil13].

The term metasurface appears for the first time in the paper by F. Falcone [Fal04]. Subsequent works by R. Marqués *et al.* also use this terminolgy in the framework of two dimensional periodic single layers of SRR ans CSRR elements. However, this term acquired much more usage after the appearance of N. Yu *et al.* work [Yu11] due to the introduction of non-uniform and gradient metasurfaces. There, by abruptly tuning adjacent scatter elements they were able to modify the phase variation and steer the incident wave in a desired manner. These phase discontinuities led them to revisit Snell reflection and refraction laws and rewrite them as the Generalized Snell laws. Then, a wide number of light manipulation applications as quarter wave plates [Yu12, Zha13], asymmetric transmission devices [Pfe14] or performing mathematical operations on the incident wave [Sil14] have been proposed among many others [Yu14].

Now, we focus on the use of metasurfaces or, more generally, thin metamaterial based structures for sensing at the THz range. As introduced before, THz is a suitable regime for sensing applications. For instance, thin-film sensing has been a quite active field during the last years as compiled in the review article of J. F. O'Hara *et al.* [O'H12]. Recently, several works dealing with asymmetric resonators to excite high Q resonances have been presented [AN13, Sin14]. In addition, metasurfaces backed with a ground plane working in absorber configuration have been presented and found to be adequate for sensing applications [Con15, Yah15].

In this thesis, a cross-dipole element will be characterized as a classical and easy to design element with sensing capabilities for oblique waves. This starting point will evolve

towards more and more complex geometries reaching a labyrinth like metasurface with extreme values of sensitivity.

1.3 Extraordinary Transmission

Extraordinary Transmission (ET) has been widely studied since its discovery in 1998 by T. W. Ebbesen [Ebb98]. The ET manifests itself in the appearance of high transmission peaks for metallic screens with sub-wavelength apertures. In other words, ET can be defined as the ability to transmit waves through sub-wavelength holes drilled on metallic sheets. Thus, high transmission is observed below the cut-off of the apertures. Ebbesen conducted his experiments in the optical regime and fully developed a theory in terms surface plasmons polaritons (SPP) [Ebb98]. Previous works by Betzig also showed these high transmission peaks and related them to surface plasmons [Bet86]. However, the physical explanation was not as complete as the one developed by Ebbesen's in his seminal and subsequent works [MM01].

Let us briefly treat the basics of SPP to fully understand its connection with ET phenomenon. At optical frequencies, metals are known to behave differently as they do at microwaves and millimeter waves. In fact, electrons are not longer attached to the nucleus. They are freely moving within the conduction band as in a plasma medium. Then, the finite conductivity model has to be replaced by a more accurate model. Lorentz and Drude dispersion models comply with the aforementioned requirements. In particular, Drude's effective permittivity, ε_d can be written as follows:

$$\varepsilon_d(\omega) = \varepsilon_0 \left(1 - \frac{\omega_p^2}{\omega^2 - j\omega\gamma_c}\right), \tag{1.9}$$

where ω_p is the plasma frequency [$\varepsilon_d(\omega_p) \approx 0$] and γ_c is the collision frequency which accounts for damping effects due to the collision between electrons in motion. Let us picture a simple scenario wherein SPP can take place: an interface between a metal and air medium [see Fig. 1.5(a)]. As mentioned above, the metal can be modeled as a medium with dispersive complex relative permittivity $\varepsilon_m(\omega) = \varepsilon_m(\omega)' - j\varepsilon_m(\omega)''$ while the air can be described by a real permittivity approximately equal to the vacuum, i.e. relative permittivity, $\varepsilon_a \approx 1$. Looking at the interface in Fig. 1.5(a), one can solve Maxwell's equations to find the propagation constant, β of a propagating wave along the y axis with TM polarization. The

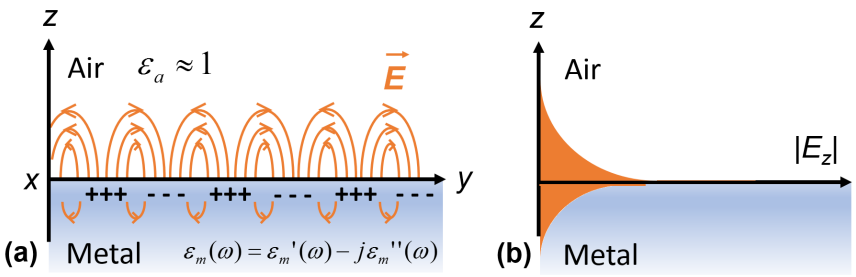

Fig. 1.5 (a) Interface between air and metal media with dielectric responses as shown. Electric field in an insulator-metal interface.

expression for β is given by [Mai07]:

$$\beta = k_0 \sqrt{\frac{\varepsilon_m \cdot \varepsilon_a}{\varepsilon_m + \varepsilon_a}}, \tag{1.10}$$

and is valid for both real (ideal lossless case) and complex ε_m. SPPs can take place at optical and near infrared frequencies where $\varepsilon_m(\omega)$ is predominantly real, negative and strongly dispersive (frequency dependent). Under these conditions, β takes complex values giving rise to propagating waves in the y axis decaying with distance. However, SPPs have also propagating character along z axis although in this case they are strongly evanescent, decaying very fast with distance. Figure 1.5(a) shows the electric field distribution of SPPs (although not shown, the magnetic field has only x-component) denoting the coupling of the EM incident field to charge oscillations in the plasma, i.e. metal, medium. In addition, the evanescent character of SPP in the z axis is given by E_z amplitude shown in Fig. 1.5(b). In the context of ET, the metal patterned sheet makes the SPP accessible for an incident wave impinging from the air. An efficiently coupling to the other interface is enabled and a transparency window that leads to high transmission is opened.

To visualize the SPPs role behind ET phenomenon an example of optical ET can be found in Fig. 1.6. A metallic holey screen whose structural parameters are like with those reported by L. Martín-Moreno *et al.* in [MM01] along with its response at optical and near infrared frequencies is presented. The simulated pierced metallic sheet is made of silver and its structural parameters can be found in the caption of Fig. 1.6. ET peaks arise well above the cut-off wavelength of the aperture[3] ($\lambda_c = \pi a/1.841 = 479\,\text{nm}$) and yet below the Rayleigh-Wood anomaly (RWA) that coincides with the periodicity, $d = 750\,\text{nm}$. The RWA represents a deep null in the transmission spectra occurring due to the onset of the first

[3] λ_c is calculated as the cut-off wavelength of the TE_{11} mode of a cylindrical waveguide.

diffraction order [Woo02, Ray07]. Moreover, the field distribution at the high transmission peak that arises at 789 nm is shown in Fig. 1.6(b). It can be observed that its profile resembles the distribution for SPPs. Therefore, it is true that SPPs play a role in the ET phenomenon occurring at optics and infrared frequencies. However, as it will be shown later, SPPs are indeed a particular case of more general complex waves previously described as classical phenomena within the microwave regime[Ish91].

Few years after Ebbesen finding, M. Beruete *et al.* replicated the experiment in the millimeter wave regime with even better results [Ber04]. Since at these frequencies metals can be certainly modeled by classical finite conductivity model, SPPs could not take place. Then, SPPs were disregarded as the origin of the ET phenomenon and rather explained in terms of classical complex wave theory. In fact, leaky waves were sufficient to explain the transmission peaks below cut-off. In another work also published in 2004, Pendry *et al.* proposed an effective medium approach to deal with holey perfect electric conductor (PEC) sheets. The surfaces waves that could take place in such hypothetical structure were termed as "spoof" plasmons [Pen04]. This work had a great impact among the optical community due to the equivalency to this phenomenon with "real" plasmons serving them as a terminology convenience of a more general notation in terms of complex waves.

Beruete's work opened up a great discussion on the underlying physics of ET and specially on the role of SPPs inspiring many others scientists in their subsequent studies of the field. A new perspective wherein equivalent circuit concepts were used was initiated by Beruete in [Ber07a]. Therein, the periodic problem was reduced to a single unit cell of the equivalent virtual waveguide with a circular diaphragm inside. The observed ET transmission peaks were related to the scattered high-order modes excited by the diaphragm.

F. Medina *et al.* followed the path initiated by Beruete and used the virtual waveguide approach to derive a more advanced equivalent circuit model presented in [Med08]. There, besides proposing a nice and accurate equivalent circuit model, the theoretical basis for understanding ET phenomenon was settled. ET peaks were related to the excitation of transverse magnetic (TM) modes that due to their capacitive character below cut-off and their divergence to infinity as they approach to cut-off, were able to compensate the intrinsic inductance introduced by the subwavelength apertures. Contrary to the commonly accepted theory in this field, Medina's paper proved that periodicity was not mandatory to obtain ET peaks. The requirement for obtaining ET peaks was to have TM modes near cut-off and this can be achieved for non-periodic scenarios. To this end, a structure composed by a cilyndrical waveguide with a subwavelength diaphragm inside was proposed. In this situation, the fundamental propagating mode is the TE_{11} and the first evanescent high-order mode is the TM_{11}. At a frequency yet below the TM_{11} cut-off, its associated capacitance cancels out the

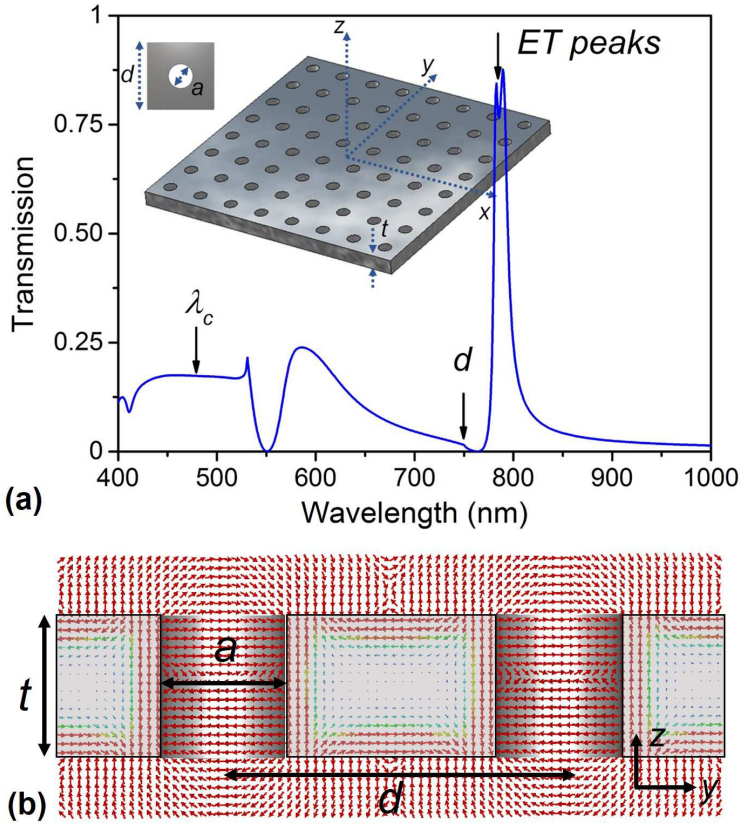

Fig. 1.6 Hole Array exhibiting ET at infrared and optical frequencies. (a) Transmission results of a metallic holey array under normal incidence. Dimensions: periodic lattice, $d = 750\,\text{nm}$; hole diameter, $a = 280\,\text{nm}$ and sheet thickness, $t = 320\,\text{nm}$. (b) Electric field distribution at 789 nm at yz plane cut.

inductance due to the diaphragm and gives rise to a total transmission peak (in the absence of losses). The excitation of transverse surface waves excitation is not possible and hence, SPPs cannot exist. This theory was later corroborated with an experiment and published in a subsequent work [Med10].

For some time ET peaks were uniquely related to TM evanescent modes. In 2006 E. Moreno *et al.* reported ET at optical frequencies for TE polatization case [Mor06]. In 2009, this was corroborated at THz frequencies in dielectric backed metallic holey screens frequencies [Kuz09]. Later, Beruete *et al.* provided a physical explanation supported by equivalent circuit techniques and experiments [Ber11b, Ber11a]. Most of the ET studies at that time were devoted to free-standing metallic sheets (where TM related ET modes were only possible) keeping this kind of ET unexplored. In fact, this phenomenon was termed as "anomalous" ET. This new discovery reinforce the way of reasoning wherein SPPs were

not essential for ET phenomenon since SPPs cannot supported in metals for TE polarization. The anomalous ET was also connected to the excitation of TE high-order modes in grounded slab configurations [Poz09]. Thus, in order to excite anomalous ET peaks, a proper selection of the dielectric slab parameters, namely, permittivity ,ε, and thickness, h, should be done [Ber11b].

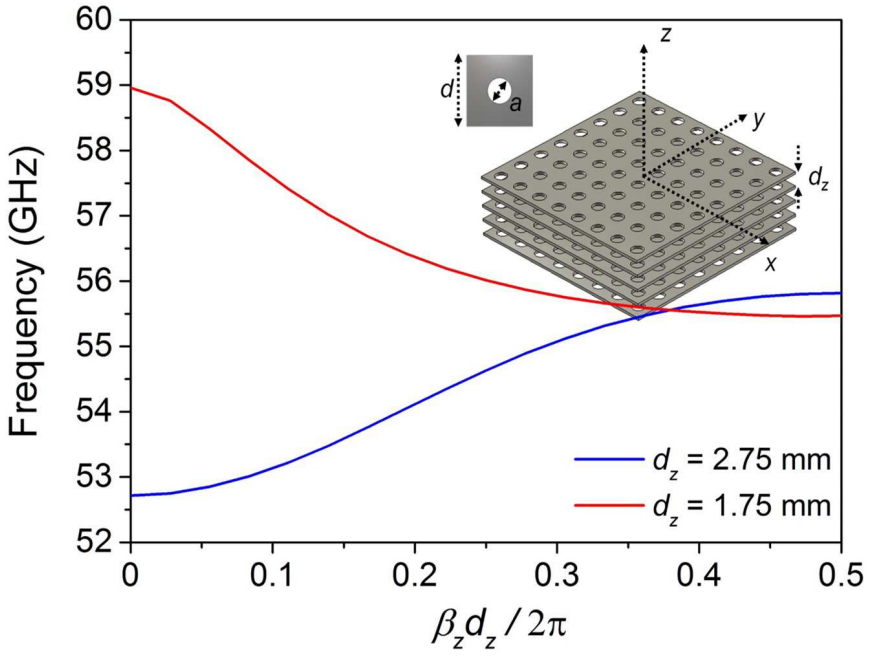

Fig. 1.7 Dispersion results of a SHA for longitudinal periods, $d_z = 1.75$ mm (red line) and $d_z = 2.75$ mm (blue line). Hole array dimensions: periodic lattice, $d = 5$ mm; hole diameter, $a = 2.5$ mm; and metal thickness, $t = 0.5$ mm.

ET phenomenon has strong bonds with metamaterials already presented in Sec. 1.2. Some metamaterials are based on structures showing ET phenomenon. Probably the most representative example relies on the stacked subwavelength hole array (SHA) also called fishnet structure. When two or more metallic perforated screens are stacked closely together a LHM medium can be synthesized. The first experiments corroborating this outstanding behavior were reported in the infrared regime by S. Zhang *et al.* [Zha05]. From then on, many researchers were interested on this structure and extended its performance to other frequency regimes contributing to the understanding of the physical phenomena behind its response. Specifically, this structure has been widely studied in optics and infrared techniques wherein this way of achieving negative refraction (among other interesting functionalities) is more efficient than the combination of metallic wires and SRRs used in for the first negative refraction experiments [Sha07, Val08, Liu08, Mar08, Ort09, GM11]. In the microwave regime the first SHA/fishnet structure showing negative refraction was reported by Beruete *et*

al. in [Ber06a]. It was also demonstrated that with a proper tuning of the longitudinal period, namely, the separation distance between hole array layers, switching from LHM to RHM propagation was enabled [Ber06a, Ber07c]. Figure 1.7 shows the dispersion diagram of a SHA with two different longitudinal periods d_z. The same structure as the one reported in [Ber06a] has been used. It can be clearly observed that for the long period a RHM behavior is obtained, i. e., the dispersion exhibits a positive slope and therefore the group velocity, v_g and phase velocity, v_p, are parallel. In contrast, for the short period case a negative slope is found and hence v_g and v_p are anti-parallel leading to LHM. These findings can be explained from transmission line theory and equivalent circuit concepts [Tor12, Tor16].

To sum up, ET has become a very important phenomenon widely studied within the last two decades. During this time, it was not free of controversy due to the lack of consensus for the origin of its underlying physics. Fortunately, this discussion was actually very enriching for the topic being benefited from the knowledge of two scientific communities, microwaves and plasmonics. In this Thesis, several devices based on ET structures will be presented besides adding our small contribution to the ET physics deriving an equivalent circuit.

1.4 Equivalent Circuit Approach for Two Dimensional Periodic Structures

Classical circuit theory assumes that the physical dimensions of the network under analysis are much smaller than the electrical wavelength. Then, the phase variation of the wave is unnoticed for the electronic components and Kirchoff's laws can be directly applied. In reality, circuit analysis theory is nothing else that a special case of EM waves described by Maxwell's equations shown in Eq. 1.1. All that matters for applying the correct theory in each situation is to consider the size of the circuits and electrical wavelength ratio. At small values, circuit analysis is enough to accurately characterize the networks. In turn, at larger values, field analysis and optical theories are required. When it comes to intermediate values, the analysis might be cumbersome.

Transmission line theory facilitates this decision when dealing with EM scenarios wherein the size of the components can be comparable to the electrical wavelength. For this reason, transmission lines have been widely used in the microwave regime becoming an essential element in microwave field theory. In Ref. [Oli84], A. A. Oliner reported a wonderful and educational review about this topic wherein, for instance, the origin of transmission line is traced back to the times of "firsts" electrical engineers as O. Heaviside. This enlightening review places microwaves in a position from which its theory, low frequency electronics

and optics can be easily approached. A transmission line represents a distributed parameter network whose size is comparable to the wavelength (or many wavelengths), where voltages and currents vary in magnitude and phase over its length [Poz09]. It brings along several concepts as characteristic impedance, attenuation constant, reflection coefficient, etc. that make it suitable for treating numerous EM problems such as propagation of plane waves, guided waves and resonances among many others. Thus, transmission lines combined with lumped elements (capacitors, inductances and resistors) form a complete toolbox for analyzing scattering and radiation problems.

In particular transmission line theory and lumped circuit elements can be very useful when applied to periodic structures. To this end, there are several major concepts that need to be addressed and put in context. First, the unit cell concept reinvented by S. Edelberg and A. A. Oliner[4] for studying phase array antennas enabled to reduce an infinite array to a single unit waveguide problem [Ede60]. This waveguide had peculiar walls termed as "phase-shift walls" where the phase difference between opposite walls depended on the periodicity and scan angle of the radiated or received beam. In the particular case of normal radiating or receiving waves, the two pairs of opposite waveguide walls can be considered as electric and magnetic walls respectively. Second, guiding structures, namely, waveguides, can be represented as transmission lines and the discontinuities inside can be modeled as lumped elements.

S. A. Schelkunoff was the first scientist who extended the concept of impedance to fields and waves [Sch38] and already treated some waveguide discontinuities problem in his book published in 1943 [Sch43]. Thereafter, the work on this topic was followed by N. Marcuvitz whose investigations were compiled in the outstanding book entitled *Waveguide Handbook* [Mar51]. These contributions enabled the practice of analyzing relatively complex EM problems through the simplified tools based on equivalent circuits. At that time, making calculations much more efficient and hence, simpler, was crucial due to the lack of powerful computer resources. Nowadays, with the available computers and computer aided design (CAD) numerical solvers, it may seem senseless keeping on developing these analytical tools. However, the computational cost of equivalent circuit techniques is still negligible when compared to full wave solutions and what is more, the physical insight that one can take out of them, is often lost when using CAD programs.

As mentioned before equivalent circuits can be used for analyzing scattering problems involving two dimensional periodic structures. Among microwave practitioners, probably frequency selective surfaces (FSS) are the most known as they have been widely used in radar

[4]It seems that H. G. Wheeler was the first one to use the waveguide approach for a periodic structure [Whe48].

systems [Mun00]. FSSs are periodic arrays of metallic resonant elements (or apertures on a metallic screen) that can have band-stop or band-pass behaviour. This resonance behavior can be modeled as classical LC resonant circuit connected in series for the array of patches and in parallel for the array of apertures (see Fig. 1.8). The element dimensions are comparable with the resonant wavelength (typically about half or one wavelength). They have been used as antenna hybrid radomes to reduce the radar cross section (RCS) by deflecting out frequencies lying out of the range of interest, as dichroic subreflectors (transparent at the operation frequency and opaque for other frequencies), circuit analog absorbers and meanderline polarizers [Mun00]. With the realm of metamaterials, FSSs have been extended to the THz regime where they are used as sensors, absorbers and spatial filters.

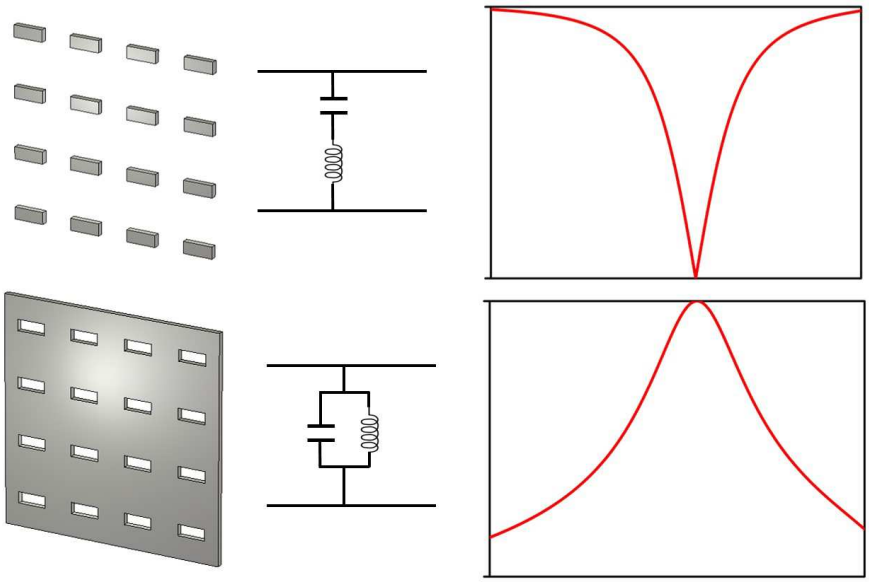

Fig. 1.8 Band-stop and band-pass FSS along with their equivalent circuit and transmission spectra.

FSSs became very popular in the 70's within the framework of radar systems. Then, many works dealing with their scattering properties and analytical techniques came out. Many works were published by recognized authors in the field such as B. A. Munk, R. Mittra or C. C. Chen (an appropriate review can be found in [Mit88]). Although, some initial works dealt with equivalent circuit analogies for treating metallic meshes at the infrared [Ulr67], the actual topic on FSSs/equivalent circuits took off in the 80's with the works of R. J. Langley *et al.* [Lan82a, Lan82b, Lan83, Lee85]. These works were oriented towards reducing the periodic problem to a simplified network of lumped elements. Multimode approaches were also derived to characterize planar strip gratings [Pal70, Gug89a, Gug89b]. The field remained quite active in the first decade of the 21^{st} century [Sav03, Mon07, Dub06, Dub09, Cos12].

An exhaustive review by F. Costa *et al.* on FSS equivalent circuit modeling has been recently published [Cos14].

In the previous section the great impact of Medina's paper on equivalent circuit for explaining the ET phenomenon has been already mentioned. This work preceded a very successful trajectory on equivalent circuits for explaining scattering problems of different nature by the Microwaves Group of the University of Seville [RB12, Mol14, RB15, Mes16]. Among these works, it is worth to highlight the paper by R. Rodríguez-Berral in [RB15] wherein a fully analytical equivalent circuit for slot/patch periodic arrays is derived for the very first principles. The computational efforts required to compute the scattering parameters over a wide bandwidth are very low. This approach is used in this Thesis for the analysis of annular apertures in Chapter 3. So to sum up, the equivalent circuit approach (ECA) can be considered not only as a powerful cost-efficient analytical tool but also a theoretic aid to understand the underlying physics of diverse EM problems.

1.5 Outline

The goal of this thesis is to provide a detailed description of the main results obtained from the research work on metamaterials and ET based devices conducted by the author during the study under the doctorate program "Communication Technology" from Universidad Pública de Navarra (UPNA), for the degree of Doctor of Philosophy (PhD) in Telecommunications Engineering. The present thesis can be divided in three differentiated parts.

In Chapter 2, the design of a metamaterial-based radome (meta-radome) is fully described. The meta-radome is intended to enhance the phased array antenna performance in the presence a blind-spot in the radiation pattern due to the antenna periodicity. The origin of such blind-spot is discussed and put into context. Two meta-radome solutions were designed in parallel from two different approaches: wire medium and meta-particle based radomes. A complete description of the design process is given, including the retrieval method for the meta-particle based radome. Finally, experimental results are shown for both solutions and proper conclusions are provided.

In Chapter 3, several devices based on different metamaterials and ET structures are presented. First, following the debate about ET introduced in this chapter, a discussion about discerning classical FSS and ET response in the framework of metallic meshes with annular apertures is conducted. This discussion is accompanied by theoretical results obtained with an ECA, complemented with numerical and experimental results. Later, unidirectional transmission devices with beam steering properties are theoretically and experimentally tested by means of a SHA structure assisted by a dielectric grating. In addition, a modified

version of the CSRR element is used for angular filtering purposes and for beam splitting when it is combined with a dielectric grating. Again, numerical and experimental results are reported.

In Chapter 4, the THz regime is targeted mainly for sensing purposes. A cross-dipole FSS is characterized as a sensor capable of operating at oblique incidence angles. From this structure, an evolution of towards enhancing the sensing performance is followed by using a cross-dipole working under extraordinary reflection (ER) regime.

Finally, the conclusions of the thesis and future work in this field are given in chapter 5. A materials and methods description of the simulation tools and experimental equipment is provided in Appendix A. The formulation required for the retrieval method used in Chapter 2 can be found in Appendix B. A summary of the author's merits is finally provided in Appendix C.

Chapter 2

Metamaterials for Radar Applications

In this chapter a metamaterial radome for phased-array antenna applications is demonstrated. The present work was part of a European Defense Agency joint investment program. The main goal of this project called METamaterials for Active eLEctronically Scanned Arrays (METALESA), was to investigate on how metamaterials could enhance antenna performance in the context of radar applications. The partners involved in this project were Fraunhofer FHR Institute from Germany, Thales Systemes and Aeroportes and ONERA - The French Aerospace Lab from France, University of Siena from Italy and TAFCO Metawireless and Universidad Pública de Navarra from Spain. The project was divided into different work packages pursuing antenna features improvement at different levels, i.e. feeding network, radome, etc. The author of this Thesis and coworkers were involved in the radome design process, corresponding to workpackage 3. This task was then subdivided into two different meta-radome solutions: one based on a wire-medium and another on a multilayer Jerusalem cross structure. The author was the main researcher involved in the second approach and participated in the discussions related with the wire-medium based solution which was developed by researchers from ONERA - The French Aerospace Lab. Both solutions are presented in this Thesis for completeness and for supporting the outlined conclusions of the work. In any case, along the Thesis it will be explicitly mentioned which results were directly generated by the author.

The main challenge of the project was to mitigate a blindspot in the radiation pattern without modifying the intrinsic geometry of the antenna array. In fact, this the mitigation had to be done accomplished solely by working at the radome level. Usually, the main function of radomes is merely to protect the antenna system from adverse weather conditions with the lowest impact possible in the radiation properties of the antenna. Then, design of a radome that is able to enhance antenna radiation to the extent that a blindspot is mitigated or even ideally eliminated, is a problem that requires a great degree of profound analysis

and imaginative solutions. Thus, the first task was to identify the blindspot origin to decide the best strategy to deal with it. It was found that the blindspot was a consequence of the onset of a grating lobe due to the array periodicity. Under this condition there exists a huge impedance mismatch between the antenna and free-space giving rise to a high active reflection coefficient value that causes a null in the radiation pattern [Mai05]. To attain this problem, as mentioned above, two distinct solutions were analyzed.

The first approach aims at reducing the coupling between elements by means of a matrix of metallic wires. In this way, the propagation of the wave originated by the onset of the grating lobe traveling along the surface of the antenna is forbidden. The second approach is formulated in terms of impedance and matching concepts. The adopted solution is based on wide angular impedance matching (WAIM) concepts. The metaradome architecture is a multilayer periodic arrangement of Jerusalem cross elements.

In this chapter a brief historical introduction of phased array antennas is given. Then, a detailed description of the design process for both adopted solutions is provided. Finally, an experimental demonstration of the proposed prototypes is performed and the obtained results are properly discussed. The work described was reported in two conference papers [Cré14, RU14] and one journal paper [RU16].

2.1 Phased Array Antennas

2.1.1 Brief History

First antenna arrays trace back to the 1920's [Han09]. They were proposed to overcome wire and aperture antennas limitations in terms of directivity, beam scanning and side lobes level. Antenna arrays are periodic arrangements of radiating elements that permit the synthesis of radiation patterns with very precise specifications. The synthesis of the radiation patterns is obtained by introducing the required phase variation between adjacent elements.

Commonly, the term of antenna array is used for those solutions where the radiation pattern is fixed. The radiating elements are specially designed to direct the beam to a certain space direction. On the other hand, phased array antennas are referred to those cases wherein the beam can be steered electronically by changing the phase and/or the amplitude of each element. However, there is a semantic disagreement between some authors about the concept of "phased array" [Han09]. Some authors use this term referring to beam steering or scanning. In contrast, other authors point out that, strictly speaking, every array is actually "phased" in agreement with our first definition for array antennas. In any case, and for the sake of simplicity, here, the term phased array is used for beam scanning steering antennas. Then,

a phased array consists of stationary antennas coherently fed where phase or time-delay variation at each element are used in order to scan a beam in a given angle in space [Mai05]. This phase/time control is performed electronically endowing phased array antennas with a great advantage with respect to fixed beam array antennas. However, the feeding network design for phased array solutions is much more complex than in fixed beam arrays.

The electronically active beam scanning capability provided by phased arrays placed them as backbone elements for radar systems since this topic took off in the 1960's. The publication of the seminal three-volume book *Microwave Scanning Antennas* by R. C. Hansen [Han64] was fundamental for the development of the field. This work was the first deep and extensive dissertation on phased array antennas. Principal emphasis was put on mutual coupling concepts as the basis of all array characteristics. Phased array antennas remained as a very hot topic in the 1970's as it is derived from the extensive and complete review article published by Stark in 1974 [Sta74]. Currently, phased-array antennas are crucial devices in the development of current and next generation systems for many military and civil applications.

2.1.2 Scan Blindness

One of the major issues of large phased array systems is the well-known artifact called scan blindness. It is a common undesired effect occurring in large phased array configurations dealing with great beam-scan ranges requirements. At certain scan angle the synthesized radiation pattern is dramatically affected leading to a "blindspot". In other words, the antenna cannot operate at this certain space direction compromising the angular range of the whole system.

Scan blindness can be seen as a strong mismatch of the active impedance. This phenomenon can be linked to two different causes, both related to the periodic nature of the structure and to the linear phasing. The first situation occurs when a higher order Floquet mode of the periodic structure transits from evanescent to propagating regime causing a strong interaction between the elements [Mai05]. This case is commonly referred to as the "onset of grating lobe" since it delimits the angular/frequency boundary between the diffraction-free and diffraction regimes. It only takes place if the inter-element spacing is greater than half the free-space wavelength. Then, this phenomenon is mostly critical for largely spaced array configurations.

The second scenario is linked to a mode interaction, namely, a synchronization of the phase velocities between a higher order Floquet mode and an eigenmode supported by the periodic structure. The seminal works published by A. A. Oliner *et al.* back in the 1960s provided a physical interpretation of this phenomenon where the reflection coefficient

nulls are related to guided and leaky waves [Hes65, Kni68]. Later, in the 1980s, Pozar and Schaubert studied the particular and simplified case of an array of printed dipoles [Poz84]. There, it was demonstrated that the scan blindness occurred when propagation constants of the first evanescent Floquet mode and the dominant surface/substrate wave are identical.

2.2 Description of the Problem

In this section the geometry of the used antenna prototype and its fundamental properties are outlined. Furthermore, the blindspot origin along with its implications in the antenna performance are analyzed.

2.2.1 Antenna Prototype

The phased-array antenna under study is an array composed of 100 patch elements arranged in a 5×20 rectangular topology. The total dimensions of the antenna are $A \times B$ =400 mm$\times$ 115 mm. To track accordingly every single element they were numerically labeled from left to right and from top to bottom. In this way, the central element can be identified as the 50^{th} element. Figure 2.1(a) shows a schematic of the array along with the system of coordinates and the E- and H-planes depicted. The final phased array antenna system, i.e., antenna plus radome, was intended to comply with the following requirements:

- Frequency bandwidth: 1 GHz with a central frequency of 10 GHz.
- Scanning range: $\pm 50^\circ$ in both E- and H-plane.
- Radome loss: -0.5 dB.

Each element of the array consists of a square patch antenna (length $a = 9$ mm) printed on a Rogers RO4003 substrate with permittivity $\varepsilon_r = 3.55$ and height $h_{subs1} = 0.81$ mm and fed with a coaxial probe. The patch element is embedded in a metallic cavity closed on the top by a parasitic square patch of slightly smaller dimensions than the radiating patch (length $b = 7.5$ mm). The parasitic element is also printed on a Rogers RO4003 dielectric substrate with height $h_{subs2} = 0.51$ mm. The cavity height, namely, the distance between patch and parasitic elements, is $H = 3$ mm. Finally, the inter-element spacing is $D = 19$ mm. A schematic of the unit cell is shown in Fig. 2.1.

To analyze the main performance of the initial antenna, the reflection coefficient of a single element and infinite array antenna was simulated with the commercial full wave solver CST Microwave Studio^{TM} (see Appendix. A). The operational bandwidth of the isolated

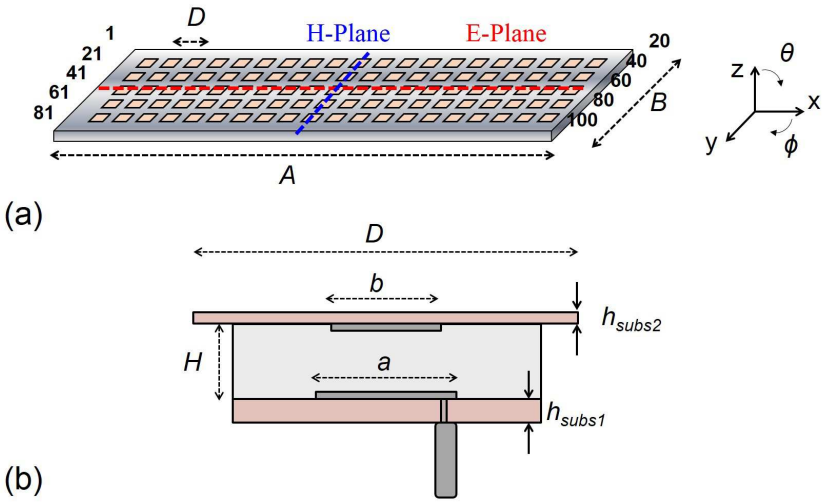

Fig. 2.1 (a) Antenna array schematic along with coordinate system and E- and H-planes. (b) Antenna element schematic. Dimensions: radiating patch length, $a = 9\,\text{mm}$; parasitic patch length, $b = 7.5\,\text{mm}$; bottom substrate thickness, $h_{subs1} = 0.81\,\text{mm}$; top substrate thickness, $h_{subs2} = 0.51\,\text{mm}$; cavity height, $H = 3\,\text{mm}$ and inter-element spacing, $D = 19\,\text{mm}$.

antenna is about 2 GHz as it can be seen in Fig. 2.2. However, for the infinite array the bandwidth is reduced due to coupling effects between elements. The results for the infinite array case are obtained for broadside scanning, namely, when all the elements are identically fed in terms of amplitude and phase.

In the case under study, a one hundred elements array, the results obtained (labeled as "Prototype" in Fig. 2.2) are half-way the single and infinite cases. The bandwidth is reduced due to the coupling effect between elements. The active reflection coefficient for the central element is added in Fig. 2.2. The active reflection coefficient is used here as an alternative to the numerical characterization of the full array that would have led to time-consuming simulations. To this end, the prototype antenna was measured and its coupling coefficients were evaluated[1]. This is done by injecting the incident signal in one element/port and collecting the reflected wave in another port while the rest of the ports are loaded with matched loads. The active reflection coefficient of the antenna can be obtained by applying the following equation:

$$R_n(\theta,\phi) = \sum_{i=1}^{N} S_{ni} e^{-j\varphi_i} \tag{2.1}$$

where θ and ϕ are the elevation and azimuth angle respectively, S_{ni} are the measured coupling coefficients and φ_i the phase difference between n and i elements.

[1]The measurement of the coupling coefficients was conducted by ONERA - The French Aerospace Lab

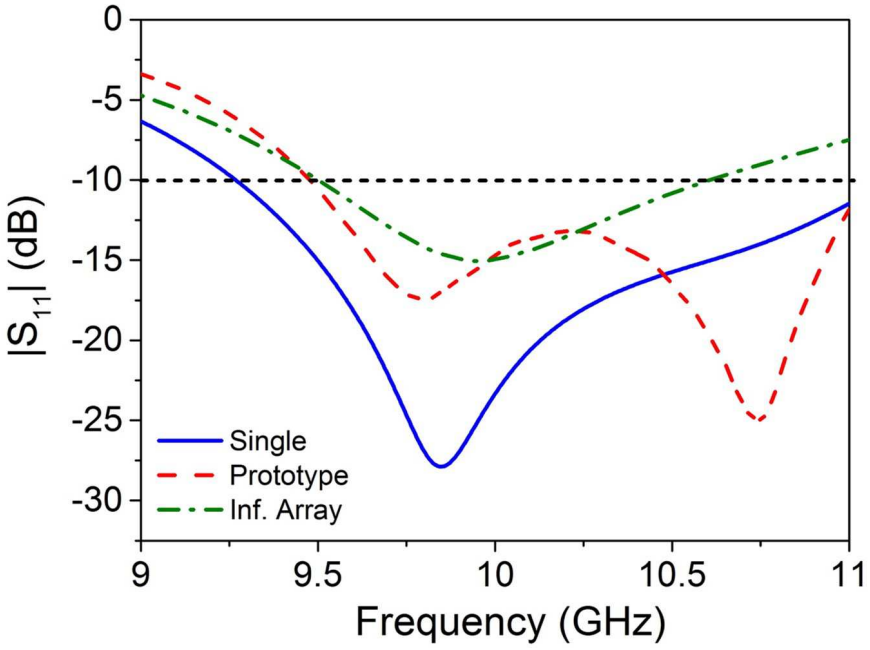

Fig. 2.2 Reflection coefficient of prototype antenna. Results for single antenna (solid blue line), prototype antenna (dashed red line) and infinite array (dash-dotted green line) cases are shown. The reflection coefficient for the prototype antenna corresponds to the central element, i.e. 50^{th} one.

The active reflection coefficient expression shown in Eq. 2.1 has been derived as follows. Let us consider an array with N elements. At each element the reflected wave, b_i, can be obtained from the combination of all the coupling contributions of the rest of elements.

$$\begin{aligned} b_1 &= S_{11}a_1 + S_{12}a_2 + \cdots + S_{1N}a_N, \\ b_2 &= S_{21}a_1 + S_{22}a_2 + \cdots + S_{2N}a_N, \\ \cdots &= \cdots + \cdots + \cdots + \cdots, \\ b_N &= S_{N1}a_1 + S_{N2}a_2 + \cdots + S_{NN}a_N, \end{aligned} \tag{2.2}$$

where the S_{ij} are the coupling coefficients between the i and j elements and a_i corresponds to the input wave at the i^{th} element. The input wave is then given as follows:

$$a_i = |a_i| e^{-jk\mathbf{r_i}\mathbf{r_0}}, \tag{2.3}$$

where k is the wavenumber, $\mathbf{r_i}$ is the position vector of the i^{th} element and $\mathbf{r_0}$ is the unit vector in the direction (θ_0, ϕ_0). Then, the active reflection coefficient for the element n^{th} by using

Eqs. 2.2 and 2.3 can be written as follows:

$$R_n(\theta,\phi) = \frac{a_n}{b_n} = \sum_{i=1}^{N} S_{ni}\frac{a_i}{a_n}. \tag{2.4}$$

Now, by assuming that the amplitude is equal in every port ($|a_i| = |a_n|$) and setting the phase of the n^{th} element as the reference, namely, $\varphi_n = 0$, we get to the expression for $R_n(\theta,\phi)$ shown in Eq. 2.1. The phase term, φ_i for each element with respect to the reference element can be calculated as follows:

$$\varphi_i = kT_{xs}(\theta,\phi) + lT_{ys}(\theta,\phi). \tag{2.5}$$

where k and l are the element indexes and T_{xs} and T_{ys} are the phase delays:

$$\begin{aligned} T_{xs} &= \frac{2\pi d_x}{\lambda_0}\sin\theta\cos\phi \\ T_{ys} &= \frac{2\pi d_y}{\lambda_0}\sin\theta\sin\phi, \end{aligned} \tag{2.6}$$

where d_x and d_y is the inter-element spacing along x and y axis respectively, λ_0 is the free-space wavelength, θ is the elevation angle and ϕ is the azimuth angle direction. In addition, the array radiation pattern can be calculated as:

$$F(\theta,\phi) = \sum_{i=1}^{N} f_i(\theta,\phi)a_n[1+R_i(\theta,\phi)]e^{jk\mathbf{r_n}\mathbf{r}}, \tag{2.7}$$

where $f_i(\theta,\phi)$ is the radiation pattern of the isolated i^{th} element.

By using previous equations, the active reflection coefficient, $R_n(\theta,\phi)$ versus frequency and scanning/incident direction can be evaluated (see Fig. 2.3). Reflection coefficient results regarding both E- and H-planes ($\phi = 0°$ and $\phi = 90°$ respectively) are depicted for the the 50^{th} (central element) versus frequency and scanning angle. The operational bandwidth of the fabricated antenna (defined as the frequency range where the active reflection coefficient is below -10 dB) extends from 9.5 GHz up to 11 GHz approximately at broadside scanning. However, for the E-plane a high reflection region appears from $f = 9\,\text{GHz}$ and $\theta = \pm 60°$ to $f = 11\,\text{GHz}$ and $\theta = \pm 25°$ approximately [see Fig. 2.3(a)]. As it will be discussed next, this high reflection region is linked to the onset of the grating lobe. On the contrary, for the H-plane this effect is much less dramatic.

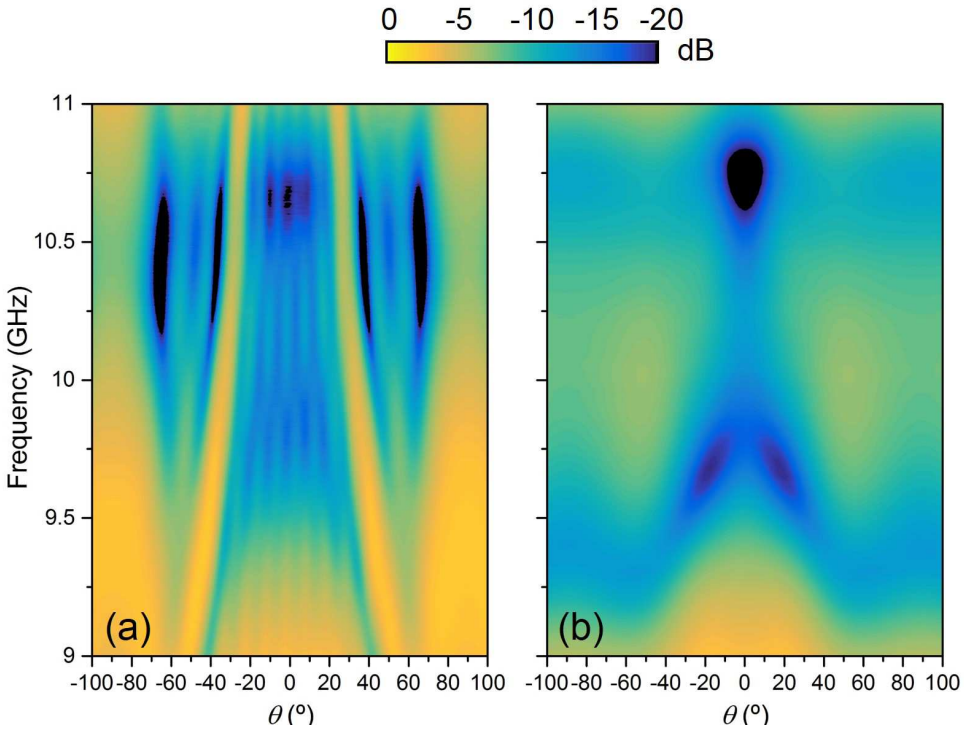

Fig. 2.3 Active reflection coefficient for the central element, R_{50}. (a) E-plane. (b) H-plane

2.2.2 Blindspot origin

As mentioned in Sec. 2.1.2, scan blindness may arise in phased-array configurations due to the interaction between grating modes and surface waves. Consequently, a blindspot can appear in the radiation pattern at the directions and frequencies where these interactions occur. In the present case, the blindspot coincides with the grating lobe emergence which is determined by the following well-known equation:

$$\frac{D}{\lambda_0} = \frac{1}{\sin\theta_{GL} + \sin\theta_0}, \tag{2.8}$$

where D is the inter-element spacing, λ_0 is the free-space wavelengh, θ_{GL} is the angle of the first grating lobe and θ_0 is the scanning/incidence angle [Mun00]. Figure 2.4 pictures this scenario for a one dimensional periodic array. There, an oblique plane wave with incidence angle θ impinges on the periodic array. Due to the phase difference caused by the extra path traveled by the wave for neighboring elements, a propagation condition for a wave having θ_{GL} direction can take place. If we particularize Eq. 2.1 to $\theta_{GL} = 90\,^\circ$ (grating lobe radiation

at grazing angle), the onset of the first grating lobe condition yields:

$$\frac{D}{\lambda_0} = \frac{1}{1+\sin\theta_0}. \tag{2.9}$$

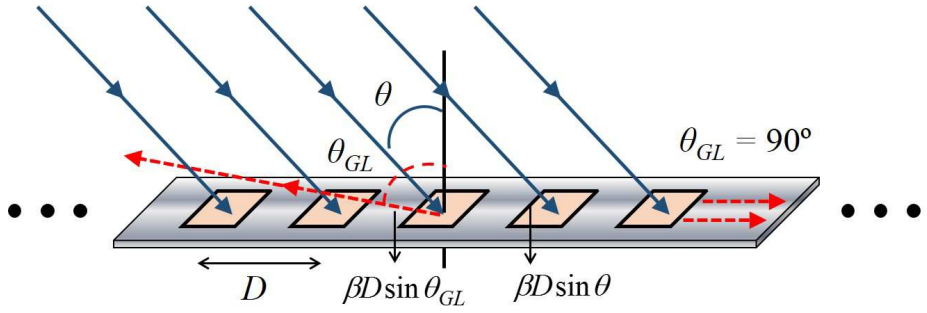

Fig. 2.4 Grating lobe appearance on a one dimensional periodic array under oblique plane wave incidence.

For instance, in our particular case, the onset of the first grating lobe at the central frequency of 10 GHz appears at $\theta_{GL} = 35.37\,°$. The appearance of grating lobes involve an energy transferred between the fundamental mode and the diffracted modes. Here, part of the total energy carried by the 0^{th}-order (or equivalently main beam) is transferred to the 1^{st}-order. To see this connection, the results of the reflection coefficient ($|S_{11}|$) for the main beam and transmitted energy ($|S_{2(m),1}|$) for the main beam ($m = 0$) and 1-order mode ($m = -1$) for an infinite array can be found in Fig. 2.5 [Cré14].[2]. There, the scanning/incidence angle is swept from 0 to 50 ° at a fixed frequency of 10 GHz. It can be observed that at the onset of the grating lobe (around 34.5 °) the reflection increases up to almost 0 dB (it does not reach 0 dB due to the losses in the substrate, otherwise total reflection would be obtained). Furthermore, a strong transmission dip appears for the $m = 0$ grating order along with an enhancement of the $m = -1$ order transmission. These results show that once the grating lobe enters into real space, it starts to radiate borrowing the energy from the main beam.

The onset of the grating lobe can be seen then as an extreme condition given by the periodic nature of the structure. This has been observed in previous results dealing with infinite array simulations. In terms of scan impedance this condition leads to a singularity going to infinity and hence results in an extreme impedance mismatch [Han09]. However, in finite structures this condition is somehow relaxed and the impact on the antenna radiation patterns is less dramatic. The impedance singularity is not so pronounced leading to a reduction of radiated power rather than a deep null. Figure 2.6 shows the element radiation

[2]Results obtained by ONERA - The French Aerospace Lab

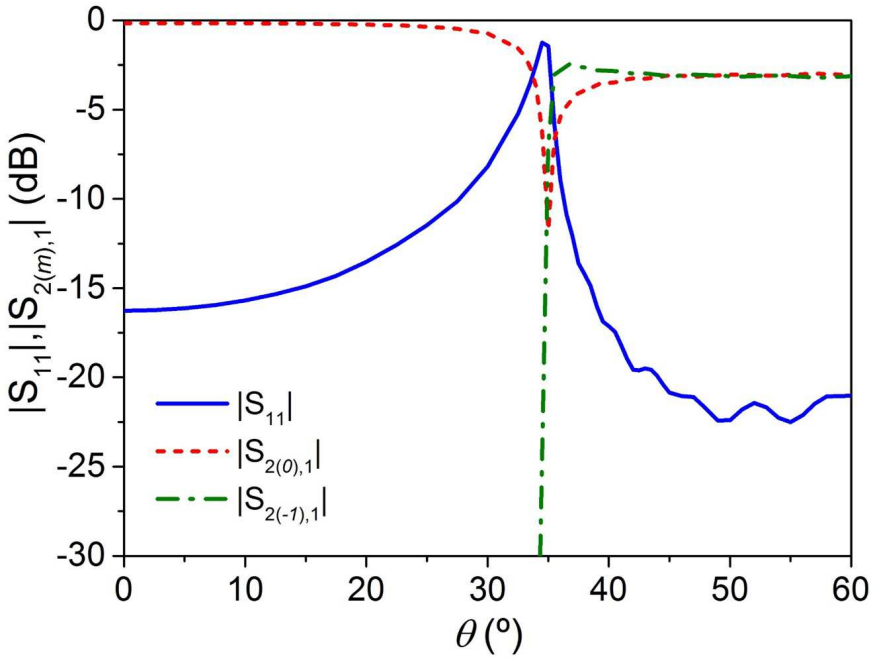

Fig. 2.5 Reflection (0-order) and transmission (0- and -1-orders) coefficients at 10 GHz versus scan/incidence angle, θ.

pattern for an array configuration of different sizes [Cré14].[3] As it can be observed, as the number of elements decreases the null in the radiation pattern at the onset angle is less marked. This fact permits a more accessible scenario when it comes to design a radome system able to cope with this strong mismatch condition.

2.3 Meta-Radome Design

In this section, a description of the adopted meta-radome solutions is provided. The first approach is based on a wire medium solution to reduce the coupling between elements at the grating lobe onset condition. Then, the excitation of the surface wave can be avoided and its associated energy can be retained in the main beam. The development of this solution was mainly carried by researchers at ONERA. Although the design process is not exhaustively described the basic assumptions and criteria are here reported.

The second approach is based on a Jerusalem cross metamaterial particle. Here, the radome is designed from a matching perspective and therefore the design is intended to match the antenna impedance to the widest angular range possible. In this section a full description

[3]Results obtained by Thales Systemes and Aeroportes.

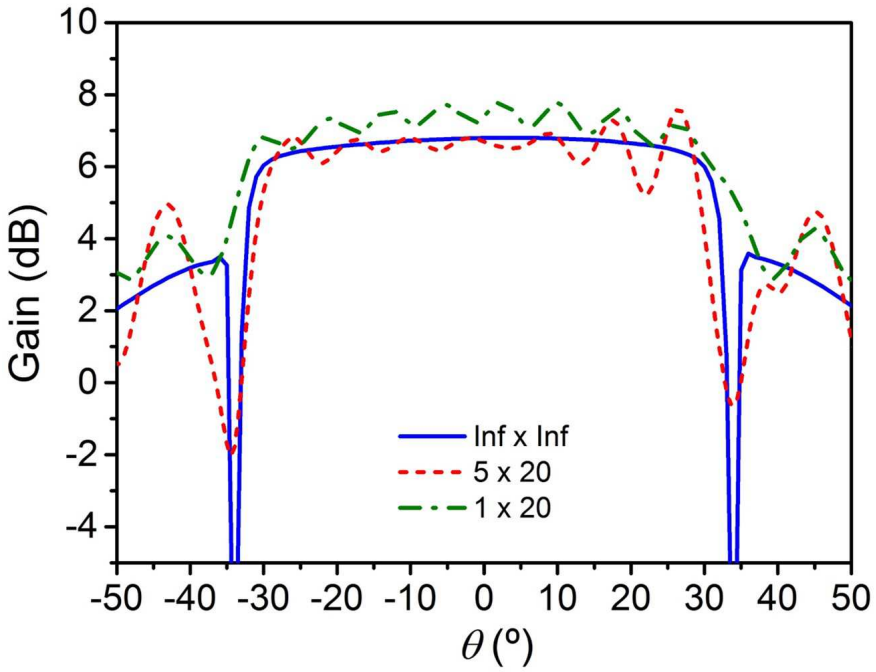

Fig. 2.6 Element radiation pattern of infinite and finite arrays. Infinite array (solid blue line), finite 5 × 20 array (dashed red line) and finite 1 × 20 array (dashed-dotted green line).

of the followed design process is given. Additional information regarding numerical and analytical techniques used in this process can be found in Appendix B.

At the light of the previous study in Sec. 2.2, it was decided to focus the design process on the central element and E-plane. First, the central element is the one which undergoes a stronger coupling from their neighbor elements, being then the most negatively affected by the blindspot. In addition, as shown before the blindspot manifests itself more dramatically in the E-plane.

2.3.1 Wire Medium Solution

The first solution adopted was a meta-radome based on the so-called Fakir's bed of nails [Kin83]. It consists of a periodic array of metallic pins connected to a metallic plane. In the absence of the metallic plane, this structure is referred to as wire medium. These structures have been known for some time in the microwave regime in the context of artificial dielectrics [Bro53]. However, they have been largely revisited with the appearance of metamaterials and its capability of emulating a plasma medium and hence, showing an effective permittivity with negative values. In 2003 P. A. Belov *et al.* published a paper highlighting the importance of the spatial dispersion in the axis parallel to the conducting wires. In past works, the wire medium was assumed to have local dispersion [Kin83].

Belov's work triggered many others scientists to follow research lines towards the derivation of accurate homogenization models able to embody the physics of wire media and bed of nails structures [Sil08, Yak09]. Due to the angular and frequency filtering properties of these structures they have been experimentally used for subwalength imaging and theoretically proposed for redshifting ET transmission peaks under TM polarization while inhibiting TE polarization peaks [Bel06, NC13].

Here, the argument for choosing this kind of structure is twofold. First, the stop band behavior of the bed of nails may prevent the propagation of the wave associated to the onset of the grating lobe. Second, its geometry is compatible with the layout of the antenna array and a practical implementation without modifying the antenna geometry becomes possible. The modeling of the wire medium is done by applying the homogenization models available in the literature [Sil08, Yak09]. From these models, there are two major indications to be considered for the design of wire medium structures. First, the wire length, L determines the upper frequency of the stop band as follows:

$$f \geq \frac{c}{4L\sqrt{\varepsilon_r}}, \tag{2.10}$$

where c is the speed of light and ε_r the dielectric permittivity of the host material of the wire medium. Furthermore, the plasma frequency f_p, namely, the frequency at which the real part of the effective permittivity of the wire medium is equal to zero, is calculated as:

$$f_p = \frac{c}{a\sqrt{2\pi\varepsilon_r}}\left(\ln\left(\frac{a}{2\pi\varepsilon_r}\right)+0.525\right)^{-1/2}, \tag{2.11}$$

where a is the inter-wire spacing and r the wire radius.

With this in mind, an initial design can be implemented by evaluating the wavenumber along the x direction, k_x (see inset in Fig. 2.7), for surface wave modes propagating along the wire medium by solving the following transcendental equation [Yak09]:

$$k_r k_p \tan(k_r L) - k_x^2\sqrt{k_x^2+k_p^2-k_r^2}\tanh\left(\sqrt{k_x^2+k_p^2-k_r^2}\right) - \varepsilon_r\sqrt{k_x^2-k_0^2} = 0, \tag{2.12}$$

where $k_r = k_0\sqrt{\varepsilon_r}$ is the wavenumber in the host medium and k_p is the plasma wavenumber. Figure 2.7 shows the real and imaginary parts of k_x for different combinations of L and a. As it can be seen, the stop band location is mainly governed by the length of the wires, L, with little dependence with the distance, a.

For a practical design and feasible integration of the bed of nails metamaterial within the antenna, a number of constraints were considered. First, the available space between the

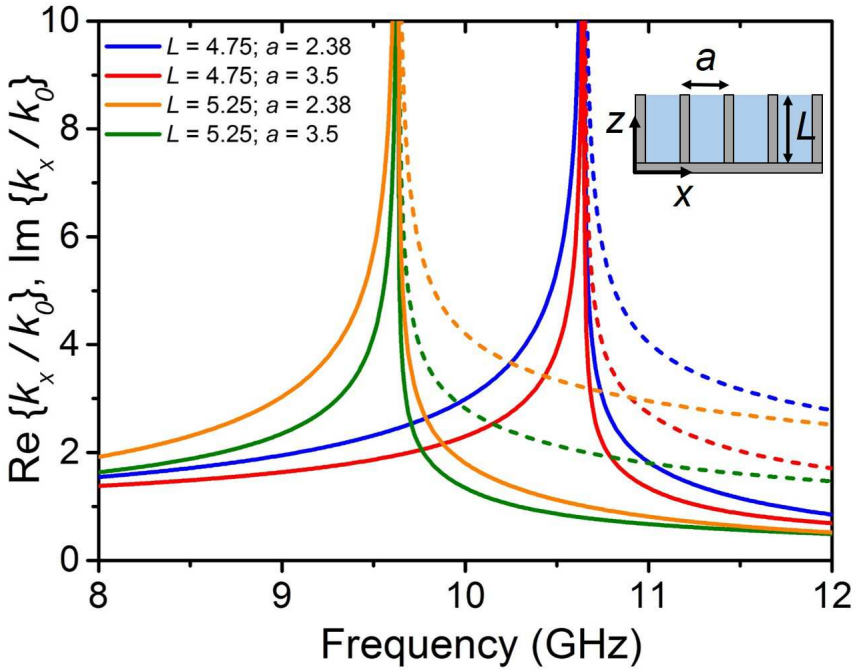

Fig. 2.7 Real (solid line) and imaginary (dashed line) part of the normalized tangent wavenumber k_x for surface wave modes in wire media for different parameter combinations.

radiating elements was determined by the array periodicity and the size of the cavity. In fact, a gap of only 7 mm was available to place the artificial medium. Furthermore, the metamaterial structure had to be placed over the layer supporting the parasitic patch to retain the original configuration of the antenna. Consequently, the metal strip that connected the wires was not in contact with the ground plane. Then, the theoretical formulas presented above could not accurately predict the stop band frequency and a complete numerical optimization was required and therefore, carried out.

The obtained solution consists of a double row of metallic wires ended with a metallic disk and embedded in a host dielectric block with permittivity $\varepsilon_r = 2.2$ [see inset and caption of Fig. 2.8(b)]. For the practical implementation, three additional dielectric layers were needed. The wires were implemented as metal vias in the first two layers whereas the third layer was used for impedance matching purposes. The effect pursued with this metaradome solution was to redirect the energy linked to surface waves to the main beam. This can be done due to the stop band properties of the metamaterial that forbid propagation of surface waves as those originated at the onset of the grating lobe. Figure 2.8(a) shows the simulated reflection and transmission coefficient for the 0- and 1-orders (similarly as Fig.2.5) [Cré14].[4]. It can be observed that now, the 0-order reflection coefficient does not show a high level peak

[4]Results obtained by ONERA- The French Aerospace Lab

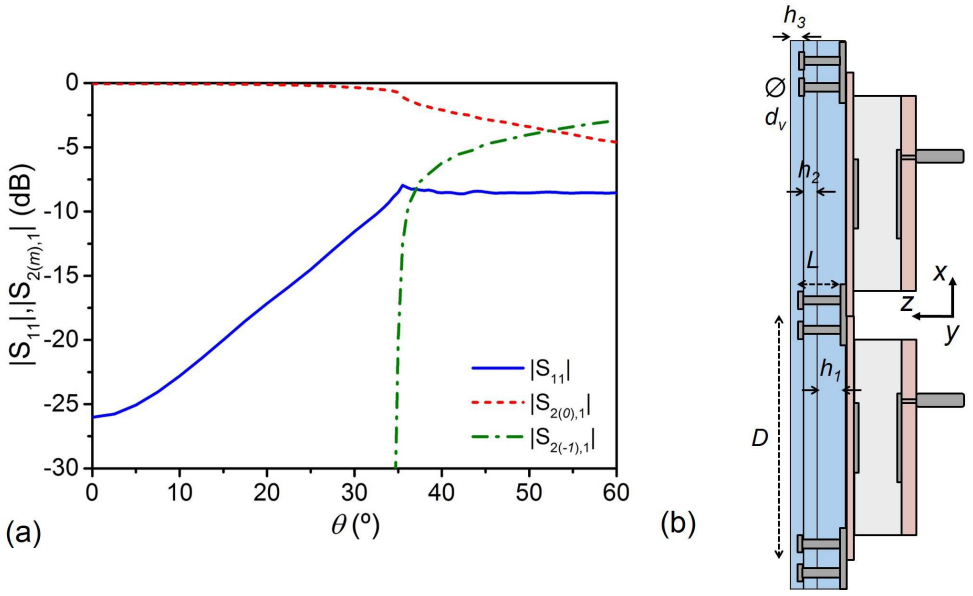

Fig. 2.8 (a) Reflection (0-order) and transmission (0- and -1-orders) coefficients at 10 GHz versus scan/incidence angle, θ for the antenna with the wire medium metaradome. (b) Schematic of the wire medium metaradome. Dimensions: inter-element spacing $D = 19$ mm; additional dielectric layers thickness $h_1 = 3.175$ mm and $h_2 = h_3 = 1.575$ mm; vias diameter $d_v = 0.4$ mm; spacing distance between vias in y direction, $a = 2.38$ mm; vias length $L = 4.75$ mm.

at the grating lobe condition which is desirable. Furthermore, the amplitude of the 0-order transmission coefficient does not drastically drop and the 1-order transmission level becomes only important at large scan/incidence angles. Then, it may be inferred that the energy is kept in the main beam and hence, improving the performance of the antenna in terms of radiation patterns.

2.3.2 WAIM Jerusalem cross-based metaradome

In this section the results concerning the second approach are described. Here, the design of the metaradome is carried out from a matching impedance perspective. In the past, conventional isotropic dielectrics, were used as wide angle impedance matching (WAIM) devices to extend the angular domain in phased array systems [Mag66]. By using metamaterials it is possible to synthesize anisotropic sheets that offer a wider range of matching possibilities. Recently, metamaterial inspired anisotropic WAIMs have been theoretically proposed for an array of open-ended waveguides [Saj10, Oli15] and for improving the performance at large scanning angles for a phased array antenna [Sil15]. In both cases, the WAIM was designed

in absence of extreme impedance conditions (grating lobes) which permits the matching for the targeted scanning angles while keeping other directions and cardinal planes unaltered.

In Sect. 2.2.1 the active reflection coefficient, $R_n(\theta,\phi)$, was evaluated from the measured coupling coefficients of the prototype antenna. Then, the scan antenna impedance, $Z_n(\theta,\phi)$, can be written as follows:

$$Z_n(\theta,\phi) = \eta_0 \frac{1+R_n(\theta,\phi)}{1-R_n(\theta,\phi)}, \tag{2.13}$$

where η_0 is the free space impedance. In terms of impedance, the onset of the grating lobe is seen as a large impedance mismatch between the antenna and free space. A very abrupt impedance profile against the scanning angle is then expected. Here, an active reflection coefficient level below -10 dB is targeted for the whole angular range by means of an anisotropic WAIM optimized at the central frequency 10 GHz and for the central element.

To this end, a two-step design process has been followed. The detailed description of the design process can be found in the Appendix B. First, it was required to find a homogenous anisotropic slab with ad-hoc constitutive parameters that provided the required impedance

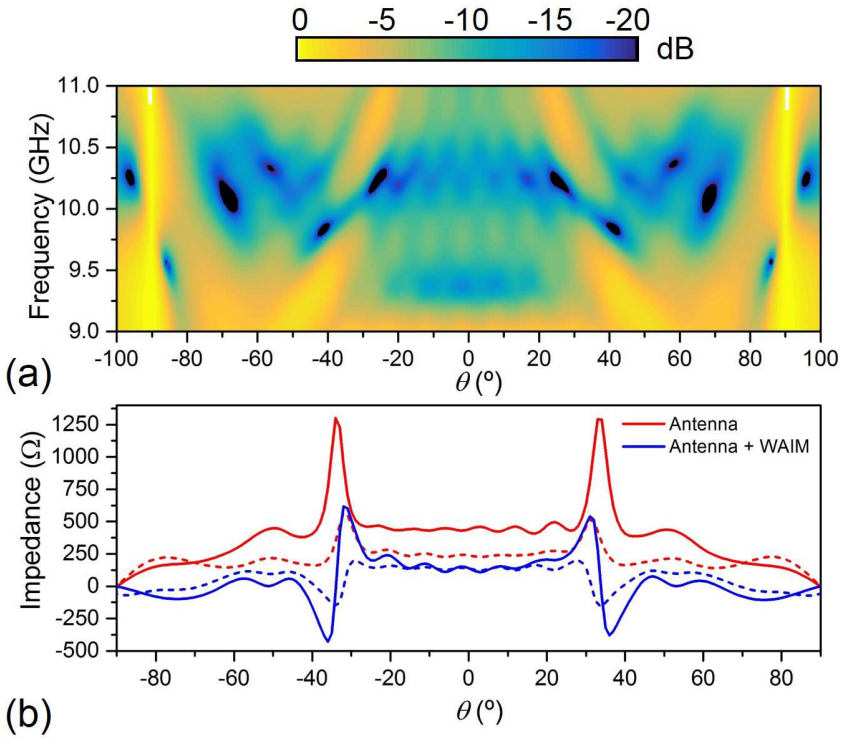

Fig. 2.9 (a) Reflection coefficient in the presence of the obtained homogeneous WAIM versus frequency and scan angle, θ. (b) Scan impedance of the antenna at 10 GHz in the cases with (blue) and without (red) the WAIM homogeneous slab. Solid line accounts for real part and dashed-line do it for imaginary part of the scan impedance.

behavior. To do this, classical transmission line theoretical concepts and analytical equations for oblique incidence on anisotropic finite thickness slabs were applied [Col60]. Then, a homogeneous anisotropic WAIM slab able to adapt the antenna impedance to the free space was obtained by running an optimization routine. The obtained WAIM was not necessarily optimal for other array elements and/or frequencies. In addition, a number of constraints were imposed in terms of feasibility and available commercial substrates. Then, an uniaxial anisotropic homogeneous WAIM with only electric response was proposed. The final constitutive parameters for the WAIM candidate were the following: $\varepsilon_{xx} = \varepsilon_{yy} = 6.8$, $\varepsilon_{zz} = 4$ and $\mu_{xx} = \mu_{yy} = \mu_{zz} = 1$. The thickness of the homogeneous slab was $d = 4.812\,\text{mm}$. Figure 2.9 shows the scan reflection coefficient in the presence of a homogeneous WAIM with the outlined constitutive parameters. As it can be seen, the matching at the central frequency improves up to levels below -10 dB for the total scanning view. On the other hand, the performance at other regions of the frequency/angle area is deprecated when compared with the response without the anisotropic WAIM [see Fig. 2.9(a)].

To prove that the impedance matching is considerably improved thanks to the anisotropic WAIM, the scan impedance (real and imaginary parts) of the antenna with and without metaradome is shown in Fig. 2.9(b). As it can be observed, with the homogeneous WAIM the impedance is modified to values close to the free space at the blindspot direction. However, the scan impedance varies also at other angles where the antenna without WAIM was well-matched, leading to a possible reduction of the performance in these directions.

Once the ideal homogeneous WAIM was obtained, the next step was to synthesize a metamaterial exhibiting the same constitutive parameters. For practical reasons, the WAIM design was simplified in order to get a feasible metamaterial particle. As mentioned above, the final results were limited to WAIMs exhibiting uniquely electric response. This can be synthesized with a purely electric resonator such as a Jerusalem cross. This particle, among others, has been widely used in frequency selective surfaces (FSS) applications. The major difference here is that the operation frequency is much below the self-resonance of the particle. A retrieval technique was used as a design tool for finding the specific cross shape that delivered the targeted constitutive parameters [Smi05, Jia11]. The retrieval routine was iteratively launched and fed with the scattering parameters obtained by full wave simulations. A detailed description of this process can be found in Appendix B. The retrieved effective constitutive parameters ε and μ along with the final metamaterial particle are shown in Fig. 2.10. It can be seen that at 10 GHz the values correspond with those obtained for the homogeneous WAIM. However, a certain dispersion is observed in the frequency response. The fabricated metaradome consists of a multilayer structure composed by three Rogers 4003

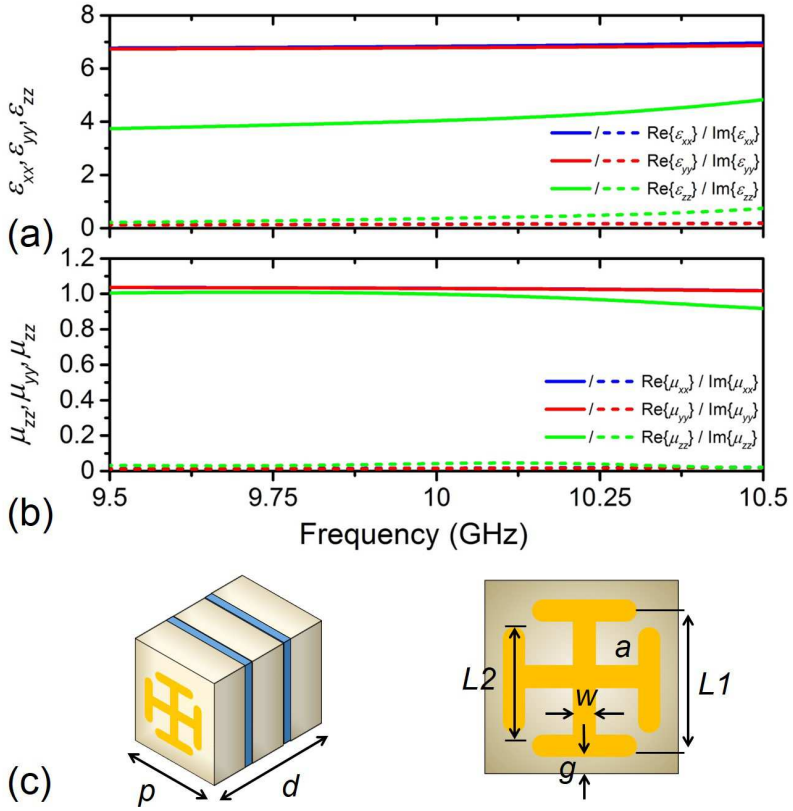

Fig. 2.10 Retrieved constitutive parameters, ε and μ for the synthesized metamaterial particle. (a) ε. (b) μ. (c) Metamaterial unit cell. Dimensions: unit cell lattice, $p = 2\,\text{mm}$; total thickness, $d = 4.812\,\text{mm}$; cross length, $L_1 = 1.6\,\text{mm}$; arm length, $L_2 = 1.1\,\text{mm}$; metal width, $w = 0.2\,\text{mm}$; distance between adjacent elements, $2g = 0.4\,\text{mm}$. The grey slabs correspond to the substrate layers and the thinner blue slabs are the prepreg films.

printed substrate layers glued by Rogers 4350B prepreg films. A foam substrate was inserted between the antenna and the metaradome for attachment purposes.

2.4 Experimental Results

Experimental demonstration of the two previously described metaradomes was run in parallel at two different consortium partnerships facilities, ONERA and Fraunhofer Institute. The wire medium metaradome characterization was performed in ONERA while the WAIM solution was tested at Fraunhofer facilities. In both cases, the measurements were conducted in anechoic chambers and each element was sequentially connected to a vector network analyzer (VNA) while the others were terminated with 50 Ω loads. With this measurement technique that includes the array environment of each radiating element, the complete antenna pattern could be calculated by summing the 100 radiation patterns by using Eq. 2.7. However, here, in line with the rest of the Chapter, a special focus is put on the central element.

Figure 2.11 shows the E-plane normalized pattern for the central element of the array antenna without [panel (a)] and with the wire medium metaradome [panel (b)]. As it can be observed, the blindspot can be clearly identified by the two low-level symmetrical lines across the angular- frequency space in Fig. 2.11(a). However, when the wire medium metaradome is added, the blind directions are significantly mitigated for a wide band operation. This enables an increment of the gain at blindspot direction. On the other hand, the frequency bandwidth is reduced at the lower part of the range. In addition, the H-plane radiation pattern is worsened (not shown here). All in all, the results delivered by this solution meet the main objective that was mitigating the blindspot direction.

The performance of the WAIM metaradome is less effective in suppressing the blindspot. Figure 2.12 shows again the E-plane normalized radiation patterns for the central element without and with the designed metaradome. It can be seen that the radiation pattern is negatively affected at the presence of the metaradome. A more careful scrutiny denotes a small reduction of the grating lobe at 10 GHz and close to it, 9.9 GHz (see Figure 2.13). However, the blindspot was split into two dips of reduced level. This is surely a consequence of the narrowband nature of the WAIM solution combined with the very abrupt profile of the active impedance exhibited by the antenna nearby the blindspot angle. It should be recalled that the WAIM metaradome was specifically optimized at the central frequency and at the blindspot angle. Then, its performance might be worse at neighboring frequencies/angles. As mentioned before, the active impedance has a very extreme value at the blindspot and an abrupt variation over the scanning angle. For these reasons, little differences between the predicted and the actual impedance can lead to strong disagreement between simulation

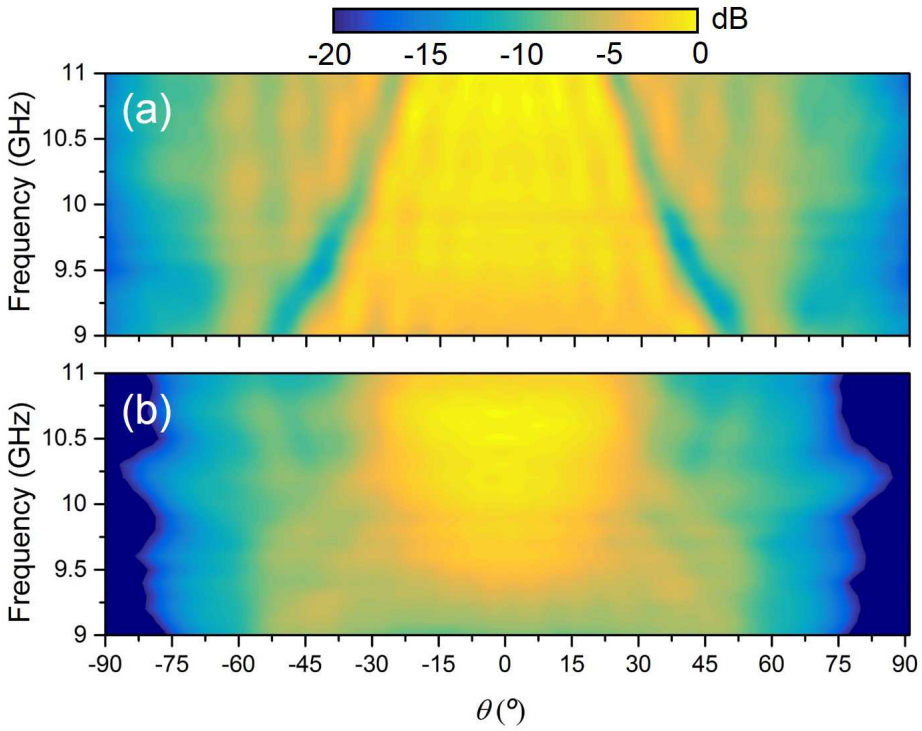

Fig. 2.11 Measured radiation patterns (normalized to the maximum) for the wire medium based metaradome. (a) Prototype antenna. (b) Prototype antenna with the wire medium based metaradome.

and measurements. Furthermore, the transmission line approach followed here is a first order approximation wherein the possible coupling between the antenna and the metaradome is not considered. The strong ripple observed in the experimental radiation patterns can be consequence of a standing wave excitation between the antenna and the metaradome. The results obtained show that the WAIM solution is not appropriate for the purposes targeted here. However, it should be noticed that in scenarios without blindspot presence, the antenna radiation properties could be benefited from WAIM metaradomes whose constitutive parameters can be designed ad-hoc.

2.5 Concluding Remarks

Given the results obtained, the optimal solution for a wide band and effective blindspot mitigation is the wire medium rather than WAIM based metaradome. The WAIM solution is not appropriate in the sense that the scan impedance variation with frequency and angle, and also between array elements, is very steep. This leads to an homogenous WAIM solution with a very narrow response and with extreme constitutive parameters that end up causing a

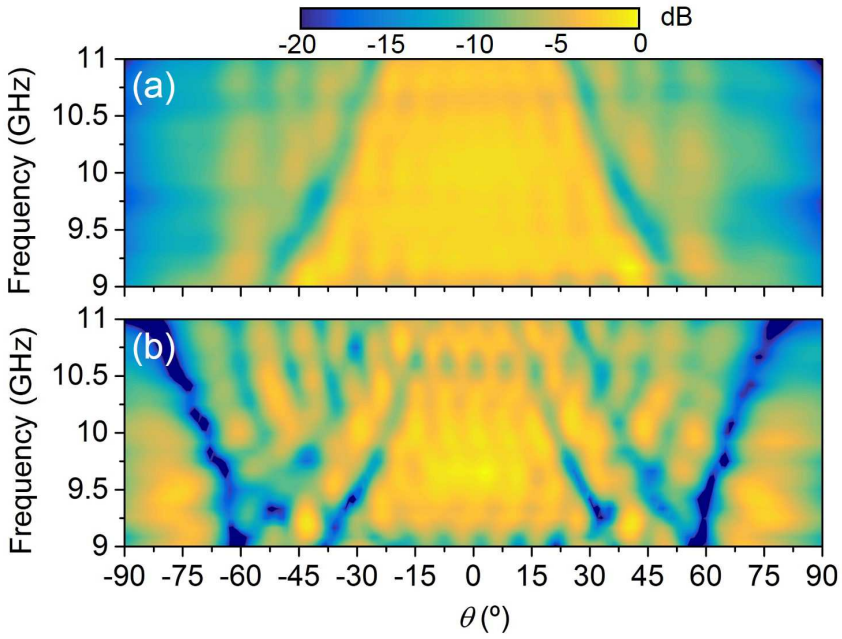

Fig. 2.12 Measured radiation patterns (normalized to the maximum) for the WAIM based metaradome. (a) Prototype antenna. (b) Prototype antenna with the WAIM based metaradome.

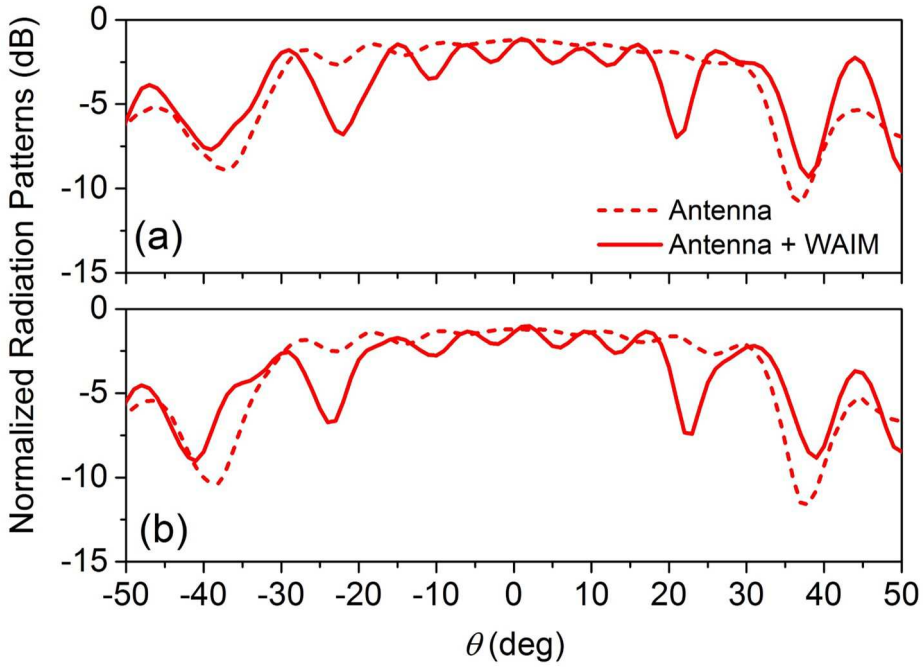

Fig. 2.13 Measured radiation patterns (normalized to the maximum) for the WAIM based metaradome. (a) 10 GHz. (b) 9.9 GHz

strong coupling between the antenna and the metaradome. For instance, it can strongly reflect other angles of incidence and negatively contribute to the metaradome-antenna coupling. In a different scenario where either the grating lobe is not so strong (e.g. by using the wire medium presented) or simply it does not appear, the WAIM metaradome can be appealing for enhancing the scanning field of view by improving the matching between the antenna and the free-space. In these situations the antenna impedance will be free of extreme values and steep profile and hence a WAIM solution will be more effective.

To sum up, the wire medium solution has been presented as a successful solution that may open up a very interesting avenue for metamaterials in the design of radomes for phased-array antennas in the special cases where reducing the inter-element spacing is not possible and grating lobes are present. Although, the WAIM based solution was not adequate for solving the same problem, it could be potentially combined with the wire medium solution to enhance the matching of the antenna and improve the matching over a wider scanning range. In addition, a further study on the feasibility synthesis of metamaterials with unrestricted constitutive parameters (note that here the WAIM had only electrical response) could lead to advanced WAIM metaradomes. However, these last solutions were not investigated since the research project was finished. Then, the author research activities were involved in other topics as it will be reported in the subsequent chapters.

Chapter 3

ET and MTMs inspired devices working at millimeter waves

In this chapter results for devices based on ET and metamaterials (MTMs) are presented. Section 3.1 presents a comprehensive behavior of the ET phenomenon from an ECA by analyzing periodic arrays of annular apertures on metallic screens. A proper distinction is made between classical FSS behavior and ET regime. In addition, the ECA is tested for various scenarios achieving very accurate results and then demonstrating its usefulness as a very cost efficient design tool for ET and FSS structures that are fundamental elements for designing advanced devices such as polarizers, spatial filters (single and multiband), etc. Furthermore, an experimental demonstration of two prototypes is presented.

Section 3.2 deals with the so called stacked hole array (SHA) structure, i.e. a multilayer arrangement of periodic hole arrays. Due to its intrinsic dispersion properties it can be used for synthesizing unidirectional and tunable structures and when it is properly combined with a dielectric grating. Unidirectional in this context means a device that allows transmission for one of two incidence directions for a certain angular and frequency range while transmission is blocked for incidence in the opposite incidence direction at the same angular/frequency conditions. In this section, a theoretical description is given to obtain unidirectional devices with maximized operation range (in terms of frequency and angle of incidence) by means of dispersion results. Furthermore, an experimental demonstration is provided in the millimeter wave regime.

In Sec. 3.3 the so called non-bianisotropic CSRR (NB-CSRR) metasurface is numerically and experimentally analyzed. This metamaterial element is an evolved version of the classical CSRR for which the bianisotropy character of the latter is inhibited. Then, a non-conventional angular response is obtained. While normally incident waves are almost totally reflected,

obliquely incident waves (with the appropriate polarization, i.e. TM) can show transmission bands.

3.1 ECA for annular aperture arrays: Discerning between ET and FSS

As described in Chapter 1, the study of the ET phenomenon has been a quite active research field since its discovery in 1998. In a few words, ET can be defined as high transmission peaks happening in metallic holey screens and appearing below the cut-off frequency of the apertures. On occasions, when a new physical phenomenon is reported there is a risk of overusing the term by ascribing it to similar physical scenarios. Time and more research effort is usually required to fully understand the underlying physics. ET has followed this path, as it will be shown below.

Leaving aside the debate on the role of plasmons in ET phenomenon briefly discussed in Chapter 1, exact delimitation of the boundary between ET and FSSs has been also a source of controversy among the scientific community. Here, a contribution to accurately settle this boundary is provided by analyzing annular aperture arrays and their analysis from an equivalent circuit perspective. The choice of the annular (or ring-slot) aperture is justified since it has been widely studied in the optical regime. Some of the previous works in this topic identified the high transmission peaks observed in annular aperture arrays with the excitation surface plasmons in combination with waveguide modes [Fan05, Bai09]. However, a more careful study can demonstrate that these peaks also occur in regimes where plasmons are not excited and they can be related only to the annular aperture resonance. In fact, they approximately appear at the cut-off frequency of the TE_{11} of the coaxial waveguide mode, much like the typical FSS operations. Orbons and Roberts properly set the limits between FSS and ET regimes in 2006 [Orb06]. The equivalent circuit approach (ECA) adds more physical insight and interesting interpretations for both FSS and ET responses.

As mentioned before, the structure under consideration is a periodic array of annular apertures in a metallic screen. Both free standing and dielectric slab backed structures are studied. The geometrical parameters of the unit cell are the internal radius a, external radius b, periodicity along x and y directions, d_x and d_y, respectively, and the dielectric substrate height h_s. The thickness of the metallic sheet was considered infinitesimal. A schematic of the structure can be found in Fig. 3.1.

In the following, the equivalent circuit is described in detail. Several practical cases are analyzed with the developed ECA and compared with full wave simulations with excellent

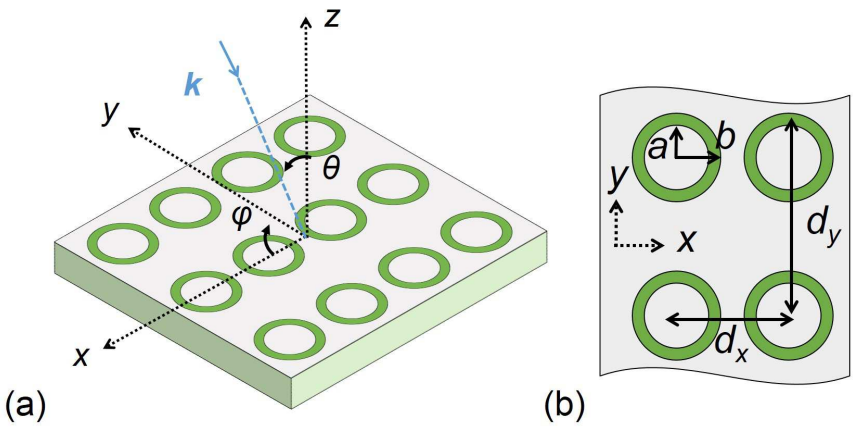

Fig. 3.1 (a) 2-D periodic structure with a rectangular array of annular apertures in a metallic screen backed with a dielectric slab. (b) Top view of a portion of the array structure.

agreement. Finally, an experimental demonstration of two selected designs, one exhibiting ET and the other one working as a classical FSS, is reported.

3.1.1 Equivalent Circuit Approach

The ECA used here is based on the approach proposed by R. Rodríguez-Berral *et al.* [RB15]. Its topology was derived from the very first principles offering a fully analytical method with low computational cost. The proposed ECA is applicable to both free-standing and dielectric backed solutions. In most practical situations, the dielectric slab is required as mechanical support of the patterned metallic screen. Hence, knowing the effect of a dielectric slab on the spectral response is very relevant for design purposes. In fact, a layered dielectric medium gives rise to additional features that need be taken into account [Lue78, Cal91]. Therefore, the response of a dielectric-backed FSS/ET structure can be relatively complex, especially in the frequency ranges where the thicknesses of the available commercial substrates can be comparable to the electrical wavelength (millimeter waves and THz).

Due to the periodic nature of the problem, Floquet analysis was employed assuming a $e^{j\omega t}$ time convention. In this way, the infinite periodic problem can be reduced to a generalized waveguide problem in which the boundary conditions can be periodic, electric, or magnetic walls [Ber07a, RB12]. The field in the aperture can be expanded in terms of Floquet modes leading to a multimodal network equivalent circuit model. Then, each harmonic is represented by a transmission line and pondered with an associated coupling coefficient [RB15]. These coupling coefficients can be interpreted as turn ratio values of standard transformers, N_h. The field expansion in terms of Floquet modes is equivalent to evaluating the corresponding

Fourier transform of the field profile at the aperture. The value of N_h can be calculated as the dot product of the Fourier transform of the field at the aperture, $\widetilde{\mathbf{E}}_a$, and the corresponding unit transverse wavevector, $\hat{\mathbf{k}}_{t,h}$, for TM harmonics or its cross-product with the unit vector $\hat{\mathbf{z}}$ for TE harmonics):

$$N_h = \begin{cases} \widetilde{\mathbf{E}}_a \cdot (\hat{\mathbf{k}}_{t,h} \times \hat{\mathbf{z}}) & \text{TE harmonics} \\ \widetilde{\mathbf{E}}_a \cdot \hat{\mathbf{k}}_{t,h} & \text{TM harmonics .} \end{cases} \tag{3.1}$$

To achieve congruent and accurate results, the assumed field profile of the aperture needs to be consistent with the aperture itself, the excitation, and the boundaries of the unit cell problem. For normal incidence, it is sufficient to set the aperture field profile as the first propagating mode of the equivalent hollow waveguide (TE_{11}). Two modes would be required for more complex situations, such as oblique incidence or double annular apertures also considered in this chapter [Mes16].

One mode in the aperture: Normal Incidence

First a linearly polarized normally-incident plane wave with vertical (i.e., parallel to y according to Fig. 3.1) polarization. In this case, the original periodic problem can be reduced to the scattering of an aperture discontinuity inside a virtual waveguide with perfect electric top and bottom walls and perfect magnetic sidewalls. Given the polarization of the impinging wave, the first waveguide mode that can be excited in the annular aperture is the TE_{11} (note that the symmetry of the incident wave precludes the excitation of the fundamental TEM mode). Thus, the first guess for the aperture field profile should resemble the field distribution of the TE_{11} coaxial waveguide mode. With these prescriptions, Dubrovka *et al.* proposed a field aperture with only radial component and an angular dependence with a sine/cosine function [Dub06]. It should be taken into account that this approximation works as long as the slot width is sufficiently small ($b/a \approx 1$). As a further simplification, the angular component $\hat{\phi}$ can be neglected and the radial component can be taken constant, independent on the radial distance (for larger b/a values, the $1/\rho$ dependence of the radial component should be considered). As the main purpose here is to study the different FSS and ET operation regimes, this simplification is applied in the following analysis. Therefore, the aperture field profile is taken as [Dub06]:

$$\mathbf{E}_a = A\cos(\varphi - \varphi_0)\hat{\rho} \tag{3.2}$$

where A is a constant, φ the azimuth angle and φ_0 the reference azimuth angle. The latter parameter just decides the azimuth location of the maximum field value given by the cosine function. By setting the field aperture as Eq. 3.2 the following expressions for N_h can be

derived [Dub06]:

$$N_h^{\mathrm{TM}} = 2\pi \frac{-k_{xn}\cos(\varphi_0) + k_{ym}\sin(\varphi_0)}{k_{\rho,h}} \cdot \frac{J_0(k_{\rho,h}b) - J_0(k_{\rho,h}a) + k_{\rho,h}[bJ_1(k_{\rho,h}b) - aJ_1(k_{\rho,h}a)]}{k_{\rho,h}^2}$$

$$N_h^{\mathrm{TE}} = 2\pi \frac{k_{xn}\sin(\varphi_0) + k_{ym}\cos(\varphi_0)}{k_{\rho,h}} \cdot \frac{-J_0(k_{\rho,h}b) + J_0(k_{\rho,h}a)}{k_{\rho,h}^2} \tag{3.3}$$

with

$$\begin{aligned} k_{xn} &= k_0 \sin\theta\cos\varphi + \frac{2\pi n}{d_x} \\ k_{ym} &= k_0 \sin\theta\sin\varphi + \frac{2\pi m}{d_y} \\ k_{\rho,h} &= |\mathbf{k}_{t,h}| = \sqrt{k_{xn}^2 + k_{ym}^2} \end{aligned} \tag{3.4}$$

where k_0 is the vacuum wavenumber, h corresponds to a nm harmonic, $J_\nu(x)$ is the Bessel function of order ν and argument x and θ and φ correspond to the elevation and azimuth angle respectively. The inclusion of θ and φ allows us to present the equations in a general manner. For the particular case of normal incidence treated here, we simply set $\theta = 0°$ and $\varphi = 0°$ or $\varphi = 90°$. When $\theta \neq 0°$, the only required modification is to replace the perfect electric or magnetic (depending on the polarization) walls of the virtual waveguide by periodic boundary conditions.

Figure 3.2 shows the equivalent network topology that results from the Floquet field expansion and application of boundary conditions and continuity of the Poynting vector at the aperture discontinuity. The N_h turn ratios for TE and TM harmonics can be directly introduced into the equations governing the circuit. The shunt admittance labeled as $Y_{\mathrm{eq}}^{(\mathrm{in})}$ accounts for the infinite summation of the modal admittances of all the harmonics (both TM and TE) excluding the impinging mode (typically the $\mathrm{TE}_{00}/\mathrm{TM}_{00}$ mode). In this case, the parallel admittance, $Y_{\mathrm{eq}}^{(\mathrm{in})}$, can be written as the summation of the admittance for each h mode looking towards the left, $Y_{\mathrm{in},h}^{(\mathrm{L})}$, and right, $Y_{\mathrm{in},h}^{(\mathrm{R})}$, sides of the circuit as follows:

$$Y_{\mathrm{eq}}^{(\mathrm{in})} = \sum_h |N_h|^2 \left[Y_{\mathrm{in},h}^{(\mathrm{L})} + Y_{\mathrm{in},h}^{(\mathrm{R})} \right] \tag{3.5}$$

where

$$\begin{aligned} Y_{\mathrm{in},h}^{(\mathrm{L})} &= Y_h^{(0)} \\ Y_{\mathrm{in},h}^{(\mathrm{R})} &= Y_h^{(1)} \frac{Y_h^{(0)} + \mathrm{j}Y_h^{(1)}\tan(\beta_h^{(1)}h_s)}{Y_h^{(1)} + \mathrm{j}Y_h^{(0)}\tan(\beta_h^{(1)}h_s)}. \end{aligned} \tag{3.6}$$

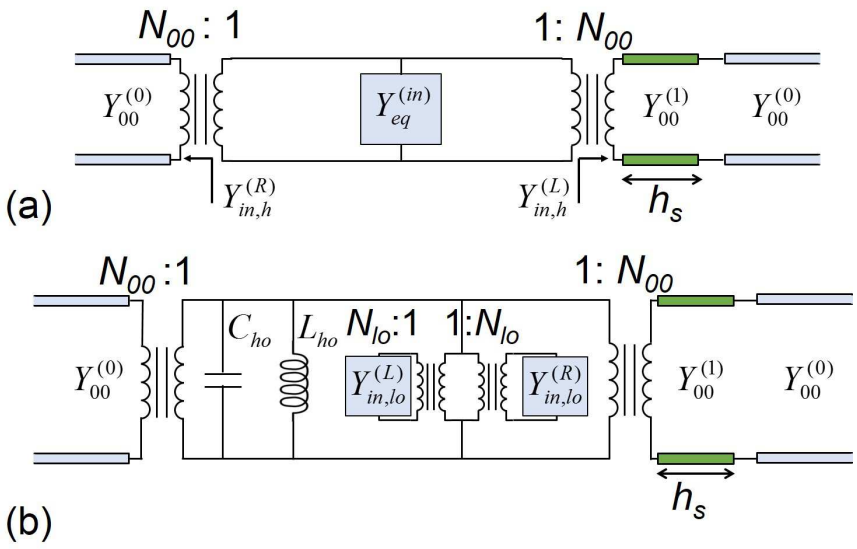

Fig. 3.2 Equivalent network for a 00 impinging harmonic. (a) Schematic for the case when all the modes are included in the equivalent admittance, $Y_{\text{eq}}^{(\text{in})}$. (b) Schematic for the case when the equivalent admittance, $Y_{\text{eq}}^{(\text{in})}$, is categorized into LO and HO modes.

In the case of a free-standing structure, $Y_{\text{in},h}^{(\text{R})} = Y_h^{(0)}$. The modal admittances $Y_h^{(i)}$ are given by:

$$Y_h^{(i)} = \frac{1}{\eta^{(i)}} \begin{cases} \beta_h / k^{(i)} & \text{TE harmonics} \\ k^{(i)} / \beta_h & \text{TM harmonics} \end{cases} \tag{3.7}$$

where

$$\begin{aligned} k^{(i)} &= \sqrt{\varepsilon_r^{(i)}} k_0 \\ \beta_h^{(i)} &= \sqrt{\varepsilon_r^{(i)} k_0^2 - k_{\rho,h}^2} \\ \eta^{(i)} &= \frac{\eta_0}{\sqrt{\varepsilon_r^{(i)}}} \end{aligned} \tag{3.8}$$

with $\eta_0 = \sqrt{\mu_0/\varepsilon_0}$ being the vacuum wave impedance and $\varepsilon_r^{(i)}$ the relative permittivity of the medium (i). At this point, a convenient distinction between low order (LO) and high order (HO) modes should be done [RB15]. The LO modes, are those in propagation (or evanescent but close to cut-off) at the frequency range of interest. Therefore, an explicit expression keeping their distributed nature (frequency dependent admittance) must be taken. On the other hand, the contribution of high order TM/TE modes can be seen as regular capacitors/inductors, which are frequency independent. In this way, the circuit elements associated with HO modes are computed only once leading to a strong reduction of computational resources. It should be

noted that the presence of a layered dielectric environment is explicitly taken into account for both LO and HO modes [see 3.2(b)]. The final expression for the equivalent input admittance yields:

$$Y_{\mathrm{eq}}^{(\mathrm{in})} = \sum_{|h|\leq M} |N_h|^2 \left[Y_{\mathrm{in},h}^{(\mathrm{L})} + Y_{\mathrm{in},h}^{(\mathrm{R})} \right] + \mathrm{j}\omega C_{\mathrm{HO}} + \frac{1}{\mathrm{j}\omega L_{\mathrm{HO}}} \tag{3.9}$$

with

$$\begin{aligned} C_{\mathrm{HO}} &= \sum_{|h|\geq M+1}^{\infty} |N_h^{\mathrm{TM}}|^2 \left[\frac{\varepsilon_0}{k_{\rho,h}} + \frac{\varepsilon_0 \varepsilon_r^{(1)}}{k_{\rho,h}} \frac{\varepsilon_r^{(0)} + \varepsilon_r^{(1)} \tanh(k_{\rho,\mathrm{h}} h_s)}{\varepsilon_r^{(1)} + \varepsilon_r^{(0)} \tanh(k_{\rho,\mathrm{h}} h_s)} \right] \\ \frac{1}{L_{\mathrm{HO}}} &= \sum_{|h|\geq M+1}^{\infty} \frac{2\mu_0 |N_h^{\mathrm{TE}}|^2}{k_{\rho,h}}. \end{aligned} \tag{3.10}$$

As it can be seen from Eqs. 3.9-3.10, the mode categorization is determined by the factor M which sets an upper limit for low order modes (in most practical cases M is a small integer number). In addition, the infinite series shown in Eq. 3.10 can be truncated by setting an upper bound N which fixes the maximum number of evanescent modes considered. Once all the circuital parameters are known, one may apply classical network theory to obtain the scattering parameters of the equivalent circuit [Poz09].

Two modes in the aperture

The inclusion of an additional mode in the assumed aperture field has been considered to enlarge the upper frequency bound of the model in metallic patch arrays and extend the approach to unit cells containing more than one scatterer by F. Mesa *et al.* [Mes16]. This leads to the equivalent circuit topology shown in Fig. 3.3.

In the case of the annular aperture arrays, this topology can be applied to model the TM oblique incidence upon a unit cell with a single aperture or to analyze a unit cell with two annular apertures under normal incidence [see Fig. 3.3(b)]. In the case of TM oblique incidence, the Y_{11} and Y_{22} admittances account, respectively, for the first and second mode considered, and Y_{12} for the coupling between both modes. In the case of the double annular aperture array, the mutual admittance Y_{12} accounts for the interaction between the inner and outer apertures whereas the self-admittances Y_{11} and Y_{22} account for the effect of each individual isolated aperture. These admittances can be evaluated as [Mes16]:

$$Y_{ij} = \sum_h \frac{N_{i,h}^* N_{j,h}}{N_{i,00}^* N_{j,00}} \left[Y_{\mathrm{in},h}^{(\mathrm{L})} + Y_{\mathrm{in},h}^{(\mathrm{R})} \right] \tag{3.11}$$

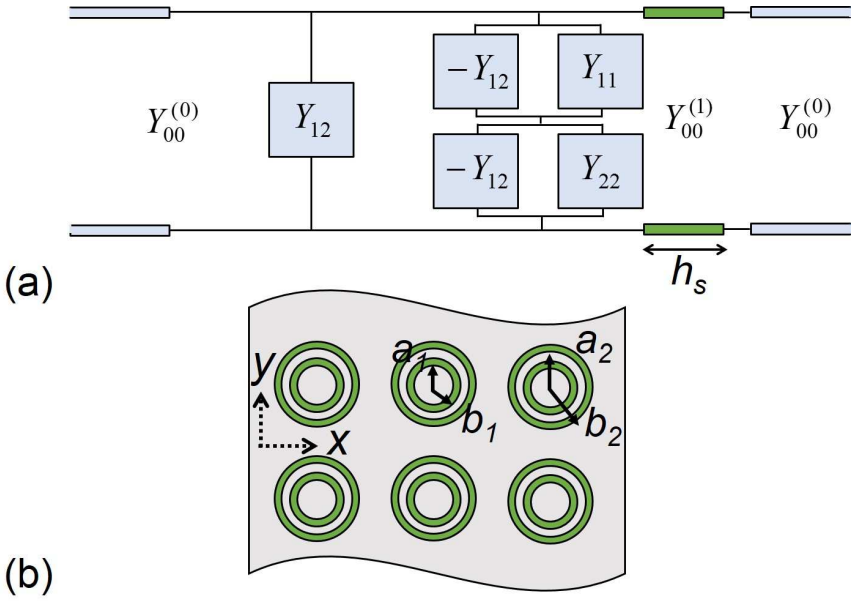

Fig. 3.3 (a) Equivalent circuit model taking into account two independent spatial field profiles. (b) Top view of a portion of a double annular annular aperture array structure.

where $(i, j) = 1, 2$ and account for either mode or aperture. The same considerations about LO/HO modes is applied here. Also, the scattering parameters are evaluated by applying classical network theory.

For the case of TM oblique incidence, a second mode is assumed in the field aperture that corresponds to the TEM mode of the coaxial waveguide. To model the TEM mode a constant spatial field profile in the radial direction is assumed:

$$\mathbf{E}_a = A\hat{\rho} \tag{3.12}$$

Then, by introducing this field profile into Eqs. 3.3 and after some manipulation, the turn ratio, N_h^{TEM} can be written as:

$$N_h^{\mathrm{TEM}} = \mathrm{j}\frac{2\pi}{k_{\rho,h}^2}\left[\int_a^b J_0(k_{\rho,h}\rho)\mathrm{d}\rho - k_{\rho,h}bJ_0(k_{\rho,h}b) + k_{\rho,h}aJ_0(k_{\rho,h}a)\right], \tag{3.13}$$

where the integral term is computed by means of Struve functions as follows:

$$\int J_0(x)\mathrm{d}x = xJ_0(x) + \Phi(x), \tag{3.14}$$

where

$$\Phi(x) = \frac{\pi x}{2}\left[J_1(x)\cdot\mathbf{H}_0(x) - J_0(x)\cdot\mathbf{H}_1(x)\right], \tag{3.15}$$

and

$$\mathbf{H}_{\nu}(x) = \left(\frac{1}{2}x\right)^{\nu+1} \sum_{k=0}^{\infty} \frac{(-1)^k \left(\frac{1}{2}x\right)^{2k}}{\Gamma\left(k+\frac{3}{2}\right)\Gamma\left(k+\nu+\frac{3}{2}\right)}, \tag{3.16}$$

being $\Gamma(z)$ the gamma function. The infinite summation in Eq. 3.16 converges rapidly and it can be truncated to a finite value since high index elements are all 0.

3.1.2 ECA and Numerical Results

In this section results obtained with the ECA are compared to full wave numerical simulations for several annular aperture structures. To begin with, some representative cases were considered to assess the validity of the ECA. The numerical results were obtained using the full wave commercial software CST Microwave Studio® (see App. A). The metallic screen was made of perfect electric conductor (PEC) with infinitesimal thickness.

Figure 3.4 shows the ECA and numerical results for different structures. Figure 3.4(a) deals with square unit cells and free-standing solutions wherein the outer/inner radius ratio, b/a, is varied. The accuracy of the circuit model is better for narrow slots ($b/a \approx 1$) as predicted. Nevertheless, the agreement is quite good until $b/a \approx 2$. Figures 3.4(b) and (c) show results for rectangular unit cells and dielectric-backed structures under vertical and horizontal polarization respectively. The agreement is very good in both cases, with a better agreement for the horizontal polarization. To test also the accuracy of the ECA for layered environments, structures with different dielectric slabs were analyzed. The dielectric loss was modeled by setting the permittivity as a complex number. It should be pointed out that the computation resources used by the ECA are negligible. As an example, for the cases selected in this section, a 2000-point frequency sweep can be run within 1 or 2 seconds. On the other hand, full wave numerical simulations usually last several minutes. This difference becomes even more important when dealing with parametric sweeps and optimization routines typically required for the design of this kind of structures.

Discerning between ET and FSS regimes

Now, a study to discern the limits between FSS and ET operation regimes is given. To this end, a square unit cell and free-standing annular array is analyzed with constant b/a ratio and period, d, ($b/a = 1.3$ and $d = 1.5\,\text{mm}$ respectively) while the mean radius, $r_{\text{m}} = (a+b)/2$, is varied. In addition, a rectangular ($d_x \neq d_y$) free-standing annular array is studied to evaluate the influence of the lattice period, d_y, in the transmission properties for both FSS and ET operation regimes. The rest of parameters are set to $d_x = 1.5\,\text{mm}$, $b = 0.65\,\text{mm}$, and $a = 0.5\,\text{mm}$.

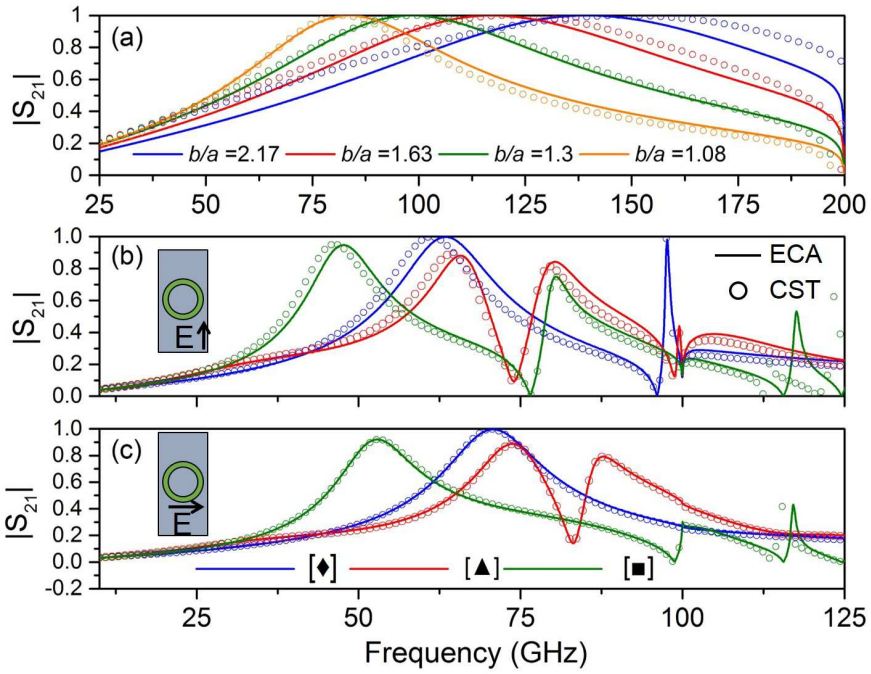

Fig. 3.4 Transmission coefficient results obtained by ECA (solid line) and CST (circles). Free standing structure: (a) $b/a = 2.17$ (blue line), $b/a = 2.17$ (red line), $b/a = 2.17$ (green line), $b/a = 2.17$ (orange line). Rest of parameters: $d_x = d_y = 1.5$ mm; $b = 0.65$ mm. Dielectric backed structure: [♦] $\varepsilon_r = 3$, $h_s = 0.2$ mm (blue line); [▲] $\varepsilon_r = 2.1 - j0.018$, $h_s = 1.6$ mm (red line). [■] $\varepsilon_r = 5$, $h_s = 0.4$ mm (green line). Rest of parameters: $d_x = 1.5$ mm; $d_y = 3$ mm; $b = 0.65$ mm; $a = 0.5$ mm. (b) Vertical polarization ($\varphi = 90°$). (c) Horizontal polarization ($\varphi = 0°$).

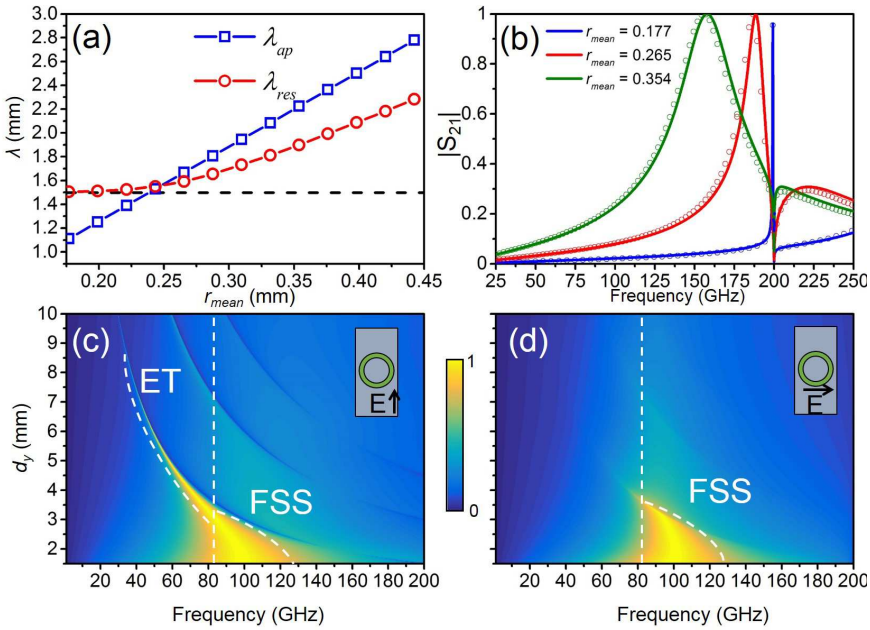

Fig. 3.5 (a) Resonant λ_{res} and cut-off aperture wavelength versus mean radius (r_{m}) for free-standing annular arrays with $b/a = 1.3$ and $d = 1.5\,\text{mm}$. (b) Transmission coefficient results obtained by ECA (solid line) and CST (circle) for $r_{\text{m}} = 0.177\,\text{mm}$ (blue line), $r_{\text{m}} = 0.265\,\text{mm}$ (red line) and $r_{\text{m}} = 0.354\,\text{mm}$ (green line). ECA results of the transmission coefficient for FSS design versus frequency and d_y; $d_x = 1.5\,\text{mm}$, $b = 0.65\,\text{mm}$, and $a = 0.5\,\text{mm}$. (c) Vertical polarization. (d) Horizontal polarization. Vertical white-dashed line accounts for the cut-off frequency aperture, f_{ap}. The white-dashed curves delimit high transmission regions and hence, the ET and FSS regimes.

Figure 3.5 shows the results obtained for these situations. Figure 3.5(a) displays the resonance wavelength, λ_{res} (defined as the wavelength at maximum transmission) and the cut-off wavelength of the aperture (in this case $\lambda_{\text{ap}} = (a+b)\pi$) versus r_{m}. It can be observed that for small radii ($0.17\,\text{mm} < r_{\text{m}} < 0.22\,\text{mm}$), λ_{res} is nearly equal to d regardless the aperture size. In addition, λ_{ap} is lower than λ_{res} denoting that the high transmission is happening below the cut-off frequency of the aperture. With these premises, ET phenomenon can be claimed within this operation range. In contrast, for large r_{m} values ($r_{\text{m}} > 0.27\,\text{mm}$), λ_{res} is linearly proportional to the aperture size, which is the classical behavior of FSS regime. Between these two regions there is a range ($0.22\,\text{mm} < r_{\text{m}} < 0.27\,\text{mm}$), wherein λ_{res} is neither equal to d nor proportional to r_{m} and that can be considered as the boundary between FSS and ET regimes. Figure 3.5(b) shows the transmission results obtained by the ECA and CST for three selected cases: ET ($r_m = 0.175\,\text{mm}$), FSS ($r_m = 0.35\,\text{mm}$) and an intermediate case ($r_m = 0.265\,\text{mm}$). The ET transmission peaks are inherently narrowband while the FSS peaks are relatively wide.

Figures 3.5(c) and (d), show transmission results of d_y variation versus frequency for vertical and horizontal polarization, respectively. The vertical white dashed line mark the aperture frequency f_{ap} that can be evaluated as, $f_{ap} = c_0/[(a+b)\pi] \approx 83$§,GHz. The curved white dashed line delimits the high transmission regions that are related wiht the FSS/ET regimes. For vertical polarization, the transmission peak shifts to lower frequencies as d_y increases. It is also worth noting the appearance of high transmission bands below and above f_{ap} in the region $3\,\text{mm} < d_y < 3.5\,\text{mm}$. This corresponds to the aforementioned transition region where the high transmittance band is due to a combination of both FSS and ET regimes. When $d_y \approx 3.5\,\text{mm}$ the transmission above f_{ap} vanishes, and for $d_y > 3.5\,\text{mm}$ the high transmittance peak is completely due to the ET resonance. For the horizontal case, it can be observed that ET does not take place, a fact that will be discussed later in this section. Thus, only the FSS regime region is highlighted in Fig. 3.5(d).

At the light of the presented results, the boundaries between ET and FSS regimes can be identified. The FSS regime is mainly related to the aperture in the metallic screen and its exact location depends on its size and geometry. On the other hand, the ET peak always appears right before the first diffraction order, independently of the aperture geometry. In fact, for the FSS case, the high-transmission frequency is independent of the period and the transmission bands are broad. In turn, for ET, the frequency of the transmission peak is governed by the period and its bandwidth is always narrow.

In the next study, two specific dielectric backed solutions are selected with their geometrical dimensions chosen to have either a FSS or an ET response (see Tab. 3.1). From now on, for convenience, the designs are labeled as FSS and ET. These designs are experimentally analyzed in a subsequent section. For this reason the selection of the substrate height, h_s and ε_r was done by considering available commercial substrates. In dielectric backed solutions, the cut-off frequency of the aperture varies with respect to the free standing solution. Here, it is approximated as the cut-off frequency of the TE_{11} mode of the equivalent coaxial waveguide divided by the square root of the effective permittivity, ε_{eff} [Poz09]:

$$f_{ap} = \frac{c_0}{(a+b)\pi\sqrt{\varepsilon_{eff}}} \tag{3.17}$$

with c_0 being the speed of light in the vacuum. The f_{ap} values for the FSS and ET designs are also included in Tab. 3.1. The exact magnitude of ε_{eff} is not easy to estimate since it depends on the electrical dimensions of the dielectric slab and the metallic geometry [Mun00]. However, its boundaries can be guessed by the surrounding media (air and dielectric slab in the current case) leading to $1 < \varepsilon_{eff} < [\varepsilon_r + 1]/2$. For the sake of simplicity, the upper-bound value of this parameter ($\varepsilon_{eff} = 1.7$) is assumed by taking $\varepsilon_r = 2.4$ (as it would be for a

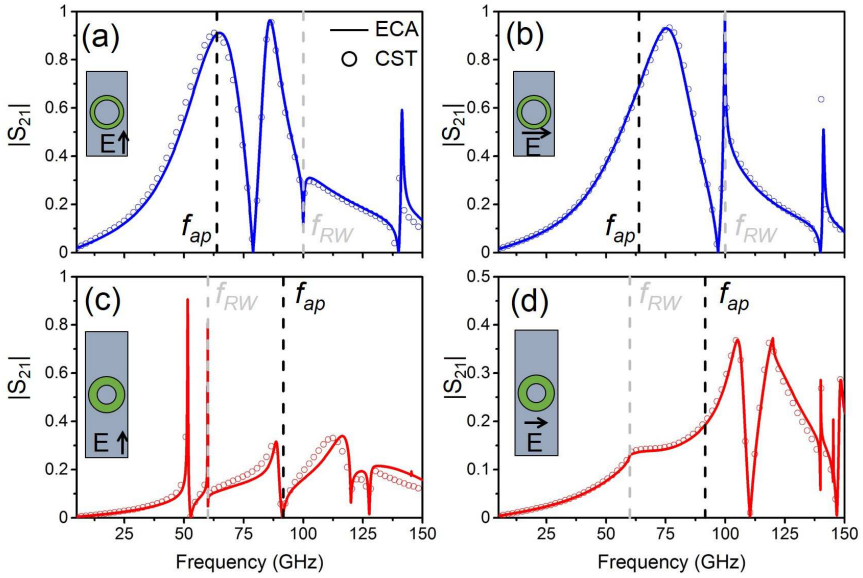

Fig. 3.6 Transmission coefficient for FSS and ET designs. ECA (solid line) and CST (circles) results are shown. (a) FSS - Vertical polarization ($\varphi = 90°$). (b) FSS - Horizontal polarization ($\varphi = 0°$). (c) ET - Vertical polarization ($\varphi = 90°$). (d) ET - Horizontal polarization ($\varphi = 0°$).

semi-infinite slab) for evaluation of the f_{ap} values shown in Tab. 3.1. It should be noted that with this assumption, f_{ap}, takes the lowest possible value.

Design	a (mm)	b (mm)	d_x (mm)	d_y (mm)	h_s (mm)	ε_r	f_{ap} (GHz)	f_{RW} (GHz)
FSS	0.5	0.65	1.5	3	0.76	2.4	63.8	100
ET	0.3	0.5	1.5	5	0.76	2.4	91.6	60

Table 3.1 Geometrical parameters of the studied FSS/ET structures along with the aperture cut-off and RW anomaly frequencies, f_{ap} and f_{RW}, respectively.

Figure 3.6 shows a comparison between numerical and analytical results for the FSS and ET designs outlined in Table 3.1. Normal incidence and both vertical [$\varphi = 90°$ - 3.6(a) and (c)] and horizontal polarization [$\varphi = 0°$ - 3.6(b) and (d)] of the incident wave were considered. An excellent agreement is obtained between CST simulation and ECA results for both designs and polarizations, even at frequencies exceeding the diffraction limit ($f > f_{\text{diff}} = c_0/d_y$). To explain the origin of the main transmission features, namely, peaks and nulls, a discussion in terms of input admittance is provided. Figures 3.7 and 3.8 show the admittance response (normalized to the free space admittance, $Y_0 = 1/\eta_0$) of the first higher order harmonic and the total input admittance seen by the structure for each analyzed case. In addition, to analyze the impact of the dielectric height, h_s, was varied from 0 to 2 mm in 0.25 mm steps. The

obtained transmission coefficient by means of the ECA is shown in Fig. 3.9 versus frequency and h_s. The particular cases shown in 3.6 are depicted by means of horizontal white-dashed lines.

For the case shown in Fig. 3.6(a), the first high transmission band of the FSS design appears near 65 GHz, slightly above $f_{\text{ap}}^{\text{FSS}} \approx 63.8\,\text{GHz}$, and well below $f_{\text{diff}}^{\text{FSS}} \approx 100\,\text{GHz}$. This transmission band precedes a null of transmission (79 GHz) and a second transmission band (84 GHz). All these features can be explained with the ECA by means of the input admittance of the first higher order mode of the equivalent virtual waveguide. In the present case, this role is played by the TM_{02} mode, whose cut-off frequency inside the dielectric is $f_{\text{c,TM}_{02}} = c_0/(d_y\sqrt{\varepsilon_r}) = 64.6\,\text{GHz}$. Figure 3.7(a) shows the normalized input admittance seen by the TM_{02} looking to the left, $Y^L_{in,\text{TM}_{02}}$, and right $Y^R_{in,\text{TM}_{02}}$ sides of the circuit which correspond to the air and dielectric interfaces, respectively. At a frequency that depends on the substrate characteristics and that is located between $f_{\text{c,TM}_{02}}$ and f_{diff}, $Y^R_{in,\text{TM}_{02}}$ diverges to infinite (i.e. it behaves as a short-circuit) giving rise to a transmission null. Below this frequency, $Y^R_{in,\text{TM}_{02}}$ is capacitive and therefore a peak must emerge in the spectral response because the inductance of the aperture will be compensated by the capacitance of this mode that runs along all possible values from 0 to infinite. The same way of reasoning can be used to explain the second transmission band in terms of the divergence of $\overline{Y}^L_{in,\text{TM}_{02}}$ in the air [Med08]. For the sake of completeness, the total normalized input admittance, $\overline{Y}_{in}$, is shown in Fig.3.7(b). There, the transmission bands can be identified as the regions where both $\text{Re}\{\overline{Y}_{in}\} \approx 1$ and $\text{Im}\{\overline{Y}_{in}\} \approx 0$ conditions are simultaneously fulfilled. Furthermore, the transmission nulls can be also identified as short-circuits (large $\overline{Y}_{in}$ values). Regarding the influence of h_s on the transmission spectra, when $h_s = 0$, a single transmission band is obtained [see Fig. 3.9(a)] . However, as h_s increases, the null is shifted to lower frequencies, with its lower bound given by $f_{\text{c,TM}_{02}}$. The null appearance splits the transmission peak into two different transmission bands as h_s increases.

For the ET case and vertical polarization shown in Fig. 3.6(c), two transmission peaks arise at approximately 51 and 59.9 GHz, well below $f_{\text{ap}}^{\text{ET}} \approx 91.6\,\text{GHz}$. Equivalently to the previous case, the main transmission features can be explained again in terms of the TM_{02} mode of the equivalent virtual waveguide. According to Fig. 3.8(a) the input admittance looking towards the dielectric interface, $\overline{Y}^R_{in,\text{TM}_{02}}$, diverges to infinity leading to a null in the transmission spectrum at 52.8 GHz. Below this frequency, the total inductance due to the aperture can be compensated by the capacitance of the TM_{02} mode giving rise to the transmission peak at 51 GHz. For the second transmission peak, the situation is similar but for the air interface. Now, the TM_{02} mode contribution adds the required capacitance at a certain frequency near and below the first RW anomaly (60 GHz) to compensate the

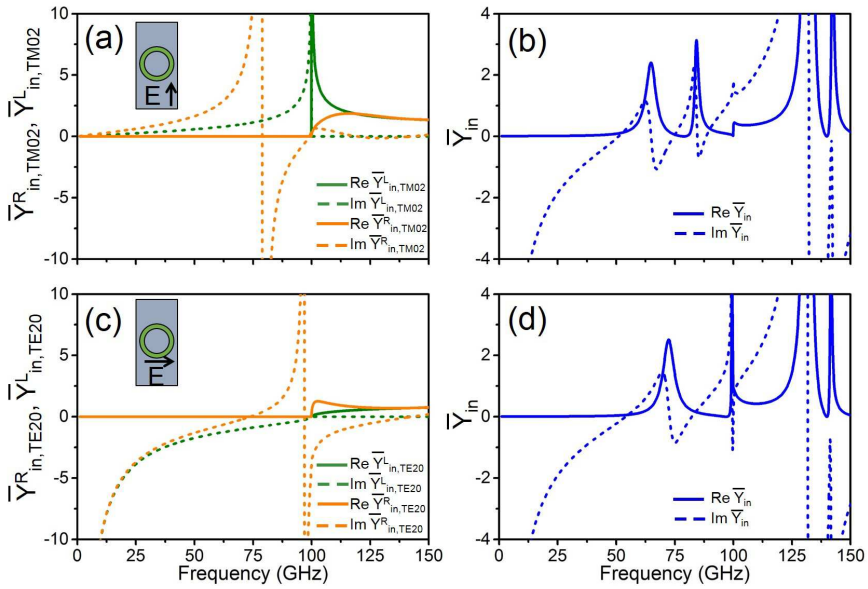

Fig. 3.7 Admittance results of the FSS design. Input admittance of the first higher order looking to the left and right of the discontinuity, $\overline{Y}^{L,R}_{in,\mathrm{TM,TE}_{XX}}$ and total input admittance, $\overline{Y}_{in}$. Both admittances are normalized to the free-space admittance, Y_0. (a) $\overline{Y}^{L,R}_{in,\mathrm{TM}_{02}}$ - Vertical polarization. (b) $\overline{Y}_{in}$ - Vertical polarization. (c) $\overline{Y}^{L,R}_{in,\mathrm{TE}_{02}}$ - Horizontal polarization. (d) $\overline{Y}_{in}$ - Horizontal polarization.

inductance introduced by the aperture. This feature is corroborated by the $\overline{Y}^{L}_{in,\mathrm{TM}_{02}}$ curves shown in Fig. 3.8(a). The inspection of the total input admittance denotes the same premises for transmission peaks and nulls as the FSS case [see Fig. 3.8(b)]. However, as it can be observed, the frequency region where free space matching is possible is much narrower. The particular origin of these two peaks can be better discerned when the substrate height, h_s, is varied [see Fig. 3.9(c)]. Two narrow-band transmission peaks arise between 45 and 60 GHz. The peak related to the dielectric appears for $h_s > 0$ and shifts to lower frequencies as h_s increases. This shift finds its limit at approximately 45 GHz. On the other hand, as expected, the transmission peak related to the air remains always right before the diffraction limit regardless the value of h_s. Furthermore, peaks with weak transmission arise within the diffraction regime between 90 and 120 GHz for the particular case shown in Fig. 3.6(c). These two low transmission peaks have the same nature as the ordinary transmission peaks of the FSS structure. They are broader than those obtained at 51 and 59.9 GHz indicating that they are related to the aperture resonance. The transmission details are now due to the TM_{04} mode. Its behavior is similar to the one observed in the TM_{02} for the FSS case as it can be seen in Fig. 3.9(c). Indeed, the partial transmission arising at lower frequencies follows the trend of the null due to the dielectric. In any case, these transmission peaks occur when

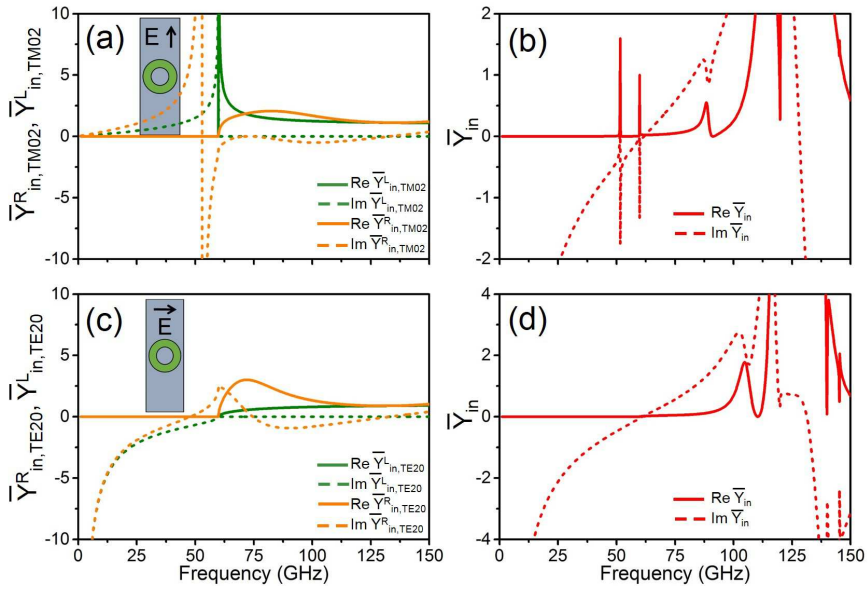

Fig. 3.8 Admittance results of the ET design. Input admittance of the first higher order looking to the left and right of the discontinuity, $\overline{Y}^{L,R}_{in,\mathrm{TM,TE}_{XX}}$ and total input admittance, $\overline{Y}_{in}$. Both admittances are normalized to the free-space admittance, Y_0. (a) $\overline{Y}^{L,R}_{in,\mathrm{TM}_{02}}$ - Vertical polarization. (b) $\overline{Y}_{in}$ - Vertical polarization. (c) $\overline{Y}^{L,R}_{in,\mathrm{TE}_{02}}$ - Vertical polarization. (d) $\overline{Y}_{in}$ - Vertical polarization.

higher orders may propagate and hence, part of the power is transferred to the diffraction modes (grating lobes) and total transmission in the fundamental mode is not attainable. Then, the interest on this frequency region is limited for practical situations.

From these results, it can be said that the ET phenomenon is responsible for the two high and narrow transmission peaks arising at 51 and 59.9 GHz. Due to the admittance divergence, high-transmission peaks arise regardless the selected aperture geometry and size. Indeed, even for very small apertures in which very high capacitance is required to compensate small inductance values, the resonance condition is attainable due to the divergence to infinity of high order modes approaching propagation [Med08]. In fact this is corroborated by the admittance results shown in Figs. 3.7(a) and 3.8(a). For the ET cases, the high transmission was obtained at very large values of $\overline{Y}^{R}_{in,\mathrm{TM}_{02}}$ and $\overline{Y}^{L}_{in,\mathrm{TM}_{02}}$. On the other hand, for the FSS cases the required capacitance values provided by $\overline{Y}^{R}_{in,\mathrm{TM}_{02}}$ and $\overline{Y}^{L}_{in,\mathrm{TM}_{02}}$ at the high transmission regions were far from extreme. In other words, the total capacitance required for resonance does not need to rely on singularities to attain the convenient value. In addition, in the ET case the inductance introduced by the aperture was low and therefore the quality factor, Q, was high. Hence, the transmission bands are inherently narrowband. On

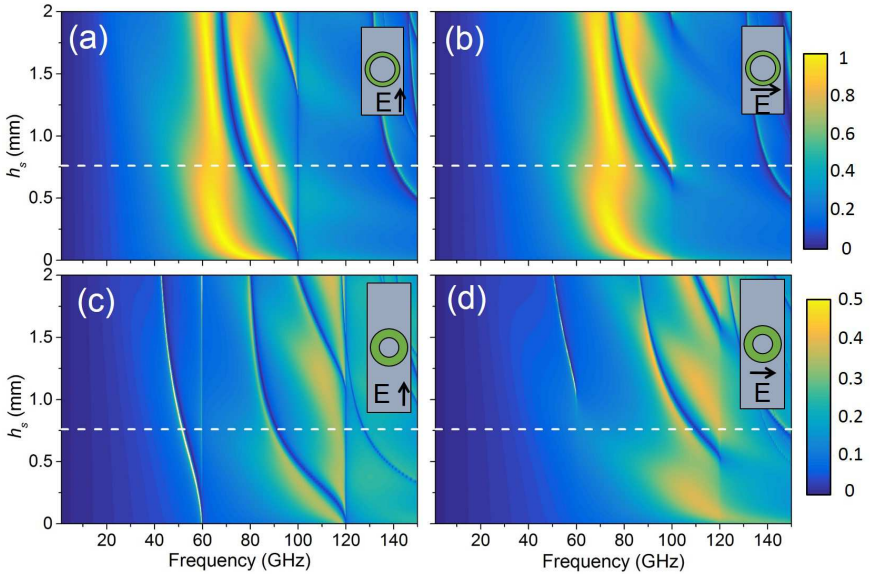

Fig. 3.9 ECA results of the transmission coefficient for FSS and ET designs versus frequency and h_s. (a) FSS - Vertical polarization ($\varphi = 90°$). (b) FSS - Horizontal polarization ($\varphi = 0°$). (c) ET - Vertical polarization ($\varphi = 90°$). (d) ET - Horizontal polarization ($\varphi = 0°$). Horizontal white dashed lines denote the particular cases shown in Fig. 3.6.

the other hand, for the FSS case, the inductance is usually large leading to low Q resonances and therefore, broadband transmission peaks.

The ET horizontal polarization case is shown in Fig 3.6(d). The results differ considerably from those obtained for vertical polarization. The most remarkable difference comes from the absence of transmission peaks within the non-diffractive regime. This can be explained again with the ECA. Now, due to the different polarization state, the first relevant high order mode is the TE_{20}. Below cut-off this mode is inductive, so its contribution is just adding an extra inductance and, therefore, the cancellation of the inductance due to the aperture does not seem possible. Figure 3.8(c) shows the input admittance of the TE_{20} to both sides of the equivalent circuit. As it can be observed there is not divergence to infinity and therefore the conditions for nearly total transmission are not fulfilled. The absence of nearly matched admittance regions in Fig. 3.8(d) corroborates the lack of high transmission bands in this case. However, as explained in [Ber11b], a proper selection of ε_r and h_s, could lead to ET resonances for dielectric backed aperture arrays with the electric field parallel to the short period [Lom05, Kuz09]. This ET resonance was termed "anomalous" ET. The condition for this phenomenon to occur is given by an F parameter defined as:

$$F = h_s[\varepsilon_r^{(1)} - 1]^{1/2}/d_y > 0.25. \tag{3.18}$$

In the case shown in Fig 3.6(d) this condition is not satisfied ($F = 0.18$) and therefore "anomalous" ET peak is not excited. In turn, an abrupt slope change appears at the first RW anomaly (60 GHz). Focusing now on the h_s study for this particular case [see Fig. 3.9(d)], it can be clearly seen this feature and how "anomalous" ET only occurs for sufficiently thick slabs, i.e., $F \approx 0.25$ ($h_s = 0.25 d_y/(\sqrt{\varepsilon_r - 1}) \approx 1.05$ mm). The F parameter can be linked to grounded slab configurations as detailed in [Ber11b]. As mentioned above, in this case the first high order mode that becomes propagating inside the dielectric slab is the TE_{20}. Unlike the TM fundamental mode that propagates even with $h_s = 0$ [notice the null excursion from $h_s = 0$ and $f = 60$ GHz to $h_s = 2$ mm and $f \approx 40$ GHz in Fig. 3.9(c)], the fundamental TE mode of a grounded dielectric slab requires a minimum h_s so that the transcendental modal equation has a valid solution [Poz09]. In addition, a weak transmission peak was observed at approximately 105 GHz in Fig. 3.6(d). This transmission feature is due to the aperture resonance influenced by the TE_{40} mode dispersion. In fact, it can be observed in Fig. 3.9(c) that for thin substrates ($h_s < 0.5$ mm) a relatively broad and weak transmission band appears, reinforcing the argument about its connection with the aperture resonance. At the second RW anomaly frequency (120 GHz), a change in the slope of the transmission is again observed for all the h_s values.

For the FSS design and horizontal polarization [Fig. 3.6(b)], a high-transmission band appears in the spectrum around 75 GHz. This is slightly different compared to the vertical polarization case [see Fig. 3.6(a)]. The transmission peak can be again directly linked to the annular aperture resonance, and its frequency shift with respect to the vertical polarization case can be attributed to the different contribution of the first higher order mode of the equivalent virtual waveguide. This contribution results in a different value of the effective permittivity; namely, ε_{eff} is higher for the vertical case than for the horizontal one. The ε_{eff} accounts for the static-capacitance variation due to the evanescent fields of cut-off TM modes. For the vertical polarization case, the electric field is parallel to the larger period, d_y. Then, the cut-off frequencies of TM modes are lower and therefore their attenuation distances are larger. In other words, the associated evanescent fields reach a larger portion of the dielectric slab and hence, a higher value of ε_{eff} is obtained. It is worth noting that TE modes at cut-off are inductive and are not affected by the surrounding medium [see Eq. 3.10]. By inspecting Fig. 3.9(a) and (b) it is observed that, indeed, the differences between the vertical and horizontal polarization performances are larger for thin substrates. As before, the first high order mode that becomes propagating inside the dielectric slab is the TE_{20} of the equivalent virtual waveguide. It can be observed that for thin substrates (up to $h_s = 0.65$ mm) a single band operation is retained while for higher h_s values the band is split in two. This is again directly connected to the F parameter presented before. In fact,

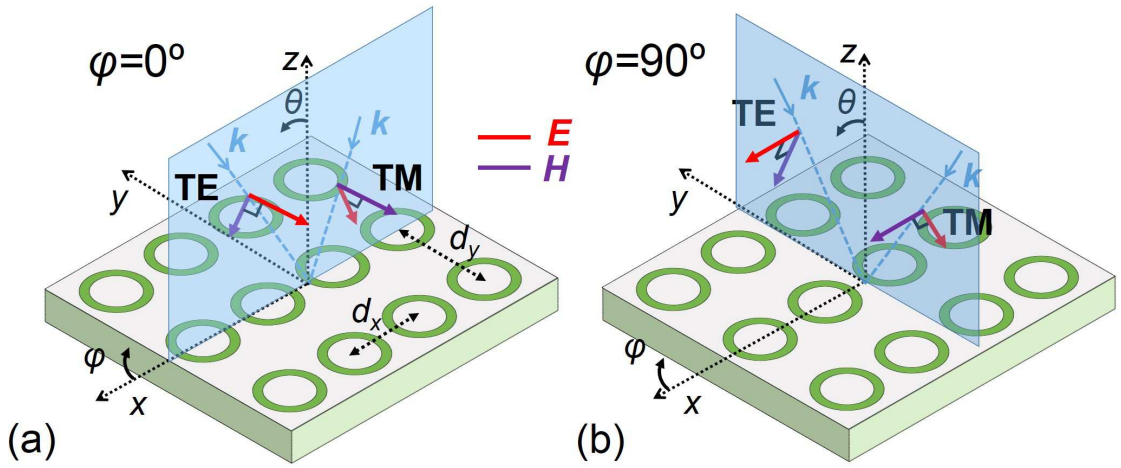

Fig. 3.10 Schematic of oblique incidence for TM and TE polarizations. (a) $\varphi = 0°$. (b) $\varphi = 90°$.

$h_s = 0.25 d_y/(\sqrt{\varepsilon_r - 1}) \approx 0.63$ mm. This feature can be tracked by observing the first null evolution in Fig. 3.9(b). It starts at $h_s \approx 0.65$ mm, $f = 100$ GHz and reaches a frequency of $f \approx 75$ GHz when $h_s = 2$ mm. In contrast, for the vertical polarization, the null in the spectrum goes from $h_s = 0$ and $f = 100$ GHz to $h_s = 2$ mm and $f \approx 70$ GHz [see Fig. 3.9(a)].

The results obtained in this study yield a quite complete understanding for accurately discerning between FSS and ET regimes. In addition, useful guidelines are given for practical design purposes when dielectric slabs are included. For instance, for the case of classical FSS design, if a single peak with nearly total transmission is required, thin substrates should be selected. For the studied case, within the range $0.5\,\text{mm} < h_s < 0.75\,\text{mm}$, a wider transmission band but with lower amplitude can be obtained. For larger h_s, double band solutions for both polarizations are possible. Similarly, for the ET case, the dependence of the high-transmission peak frequency location with h_s has been demonstrated.

Oblique Incidence

In this section some results for oblique incidence are presented. Under TM polarization incidence, a TEM mode can be excited in the aperture. In turn, due to symmetry mismatch the TEM mode is not accessible under TE incidence. Here, the two modes approach described in Sec. 3.1.1 is used for the evaluation of the scattering parameters of annular aperture arrays under TM oblique incidence. Figure 3.10 shows a schematic wherein TM and TE plane wave incidence at both principal planes, i.e. $\varphi = 0°$ and $\varphi = 90°$, is depicted.

Figure 3.11 shows the transmission coefficient for the FSS and ET designs presented before, considering TM incidence at $\theta = 45°$. Both principal incidence planes, $\varphi = 90°$ and

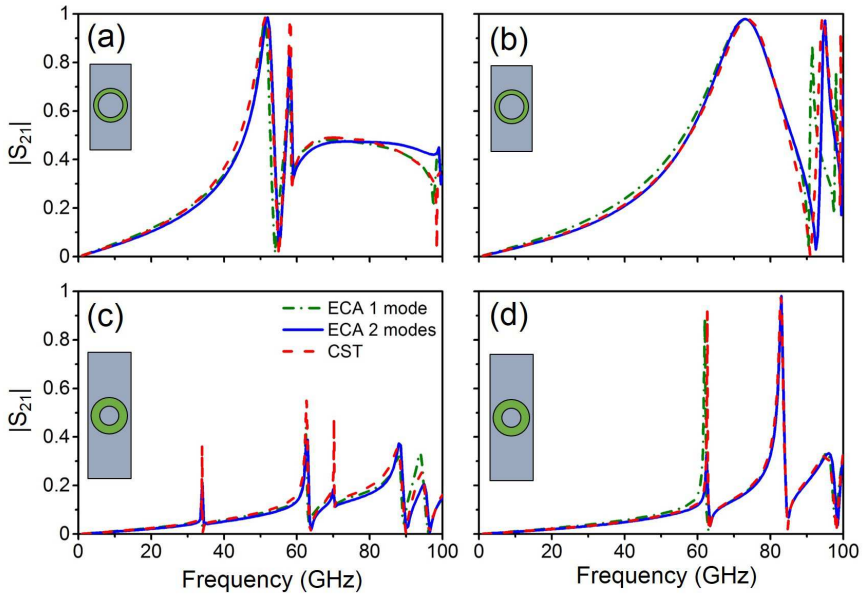

Fig. 3.11 ECA results of the transmission coefficient for FSS and ET designs for $\theta = 45°$. (a) FSS, $\varphi = 90°$. (b) FSS, $\varphi = 0°$. (c) ET, $\varphi = 90°$. (d) ET, $\varphi = 0°$.

$\varphi = 0°$ are considered. As it can be seen in Fig. 3.11(a), for the FSS case and $\varphi = 90°$, the inclusion of the second mode slightly improves the accuracy of the equivalent circuit (especially in the prediction of the null at 55 GHz). For the orthogonal plane shown in Fig. 3.11(b), the accuracy of the model at low frequencies is qualitatively improved when the contribution of the TEM mode is taken into account. In addition, the transmission peak observed after the null at approximately 95 GHz is much better predicted by the ECA considering two modes. For the ET case shown in Figs. 3.11(c) and (d) the inclusion of the second mode also improves the accuracy of the circuit although in a lesser extent.

Layered Medium

In the previous sections, dielectric-backed solutions were considered with a single dielectric slab. This consideration was taken to keep the studied structures as simple as possible since the main purpose was to validate the ECA in the context of ET and FSS structures. In addition the experimental characterization treated in a subsequent section, single dielectric slabs solutions are preferable because they are easier to manufacture.

Nevertheless, sandwiched or layered solutions [two or more dielectric slabs at both sides of the FSS/ET structure, see Fig. 3.12(a)] are also of great importance. In fact, sandwiched solutions between identical slabs allow for total transmission in the absence of losses. In contrast, single slab solutions presented in previous section always suffer from an impedance

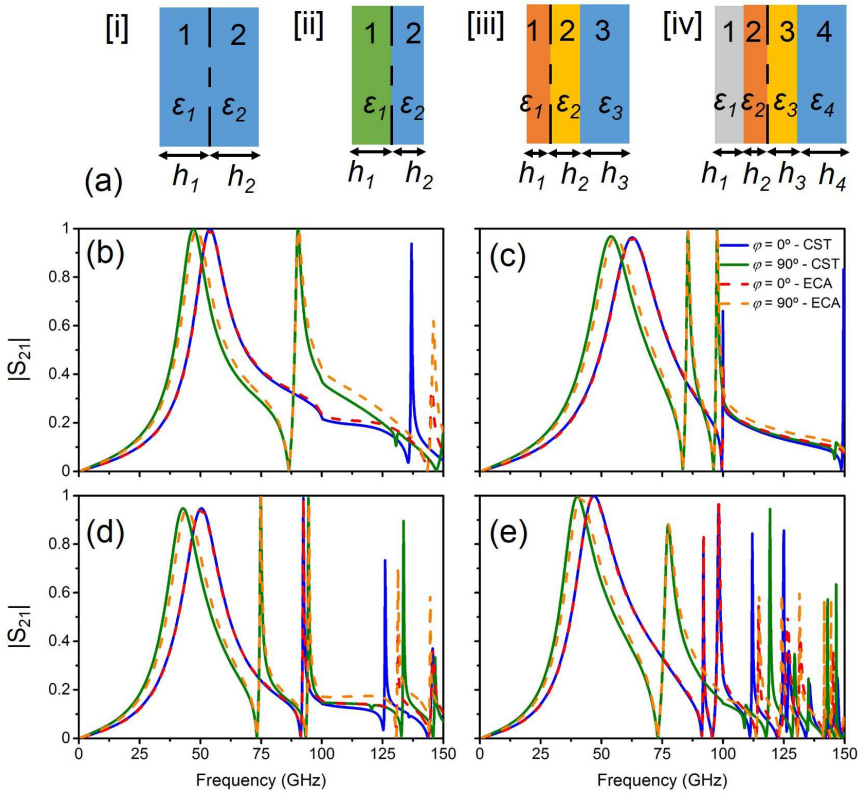

Fig. 3.12 (a) Schematic of sandwiched and layered solutions: [i] $\varepsilon_1 = \varepsilon_2 = 3$; $h_1 = h_2 = 0.4\,\text{mm}$. [ii] $\varepsilon_1 = 2$, $h_1 = 0.8\,\text{mm}$ $\varepsilon_2 = 3$, $h_2 = 0.2\,\text{mm}$. [iii] $\varepsilon_1 = 5$, $h_1 = 0.2\,\text{mm}$; $\varepsilon_2 = 3$; $h_2 = 0.4\,\text{mm}$; $\varepsilon_3 = 2$; $h_3 = 0.7\,\text{mm}$. [iv] $\varepsilon_1 = 4$, $h_1 = 0.3\,\text{mm}$; $\varepsilon_2 = 5$; $h_2 = 0.2\,\text{mm}$; $\varepsilon_3 = 3$; $h_3 = 0.4\,\text{mm}$; $\varepsilon_4 = 2$; $h_4 = 0.7\,\text{mm}$. ECA results of the transmission coefficient for double aperture designs. (b) Sandwiched [i]. (c) Sandwiched [ii]. (d) Layered [iii]. (e) Layered [iv].

mismatch due to the different impedance at each interface (note that previous studies never reached total transmission). The ECA developed here allows for the inclusion of additional dielectric slabs with low effort and very accurate results. Figure 3.12 shows some examples of sandwiched and layered solutions with ECA and full wave numerical results with the following geometrical parameters: $d_x = 1.5\,\text{mm}$, $d_y = 3\,\text{mm}$, $a = 0.5\,\text{mm}$ and $b = 0.65\,\text{mm}$. Figure 3.12(b) shows a sandwiched solution between two identical slabs exhibiting a total transmission band for both vertical and horizontal polarizations. In turn, a design with two different slabs on each side is shown in Fig. 3.12(c). As it can be seen total transmission cannot be attained for the first transmission bands. Figures 3.12(d) and (e) show layered solutions with three and four dielectric slabs respectively. A very good agreement is obtained specially below the diffraction limit in all cases.

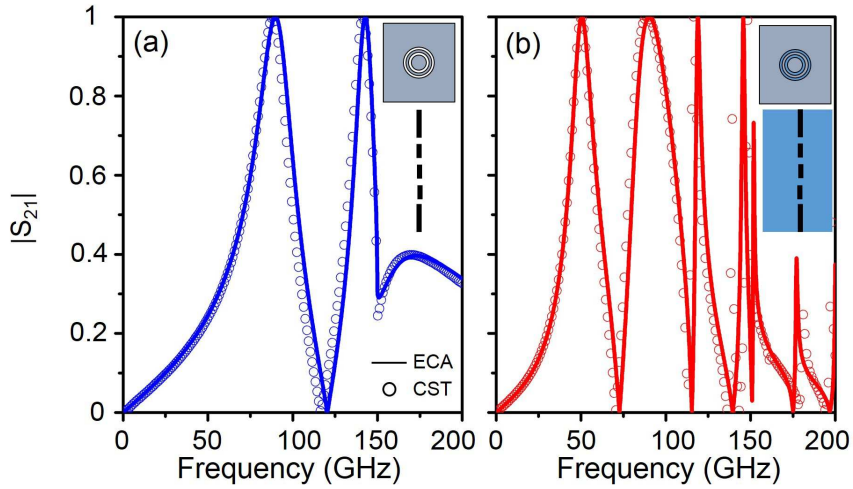

Fig. 3.13 ECA results of the transmission coefficient for double aperture designs. (a) Free-standing. (b) Sandwiched.

Double Annular Aperture

Now the particular case of a unit cell with double annular aperture is briefly addressed. With this configuration double band solutions can be obtained. Thus, the geometry depicted in Fig. 3.3(b) is considered with the following structural parameters: a_1=0.3 mm, b_1=0.4 mm, a_2=0.55 mm, b_2=0.65 mm, $d_x = d_y$=2 mm. Free-standing and a sandwiched solution between identical slabs with relative permittivity, $\varepsilon_r = 2.8$ and thickness, $h_s = 0.5$ mm are considered.

Figure 3.13 shows the transmission results for the ECA and full wave numerical simulations. Again a good agreement is achieved for the two considered cases. In this way, double band solutions can be easily designed by means of the presented ECA in a fast an efficient way. This could be exploited in the synthesis of ad-hoc spatial filters of applications with double band requirements.

3.1.3 Experimental Results

In this section, an experimental demonstration of the FSS and ET designs presented in the previous section is provided. To this end, two prototypes featuring the FSS and ET geometries considered in Sec. 3.1.2 were fabricated by milling machining. The annular apertures were patterned on the commercial substrate ULTRALAM 2000 from Rogers Corp. The dielectric properties given by the manufacturer are a dielectric constant $\varepsilon_r = 2.4$ - 2.6 and a loss tangent $\tan\delta = 0.0022$ (measured at 10 GHz). The thickness of the copper cladding is 35 μm. The measurements were performed with an AB-Millimetre vector network analyzer (VNA)

equipped with a quasi-optical (QO) bench (see App. A). The experimental setup consisted of two corrugated horn antennas as transmitter (TX) and receiver (RX), four ellipsoidal mirrors to get a focused Gaussian beam illumination at the sample position, and an automatic rotatory platform where the sample is placed to perform oblique incidence measurements. The experimental characterization was carried out through a frequency sweep between 45 and 110 GHz in steps of 25 MHz. Two independent sets of transmitters and receivers were employed to cover the V band (45 - 75 GHz) and the W band (70 - 110 GHz).

Figure 3.14 shows a comparison between the obtained experimental and full wave simulation results of the whole structure under normal incidence (microscope photographs of the unit cells of both fabricated prototypes can be found in the insets). The structural parameters of the fabricated prototypes differ slightly from the designed ones due to fabrication tolerances (see Tab. 3.2). These parameters were used in the CST full-wave simulation results shown in Fig. 3.14. In addition, the dielectric permittivity was taken as $\varepsilon_r = 2.5$ and losses were included with a loss factor $\tan\delta = 0.006$. These values were fit with the experimental results being congruent with the values reported in the literature.

Fabricated Prototype	a (mm)	b (mm)	d_x (mm)	d_y (mm)	h_s (mm)	ε_r
FSS	0.48	0.67	1.5	3	0.65	2.5
ET	0.27	0.56	1.5	5	0.72	2.5

Table 3.2 Geometrical parameters of the fabricated FSS/ET prototypes.

The full-wave simulation of the actual finite structure was performed with the time domain solver by using a Gaussian beam source. The Gaussian-beam field profile was set to have the focus exactly at the sample surface. The beam-waist diameter ($2w_0$) was 23 mm in agreement with the experimental value, so that it covered approximately half of the sample (the sample diameter was about 52 mm). The chosen frequency for the Gaussian beam definition was 75 GHz, roughly the center frequency of the range of interest. The finite simulation results were evaluated as the field recorded at a distance of 15 mm away from the center of the prototype sample properly averaged by the spatial profile of the receiving antenna.

As it can be observed in Fig. 3.14, there is an overall good agreement between experimental and simulation results. For the FSS structure [Figs. 3.14(a) and (b)], an excellent concordance is achieved for both polarizations despite a small frequency downshift observed in the simulation. This disagreement can be attributed to possible errors in the assumption of ε_r and/or h_s or to the deficiency in modelling the frequency-dependent beamwaist of the Gaussian beam. In any case, the frequency shift is about 2.5% at 80 GHz. It can be observed

that the second transmission band is seriously degraded in the experiment and finite structure simulation for the vertical polarization case. A transmission dip appears due to splitting of the transmission peak into two. This can be attributed to the non-uniformity of the wave that impinges onto the sample. In fact, due to the intrinsic propagation properties of the Gaussian

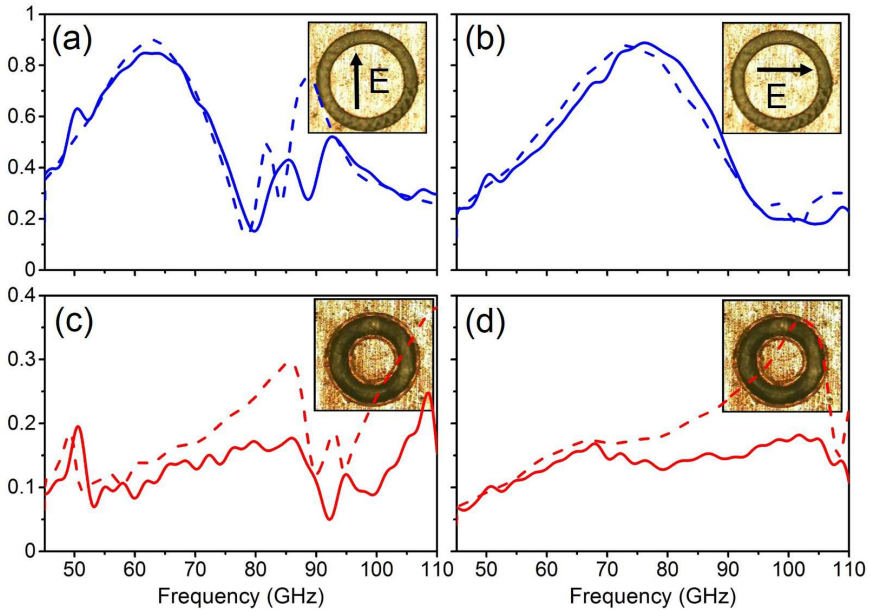

Fig. 3.14 Experimental results for FSS and ET prototypes. Experiment (solid line) and full wave simulations of the finite structure (dashed line). (a) FSS - Vertical polarization ($\varphi = 90°$). (b) FSS - Horizontal polarization ($\varphi = 0°$). (c) ET - Vertical polarization ($\varphi = 90°$). (d) ET - Horizontal polarization ($\varphi = 0°$).

beam, oblique wavevectors are present at the illumination plane even under normal incidence. For this reason, the obtained response in this case shows the splitting of the RW anomaly into two dips, as it occurs (and shown later) for oblique incidence under TM polarization and $\varphi = 90°$. To support this argument, a field inspection of the full-wave simulation results for the FSS case at vertical polarization is presented in Fig. 3.15. There, the electric field distribution of the y and z components at different frequencies, $f = 63$, 78 and 84 GHz is shown. The yz-plane ($x = 0$) is chosen with the impinging wave propagating forward along z. At 63 GHz the impinging wave is almost totally transmitted through the array. The field is mostly contained in the y component [see Figs. 3.15(a) and (b)]. In contrast, a very high reflection appears at 78 and 84 GHz. At these frequencies, one can see waves running along the surface (which are related to the RW anomaly unfolding), that eventually reach the prototype edges and radiate in endfire direction. Another feature observed in both simulation and experimental results is a smoother RW anomaly compared to the one predicted by the ECA results. This is due to the finite size of the fabricated samples [Cam16] and the

focused Gaussian beam illumination. For the horizontal polarization case [Fig. 3.14(b)], the agreement is again good despite a slight frequency shift.

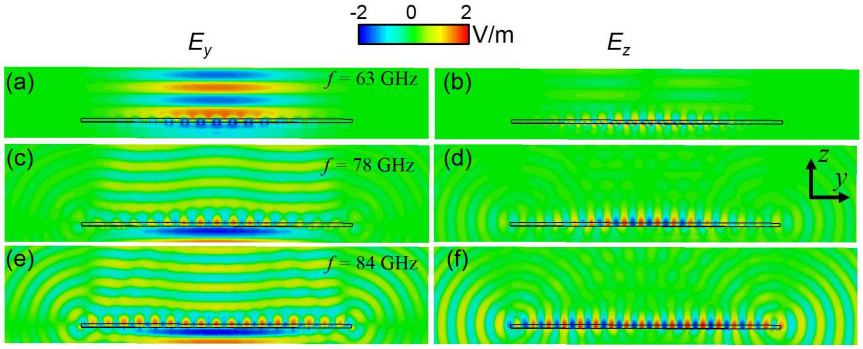

Fig. 3.15 Electric field distribution for the FSS design $\varphi = 0°$ incidence plane. (a) E_y - $f = 63$ GHz. (b) E_z - $f = 63$ GHz. (c) E_y - $f = 78$ GHz. (d) E_z - $f = 78$ GHz. (e) E_y - $f = 84$ GHz. (f) E_z - $f = 84$ GHz.

Regarding the ET design results shown in Fig. 3.14(c) and (d), it can be seen that the differences for the ET transmission peaks between simulations and measurements are larger. For vertical polarization, it can be observed that the first transmission peak exhibits a lower amplitude than the one predicted by ECA results [see Fig. 3.6(c)]. Furthermore, the second transmission peak expected at 59 GHz according to the ECA results, is absent both in simulation and experimental results. These two features can be attributed to an insufficient illumination of the annular apertures, as discussed in [Ber05, Ber07d]. In addition, as discussed in the previous section, ET resonances have a very high Q and thus, losses can dramatically affect the transmission amplitude. It should be remarked here that the annular aperture dimensions have been chosen to work deeply in the ET regime, so the apertures are very small compared to the wavelength that results in an enhanced quality factor of the ET resonance [Med10]. The large differences above 65 GHz between the finite simulation and the measurements are minimized when the detection plane is shifted farther away from the sample. For computational saving issues, the detection plane was set to a shorter distance as compared to the experiment. This means that some energy contribution due to the grating lobes (note the diffraction limit for the ET structure is at 60 GHz) is recorded in the simulation results which is not captured in the experiment.

Next, the oblique-incidence response for both prototypes is provided. The rotatory platform was used for selecting the angle of incidence (θ_{in}). TE and TM polarization was selected by switching the TX and RX antennas from vertical to horizontal position, TE and TM polarization was selected. Finally, the rotation angle of the sample determines the plane of incidence; namely, the alignment with $\varphi = 0°$ or $\varphi = 90°$ planes. The angular

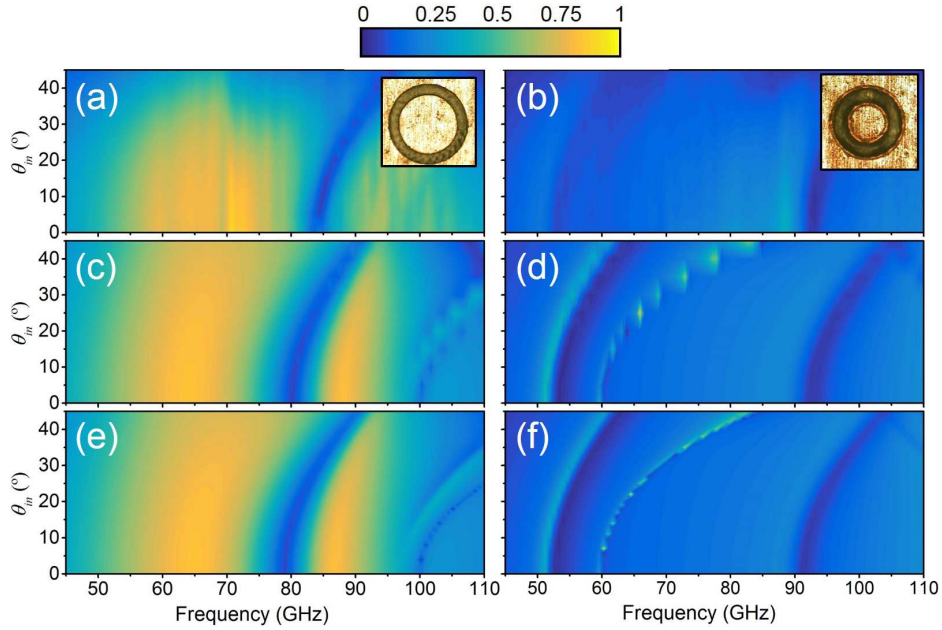

Fig. 3.16 Transmission coefficient versus frequency and θ_{in} for TE polarized impinging wave and $\varphi = 90°$ incidence plane for FSS and ET prototypes. (a) Experiment-FSS. (b) Experiment-ET. (c) CST-FSS. (d) CST-ET. (e) Equivalent Circuit-FSS. (f) Equivalent Circuit-ET.

step is set to 5° and θ_{in} is swept from 0 to 45°. To fully characterize both prototypes, eight independent measurements were made in total (2 incidence planes $\times$ 2 polarizations (TE/TM) $\times$ 2 prototypes). For the sake of brevity, only results concerning TE incidence at $\varphi = 0°$ and TM incidence at $\varphi = 90°$ are shown for both FSS and ET designs in Figs. 3.16 and 3.17, respectively. In addition, CST simulation results of the infinite structure are shown. The computational effort required to characterize the oblique incidence of the finite structure would be enormous and, for a qualitative comparison, simulations of the infinite sample were found sufficiently accurate. For completeness, ECA results are also included, and due to its low computational cost an angular step of 1° has been taken.

Regarding the FSS design in 3.16, an overall good agreement is obtained for the TE incidence at $\varphi = 0°$. The shift of the first null with increasing θ_{in} is clearly observed in the experiment [Fig. 3.16(a)]. As θ_{in} approaches 45°, the sample holder starts to block the impinging wave, resulting in a reduction of the transmitted power. For the ET case in Fig. 3.16, the differences are higher. As predicted in the finite-structure simulation presented in 3.14(c), the amplitude of the first ET peak is highly reduced and the second one (just before f_{diff}) vanishes. Thus, we have found some transmission features in the CST unit-cell simulation and ECA results [Figs. 3.16(d) and (f)] that are not present in the experimental results [Fig.

3.16(b)]. Despite this, the low transmission peak before the null located near 92 GHz is retained in the experiment.

For the case of TM polarization and $\varphi = 90°$ shown in Fig. 3.17, there is also a qualitative good agreement between the experiment, simulations, and ECA results. However, in this case, an additional error source arises from the experimental setup since now the electric field emanating from the antenna is horizontally polarized. Although absorbent material is placed on the metallic bench, a ground effect on the measurements is hardly avoidable. In any case, for the FSS design [Figs. 3.17(a), (c) and (e)], the shift of the transmission band is retained in the experiment. Specifically, it is clearly observed in the angle dependency of the dip that appears right after the transmission peaks. The discontinuities observed for the CST results [Fig. 3.17(c)] come from the angular step considered, and the subsequent interpolation. This artifact does not appear for the equivalent circuit model due to the smaller angular step taken. Regarding the ET design [Figs. 3.17(b), (d), and (f)], again very low transmission levels are obtained. Nevertheless, the experimental results still keep a good agreement with the simulations and EC results for the most important features. In fact, the "diamond-shape" regions delimited by the nulls are present in both simulations and experiments.

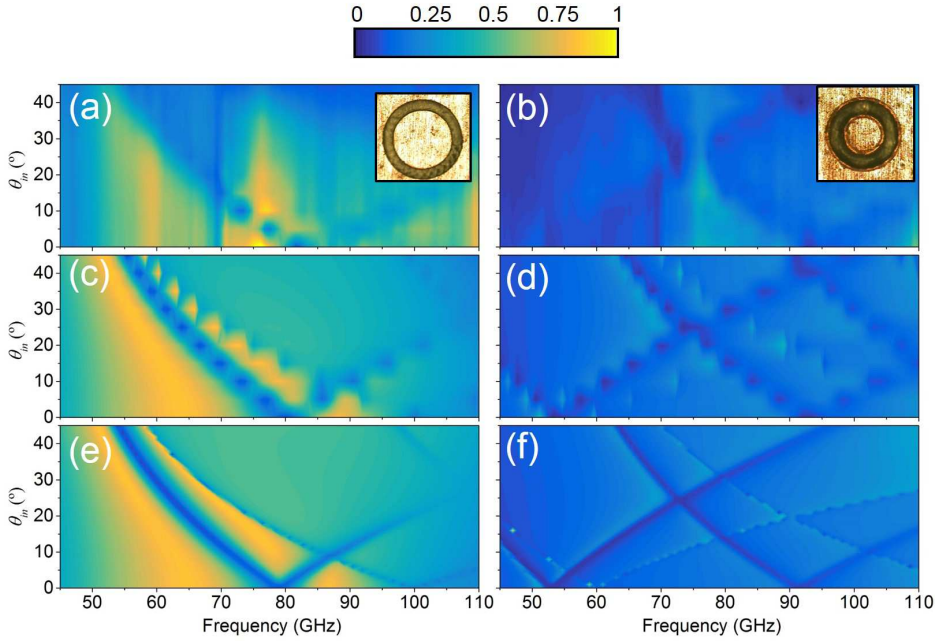

Fig. 3.17 Transmission coefficient versus frequency and θ_{in} for TM polarized impinging wave and $\varphi = 90°$ incidence plane for FSS and ET prototypes. (a) Experiment-FSS. (b) Experiment-ET. (c) CST-FSS. (d) CST-ET. (e) Equivalent Circuit-FSS. (f) Equivalent Circuit-ET.

3.2 Unidirectional devices combining stacked hole arrays and gratings

In this section an application of stacked hole arrays (SHA) in asymmetric transmission devices with enabled beam steering of the transmitted wave is theoretically and experimentally studied. To accomplish this, the SHA is assisted by a dielectric grating properly engineered in such a way that the $m = -1$ grating order can be coupled for a wideband frequency region while the $m = 0$ grating order is kept uncoupled. Furthermore, by a proper selection of the structural parameters, wide ranges with tunable refraction and deflection angles achieved by varying frequency and/or angle of incidence of the impinging wave can be obtained.

Asymmetric transmission is known to appear in finite thickness structures with broken spatial inversion symmetry that can be achieved by means of the addition of grating structures at one of the two interfaces of the finite thickness structure. This grating can excite higher order modes and efficiently couple them to outgoing waves at the given interface. For the opposite interface, due to the absence of the grating high order mode excitation cannot take place and therefore there are not transmission channels associated to them, while zero order is uncoupled for both interfaces. This is one of the asymmetric transmission regimes generally referred to as unidirectionality. High transmission is obtained for impinging waves at one interface while it vanishes for one of the two opposite incident directions. Of course, strict unidirectional performance can only would occur in an ideal scenario, i.e. when transmission is perfect for one direction and vanishing for the opposite one. In general some energy can be transmitted even in the case of incidence on the non-grating interface, and unidirectionality with a very high transmission contrast between forward (grating side) and backward transmission (non-grating side) takes place.

To support the theoretical discussion and provide the general theory regarding unidirectional regimes, equifrequency dispersion contours (EFCs) are used along with construction lines of the grating orders. To this end, the lowest Floquet-Bloch (FB) of the SHA was evaluated by means of the eigenmode solver of the full wave numerical solver CST Microwave Studio. A comprehensive analysis of the unidirectional transmission regimes is provided with the aid of transmission results obtained for infinite structures. In addition, by field inspection, the tunability of the transmitted wave with the angular incidence and frequency of the impinging wave is evaluated.

These theoretical findings are experimentally demonstrated in the millimeter wave regime. The obtained results theoretical and numerical results are in good agreement leading to a new device with very interesting properties associated with tunable deflectors and angular filters. The results described in this section were reported in two journal papers [RU13, RU15].

3.2.1 Unidirectional Transmission and Deflection Ranges: Dispersion Based Approach

As mentioned before, a diffraction inspired unidirectional transmission device is considered here. To achieve it, the zero order must be uncoupled, while one or several higher orders need to be coupled at one of the interfaces, e.g., by means if one-side grating loading. Before describing the particular device presented here we study in detail the conditions to get a wideband frequency unidirectional transmission regimes and tunability of the deflection angle.

We consider a generalized structure with circular EFCs as a host material. To enable the asymmetric transmission, a grating structure is placed on one of the sides of the host material slab of finite thickness. Figure 3.18 shows a schematic of the resulting structure with the important parameters highlighted. In line with the grating theory, the m^{th}-order diffraction angle, which is also called the deflection angle in transmission, is determined as:

$$\sin\phi_m = \sin\theta + m\Delta_k/k, \tag{3.19}$$

where $\Delta_k = 2\pi/L$ is the distance between consecutive construction lines, L is the grating period, $k = \omega/c$ is the wavenumber and $m = 0, -1, -2, \ldots$ is the grating order. In Eq. 3.19, ϕ_m is measured in the counter-clockwise direction with respect to the normal to the exit interface, while θ is measured in the counter-clockwise direction with respect to the normal to the incidence interface. In Fig. 3.18 the refraction angles, θ_0' and θ_{-1}' are assumed to correspond to a LHM. Here, circular EFCs have been used because the mechanism relies mainly on their width and location in $\mathbf{k}-$space rather than their actual shape. Therefore, the following discussion is valid, as it will be demonstrated afterwards for a hybrid structure/material with non circular EFCs.

Figure 3.19 illustrates the general scenario of unidirectional transmission with tunable refraction and deflection. The EFCs for the host material and air are schematically shown together with the construction lines corresponding to zero and higher orders. Higher orders are assumed to be propagating in air only due to the one-side grating. The EFC for the host material is narrower than the one for air. This is the case for materials with effective refraction index lower than unity. In such situation, it is possible to find an incidence angle where the zero order is not coupled to the wave(s) allowed to propagate inside the host material. In this way, there would be no transmission for impinging waves at the non-grating side. In turn, it can occur that the order $m = -1$ may propagate and, hence, be coupled when the grating side is illuminated by an incident wave. Therefore, unidirectional transmission can be expected to appear similarly to structures and regimes already reported

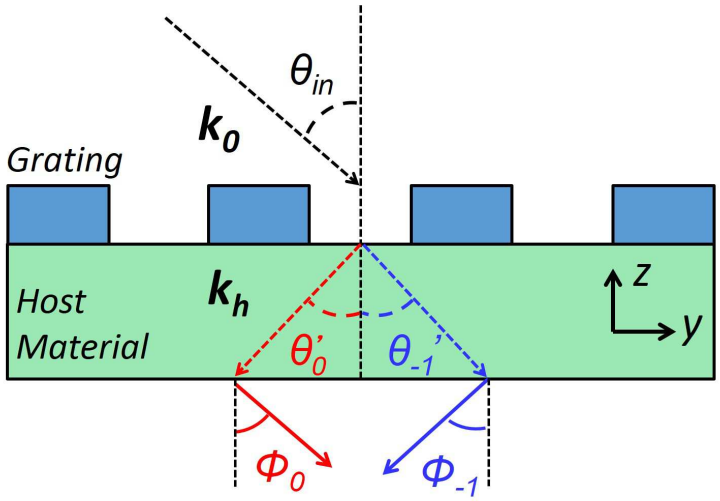

Fig. 3.18 Schematic diagram of the slab of host material with the dielectric grating. $\mathbf{k_0}$ is the free-space wave vector, θ_{in} is the incidence angle, θ_0' and θ_{-1}' are the refraction angles for diffraction orders $m = 0$ and $m = -1$, respectively, $\mathbf{k_h}$ is the wave vector in the host material, and ϕ_0 and ϕ_{-1} are the deflection angles for orders $m = 0$ and $m = -1$, respectively. Both diffraction orders are assumed to be propagating in surrounding air and coupled to the waves that may propagate in the host material. Order $m = -1$ is positively refracted at the upper interface leading to negative deflection of the outgoing wave. Order $m = 0$ is negatively refracted leading to positive deflection.

in the literature [Ser09a, Ser09b, Ber11c]. . At a fixed frequency the construction lines in Fig. 3.19 can be shifted to the left and right, by reducing or increasing θ_{in} respectively. Then, one can obtain zero (case I), negative (case II), or positive (case III) deflection of the single outgoing wave. Both negative and positive refraction at the grating side can correspond to negative deflection ($k_y < 0$), for the cases of RH and LH propagation inside the host material, respectively. These cases have counterparts for positive deflection ($k_y > 0$). For the used shape and location of EFCs, signs of refraction at the corrugated interface and deflection of the outgoing wave are changed simultaneously.

To show the possible regimes depending on the selected host medium and diffraction grating let us consider different values of k_h/k_0, being k_h and k_0 the wavenumbers in the host material and free space, respectively, and the distance between construction lines Δ_k . Figure 3.20 shows three examples of coupling scenarios for $\Delta_k > 2k_h$. The limiting case when $\Delta_k = k_h + k_0$ is shown in Fig. 3.20(a). In this case, the $m = -1$ order cannot be coupled for the complete range of k_y variation. As it can be seen at the maximum k_y value, i.e, $\theta_{in} \approx 90°$ the $m = -1$ order is still uncoupled. On the other hand, by taking a smaller value of Δ_k, i.e., $2k_h < \Delta_k < k_h + k_0$, one can obtain a narrow range of k_y variation, in which the order $m = -1$ can be coupled to the wave that propagates in the host material. Figures 3.20(b) and

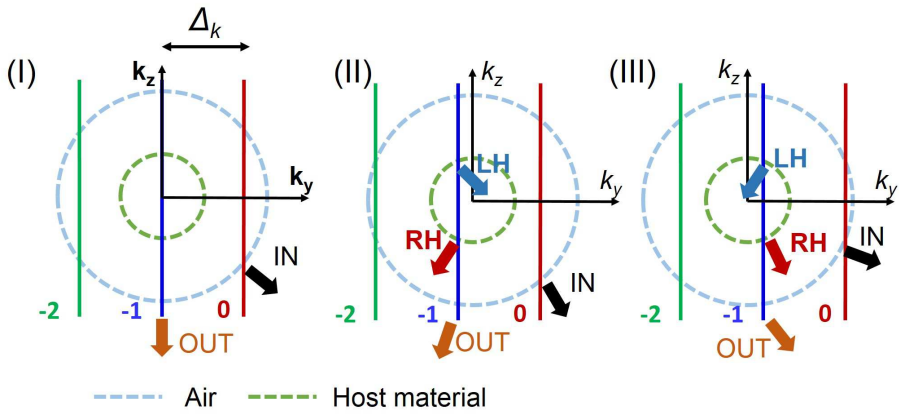

Fig. 3.19 General idea of tunable unidirectional transmission. Dashed circles represent the EFCs plotted in the (k_y, k_z) plane for air and host material. Straight solid lines are construction lines for orders $m = -2, -1,$ and 0 at a fixed frequency for different angles of incidence. Arrows indicated by "IN" and "OUT" schematically depict directions of incident and transmitted waves. Arrows indicated by "LH" and "RH" do so for the refracted beams at the grating interface in case of left-handedness and right-handedness. Cases (I), (II), and (III) correspond to normally propagating and negatively and positively deflected outgoing waves, respectively.

(c) show this scenario for two different angles of incidence. In such situation unidirectional transmission is possible with small range of attainable deflection angle. It can be seen that $\phi_{-1} \in [\Phi_{min}, \Phi_{max}]$ range whose limits can be written as:

$$\begin{aligned} \Phi_{min} &= -\arcsin\left(\frac{k_h}{k_0}\right) \\ \Phi_{max} &= -\arcsin\left(\frac{k_h + k_0 - \Delta_k}{k_0}\right). \end{aligned} \tag{3.20}$$

As it can be seen the complete range of ϕ_{-1} corresponds to negative values. In other words, only negative deflection can be obtained under unidirectional conditions. The width of the unidirectional regime in terms of k_y in this case is given as:

$$K^{\mathrm{UD}} = k_0 + k_h - \Delta_k. \tag{3.21}$$

Regarding the refraction angle, θ, at which coupling may exist , $\theta \in [\theta_{min}, \theta_{max}]$, the limits are:

$$\begin{aligned} \theta_{min} &= -\arcsin\left(\frac{\Delta_k - k_h}{k_0}\right) \\ \theta_{max} &= \pi/2. \end{aligned} \tag{3.22}$$

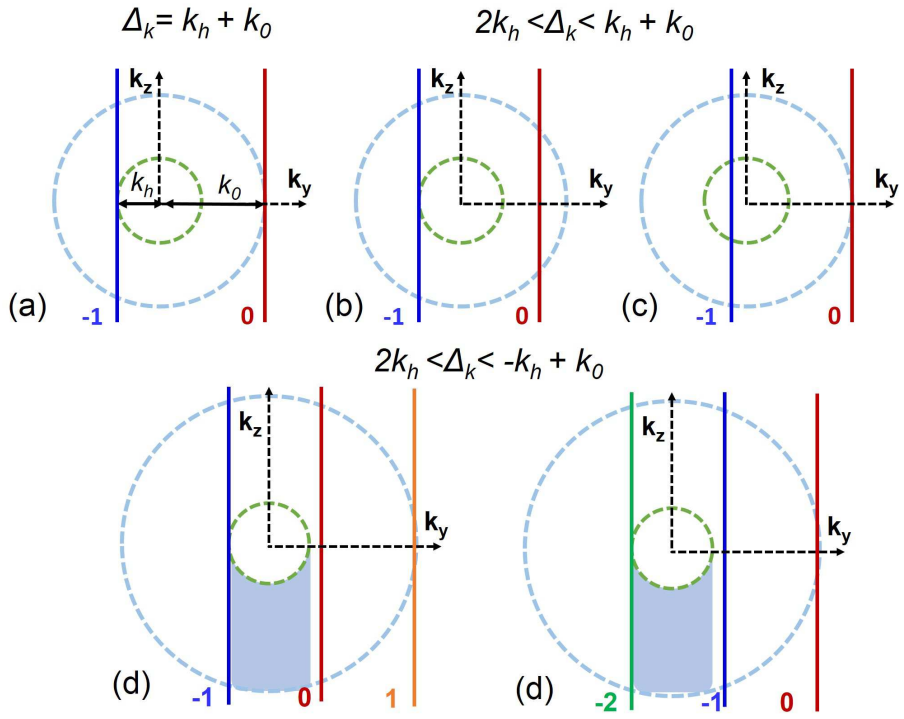

Fig. 3.20 Coupling scenarios at $\Delta_k > 2k_h$. (a) $\Delta_k = k_h + k_0$. (b) and (c) $2k_h < \Delta_k < k_h + k_0$ at two different angles of incidence. (c) $2k_h < \Delta_k < -k_h + k_0$ for two different angle incidence scenarios. EFCs are shown in the (k_y, k_z) plane. Construction lines are shown for $m = -2, -1, 0,$ and 1. The shadowed area covers the k_y range, for which unidirectionality can appear.

To extend the range to the complete set of refraction angles (i.e. from $-\pi/2$ to $\pi/2$) while keeping the $m = -1$ order as the only one coupled the following condition must be satisfied by the air and host medium EFCs:

$$2k_h < \Delta_k < k_0 - k_h, \tag{3.23}$$

so that $k_0 \geq 3k_h$. Figures 3.20(d) and (e) accounts for this scenario resulting in unidirectional regime of width K^{UD} and deflection angle range $\phi_{-1} \in [\Phi_{min}, \Phi_{max}]$ as follows:

$$\begin{aligned} K^{\mathrm{UD}} &= 2k_h \\ \Phi_{min} &= -\arcsin\left(\frac{k_h}{k_0}\right) \\ \Phi_{max} &= \arcsin\left(\frac{k_h}{k_0}\right). \end{aligned} \tag{3.24}$$

Let us consider an additional scenario where $\Delta_k = 2k_h$ to fully understand the required conditions for combination of unidirectional transmission and tunability of the deflection angle (see Fig. 3.21). Two different k_h/k_0 values are considered, namely, $k_h = k_0/3$ [Figs. 3.21(a)-(c)] and $k_h = k_0/2$ [Figs. 3.21(d)-(f)]. For the former case the unidirectional and tunability properties are characterized by the following quantities:

$$\begin{aligned} K^{\mathrm{UD}} &= 2k_h \\ \Phi_{min} &= -\arcsin\left(\frac{1}{3}\right) \\ \Phi_{max} &= \arcsin\left(\frac{1}{3}\right). \end{aligned} \tag{3.25}$$

The deflection angle at the grating interface for the $m = -1$ order, $\theta' = \theta'_{-1}$ can run over all the possible angles when the angle of incidence, θ_{in} of the incident wave (and, hence, k_y) is varied. For the second case, $k_h = k_0/2$, coupling of the $m = -1$ order is achieved for refraction angles, θ'_{-1} between $-\pi/2$ to 0. This leads to the following unidirectional width and deflection angle limits:

$$\begin{aligned} K^{\mathrm{UD}} &= k_h \\ \Phi_{min} &= -\arcsin\left(\frac{1}{2}\right) \\ \Phi_{max} &= 0. \end{aligned} \tag{3.26}$$

As it can be seen, the tunability of the deflection angle is restricted to negative values uniquely. Therefore, switching between negative and positive deflection is not possible.

In the case where $k_0 > 3k_h$, the $m = -2$ order can be additionally coupled and therefore two output beams will be obtained. To keep a single-beam operation, i.e. coupling uniquely the $m = -1$ order, one should choose $k_0 \leq 3k_h$. At the light of the above considerations, the conditions for sign switching of the deflection angle and single-beam unidirectional regime with the widest possible angular range can be summarized as follows:

$$\begin{aligned} k_h &< k_0/2 \\ k_h &= k_0/3, \end{aligned} \tag{3.27}$$

It is worth noting that the general condition of unidirectional transmission for EFCs located around the $(k_y = 0, k_z = 0)$ point, namely, $k_h < k_0$, is less restrictive than these requirements. In particular, the first condition in Eq. 3.27, gives the necessary scenario for simultaneous appearance of unidirectionality and deflection sign switching. In addition, the second

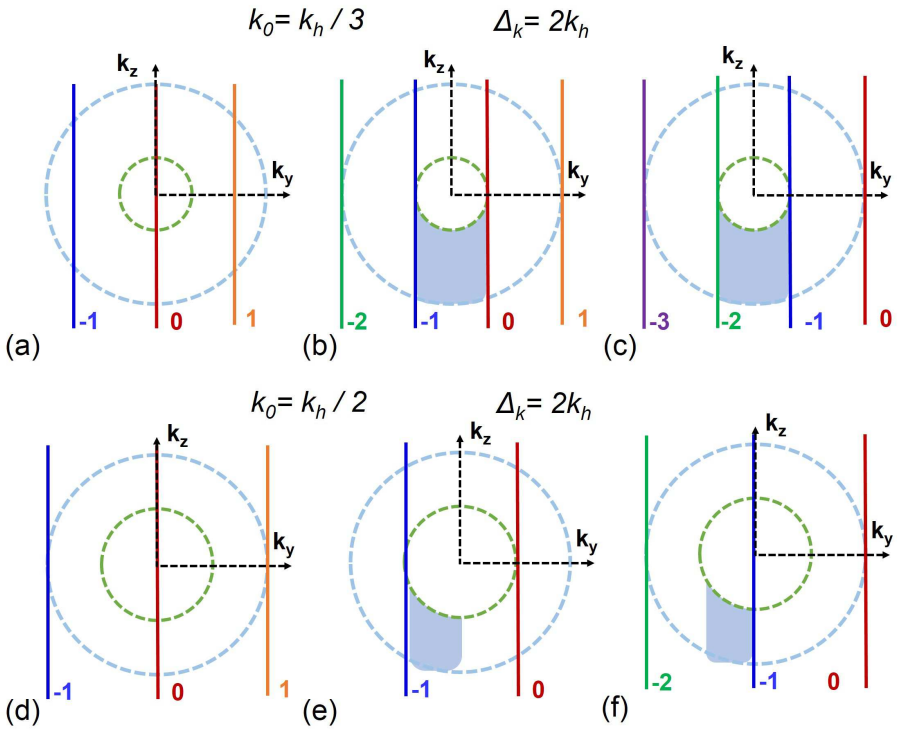

Fig. 3.21 Coupling scenarios at $\Delta_k = 2k_h$. (a)–(c) $k_h = k_0/3$; (d)–(f) $k_h = k_0/2$. EFCs are shown in the (k_y, k_z) plane. Construction lines are shown for $m = -3, -2, -1, 0,$ and 1. The shadowed area shows the k_y range with possible unidirectional transmission.

condition ensures that the negative and positive deflection angle ranges are identical and single-beam operation is preserved. A summary of the described coupling scenarios can be found in Tab. 3.3. Coupling-free regime, unidirectionality without deflection sign switching property and unidirectionality plus switching capability from negative to positive deflection are outlined.

Δ_k	k_h	K^{UD}	Deflection
$k_h + k_0$	$< k_0$	—	—
$2k_h$	$k_0/2$	$k_h + k_0 - \Delta_k$	Negative
$2k_h$	$k_0/3$	$2k_h$	Negative/Positive

Table 3.3 Coupling scenarios summary

3.2.2 SHA and Dielectric Gratings as Unidirectional Tunable Devices

In this section we corroborate the general theory provided in the previous section by means of an engineered structure based on a SHA in combination with a dielectric grating. SHAs have the required dispersion properties for unidirectionality and tunability even for quite compact structures. As introduced in Chapter 1 of this Thesis, SHAs can be designed in such a way that resonant modes with different nature can appear. For small longitudinal periods (i.e. low separation between layers), d_z, ET resonance leads to LH propagation. In contrast, for large d_z, Fabry-Perot resonances exhibiting RH propagation may appear. For the sake of compactness, the solution proposed here was designed to operate within the first regime, namely, the SHA exhibits ET resonance and LH behavior. Then, this regime accordingly combined with the diffraction properties provided by a dielectric grating leads to the implementation of a unidirectional and tunable device.

Figure 3.22 shows a schematic of the proposed SHA plus grating structure along with the reference coordinate system and details regarding the SHA and dielectric grating unit cells. The incidence plane is the yz-plane and TM polarization is selected for the incident wave. The dimensions and dielectric properties of all the materials are included within the caption. The metallic parts are made of Copper with a nominal conductivity $\sigma_{Cu} = 5.8 \times 10^7$ S/m. The total thickness of the structure is given by $D = Nh + (N+1)t + a_z$, where N is the total number of hole array layers and t and h are the metal and substrate thickness respectively. Two different sets of simulations were carried out to characterize the SHA and grating response. To evaluate the dispersion properties of the infinite three-dimensional SHA, the eigenmode solver of CST Microwave Studio was used (see App. A). Then, the dispersion of the lowest Floquet-Bloch mode was obtained For the transmission results of the complete structure, i.e. SHA plus grating, the frequency domain solver with unit cell boundary conditions was used.

To demonstrate the tunability capability of the presented structure an analysis in terms of coupling between the lowest FB mode and the isolines for the incidence angle, $\theta_{in} = \theta_{in,m}$ (where m is the grating order), at a given frequency is provided. Then $\theta_{in,m}$ is evaluated as follows:

$$\theta_{in,m} = \arcsin[k_y'^m/k_0] = \arcsin[c_0 k_y'^m/(2\pi f)], \tag{3.28}$$

where $k_y'^m$ is the tangential wavenumber for the incident wave on the dielectric grating. It can be calculated as:

$$k_y'^m = k_y^m - \frac{2\pi m}{L}, \tag{3.29}$$

where $L = 3d_y$ is the grating period. In fact, this calculation reveals the angle of incidence (from air) enables excitation of the diffraction order m and coupling through the SHA host. Then for an arbitrary pair of values of k_y^m and frequency, f, there is an unique solution for

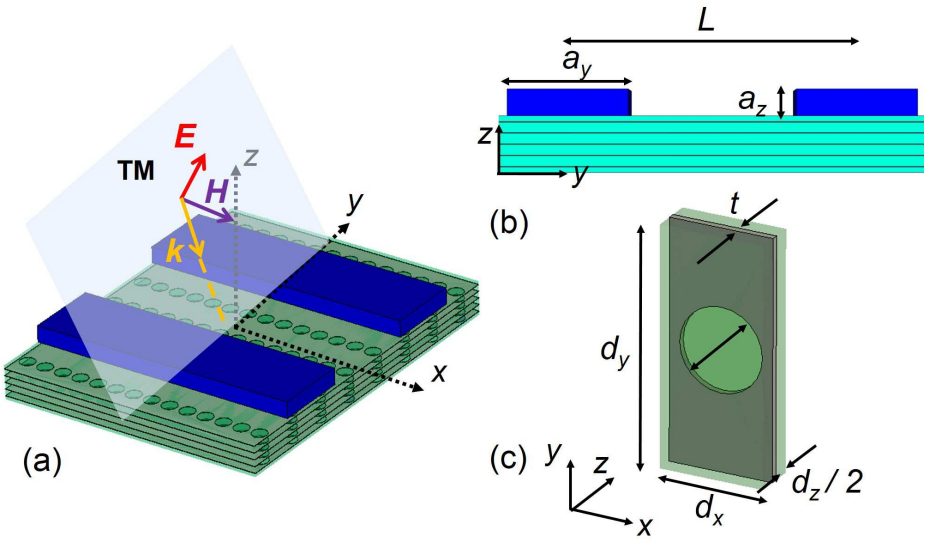

Fig. 3.22 Schematic of SHA and dielectric grating structure. (a) SHA+grating schematic along with the impinging wave at the selected reference coordinate system. (b) Side view. (c) Unit cell of the SHA. Grating parameters: period, $L = 3d_y$; thickness $a_z = 1.27\,\text{mm}$; length, $a_y = 5.68\,\text{mm}$; permittivity, $\varepsilon_g = 10.2$. SHA parameters: in-plane period dimensions, $d_x = 1.5\,\text{mm}$ and $d_y = 3.4\,\text{mm}$; metal thickness, $t = 35\mu\,\text{m}$; substrate permittivity, $\varepsilon_s = 2.43$; substrate thickness, $h = 0.49\,\text{mm}$; axial period, $d_z = 0.525\,\text{mm}$.

the incidence angle. Figure 3.23 shows the EFCs for the lowest FB mode of the SHA and the isolines for the grating orders $m = 0$, $m = -1$ and $m = -2$. To obtain these results both the tangential wavenumber, k_y^m, and frequency, f, are swept leading to a unique solution for the incident angle for each iteration. As it can be observed the EFCs corresponding to the lowest FB mode of the SHA are not circular but ellipsoidal. This fact reveals that indeed the SHA host is anisotropic and, thus, the iso-angle curves are not straight lines. By using the information contained within Fig. 3.23 it is possible to identify whether coupling between the diffraction orders and the FB mode is possible at a given pair of k_y^m and f or not. For instance, according to Fig. 3.23(a) there is no coupling for $m = 0$ at frequencies ranging from 50 to 55 GHz when the incidence angle is $|\theta_{in}| > 20°$. At the same time, the $m = -1$ order can be coupled to the FB mode at these frequencies for θ_{in} ranging from 25° to 52° approximately [see Fig. 3.23(b)]. Furthermore, the $m = -2$ order can be only coupled in this frequency range for $\theta_{in} > 82°$. Therefore, it results that single beam unidirectional regime can be obtained for a wide range of f and θ_{in}. In addition, at a fixed f and varying θ_{in}, a switching of the deflection angle sign can be obtained (i.e. the sign of k_y is changed). In connection with the theoretical analysis conducted in the previous section, it should be noted that for the $\phi_{-1} < 0$ ($k_y < 0$) case, positive refraction ($\theta'_{-1} > 0$) is observed. On the

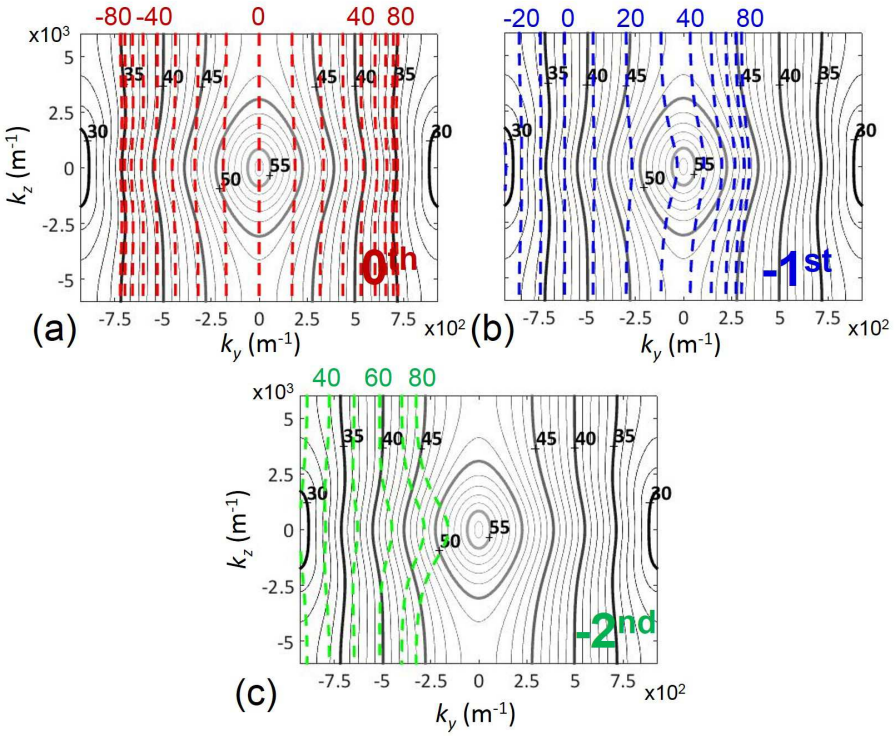

Fig. 3.23 EFCs (solid lines) for the lowest FB mode and isolines (dashed lines) in the (k_y, k_z) plane. Numbers near EFCs show frequency in GHz. The iso-angle lines are plotted at steps of 10°. Numbers at the top show the angle value in degrees. $k_y = k_y^{(m)}$ and k_z are the tangential and longitudinal wavenumbers respectively. (a) $\theta_{in,0}$. (b) $\theta_{in,-1}$. (c) $\theta_{in,-2}$.

contrary, when $\phi_{-1} < 0$ $(k_y < 0)$, negative refraction $(\theta'_{-1} < 0)$ appears because $\mathbf{S} \cdot \mathbf{k_{FB}} < 0$ ($\mathbf{S}$ is the Poynting vetor; $\mathbf{k_{FB}}$ is the wave vector of the FB mode) in the SHA. Furthermore, tunability of ϕ_{-1} can also be obtained when $sgn(\phi_{-1}) = sgn(\theta'_{-1})$ that corresponds to modes with $\mathbf{S} \cdot \mathbf{k_{FB}} > 0$.

The results presented above can be translated to a two dimensional plot where the iso-angles contours of Fig. 3.23 along with their corresponding output deflection angle, ϕ_m can be plotted versus θ_{in} and f (see Fig.3.24). There isolines for ϕ_0, ϕ_{-1} and ϕ_{-1}(degrees) are shown with a step size of 2° (labels indicating the ϕ_m value are placed every 10°). It can be clearly observed that single beam unidirectional regimes are obtained when $m = -1$ or $m = -2$ orders are coupled and $m = 0$ is uncoupled. From a practical point of view, the regime provided by the $m = -1$ order is more interesting. First, coupling for the $m = -1$ order is allowed for a wider θ_{in} range. Second, the ϕ_{-1} range enables a wider range of tunability along with a sign switching of the deflection angle. Two distinct regions are highlighted within Fig. 3.24. The first one, labeled as I, delimits the region where sign switching can be obtained for a fixed f at two discrete θ_{in}. In contrast, region II represents

the $f-\theta_{in}$ area wherein a sign switching of ϕ_{-1} can be obtained by varying continuously θ_{in}.

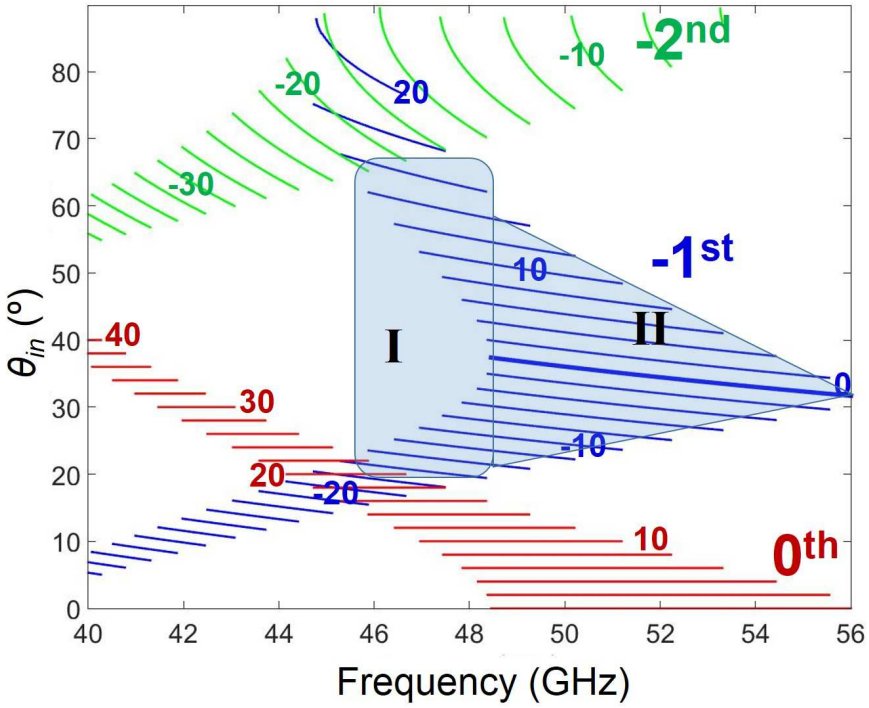

Fig. 3.24 Isolines for ϕ_0, ϕ_{-1} and $\phi_{-1}(^\circ)$ in (f, θ_{in}) plane within the area where coupling to the lowest FB wave is possible.

Next, transmittance results of the SHA plus the dielectric grating structure are presented. The simulated structure is considered as infinite along the x and y axes while is finite along z axis. Two designs with different number of layers, $N = 4$ and $N = 10$ are evaluated. To demonstrate the unidirectional behavior, forward transmittance, $T^{\rightarrow}$, i.e. transmitted energy for waves impinging at the grating side, backward transmittance, $T^{\leftarrow}$, i.e. transmitted energy for waves impinging at the opposite side, and forward-to-backward contrast $\Theta = T^{\rightarrow}/T^{\leftarrow}$ are evaluated and shown in the frequency-incidence angle, (f, θ_{in}), plane (see Fig. 3.25). The (f, θ_{in}) range runs from 45 to 55 GHz and from 20 ° to 80 °. For all cases, the transmittance, T, accounts for the summation of transmission results obtained for the grating orders, $m = 0, -1,$ and -2, namely $T^{\rightarrow} = t_0^{\rightarrow} + t_{-1}^{\rightarrow} + t_{-2}^{\rightarrow}$ and $T^{\leftarrow} = t_0^{\leftarrow} + t_{-1}^{\leftarrow} + t_{-2}^{\leftarrow}$ (where t accounts for transmittance in the corresponding order and incidence direction). To identify the expected regions with unidirectional regime, the deflection angle linked to the $m = -1$ order, ϕ_{-1} is depicted with white labels accompanying solid white lines (where coupling between SHA FB mode and $m = -1$ may occur). The dashed white lines account for ϕ_{-1} where coupling is not possible. As it can be seen, a high transmittance region can be readily distinguished for

the forward incidence for both N values. In turn, the transmission for each grating order can be easily identified by comparing these results with those shown in Fig. 3.24. It can be seen how at f, θ_{in} between 45 GHz, 65 ° and 47 GHz-80 ° coupling from $m = -1$ and $m = -2$ coexist leading to non-single beam unidirectional transmission. Furthermore, at $\theta_{in} \gtrapprox 70°$ and $f \approx 50$ GHz, the $m = -2$ is the only order coupled to the SHA-FB mode leading then to the second band of single-beam unidirectional regime. Regarding the backward transmission results, $T^{\leftarrow}$, the amplitude is much lower for the two cases, $N = 4$ and $N = 10$ [see Fig. 3.25(b) and (e)]. However, it is true that for the bulkier case ($N = 10$) the $T^{\leftarrow}$ is minimized. This can be easily explained from the closest resemblance of the $N = 10$ dispersion performance to the one exhibited by the infinite volumetric structure. In terms of forward-to-backward contrast, Θ, again the performance of the $N = 10$ design is better (especially for the unidirectional region connected with $m = -2$). In any case, maximum $\Theta \approx 60$ dB are obtained for both designs, and $20 < \Theta < 40$ dB within the f, θ_{in} range of interest, namely, between 47.5 GHz-25 ° and 52.5 GHz-60 °.

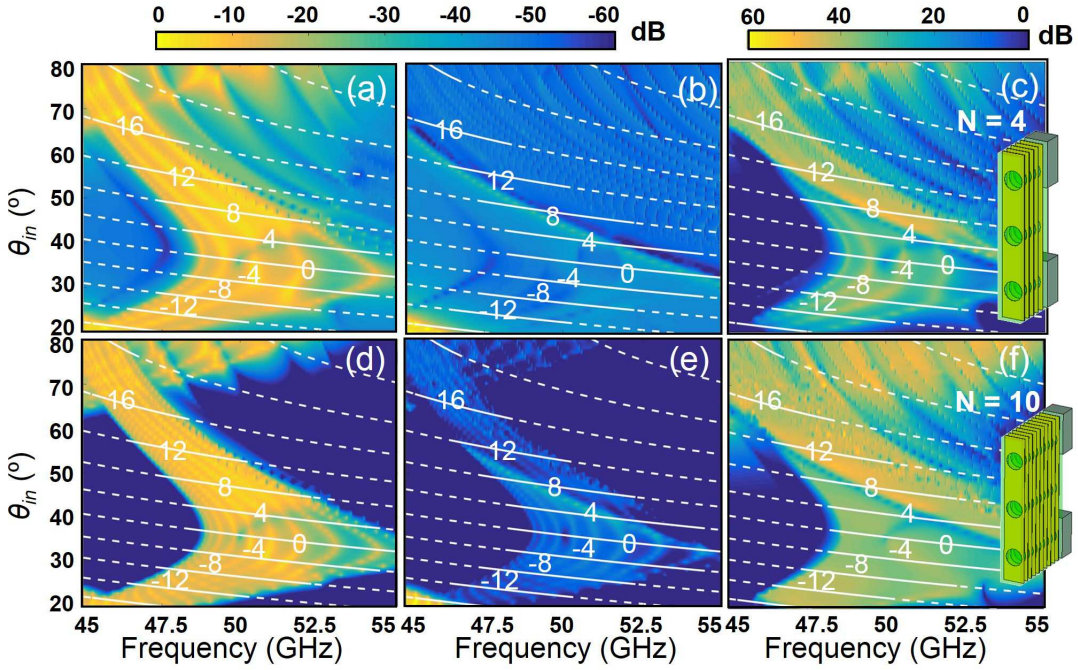

Fig. 3.25 Forward transmittance, $T^{\rightarrow}$, backward transmittance, $T^{\leftarrow}$ and forward-to-backward transmission contrast, $\Theta = T^{\rightarrow}/T^{\leftarrow}$. (a) $T^{\rightarrow}$ and $N = 4$. (b) $T^{\leftarrow}$ and $N = 4$. (c) Θ and $N = 4$. (d) $T^{\rightarrow}$ and $N = 10$. (e) $T^{\leftarrow}$ and $N = 10$. (f) Θ and $N = 10$.

From a practical point of view, the advantage of the $N = 4$ design relies obviously on the higher compactness compared to $N = 10$. On the other hand, as it can be inferred from the latter results, the $N = 10$ design is preferred from the perspective that the dispersion response

of the FB mode should be preserved. However, as inferred from the transmission results it can be assumed that $N = 4$ is sufficient for this purpose. This structure exhibits a total thickness $D \approx 0.64\lambda_0$ with being λ_0 the free-space wavelength at 50 GHz. This value is very competitive compared to typical performances of nonsymmetric photonic crystal gratings that enable asymmetric transmission for which total thickness is usually between $2\lambda_0$ to $6\lambda_0$ [Ser09b].

Next, the unidirectional regimes are tested by inspecting the field distribution for the selected set of cases. Figure 3.26 shows the x-component of the magnetic field for a SHA with $N = 10$ at two different θ_{in} cases, $\theta_{in} = 20°$ and $\theta_{in} = 60°$, that result in deflection angles of different sign. According to the regions depicted in Fig. 3.24 these cases correspond to region I where opposite sign of the deflection angle can be obtained at a fixed frequency. Thus, a variation of ϕ_{-1}, $\Delta\phi_{-1} \approx 30°$ involving sign switching can be obtained at $f = 47$ GHz when an incident wave impinges the side where the grating is placed. On the other hand, when the incident wave illuminates the structure from the opposite side, the wave is totally reflected in the specular direction [see Fig. 3.26]. As it can be observed, the case of negative deflection coincides with positive refraction at the grating side [see Fig. 3.26(a)]. In contrast, negative refraction appears at the grating interface for positive deflection angle [see Fig. 3.26(c)].

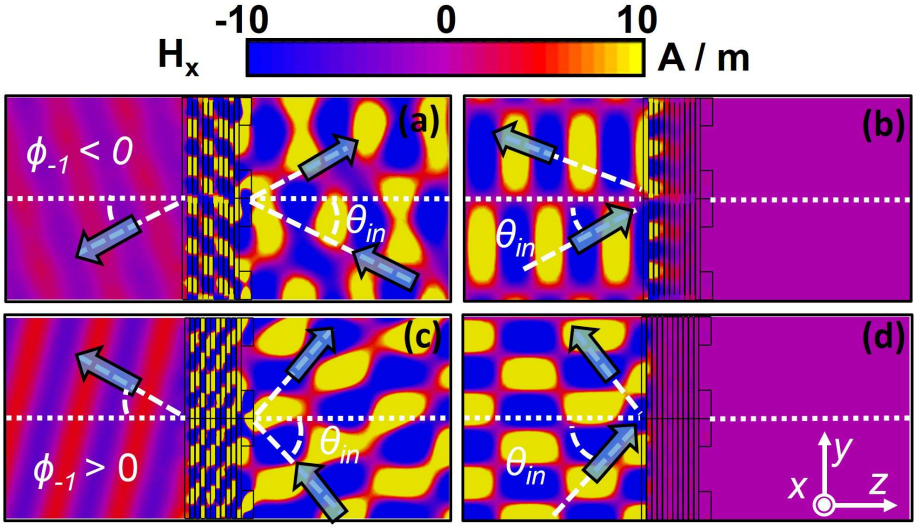

Fig. 3.26 Field distribution of the x-component of the magnetic field at $f = 47$ GHz for $N = 10$. (a) Forward illumination and $\theta_{in} = 20°$. (b) Backward illumination and $\theta_{in} = 20°$. (c) Forward illumination and $\theta_{in} = 60°$. (d) Backward illumination and $\theta_{in} = 60°$. Arrows indicate directions of incident, reflected and transmitted waves.

Now we analyze the operation regime of region II, where continuous variation and sign switching of ϕ_{-1} are possible (see Fig. 3.27). To this end, the operation frequency is set

now to 50 GHz for which a θ_{in} variation of just 6° (from $\theta_{in} = 32°$ to $\theta_{in} = 38°$) permits a tunability of $\Delta\phi_{-1} \approx 5°$ also with sign switching capability. As it can be observed, the field maps corroborate the dispersion and iso-lines results. The backward transmission is again very low. In fact, almost total reflection is achieved as the field distribution shows a self-imaging appearance that is known as Talbot effect. For the forward transmission case, a transmitted wave is observed at both θ_{in} values with the corresponding sign of the deflection angle, negative for $\theta_{in} = 32°$ and positive for $\theta_{in} = 38°$.

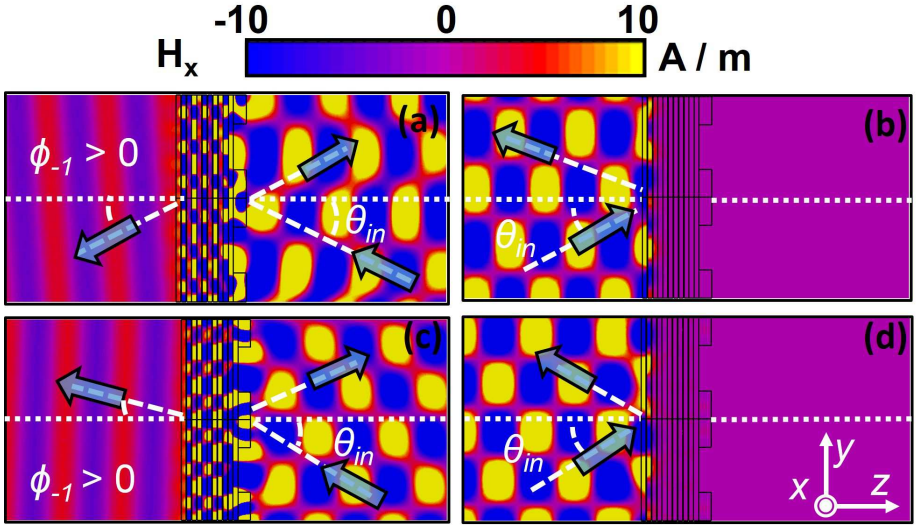

Fig. 3.27 Field distribution of the x-component of the magnetic field at $f = 50$ GHz for $N = 10$. (a) Forward illumination and $\theta_{in} = 32°$. (b) Backward illumination and $\theta_{in} = 32°$. (c) Forward illumination and $\theta_{in} = 38°$. (d) Backward illumination and $\theta_{in} = 38°$. Arrows indicate directions of incident, reflected and transmitted waves.

To test the performance of the most compact device attainable, the number of layers is reduced to the minimum, i.e. $N = 2$. The field distribution results for $f = 47$ GHz for $\theta_{in} = 20°$ and $\theta_{in} = 60°$ are shown in Fig. 3.28. As it can be observed for the positive deflection case a well defined wave front is obtained under forward illumination [see Fig. 3.28(c)]. In addition although low transmission is exhibited when the incident wave impinges on the opposite side [see Fig. 3.28(d)] the blocking for the non-grating side is less efficient than the case with $N = 10$. For the negative deflection case, the performance is deprecated. For forward illumination, the obtained transmission has low amplitude. Besides, the field distribution does not show any signature of single beam regime [see Fig. 3.28(a)]. The reason for this misbehavior is that for such a thin structure the $m = 0$ order may not be uncoupled and starts to interfere with the $m = -1$ order. It must be noted that for the considered f and θ_{in} the coupling regions of both $m = 0$ and $m = -1$ orders are close to each other (see Fig. 3.24).

For backward illumination, it can be seen that indeed there is some transmission that can be attributed to the imperfect uncoupling of the $m = 0$ order.

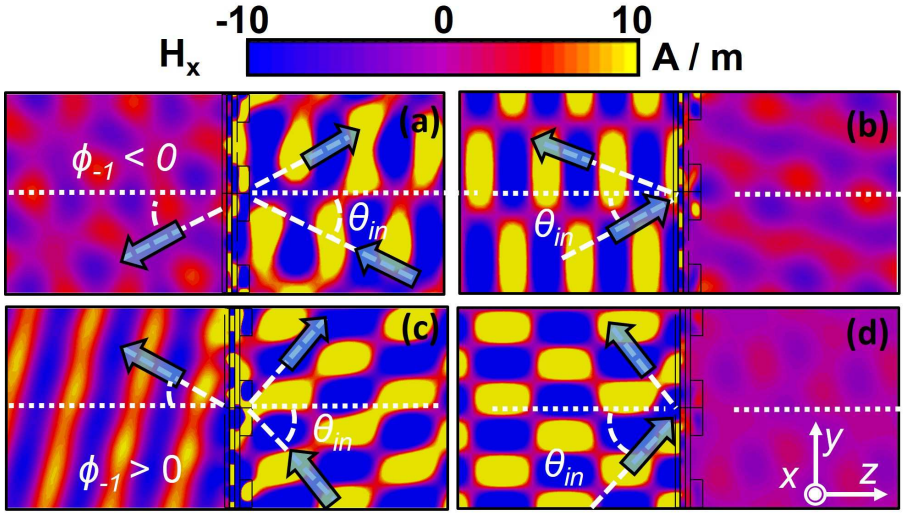

Fig. 3.28 Field distribution of the x-component of the magnetic field at $f = 47$ GHz for $N = 2$. (a) Forward illumination and $\theta_{in} = 20°$. (b) Backward illumination and $\theta_{in} = 20°$. (c) Forward illumination and $\theta_{in} = 60°$. (d) Backward illumination and $\theta_{in} = 60°$. Arrows indicate directions of incident, reflected and transmitted waves.

Now the focus is set on continuous regime (i.e. region II of Fig. 3.24) by varying both the operation f and θ_{in} to 50 GHz and to 32° and 38°, respectively. Figure 3.29 shows the magnetic field distribution. Although, a clear asymmetry in transmission can be observed for both θ_{in} cases, the wavefront recovered for forward transmission shows features of multi-order regime. Indeed, sign switching can be realized but due to the thin nature of the SHA the $m = 0$ order is not perfectly uncoupled leading to a worsening of the overall performance of the device.

3.2.3 Experimental Results

In this section an experimental demonstration of a SHA structure loaded with a dielectric grating is provided. As pointed out in Sect. 3.2.2 there is a trade-off when selecting the number of layers, N, of the SHA structure between getting the most compact device possible and achieving the dispersion behavior most approximat to the one exhibited by the infinite structure. Of course, a reduced number of layers leads to more compact devices, and therefore, more interesting solutions from a practical point of view. However, to achieve a dispersion performance, which is more similar to the infinite volumetric structure, large N would be preferred. With these prescriptions a final device with $N = 4$ has been experimentally

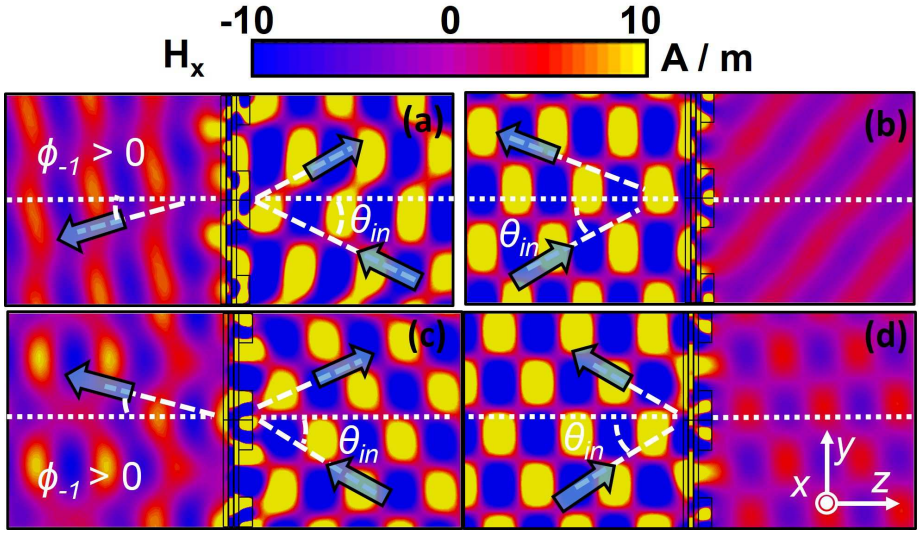

Fig. 3.29 Field distribution of the x-component of the magnetic field at $f = 50\,\text{GHz}$ for $N = 2$. (a) Forward illumination and $\theta_{in} = 32°$. (b) Backward illumination and $\theta_{in} = 32°$. (c) Forward illumination and $\theta_{in} = 38°$. (d) Backward illumination and $\theta_{in} = 38°$. Arrows indicate directions of incident, reflected and transmitted waves.

characterized. This structure was used in the previous section and also studied in a previous work by Beruete *et al.* [Ber11c]. The results here are extended to test the tunability and unidirectional regimes over a wide angular and frequency range.

The fabricated prototype is a $N = 4$ structure with the same dimensions as shown in Fig. 3.22 caption. The dielectric grating is made of ARLON AD 1000 commercial substrate material. The total thickness of the structure (including the grating) is 3.86 mm (that corresponds to $0.77\lambda_0$ at 60 GHz). The prototype was fabricated via milling machining and the SHA layers and the grating were stacked together by mechanical pressure and attached by using dielectric screws situated close to the edges of the wafers. For the experimental characterization an AB-Millimetre^{TM} VNA was used operating at the V-band of the millimeter wave regime. A schematic and picture of the experimental setup are shown in Fig. 3.30. The transmitter (TX) and receiver (RX) antennas along with a rotatory platform and positioners were mounted on a metallic bench. The TX was fixed while the RX, sample holder and a manually rotating positioner were placed on top of the rotatory platform to allow scanning over incidence and output angles simultaneously. The rotatory platform was electronically controlled with a very accurate precision. The angle of incidence (or input angle), θ_{in}, was varied with the mentioned electronically controlled turning platform. In turn, positive/negative deflection angles (output angles) were scanned by rotating the sample clockwise/counterclockwise with the manual rotating positioner. The orientations of the TX

and RX antennas were selected to properly excite the ET resonance related to the SHA [see electric field orientation in Fig. 3.30 (a)].

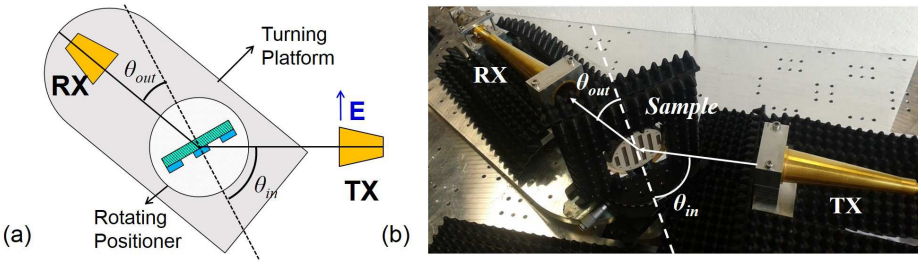

Fig. 3.30 (a) Schematic of the experimental setup in case of configuration for positive deflection angle measurement. (b) Experimental set-up picture. TX and RX antennas are shown. Sample holder mounted on top of the rotating positioner together with its normal axis and input and output angles are depicted.

Due to the distances between TX and RX antennas and the prototype sample, the measurements were performed in the near-field (i.e., $d_i < 2D_a^2/\lambda$, where d_i is the distance between the TX or RX and the sample, and D_a is the diameter of the antenna horn). With this configuration, the Gaussian beam emitted by the TX antenna has a beam radius of 18.3, 16.9, and 16.2 mm at 45, 60, and 75 GHz which represents the 58.19%, 53.7%, and 51.48% of the sample radius (31 mm), respectively. In this way, reflection and diffraction effects due to interference with sample holder and positioners are minimized. On the other hand, non-uniform illumination is unavoidable and therefore, some deviation from the theoretical/numerical expectations can occur. Another potential source of disagreement between theory and experiment is the presence of air gaps between the metallic layers comprising the SHA structure [Ber07b]. A direct consequence of these air gaps is that the effective permittivity of the whole structure decreases and then, the response is shifted to higher frequencies. As it will be shown later, numerical simulations with air gaps were run and the obtained results corroborate the aforementioned hypothesis.

Besides demonstrating the unidirectional performance of the device, experimental evidence of the deflection angle ϕ_m tunability with special emphasis on the sign-switching feature is targeted here. To this end, five selected output angles were chosen ($\theta_{out} = -10°, -5°, 0°, 5°, 10°$) while the incident angle, θ_{in}, and frequency, f, were varied from 10° to 80° (with a step of 1°) and from 45 to 75 GHz, respectively. In addition, illumination of both opposite sides, with/without gratings, is considered. As in the previous section, grating side illumination is identified as forward and the opposite case as backward illumination. Again, Θ is the forward-to-backward transmission contrast.

Figure 3.31 shows forward transmission, $T^{\rightarrow}$, backward transmission, $T^{\leftarrow}$, and contrast, Θ, obtained at $\theta_{out} = 0°$. Furthermore, isolines denoting the ouput angle for diffraction

orders $m = -1$ and $m = -2$, i.e. deflection angle ϕ_m are added (these lines are evaluated by the grating formula Eq. 3.19). The most evident difference with respect to the numerical results is an blueshift of the operation frequency (see Fig. 3.25). This effect is due to the existence of the mentioned air gaps between adjacent hole array layers. As is will be demonstrated later, this fact leads to a higher internal effective permittivity that provokes a shift of the unidirectional regime to higher frequencies. As it can be seen in Fig.3.31(a) a high transmission band is obtained between 57.5 and 67 GHz for θ_{in} between 38° and 24° approximately. This can be directly linked to the first diffraction order excitation $m = -1$ as corroborated by the corresponding ϕ_{-1} isolines overlapped in the figure. The second high transmission region appears between 60 and 74 GHz and 70° and 50° that can be assigned to the excitation of the $m = -2$ order. Backward illumination results denote a much lower transmission amplitude. This fact is even more evident when observing the Θ results where differences between $T^{\rightarrow}$ and $T^{\leftarrow}$ reach values of 35 dB and 30 dB for $m = -1$ and $m = -2$ regimes.

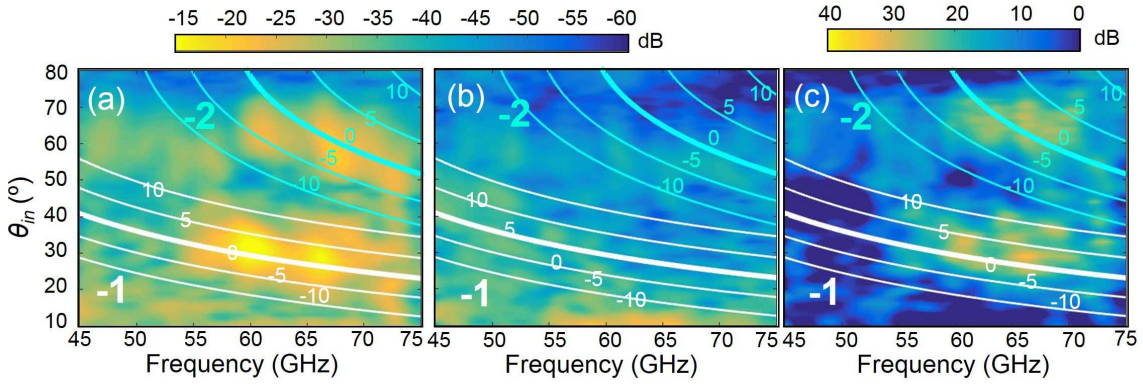

Fig. 3.31 Experimental results for $\theta_{out} = 0°$. (a) $T^{\rightarrow}$. (b) $T^{\leftarrow}$. (c) $\Theta = T^{\rightarrow}/T^{\leftarrow}$.

From these results, it can be seen that high transmission also appears at $f - \theta_{in}$ regions where according to ϕ_m isolines should correspond to different output angles. Under ideal conditions with infinitely directive receiver antennas, the energy collected by the antenna would correspond uniquely to a single output angle. However, the antennas receive waves arriving within a limited angular range rather than to a single direction. In addition, as mentioned before, these measurements were performed in the near field region so coupling within a wider angular range can be expected. In any case, unidirectionality is clearly observed for the normal deflection angle, $\theta_{out} = 0°$. Two $f - \theta_{in}$ regions exhibiting unidirectional performance are observed that are connected to the diffraction orders $m = -1$ and $m = -2$. The results for the $m = -1$ order show more evident unidirectional features than those for the $m = -2$.

Let us now discuss the experimental results for positive and negative θ_{out} to test the sign switching and tunability performance of the fabricated prototype. To this end, $T^{\rightarrow}$ and $T^{\leftarrow}$ for $\theta_{out} = 10°, 5°, -5°, +10°$ are shown in Fig. 3.32. As it can be observed, for the positive

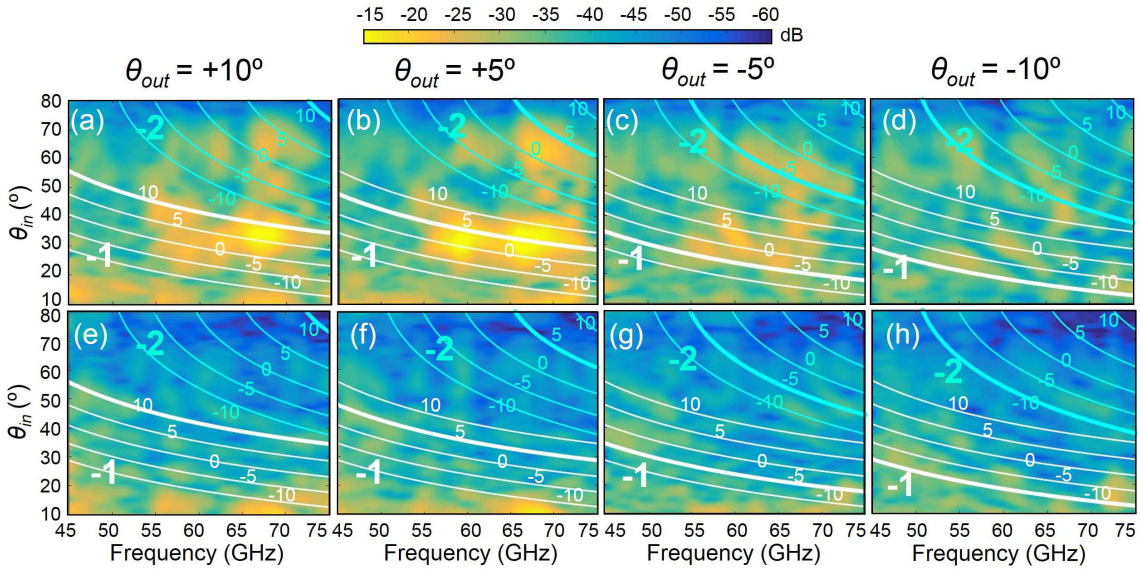

Fig. 3.32 Experimental results for $\theta_{out} = \pm 10°, \pm 5°$. (a) $T^{\rightarrow}$ and $\theta_{out} = 10°$. (b) $T^{\rightarrow}$ and $\theta_{out} = 5°$. (c) $T^{\rightarrow}$ and $\theta_{out} = -5°$. (d) $T^{\rightarrow}$ and $\theta_{out} = -10°$. (e) $T^{\leftarrow}$ and $\theta_{out} = 10°$. (f) $T^{\leftarrow}$ and $\theta_{out} = 5°$. (g) $T^{\leftarrow}$ and $\theta_{out} = -5°$. (h) $T^{\leftarrow}$ and $\theta_{out} = -10°$.

deflection cases, $\theta = +10°, +5°$, a high transmission band arises at the corresponding ϕ_m isolines [see Figs. 3.32(a) and (b)]. Better concordance is obtained for the case with $\theta = +5°$. Again backward transmittance is low at both cases [see Figs. 3.32(e) and (f)] leading to great Θ values at the corresponding $f - \theta_{in}$ regions [see Figs. 3.33(a) and (b)].

On the other hand, the results obtained for the negative deflection cases do not show a clear evidence of unidirectionality. In fact, high values of $T^{\rightarrow}$ are obtained for $\theta_{out} = -5°$ at $f - \theta_{in}$ regions (60 GHz - 35°) that according to theory corresponds to different output angles, namely, $\theta_{out} = 0, 5°$ [see "hot-spots" coinciding with isolines 0 and 5° in Fig. 3.32(c)]. Although $T^{\leftarrow}$ is relatively low [see Fig. 3.32(h)], this is not translated into a very high Θ for the isolines corresponding to $\theta_{out} = -5°$ for the $m = -1$ order [see Fig. 3.33(c)]. However, for the $m = -2$ order a high Θ "hot-spot" can be seen at approximately 67.5 GHz and 55°. In fact, a more thorough scrutiny denotes a $f - \theta_{in}$ region where indeed high $T^{\rightarrow}$ is obtained at the theoretical isolines for both $m = -1$ and $m = -2$ orders. The region for the first case lies at $f - \theta_{in} = 56$ GHz - 28° and the second case at $f - \theta_{in} = 65$ GHz - 55° [see Fig. 3.32(c)].

For the case of $\theta_{out} = -10°$ there is also some misbehavior when compared to the theoretical results. Although some high transmission is found for $T^{\rightarrow}$ between 50 and

60 GHz at approximately $\theta_{in} = 25°$ which corresponds to the theoretical isoline, the $T^{\leftarrow}$ recorded is also relatively high [see Figs. 3.32(d) and (h)]. In fact, the Θ results in Fig. 3.33(d) do not show a clear evidence for unidirectional transmission.

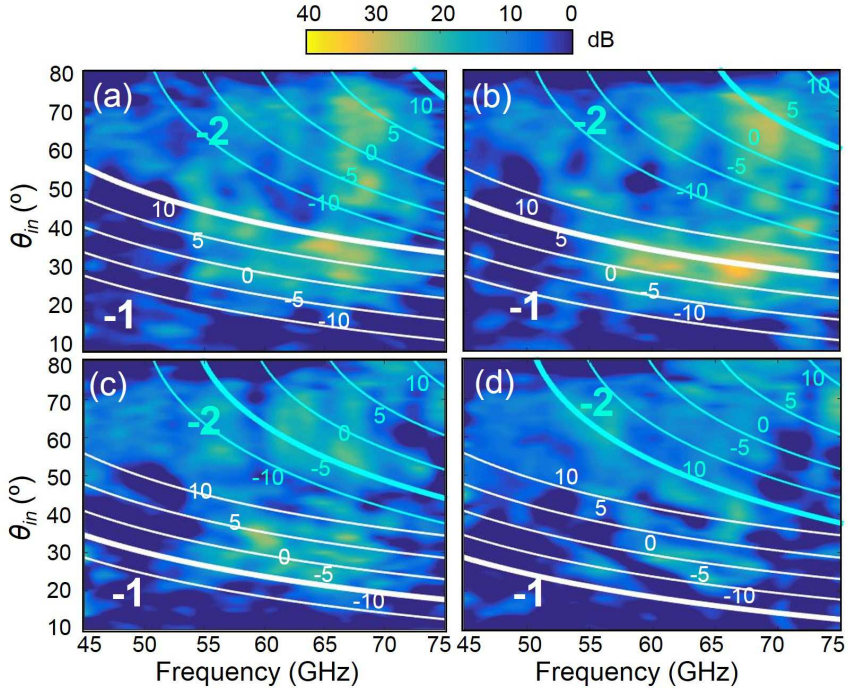

Fig. 3.33 Experimental results of Θ for $\theta_{out} = \pm 10°, \pm 5°$. (a) $\theta_{out} = +10°$. (b) $\theta_{out} = +5°$. (c) $\theta_{out} = -5°$. (d) $\theta_{out} = -10°$.

To evaluate the influence of the air gaps between adjacent layers, numerical simulations are carried out with air gaps of 35μ m between hole array layers. Figure 3.34 shows the $T^{\rightarrow}$ and Θ results. Indeed, a blue shift is obtained with respect to the theoretical findings shown in Sec. 3.2.2. In addition, it can be seen how the $T^{\rightarrow}$ is somehow enhanced for the $m = -2$ order while the performance for the $m = -1$ is deprecated. In general, positive deflection cases are benefited at the operation regime corresponding to $m = -1$ and low frequencies. In any case, besides the blueshift it can be observed that the influence of the air gaps may have more dramatic consequences. However, it is also difficult to infer from these results the direct effects on the unidirectionality, sign-switching and tuning regimes. It should be mentioned, that the simulation of the SHA plus grating structure with air gaps considers infinite structures. Then, differences between simulation and experiments could be due also to the finite nature of illumination and structures. Nevertheless, here, it is shown qualitatively that indeed, air gaps can be seen as a source of disagreement between theoretical, numerical and experimental results.

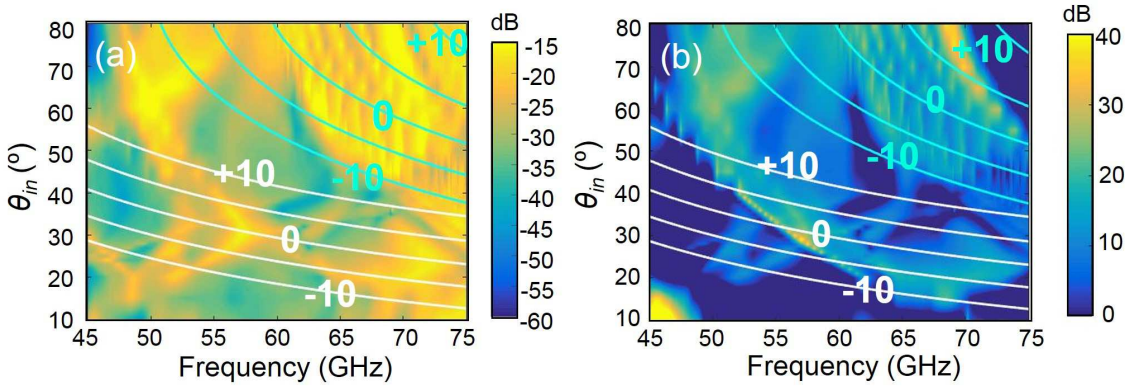

Fig. 3.34 Simulation results of a device with air gaps of thickness $g = 35\mu$ m between hole array layers. (a) $T^{\rightarrow}$. (b) Θ.

Now, the results shown in Fig. 3.31-3.33 are represented in a different manner to provide additional evidences of the tuning and sign-switching capabilities for the deflection angle. Maps of forward-to-forward transmission, Θ^{FTF}, contrast maps are used for different output (deflection) angles, i.e., $\Theta^{FTF} = T^{\rightarrow}(\theta_{out} = \theta_1)/T^{\rightarrow}(\theta_{out} = \theta_2)$, see Fig. 3.35. For consistency purposes, we always keep $\theta_1 > 0$ and $\theta_2 \leq \theta_1$. With these prescriptions, positive/negative forward-to-forward transmission contrast values correspond to positive/negative deflection respectively. In this way, sign-switching of the deflection angle can be claimed if a great excursion from positive to negative contrast values, or vice versa, is observed at a fixed frequency. In other words, different ranges of θ_{in} may correspond to different sign of deflection angle, ϕ_m. Figure 3.35 shows the forward-to-forward transmission contrast between $\theta_1 = +5°$ and $\theta_2 = -5°$, and between $\theta_1 = +10°$ and $\theta_2 = 0°$. In this way, a demonstration of sign-switching and tuning of the deflection angle is provided. In particular, sign-switching can be observed at the vicinity of 65 GHz [see Fig. 3.35(a)], where blue areas correspond to negative deflection and yellow ones to positive deflection. By varying θ_{in}, steering of the output beam becomes possible. In other words, θ_{out} varies from negative to positive values and vice versa. When Θ^{FTF} switches from positive to negative values when varying θ_{in} at a fixed frequency, a transition from positive to negative deflection is obtained. In the same way, tuning of the deflection angle from $\theta_{out} = 0°$ to $\theta_{out} = 10°$ by sweeping frequency and/or θ_{in} can be also obtained [see Fig. 3.35(b)]. In this case, negative values of Θ^{FTF} account to normal direction of the output beam, while positive values do it for output waves with $\theta_{out} = 10°$. It can be noticed that both $m = -1$ and $m = -2$ diffraction orders can be simultaneously employed.

Let us select some cuts of Fig. 3.35 to better observe the sign-switching and tuning features so as the previous discussion is reinforced. To this end, the operation frequency is

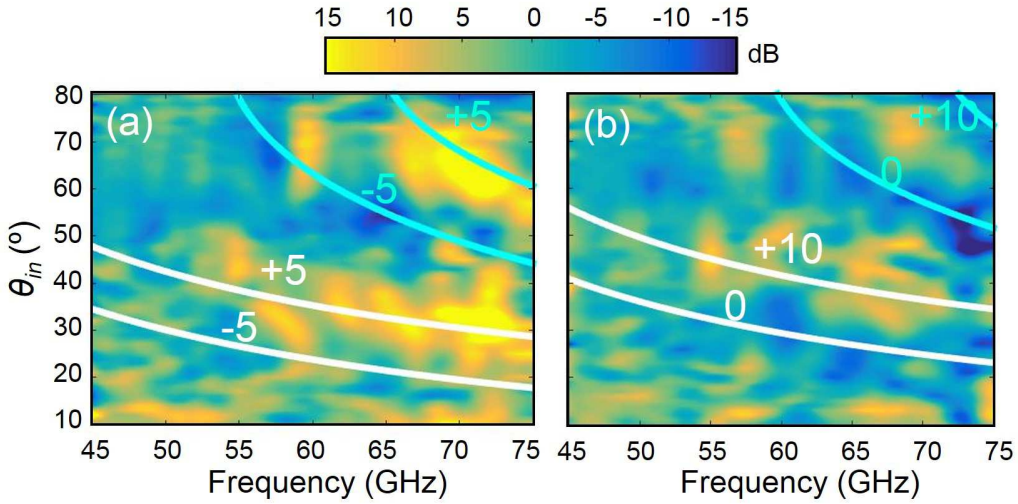

Fig. 3.35 Experimental results of Θ^{FTF} contrast maps. (a) $\Theta^{FTF} = T^{\rightarrow}(+5°)/T^{\rightarrow}(-5°)$. (b) $\Theta^{FTF} = T^{\rightarrow}(+10°)/T^{\rightarrow}(0°)$.

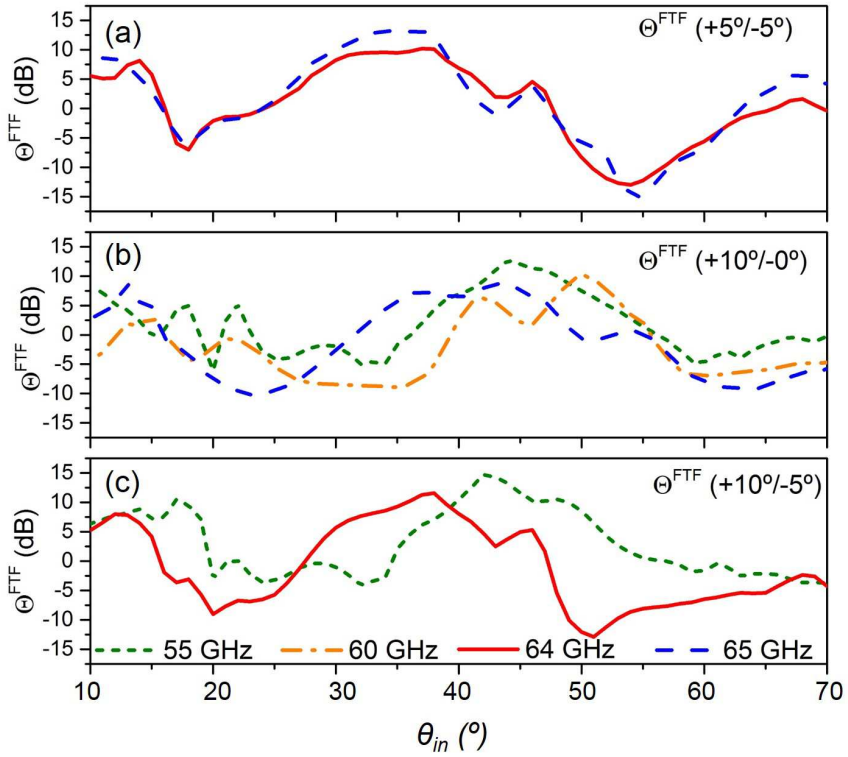

Fig. 3.36 Experimental frequency cuts of Θ^{FTF} at 55 GHz (green-dashed line), 60 GHz (orange-dashed-dotted line), 64 GHz (solid red line) and 65 GHz (blue long-dashed line). (a) $\Theta^{FTF}(+5°/-5°)$. (b) $\Theta^{FTF}(+10°/0°)$. (c) $\Theta^{FTF}(+10°/-5°)$.

fixed while θ_{in} is varied. In particular, at 65 GHz, positive deflection is observed at 35° and 40° due to the order $m = -1$ in Figs. 3.36(a) and (b), respectively. Switching to negative deflection is obtained by varying θ_{in} up to 55° [see Fig. 3.36(a)]. In this case, the transmission is linked to the $m = -2$ diffraction order. Similar performance is obtained at 64 GHz cut. In turn, for the case shown in Fig. 3.36(b), for a fixed frequency of 65 GHz, a slight variation in θ_{in} results in the change from positive deflection at nearly 40° ($m = -1$) to a normal output beam case near 60° ($m = -2$). Frequency cuts at 55 and 60 GHz are also added showing similar results. Furthermore, an additional switching scenario can be found at 55 and 64 GHz by using $\theta_{out} = +10°$ and $\theta_{out} = -5°$. For the first case, negative to positive deflection transition can be achieved by varying θ_{in} from 30° to 45°. For the second case, a more evident sign-switching (from positive to negative deflection) feature is observed when sweeping θ_{in} from 38° to 51° (see Fig. 3.36(c)).

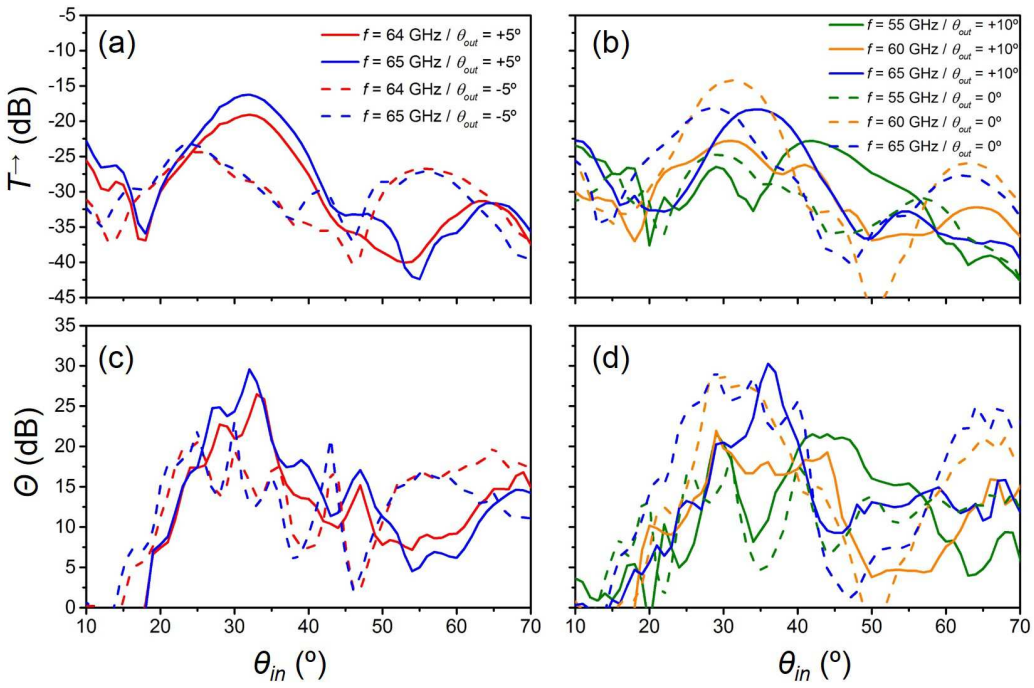

Fig. 3.37 Experimental frequency cuts of $T^{\rightarrow}$ and Θ at 55 GHz (green-dashed line), 60 GHz (orange-dashed-dotted line), 64 GHz (solid red line) and 65 GHz (blue long-dashed line). (a) $T^{\rightarrow}$ for $\Theta^{FTF}(+5°/-5°)$. (b) $T^{\rightarrow}$ for $\Theta^{FTF}(+10°/0°)$. (c) Θ for $\Theta^{FTF}(+5°/-5°)$. (d) Θ for $\Theta^{FTF}(+10°/0°)$.

To prove that the selected cases are indeed appropriate for tunable deflection in the unidirectional transmission regime, the forward-to-backward transmission contrast, Θ, is inspected. In addition, forward transmission, $T^{\rightarrow}$, needs to be far from the noise floor of the considered instrumentation. To assess both conditions, frequency cuts of $T^{\rightarrow}$ and Θ for the

corresponding cases of 3.33 are shown in Fig. 3.37. As it can be seen, these prescriptions are fulfilled and then the cases selected in Fig. 3.36 are positively corroborated. In other words, unidirectionality is assured by high values of $T^{\rightarrow}$ and Θ (note that Θ values between 20 and 30 dB are obtained at the $f-\theta_{in}$ ranges of interest). For instance, for 64 and 65 GHz, high $T^{\rightarrow}$ is obtained at about $\theta_{in}=32°$ for $\theta_{out}=+5°$ [see Fig. 3.37(a)] and it is also verified by a high Θ at this θ_{in} range [see Fig. 3.37(c)]. Similarly, this performance is obtained at $\theta_{in}=55°$ for output beams with $\theta_{out}=-5°$. Figures 3.37(b) and (d) deal with similar results regarding the tuning scenario between $\theta_{out}=+10°$ and $\theta_{out}=0°$. Let us focusing on the 65 GHz cuts (blue lines). It can be seen that normal output beams with great Θ are obtained at about $\theta_{in}=30°$. If θ_{in} is slightly increased up to 35° the high $T^{\rightarrow}$ and Θ are more evident for output waves with $\theta_{out}=+10°$ [see Fig. 3.37(b)]. In both situations, high Θ values are retained indicating that unidirectionality holds [see Fig. 3.37(d)].

Summarizing, in this section a compact diffraction inspired unidirectional transmission device has been experimentally demonstrated in the V-band of the millimeter wave regime. The obtained results do confirm the possibility of tuning and sign-switching of the output beam by varying the angle of incidence and/or frequency of the incident wave. This is done under unidirectional transmission, i.e. forward transmission is much greater than the transmission obtained when the input interface is set to be the opposite one.

3.3 Metasurfaces based on NB-CSRR

In this section a metasurface based on non-bianisotropic CSRR (NB-CSRR) particles is analyzed both numerically and experimentally and proposed as a potential device with very interesting angular selective properties. The NB-CSRR is a modified version of the classical CSRR. In turn, the CSRR is the complementary particle of the SRR which is probably the most paradigmatic metamaterial particles. The SRR was proposed by J. B. Pendry in 1999 [Pen99]. The SRR is a metamaterial element formed by two subwavelength metallic rings (one larger and the other shorter) with air gaps at opposite sides. Even without having any constituent element with magnetic character (only metallic rings and dielectric substrates), the SRR exhibits a strong magnetic response. Indeed, it was found that when multiple SRR elements were arranged into a periodic array, a negative effective permeability could be obtained in a limited frequency range [Pen99]. Due to this uncommon and exotic response, the SRR received great attention for scientific community.

In particular, SRRs were thoroughly studied in the context of equivalent circuit models and planar technology [Mar02, Mar05, Bae05]. A comprehensive theoretical study devoted to understanding of the underlying physics of the SRR performance was published by R. Marqués *et al.* [Mar02]. The bianisotropic character of the SRR was reported by corroborating that an electric response was obtained by magnetic excitation (and vice versa). In 2004, F. Falcone *et al.* reported for the first time the complementary version of the SRR (called CSRR)[Fal04]. There, the Babinet's principle was exploited under assumptions of infinitely thin and perfectly conducting metallic screens for which Babinet's theory is strictly valid. In addition, an experimental demonstration of the bandstop/bandpass character of SRR/CSRR metasurfaces was also reported. Since then, SRRs and CSRRs have been widely used for filter applications and mostly analyzed in waveguides and planar circuit devices [Bae05] as well as spatial filters in the metasurface versions [Ber06b, Azn08].

In this section, the classical CSRR proposed by F. Falcone *et al.* is modified by connecting the internal and external rings by two air gaps at opposite sides. The resulting element is the non-bianisotropic CSRR (NB-CSRR) [Bae05, Agu15, Naq13]. Due to the new configuration the NB-CSRR metasurface exhibits a non-conventional angular response. For instance, normally incident waves can be totally reflected while obliquely incident waves with TM polarization can be partially or even totally transmitted. A numerical study of the NB-CSRR particle is performed to obtain an initial knowledge of the transmission phenomena exhibited by this kind of structure. To this end, mono and multi-layered solutions are considered. Furthermore, an experimental demonstration of a bi-layered design is provided. The results described in this section have been reported in one journal paper [RU17a].

3.3.1 From SRR to NB-CSRR

First, let us briefly introduce the involved physical mechanisms in the SRR, CSRR and NB-CSRR particles. To this end, a schematic representation of thew unit cells of the three metamaterial particles along with their corresponding magnetic and electric dipoles is shown in Fig. 3.38. As mentioned above the SRR can be excited magnetically and electrically provided the applied fields have the required field components. Thus, the SRR exhibits both magnetic and electric dipoles. It should be mentioned that this reasoning applies to the quasistatic resonance, i.e. the element is very subwavelength. For the first case, the situation can be described as follows [Mar02]. An incident magnetic field with axial component generates an electric field that creates a current flow along the rings (note that the rings are strongly coupled) which is closed by displacement currents appearing within the narrow gaps. This current loop can be represented as a magnetic dipole moment in the particle. In turn, the electric dipole is explained due to the fact that the quasistatic potentials and charges created at the upper part are electrical images of those appearing at the lower part [see Fig. 3.38].

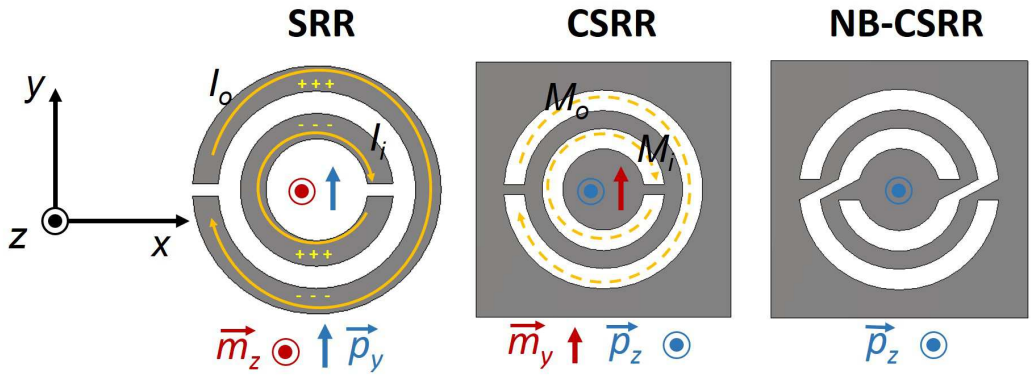

Fig. 3.38 Schematic of SRR, CSRR and NB-CSRR unit cells along with their magnetic/electric dipoles. Solid yellow lines account for electric current flow (I_i and I_o denote the induced currents in the inner and outer metallic rings). Dashed yellow lines account for virtual magnetic current flow (M_i and M_o denote the induced currents in the inner and outer metallic rings).

The CSRR element, as expected, exhibits the complementary behavior of the SRR in terms of the magnetic/electric character of excitation and response. Thus, an equivalent magnetic current is created in the air rings for an applied electric field with axial component leading to a total electric moment. In addition, an applied magnetic field with y component creates an equivalent magnetic dipole moment [see Fig. 3.38]. Indeed, these features denote the bianisotropy nature of the CSRR particle. To avoid this, a possible strategy is to connect

the inner and outer ring apertures with two air bridges. The resulting structure is the NB-CSRR [see Fig. 3.38].

These air connections present in the NB-CSRR forbid the existence of the magnetic dipole. On the other hand, the electric dipole is still accessible as long as the applied electric field has an axial component. Therefore, the excitation of the NB-CSRR is only possible for transverse magnetic (TM) plane waves at oblique incidence. Then, a NB-CSRR metasurface presents a singular angular transmission performance: under normal and TE incidence, waves are reflected whereas under TM incidence, waves can be partially or totally transmitted. These features are thoroughly studied in the subsequent sections.

3.3.2 CSRR and NB-CSRR Transmission Results

Here, an exhaustive comparison between CSRR and NB-CSRR transmission results under normal and oblique incidence for transverse magnetic (TM) and transverse electric (TE) incidence is provided. To this end, numerical simulations are carried out with the full wave simulator CST Microwave Studio by using the frequency domain solver and unit cell boundary conditions. Mono-layer and bi-layer configurations are considered. Figure 3.39 shows a schematic of both CSRR and NB-CSRR particles along with their dimensions and selected coordinate system. Transmission results for obliquely incident waves parallel to the two principal incidence planes, $\phi = 0°$ and $\phi = 90°$, are presented.

Monolayer Structure

Figure 3.40 shows the transmission results for CSRR and NB-CSRR mono-layer structures at different angles of incidence ($\theta = 0°, 30°$ and $60°$) under TE and TM polarization. In this preliminary study, the metal and the dielectric substrate are assumed to be made of perfect electric conductor (PEC) material and lossless dielectric material with relative permittivity $\varepsilon_s = 2.35$, respectively. The CSRR transmission results, copolar and crosspolar components, are shown in Fig. 3.40(a)-(d). In turn, the corresponding NB-CSRR results are shown in Fig.3.40(e)-(h).

First, the results regarding the CSRR structure are discussed. Under TE wave incidence in the xz-plane (labelled as $\text{TE}_{\phi=0°}$) the relevant field components of the incident wave are E_y, H_x and H_z. Since none of these components is parallel to any of the resonant dipoles, p_z or m_y, the CSRR is not excited. In this case, the metasurface is nearly opaque [see Fig. 3.40(a)]. Nevertheless, if one switches to the yz-plane, i.e. $\text{TE}_{\phi=90°}$, now the incident wave has a magnetic field with y component, H_y, which is able to excite the tangent magnetic dipole, m_y. Then, a resonance peak appears at roughly 98 GHz, even at normal incidence

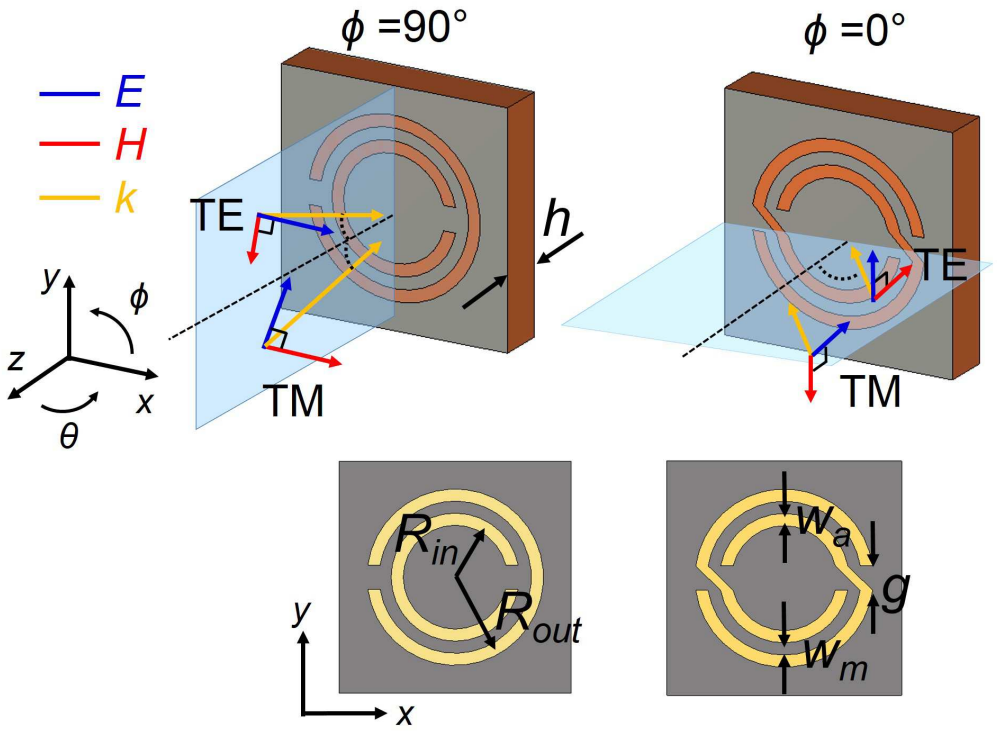

Fig. 3.39 Schematic of CSRR and NB-CSRR unit cells along with the incidence planes under TM/TE plane wave illumination. Dimensions: outer radius, $R_{out} = 170\,\mu$m; inner radius, $R_{in} = 120\,\mu$m metal and air widths, $w_m = w_a = 25\,\mu$m; gap between ring edges, $g = 25\,\mu$m.

[see Fig. 3.40(b)]. For oblique incidence, $\theta \neq 0$, the resonance peak is still present in the spectrum but with a reduced transmission level. As explained in [Mar05, Ber06b], the energy is transferred to the crosspolar component due to the strong bianisotropy of the CSRR. Indeed, for $\theta = 60°$, the cross polarization peak may exhibit even higher transmission levels than the copolar component. For the $\text{TM}_{\phi=0°}$ case, the incident wave has H_y, E_x and E_z components. In this situation, the CSRR can be excited magnetically under normal incidence and both magnetically and electrically under oblique incidence. In the latter scenario, a pass band with larger bandwidth is obtained due to coexistence of both resonance dipoles. For the $\text{TM}_{\phi=90°}$ case the only field component compatible with excitation of the CSRR is the axial electric field, E_z. Hence, a transmission peak appears only under oblique incidence. Cross polarization effects arise as well, due to the magnetic dipole excited through the electric dipole resonance. Looking at these results, it is noticed that cross-polarization is present only when the incidence is in the yz-plane. All these results are in good agreement with those reported in [Mar05, Ber06b].

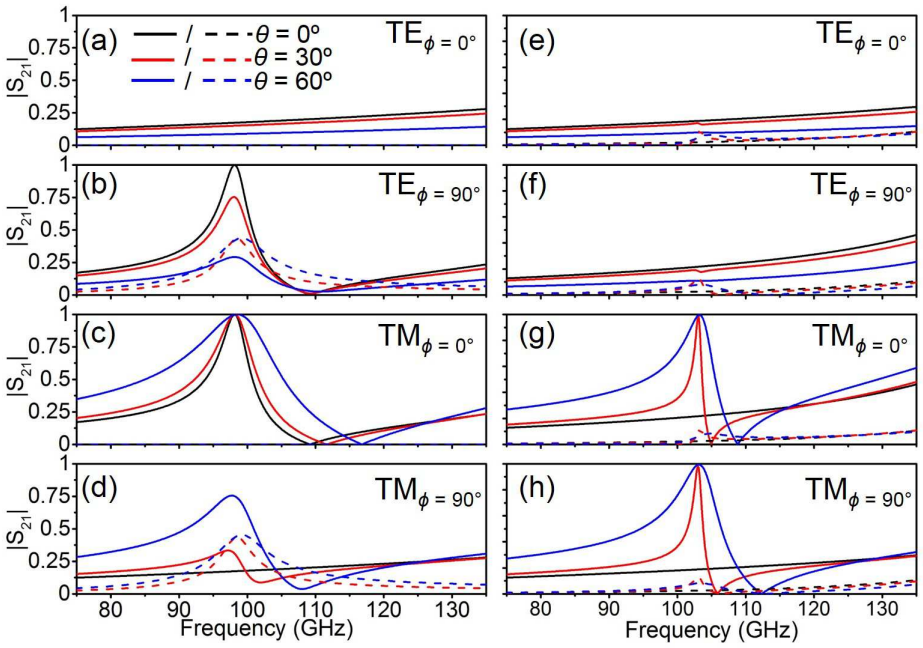

Fig. 3.40 Transmission results for monolayer structure. Co-polar (solid line) and cross-polar (dashed line) components obtained at $\theta = 0°$ (black line), $\theta = 30°$ (red line) and $\theta = 60°$ (blue line) are shown. (a) CSRR - TE$_{\phi=0°}$. (b) CSRR - TE$_{\phi=90°}$. (c) CSRR - TM$_{\phi=0°}$. (d) CSRR - TM$_{\phi=90°}$. (e) NB-CSRR - TE$_{\phi=0°}$. (f) NB-CSRR - TE$_{\phi=90°}$. (g) NB-CSRR - TM$_{\phi=0°}$. (h) NB-CSRR - TM$_{\phi=90°}$.

As advanced in the previous section, the NB-CSRR transmission properties should be quite different in comparison with those obtained for the CSRR. Obviously, the cross polarization effects must be lower provided that the bianisotropy is largely mitigated by the additional air connections between the inner and outer rings. Figure 3.40(e)-(h) corroborates the previous statement since the cross-polarization level is quite low for all cases. The NB-CSRR does not exhibit a magnetic dipole and therefore, the only way to excite the quasistatic resonance of this structure is by means of the electric dipole, p_z. Then, the NB-CSRR can be excited only under TM oblique incidence, for which the incident field has the required E_z component. Figure 3.40(e) and (h) show low transmission under normal incidence and lack of resonance effects for all cases. In contrast, under TM incidence and when $\theta = 30°$ and $\theta = 60°$ a resonant transmission peak with almost unity transmission arises near 103 GHz. These results clearly reveal the angular selectivity feature of the NB-CSRR metasurface. In the following the addition of a second layer is analyzed.

Bi-layer Structure

With the target of enhancing the rejection of normally incident waves, a structure with an additional NB-CSRR layer is studied. Furthermore, a direct consequence of stacking another layer is the splitting of the resonance peak due to the coupling between adjacent layers [NC11, Ort09]. This feature can be utilized for extending the frequency range in the context of dual band solutions. In fact, the separation distance determines the degree of coupling between layers, and depending on its magnitude the additional peaks appear near or far away from the fundamental resonant frequency. A more thorough study of the separation distance is conducted later in this section. Concentrating on the performance at the different polarization cases, it is observed in Fig. 3.41 that the NB-CSRR metasurface has transmission bands only under oblique TM incidence, in good agreement with the results of Fig. 3.40. Moreover, the inclusion of an additional layer increases the rejection level for normally incident waves and the cross polarization levels are practically negligible for all cases.

Figure 3.41 shows the simulation results for CSRRs [Fig. 3.41(a)-(d)] and NB-CSRRs [Fig. 3.41(e)-(h)]. In general, the results follow the tendency shown in Fig. 3.40 for the monolayer structure. The most remarkable feature is the splitting of the resonance peak in two due to the aforementioned coupling of resonators between the consecutive layers.

Another aspect that may be relevant for practical bi-layered designs is the transmission performance when the second layer has different orientations. To study this, simulations with different rotation schemes of the second layer are run for both the CSRR and NB-CSRR structures. Rotations along y and z axes have been applied. Figure 3.42(a)-(d) shows transmission results for bi-layer NB-CSRR structures under oblique incidence ($\theta = 60°$) and different rotations of the outer particle in both principal polarization planes ($\phi = 0°$ and $\phi = 90°$). As it can be seen, aside from a small frequency shift the transmission spectra are similar for all cases. Then, it can be stated that the NB-CSRR has a robust performance for different rotation of the second layer scenarios.

In contrast, the obtained CSRR results for different orientations of the second layer differ considerably [see Fig. 3.42(e)]. The design for which the second layer is rotated 180 degrees along the y axis of rotation (red line) is actually a double band version of a broadside coupled CSRR (BC-CSRR) described by R. Marqués *et al.* in Ref [Mar02]. In contrast, when there is no rotation, the transmission performance is similar to the one obtained for the NB-CSRR in the sense that the main resonance is split in two peaks due to coupling. Thus, the independency of the NB-CSRR bi-layer configuration for the second layer orientation, enables integration of the two patterned layers in one substrate (using only one photo-mask) without changing the overall performance.The reason is that the NB-CSRR has a higher

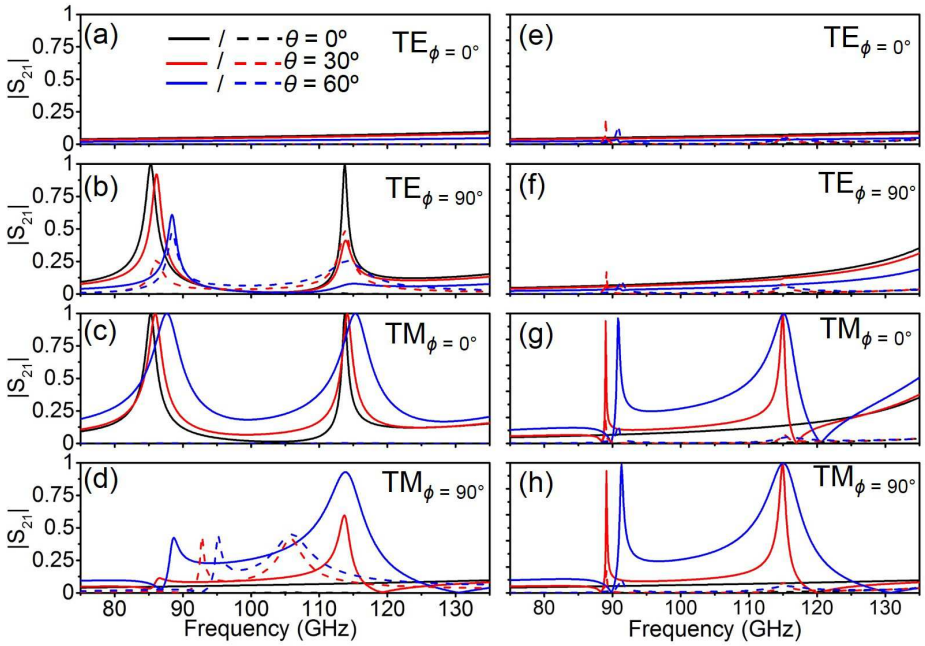

Fig. 3.41 Transmission results for bi-layer structure. Co-polar (solid line) and cross-polar (dashed line) components obtained at $\theta = 0°$ (black line), $\theta = 30°$ (red line) and $\theta = 60°$ (blue line) are shown. (a) CSRR - TE$_{\phi=0°}$. (b) CSRR - TE$_{\phi=90°}$. (c) CSRR - TM$_{\phi=0°}$. (d) CSRR - TM$_{\phi=90°}$. (e) NB-CSRR - TE$_{\phi=0°}$. (f) NB-CSRR - TE$_{\phi=90°}$. (g) NB-CSRR - TM$_{\phi=0°}$. (h) NB-CSRR - TM$_{\phi=90°}$.

degree of symmetry than the CSRR and therefore is less sensitive to a rotation of the elements and/or incidence plane.

Now, the influence of the separation distance between adjacent layers,i.e. substrate height, h, is studied. To this end a parametric study of h is performed for TM incidence with $\phi = 0°$ and $\theta = 60°$ [see Fig. 3.43]. Four different h values, 0.075, 0.15, 0.225 and 0.3 mm that correspond to 0.038λ, 0.077λ, 0.115λ and 0.153λ, with λ being the wavelength at 100 GHz within the substrate slab, have been considered. Simulations without and with losses (Copper conductivity is set for the metal parts $\sigma_{Cu} = 5.8 \times 10^7$ S/m and a loss tangent $tan\delta = 0.001$ defined at 100 GHz for the dielectric material) are shown in Fig. 3.43(a) and (b), respectively.

When h is very small the two NB-CSRR layers are strongly coupled and a new resonance peak appears being well separated in frequency from the dominant resonant frequency mode. This new peak shows an inherent narrowband response, namely a very high quality factor, Q, and almost total transmission in the losssless case [see Fig. 3.43(a)]. As h increases both resonances approach fast to each other. In fact, at a particular value $h = 0.153\lambda$ mm, a strong reduction of the transmission amplitude is observed due to a mutual cancellation that is a

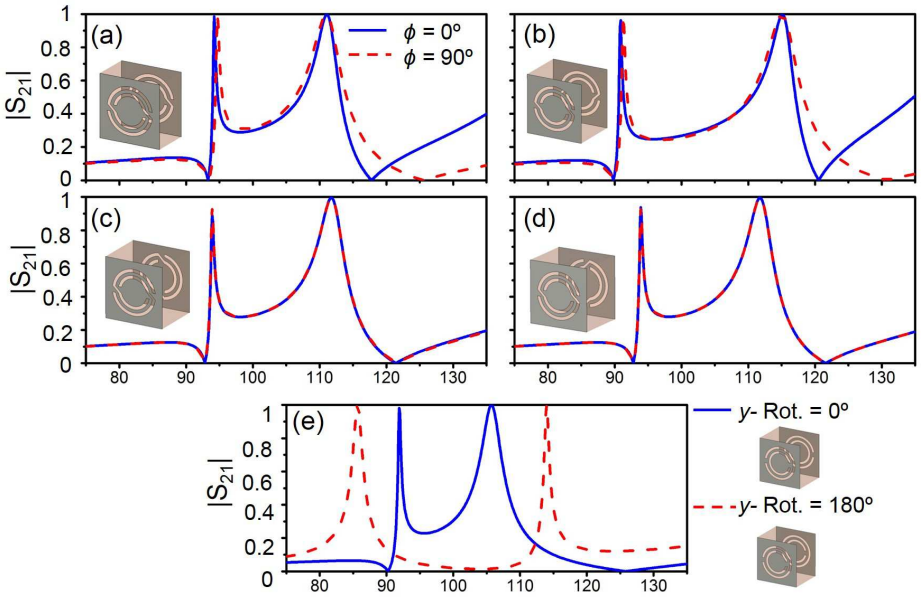

Fig. 3.42 Transmission results under different rotation scenarios of the second NB-CSRR and CSRR layer. (a) NB-CSRR, y-Rotation = 0°; (b) NB-CSRR, y-Rotation = 180°; (c) NB-CSRR, y-Rotation = 180° and z-rotation = 90°; (d) NB-CSRR, y-Rotation = 0° and z-rotation = 90°. (e) CSRR, y-Rotation = 0, 180°.

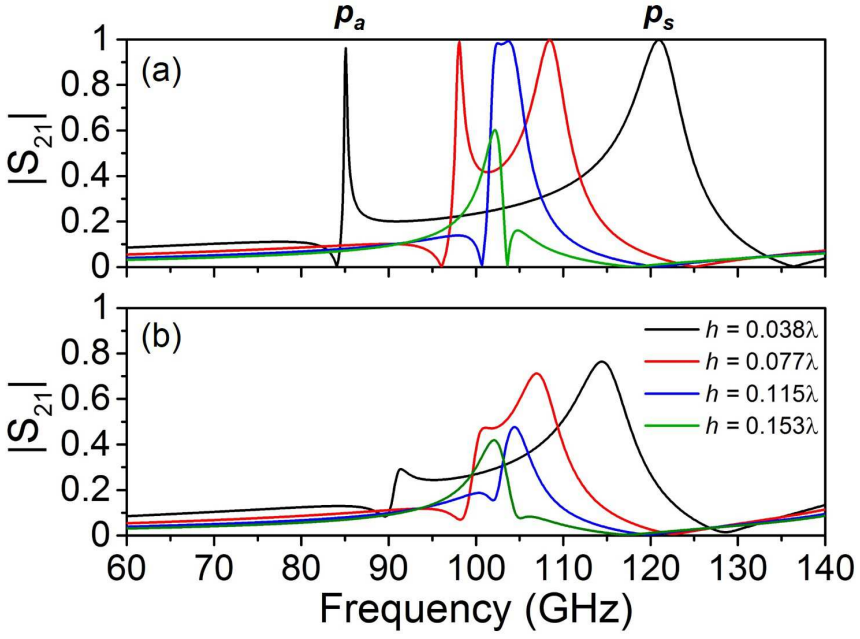

Fig. 3.43 Transmission results for bi-layer configurations of NB-CSRR - $TM_{\phi=0^\circ}$ ($\theta = 60^\circ$) with varying h. (a) Ideal lossless case. (b) Lossy case with metal thickness, $t = 1.5\,\mu$m.

consequence of a mode hybridization phenomenon. Actually, at the frequency of minimum transmission the incident wave experiences a strong reflection. When losses are included it can be noticed that the peak appearing at lower frequencies for the ideal case practically disappears. This effect is expected due to the exhibited high Q of the resonance. In addition, the fundamental resonance is also deprecated by the inclusion of losses. It should be taken into account that thicker substrates allow for more energy dissipation and therefore, higher losses.

From the obtained results it can be stated that the original transmission peak is split in two peaks as a consequence of the coupling between layers. Moreover, these two peaks can be linked to two distinct resonant modes showing different field distribution symmetries. While the original resonant mode shows a symmetric field distribution, the field related to the new resonance peak is asymmetric. Figure 3.44 shows the field distribution for the NB-CSRR lossless case for the two highlighted frequencies, p_a and p_s in Fig. 3.43(a) which correspond to $f_a = 85.1$ and $f_s = 121$ GHz respectively. The asymmetric character of the field distribution at p_a can be clearly noticed. In contrast, the field distribution at p_s denotes a symmetric mode excitation. While the asymmetric mode excitation is due to internal coupling between adjacent layers that is mainly related to the resonance of the isolated NB-CSRR elements plus the coupling of the neighboring elements which act as loads leading to a slightly different frequency with respect to the mono-layer case. An extensive analysis of this phenomenon occurring for bi- and multi-layer slot-type metallic screens can be found within the literature [Tor16, Kai10]. Here, uniquely the basic concepts and main implications on the transmission properties of bi-layered structures are discussed.

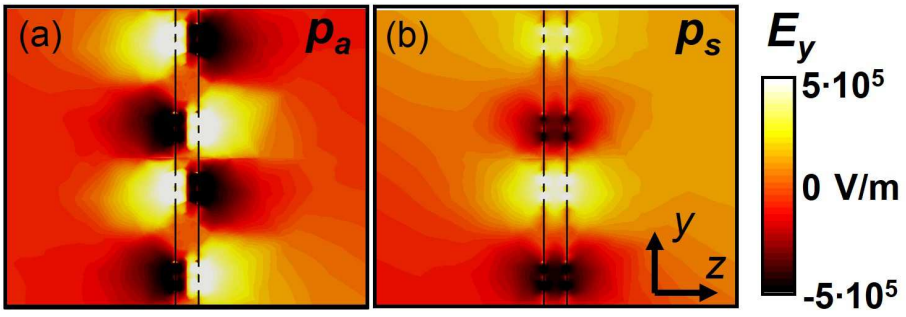

Fig. 3.44 Electric field distribution of y component. (b) p_a ($f_a = 85.1$ GHz) (c) NB-CSRR – p_s ($f_s = 121$ GHz).

3.3.3 Experimental Results

In this section an experimental demonstration of a bi-layer NB-CSRR structure is provided. To this end, a stacked NB-CSRR metasurface prototype was fabricated by means of photolithography techniques. The substrate used is a cyclic olefin copolymer (COC) film which is a flexible material and has low loss and low dispersion at millimeter-wave and THz frequencies. The chosen substrate has a constant permittivity $\varepsilon_s = 2.35$, a loss tangent $\tan\delta = 0.001$ and a thickness $h = 0.1$ mm. Regarding the metallic parts they were etched on Copper with a final thickness of 1.5 μm and nominal conductivity $\sigma_{\text{Cu}} = 5.8 \times 10^7$ S/m. With the aim of using the same photomask and substrate slab for fabricating the two metasurface layers, the final device results in a structure with the two printed layers with a rotation of 180° between them. However, as seen in the previous section, the NB-CSRR performance is quite robust with respect to rotation of the adjacent layers with respect to each other.

To corroborate the experimental results, infinite simulations obtained with the frequency domain along with unit cell boundary conditions of CST Microwave Studio are presented . In turn, the measurements were performed using an AB-Millimetre$^{\text{TM}}$ VNA operating at the W and D-bands of the millimeter wave regime, namely between 70 and 130 GHz approximately. The VNA was used along with a quasi-optical bench along with a system of ellipsoidal mirrors that allow focusing of the beam onto the sample [see Fig. 3.45(a)]. As in previous experiments presented in this Chapter, the transmitter (TX) and receiver (RX) are corrugated horn antennas . In addition, microscope pictures of the fabricated prototype can be found in Fig. 3.45(b). To have control over the incidence angle, θ, the sample was mounted on a rotary platform. By rotating the whole antenna system by 90°, the polarization state can be switched between TM and TE. To fully characterize the transmission performance of the NB-CSRR metasurface, both frequency and θ were swept from 80 to 130 GHz (with a step of 25 MHz) and from 0° to 70° (with a step of 2.5°), respectively. It should be noted, that larger θ values were not achievable due to the experimental set-up limitations. At such large oblique angles, the input and output beams start to interfere with the sample holder leading to undesired diffraction and reflection effects.

Figure 3.46 shows the experimental and simulated transmission results for the fabricated NB-CSRR prototype considering both TM and TE polarization in the two principal planes ($\phi = 0°$ and $\phi = 90°$). In general, a qualitative good agreement is obtained between measurements and simulations. It can be seen, that indeed, for TE polarization there is not signature of resonance peaks within the analyzed frequency for neither experiments nor simulations [see Figs. 3.46(a),(b),(e) and (f)]. Regarding the case of TM polarization, for the two principal planes, the experimental results undergo a small shift towards lower frequencies. In addition, the amplitude is reduced in comparison with the simulation results.

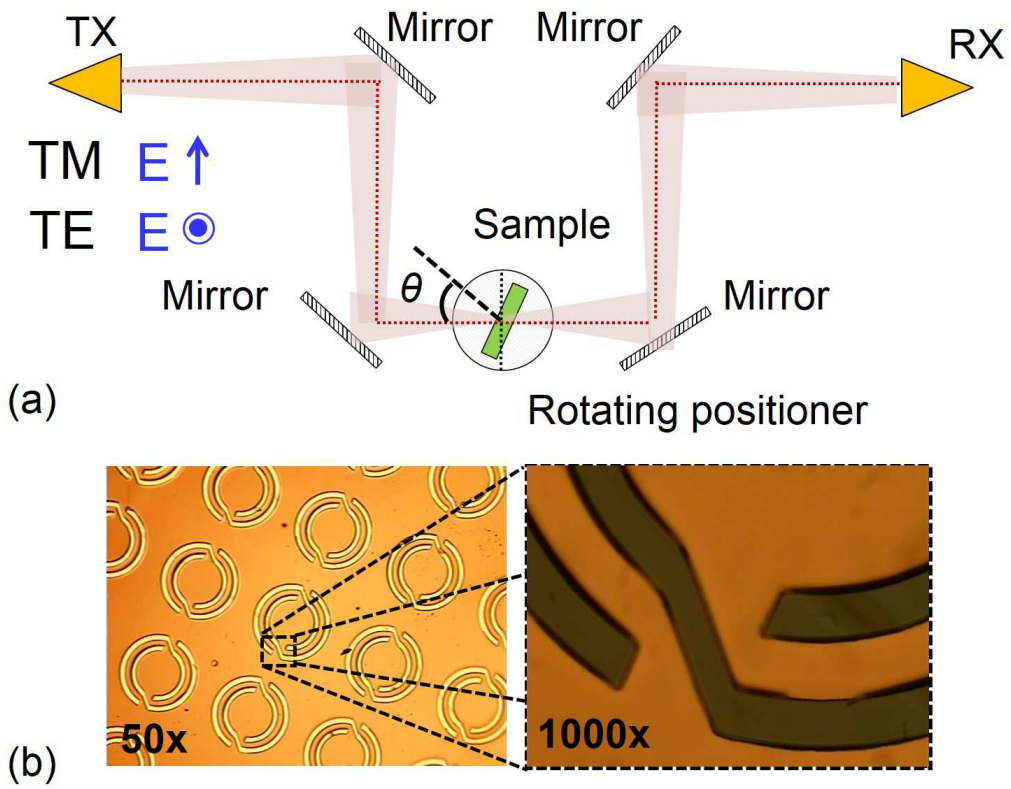

Fig. 3.45 (a) Top view of a schematic depicting the experimental set-up for oblique incidence measurements. To perform measurements under TM polarization, the electric field must be horizontally polarized. In contrast, for TE the electric field is vertically polarized. (b) Microscope pictures of the fabricated prototype with 50x and 1000x magnification.

Another important remark is that the asymmetric mode resonance is practically absent in the measurements. As discussed in Sect. 3.3.2, it should be considered that this resonance has a very high Q and therefore is very sensitive to losses and fabrication tolerances. In fact, a small difference between simulated and actual structural values such as longitudinal period, sample alignment, etc., could lead to large differences. Another source of losses is that due to the non-uniformity of the substrate during the fabrication process, the metallic parts of the structure acquire a roughness that leads to a lower effective conductivity of the metal. From these results, it can be stated that losses affect drastically the overall performance of the NB-CSRR metasurface.

The experimental results obtained for the symmetrical mode resonance also show lower amplitude with respect to numerical simulations [see Figs.3.46(c),(d),(g) and (h)]. Besides, the influence of losses mentioned above, it should be noted that simulations consider infinite structures while in the experiment a limited number of elements are efficiently illuminated.

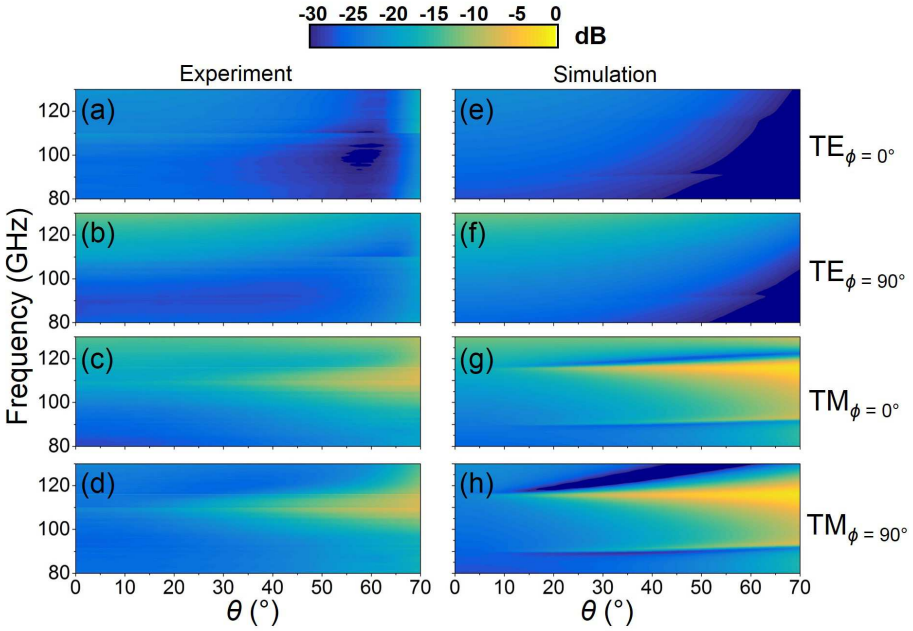

Fig. 3.46 Transmission results for NB-CSRR bi-layer configurations. (a) Experiment - TE$_{\phi=0°}$. (b) Experiment - TE$_{\phi=90°}$. (c) Experiment - TM$_{\phi=0°}$. (d) Experiment - TM$_{\phi=90°}$. (e) Simulation - TE$_{\phi=0°}$. (f) Simulation - TE$_{\phi=90°}$. (g) Simulation - TM$_{\phi=0°}$. (h) Simulation - TM$_{\phi=90°}$.

In addition, under oblique incidence the focused beam does not effectively illuminate the same amount of elements as for the normal incidence case. All in all, although there is a room for improvement of the experimental results, they show a good qualitative agreement with the numerical simulations.

3.4 Concluding Remarks

In this section results concerning three distinct topics have been presented. All of them involved theoretical and numerical studies accompanied by experimental demonstration within the millimeter wave regime. First, two-dimensional periodic structures composed of annular apertures drilled on metallic screens have been analyzed in terms of a ECA. The ECA allowed us to provide an insightful understanding of the physical mechanisms involved in classical FSSs and ET devices. The theoretical, numerical and experimental results are in general in good agreement. Obviously, the used ECA shows some limitations. For instance, the ECA fails with large values of the outer/inner radii ratio b/a. In addition, thickness and losses are not included in the ECA for the metallic parts. A next step can be to deal with these limitations trying to incorporate these parameters to the ECA.

In the second part the basics for designing unidirectional devices by using SHA structures and dielectric gratings have been provided. A thorough and general theoretical analysis has been presented which in fact can be applied to any metamaterial device, provided that its dispersion properties can be obtained. The proposed unidirectional devices are then based on a combination of both dispersion and diffraction effects. In the last part of the section, a experimental demonstration was delivered with qualitatively good agreement. However, it has been found that the experiment could be greatly improved by mitigating the possible air gaps between the adjacent SHA layers. Then, a future work could be devoted to improvement of the stacking process by applying press techniques available for multilayer circuit fabrication.

Finally, the third part has dealt with a modified version of the classical CSRR metasurface, the NB-CSRR metasurface. This element has been numerically and experimentally characterized. At the light of the obtained results, the NB-CSRR metasurface shows a very interesting angular performance that deserves further study for the future. The next step would be to exploit such exotic angular performance in combination with diffraction inspired structures (as done for the second part of the section) to propose advanced devices with directional selectivity.

Chapter 4

Sensing at THz frequencies with metamaterial-inspired devices

In this chapter the specific application for sensing at THz frequencies is targeted by means of different metasurface designs inspired by classical FSS structures. As discussed in Chapter 1, the THz band is very appealing for sensing applications given that many molecular bonds have footprints at these frequencies. In fact, lately great research activity has been directed towards this topic. Given the location of this band, sensing THz solutions have been proposed from different disciplines such as microwaves, plasmonics and optics [RU17b]. Then a myriad of possibilities are opened to design sensing platforms based on resonant structures, plasmonic waveguides or optical fibers to name a few. Here, we deal with the first kind, namely sensors based on resonances.

In Section 4.1 a brief introduction to THz sensing solutions using classical FSS and metasurfaces is provided. Besides describing their operation principle, a brief historical review is given. Finally, the key parameters for the assessment of the sensor performance are described.

Section 4.2 deals with numerical and experimental results of a sensor based on a cross-dipole FSS with wide angular performance. Next, a modification of this structure is proposed to enhance the performance of the device by working in the extraordinary reflection (ER) regime. For this case, a preliminary numerical study is presented which needs further experimental demonstration in the future.

Finally some concluding remarks and future guidelines for the development of new and competitive sensing devices are provided in Section 4.3.

4.1 Sensing with Frequency Selective Surfaces and Metasurfaces

FSSs are commonly used in the microwave regime for far-field manipulation as antenna radomes or spatial and dichroic filters. Lately their use has been extended to sensing applications at THz [Deb07]. In this new realm, FSSs are grouped together with metamaterials and referred under the general denomination of metasurfaces. However, in this Thesis with the aim of preserving classical terminology, FSS term is preferred for those cases where the unit cell element are comparable to the operation wavelength and metasurface is used when subwavelength elements are involved.

FSS and metasurfaces can be used for the development of high sensitivity and free-space sensors. This later feature enables the possibility of implementing sensing schemes where the sensing part and the readout can be located at different places. This is very useful in those applications where contamination between samples becomes critical and disposable sensors are required. The operation principle of FSS/metasurface based sensors is actually quite simple. This kind of structures do show either a peak or dip (depending on the character of the FSS/metasurface, one can have either band-pass or notch response) at resonance. The frequency/wavelength for which the resonance appears is taken as a reference. Then, this resonance can be shifted when an analyte sample is placed near the structure. The performance on the sensor is customarily evaluated in terms of the maximum frequency shift and the linewidth of the resonance as it is later explained.

In 2007, C. Debus and P. H. Bolivar published one of the very first works where FSS-based THz sensors were used [Deb07]. Since then, the research interest on periodic structures for sensing applications has grown enormously. Many examples based on symmetric and asymmetric SRR [Dri07, AN08], gap capacitive resonators [Par14] and metasurfaces showing Fano-like resonances [Sin14] can be found within the literature. As it can be seen, the interest of the scientific community on developing THz sensors is increasing. In the subsequent sections our intention is to contribute to this trend.

4.1.1 Sensor parameters: Sensitivity and Figure of Merit

Here, some basic concepts regarding the parameters that measure the performance of a sensor are provided. The key parameters that determine the quality of a sensor device are the sensitivity and the resonance linewidth. Generally the sensitivity, S, is given as the displacement of the resonance ($\Delta\lambda_{res}$) with a variation of other parameter. For instance, this variation can be related to the refractive index unit (RIU) of the surrounding media as

follows:

$$S = \Delta\lambda_{res}/\Delta n[\mu\text{m/RIU}], \tag{4.1}$$

where n is the refractive index of the analyte. Another usual definition for S is to relate $\Delta\lambda_{res}$ to a variation of the analyte thickness, Δt, yielding:

$$S = \Delta\lambda_{res}/\Delta t[\text{dimensionless}]. \tag{4.2}$$

However, S can be also related with other parameters linked to the analyte such as volume, or concentration [O'H12].

The other mentioned parameter, i.e. the resonance linewidth, is connected with the spectral resolution of the resonance. It is defined as the full-width at half-maximum (FWHM) which gives an estimation of how narrow the resonance is. Putting this in terms of the quality factor, Q, small FWHM values lead to high Q and vice versa.

A final parameter that enables a complete assessment of the performance of a sensor device is the figure of merit, FoM. The FoM relates the sensitivity and resonance linewidth as follows:

$$FoM = S/\text{FWHM}. \tag{4.3}$$

With these premises, it is clear that in practice, large sensitivities and narrow spectral widths are targeted for high performance sensors.

4.2 Wide Angular Sensing with Cross Dipole FSS

As described in Sect. 4.1 there are many examples of THz sensors within the literature. On occasions the design of such devices is not intuitive due to their relatively complex geometries. In this part of the Thesis, our aim is to propose a rather simple geometry while keeping an acceptable sensing performance. To this end, a periodic arrangement comprising the well-known cross-dipole element is designed to operate near 0.8 THz. It will be also shown that by using oblique incidence the performance of the sensor can be enhanced.

4.2.1 Sensing performance under normal incidence

Figure 4.1(a) shows a schematic of the cross-dipole FSS unit cell and a picture of the fabricated sample along with its physical dimensions. The cross-dipole prototype was fabricated on a thin-film polypropylene (PP) substrate. The selection of this material is based on its low absorptivity and dispersion in the THz band [Ort14, NC11]. The metallic cross-dipole FSS was patterned on an aluminum (Al) layer with a thickness of $t_{Al} = 0.35\mu$ m

by means of a contact photolithography technique. To test the sensing capability of the cross-dipole FSS a thin layer of a photoresist material (AZ9260 from Microchemicals^{TM}) was spin-coated over the fabricated sample acting as the analyte.

The experimental measurements were performed with a TPS Spectra 3000 from Teraview (see App. A). For comparison, numerical simulations were carried out using CST Microwave Studio along with unit cell boundary conditions. The permittivity of the PP material was modeled as complex with both real part and loss tangent retrieved from the literature ($\varepsilon_{PP} = 2.25$ and $\tan\delta_{PP} = 0.0005$) [Ort14]. For the photoresistive material used as analyte the dielectric properties were fit to the simulations from the experimental data due to the lack of information regarding them. After this procedure, the material properties were set to $\varepsilon_a = 2.855$ and $\tan\delta_a = 0.05$. Solutions with two different analyte thicknesses, h_a, of 9 and 20 μm were numerically and experimentally investigated. The h_a values were obtained after deposition by using a micrometer.

The obtained transmission results (both numerical and experimental) for the bare cross-dipole FSS (namely, without photoresist material) and when the analyte material is deposited on top, are shown in Fig. 4.1(b). A very good agreement is obtained. The discrepancies can be assigned to possible errors made when determining the analyte thickness. A stop-band resonance can be clearly noticed at 0.77 THz for the sample without photoresist material. This resonance is related to the fundamental dipolar resonance of the metallic cross-dipole elements. The free-space resonance wavelength λ_{res} can be determined as follows:

$$\lambda_{res} = \chi L \sqrt{\varepsilon_{eff}} \tag{4.4}$$

where L is the cross arm length, ε_{eff} is the effective permittivity and χ is a constant. The ε_{eff} depends of the dielectric media placed at both sides of the FSS. In our case, these media are the air and the PP substrate. Given that the PP thickness is $h_{PP} \geq 0.1\lambda_{res}$, the ε_{eff} can be approximated as $\varepsilon_{eff} = (1+\varepsilon_{PP})/2$ [Mac00, Mun00]. The χ parameter is known to be close to 2 for cross dipoles with narrow arms [Mac00, Mun00]. However, the exact value depends on the cross geometry and more precisely to the inter-cross spacing (d˜L) and the cross arm width w [Möl99, Cun83]. In the present case according to the physical dimensions of the cross-dipole depicted in Fig. 4.1(a) it is obtained that $\chi = 1.75$.

Let us now evaluate the influence of the analyte thickness on the transmission response. To this end, the frequency shift experienced by the resonance, Δf_{res}, is studied as h_a is varied, see Fig. 4.1(c). As expected, the presence of the analyte increases ε_{eff}, and therefore, a redshift of the dipolar resonance is obtained. In addition, for thin analytes, i.e. $h_a < 0.1\lambda_{res}$, Δf_{res} rapidly grows as h_a increases as consequence of a higher total ε_{eff}. In fact, Δf_{res} approaches asymptotically to the saturation level given by the maximum effective permittivity attainable,

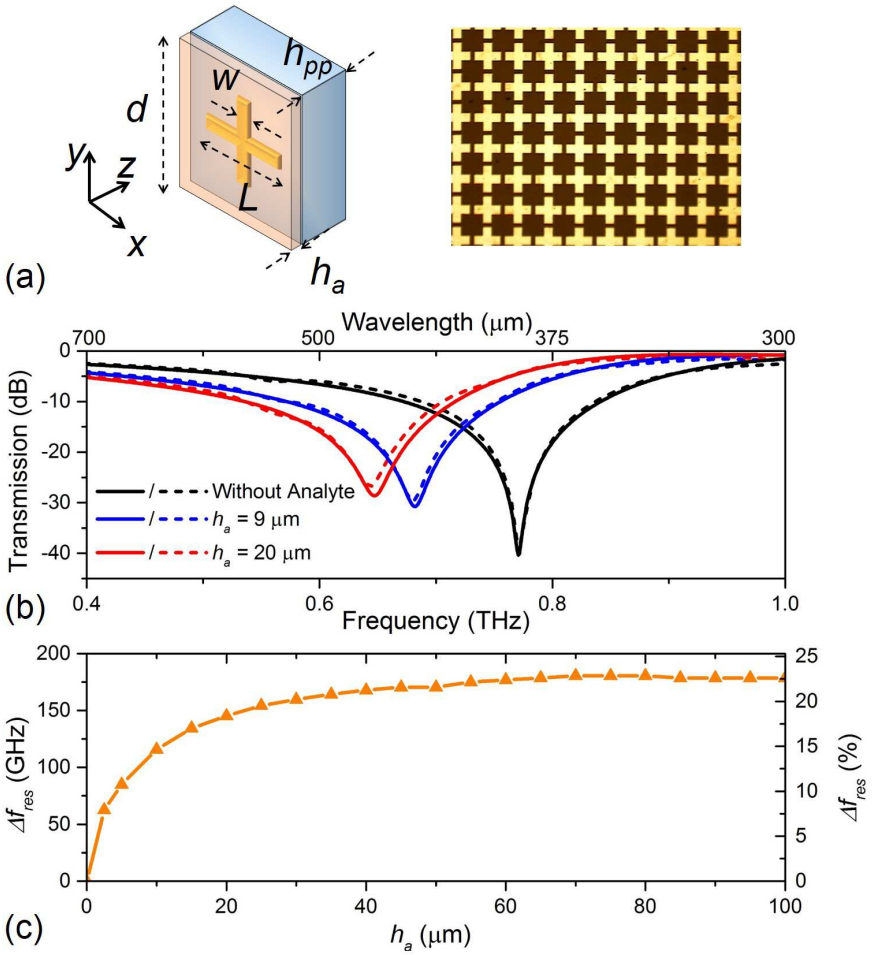

Fig. 4.1 (a) Schematic of the fabricated unit cell (left) and microscope picture of the cross-dipole FSS pattern on the PP substrate (right). Dimensions: unit cell lateral period, $d = 200\,\mu$m; cross length, $L = 175\,\mu$m; strip width, $w = 57\,\mu$m; polypropylene substrate height, $h_{PP} = 41\,\mu$m; analyte thickness $h_a = 9, 20\,\mu$m . Dielectric properties of PP and analyte photoresist material: PP permittivity, ε_{PP} = 2.25; PP loss tangent $\tan\delta_{PP} = 0.0005$; photoresist analyte permittivity, $\varepsilon_a = 2.855$; photoresist analyte loss tangent $\tan\delta_a = 0.05$. (b) Transmission results for the fabricated structure. Simulation (solid line) and measurement (dashed line) results for the analyte-free prototype (black curve), and the analyte deposited on top with thicknesses of $h_a = 9\,\mu$m (blue curve) and $h_a = 20\,\mu$m (red curve). (c) Simulation results of the dipolar resonance frequency shift, Δf_{res}, versus analyte thickness; (left axis) absolute frequency shift; (right axis) frequency shift normalized to the resonance frequency expressed in percentage.

$\varepsilon_{eff}\,|_{h_a\to\infty} = (\varepsilon_a + \varepsilon_{PP})/2 = 2.55$. A maximum absolute of $\Delta f_{res} = 180$ GHz is obtained. In percentage [right axis of Fig. 4.1(c)], evaluated as $\Delta f_{res}(\%) = \frac{\Delta f_{res}(h_a=0) - \Delta f_{res}(h_a\neq 0)}{\Delta f_{res}(h_a=0)} \times 100$, the maximum value of 22.5% is obtained. For the purpose of thin film sensing, a fast change

of ε_{eff} versus h_a is of primary importance. In this way, one could measure small values of h_a by tracking the resonance frequency shift $\Delta f_{res}(h_a) = |f_{res}\,|_{h_a \neq 0} - f_{res}\,|_{h_a=0}\,|$.

Next, a numerical study to measure the performance of the sensor is conducted in terms of S and FoM. To this end, we use the refractive index, n, instead of ε, since it allows for a better description. A numerical simulation wherein the real part of n is varied from 1 to 2 with a step of 0.2 for h_a values of 9 and 20 μm is run. Figure 4.2(a) and (b) show the obtained transmission results for $h_a = 9\,\mu$m and $h_a = 20\,\mu$m, respectively. These results are represented in terms of resonance frequency shift in Fig. 4.2(c). Maximum frequency shifts of about 128.8 GHz and 180 GHz are obtained for $h_a = 9\,\mu$m and $h_a = 20\,\mu$m, respectively. The S and FoM are evaluated by using Eqs. 4.1 and 4.3 and plotted in Fig. 4.2(d). The obtained S varies between 68.7 and 89 μm/RIU for $h_a = 9\,\mu$m and between 102.6 and 138.6 μm/RIU for $h_a = 20\,\mu$m. In terms of FoM the results are moderate as consequence of the low Q exhibited by the dip resonance. FoM values within the ranges [0.12 – 0.15] and [0.16 – 0.22] are obtained for $h_a = 9\,\mu$m and $h_a = 20\,\mu$m, respectively.

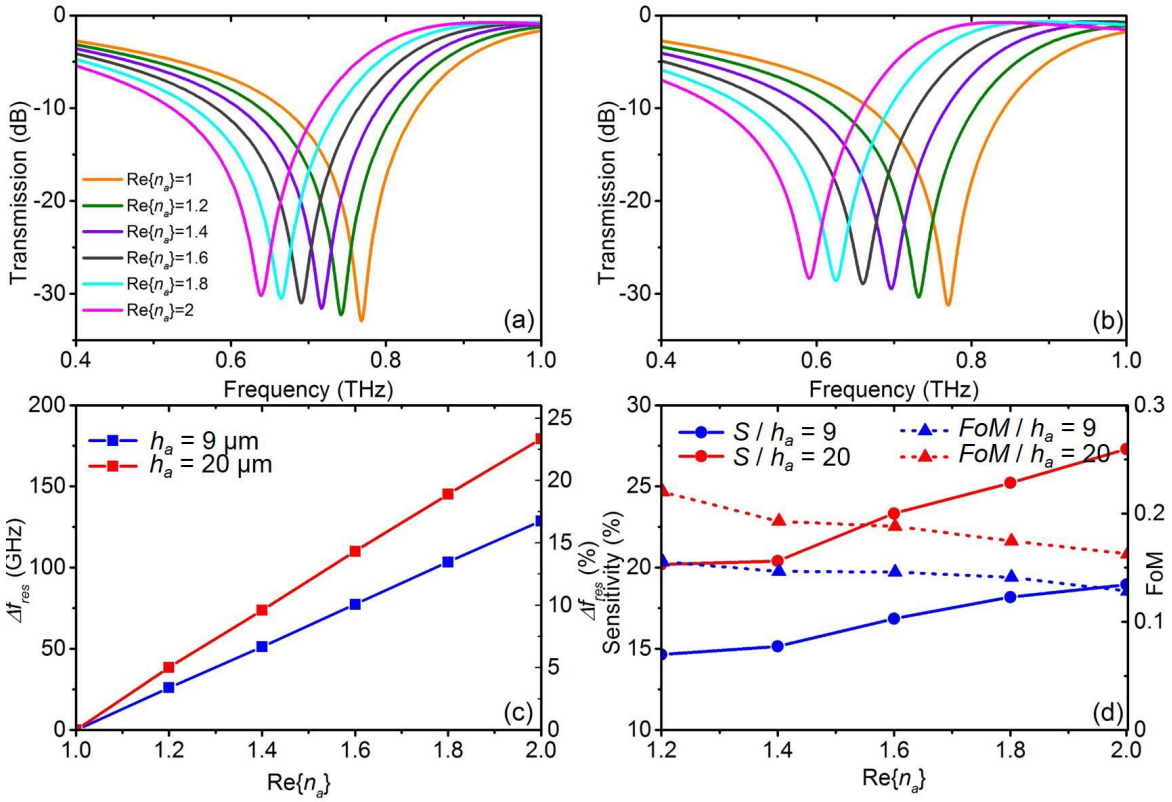

Fig. 4.2 (a) Simulated transmission results for the prototype with analyte thickness of $h_a = 9\,\mu$m. Real part of n is varied from 1 to 2. (b) Same as (a) for $h_a = 20\,\mu$m. (c) Δf_{res} versus variation of n (absolute values are used for left axis and percentage values for right axis) (d) Sensitivity (left axis) and FoM (right axis).

4.2.2 Extending Sensing to oblique incidence

To extend the sensing operation to other regimes, obliquely incident waves are used in this section. First, obliquely incident waves can create additional resonance dips that could be also used for sensing purposes. In addition, under oblique TE incidence the dip resonance is redshifted and hence, the sensing performance can be transferred to other frequencies.

As usual, the oblique incidence characterization provided here involves the two principal polarization planes, TE and TM (note that the unit cell is square). Figures 4.3(a) and (b) show the transmission results obtained at different values of the real part of n for an analyte with thickness $h_a = 9\,\mu$m under TM and TE incidence, respectively. The incidence angle, θ, is set to 45°. For the TM polarization case, the most remarkable feature is the appearance of two small resonances in the spectrum. These new dips are located at 838 GHz and 877 GHz for the case of $\mathrm{Re}\{n_a\} = 1$. The resonance occurring at 838 GHz when $\mathrm{Re}\{n_a\} = 1$ shifts down to approximately 640 GHz when $\mathrm{Re}\{n_a\} = 2$. This resonance corresponds to the so called bent mode that arises only under TM oblique incidence [Mun00, Pel79, Tsa84]. In this situation, an asymmetrical current can be induced due the phase difference that acquires the impinging electric field between the horizontal and vertical arms. This resonance has quadripolar character and presents a very high Q. Figure 4.4 shows the current distribution extracted from simulation results for the case of the cross-dipole without deposited material on top. The current distribution at the fundamental and bent mode is shown denoting a clear evidence of a dipolar and quadripolar resonance for the first (fundamental) and second mode (bent mode), respectively (see Fig. 4.4). Finally, the third resonance is related with the onset of the first grating lobe.

The results obtained for TE polarization differ considerably. First, the bent mode excitation is not possible since now the electric field is always paralell to one of the cross arms. In addition, at the onset of the grating lobe an abrupt slope change is observed instead of the additional dip obtained for the TM polarizations [see Fig. 4.3] However, the principal resonance experiences a redshift of 94.5 GHz that corresponds to approximately a 10% of the resonant frequency. This is a well-known and classical effect on dipole and cross-dipole FSS under TE incidence as it can be found within the literature [Pel79, Tsa84, Kia08, GV12]. As reported in [GV12], this shift can be explained by means of equivalent circuits as the ones used in this Thesis in Chapter 3. At larger θ, the cut-off of the first higher-order TE harmonic is shifted toward lower frequencies and so is the condition for resonance of the cross dipole. This feature can be exploited to extend the operation regime of the sensor to lower frequencies by simply varying the angle of incidence of the impinging wave.

To provide a full characterization of the sensing performance within the whole angular range, additional simulations were carried out by varying θ from 0 to 85° with a step of

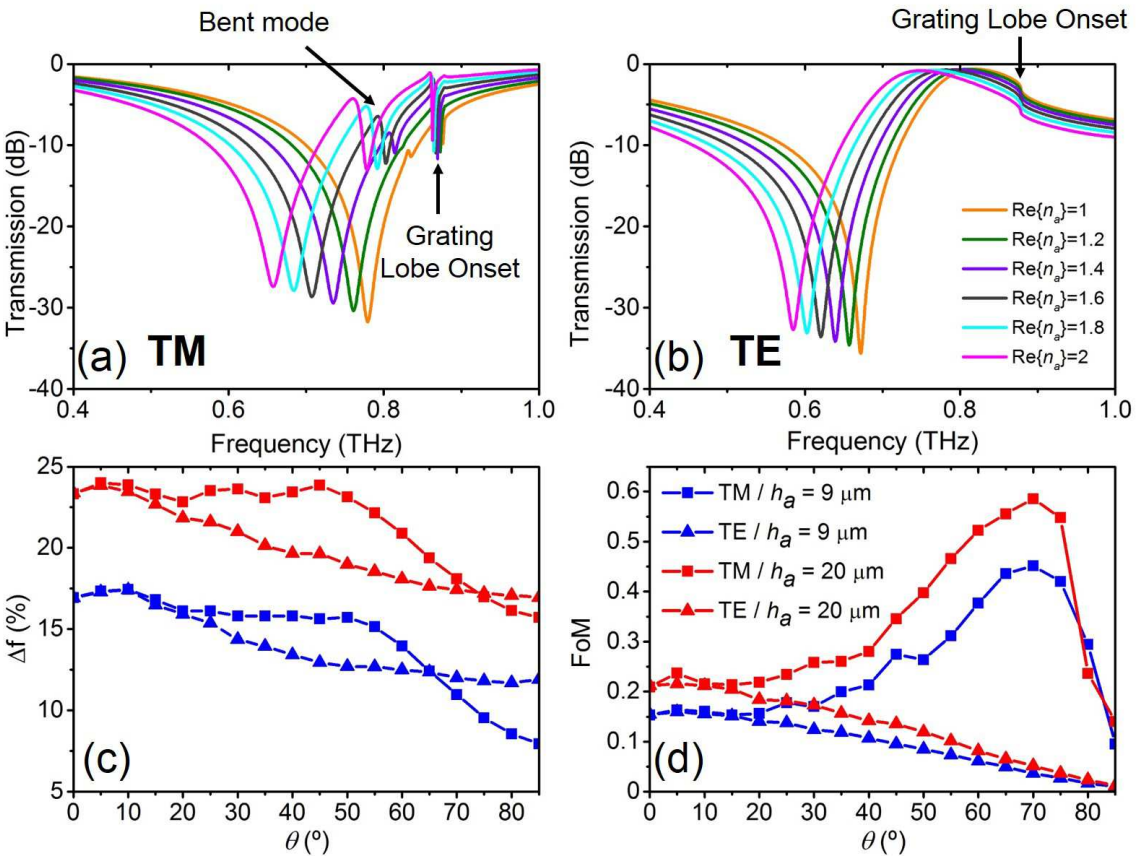

Fig. 4.3 Simulated transmission results for the prototype with an analyte of thickness $h_a = 9\,\mu$m and $\theta = 45°$. (a) TM polarization. (b) TE polarization. (c) Maximum frequency shift, Δf_{res} versus θ for $h_a = 9$ (blue lines) and $20\,\mu$m (red lines) under TE (triangles) and TM (squares) incidence. (d) Maximum *FoM* versus θ for $h_a = 9$ (blue lines) and $20\,\mu$m (red lines) under TE (triangles) and TM (squares) incidence.

5°. As done for normal incidence (treated in Sect. 4.2.1), the *S* and *FoM* parameters are obtained for each θ. Figure 4.3(c) shows the maximum frequency shift, Δf_{res} of the dipolar resonance under TM (squares) and TE (triangles) incidence and for $h_a = 9\,\mu$m (blue lines) and $h_a = 20\,\mu$m (red lines). For the TM polarization case, good sensitivity performance is obtained within a wide angular range (from 0 to 60° approximately). On the other hand, for the TE case the sensitivity performance decreases linearly with θ. Figure 4.3(d) shows the maximum *FoM* values versus θ. Again, wide angle operation is achieved under TM illumination. In fact, the largest value appears near 70°, where $FoM = 0.6$, i.e. it is three times larger than in the case of normal incidence. This relatively large *FoM* might seem surprising at first sight given that *S* is actually lower than under normal incidence. However, it should be recalled that the *FoM* also depends on the FWHM of the fundamental resonance which in the case of large θ is narrower due to the excitation of the aforementioned bent

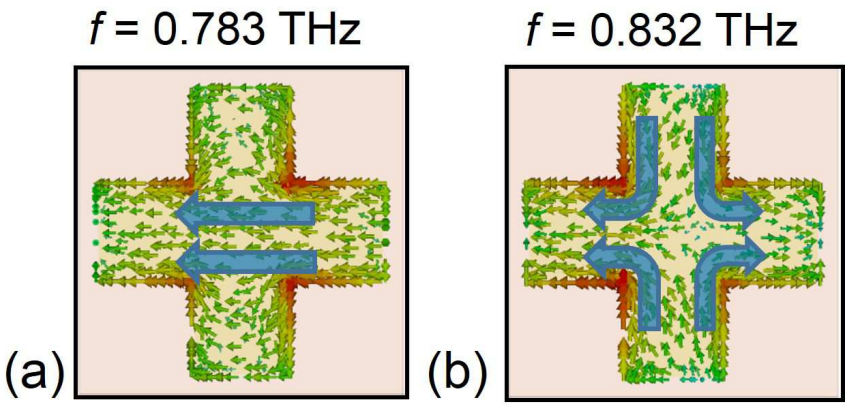

Fig. 4.4 Surface currents distribution. (a) Fundamental mode resonance, $f = 0.783\,\text{THz}$. (b) Bent mode resonance, $f = 0.832\,\text{THz}$.

mode that compresses it. For TE polarization, the *FoM* linearly decreases with θ. In any case, an acceptable performance is obtained within an angular width of 40°. At the light of the obtained results, oblique incidence enhances the overall sensing performance of the device. The most evident improvement is obtained for the TM polarization case for which the maximum *S* and *FoM* values are obtained. In addition, for TE scenario, keeping in mind that the sensing performance is less competitive, one may think of using oblique incidence to inspect lower frequencies.

Next, the oblique incidence for the cross-dipole FSS with an analyte thickness, $h_a = 20\,\mu\text{m}$ is experimentally characterized. To this end, unlike the experiments presented for normal incidence, an AB-Millimetre VNA was used. This decision was made based on the fact that with the current experimental facilities, oblique incidence measurements were not possible to be performed with the TDS-Teraview system. In this case then, the measurements were performed from 0.63 to 1 THz with a step of 0.2 GHz. The angle of incidence, θ, was swept from 0° to 60° with a step of 5°. The angular measurements were restricted to this upper limit, since at larger θ values the sample holder would strongly interfere with the incident beam. Figure 4.5 shows the simulation and experimental results for TM and TE polarization. In addition, the onset of the grating lobe is superimposed as a dash-dotted white line evaluated by the well-known equation shown in Eq. 2.9. In general, the agreement between simulations and experiments is qualitatively good. It can be seen, how the bent mode is highly mitigated in the experiment. This is due to the high *Q* of the resonance that makes it more sensitive to losses. However, some signatures of the bent mode can be observed between $\theta = 30°$ and 40°. On the other hand, the small resonance just before the onset of

the grating lobe vanishes in the experiment. In addition, it can be seen that for $\theta \geq 40°$ the experimental results deviate from the simulations.

For TE polarization the agreement is better in a wider frequency and angular region. Only a small blueshift in frequency is noticed in the experimental results as well as a small ripple coming from multiple reflections occurring in the set-up. The differences between measurements and simulations are mainly due to finite structure effects. Moreover, in the experiment the structure is excited by a Gaussian bean instead of a pure plane wave. In addition, only a limited number of cross elements are illuminated.

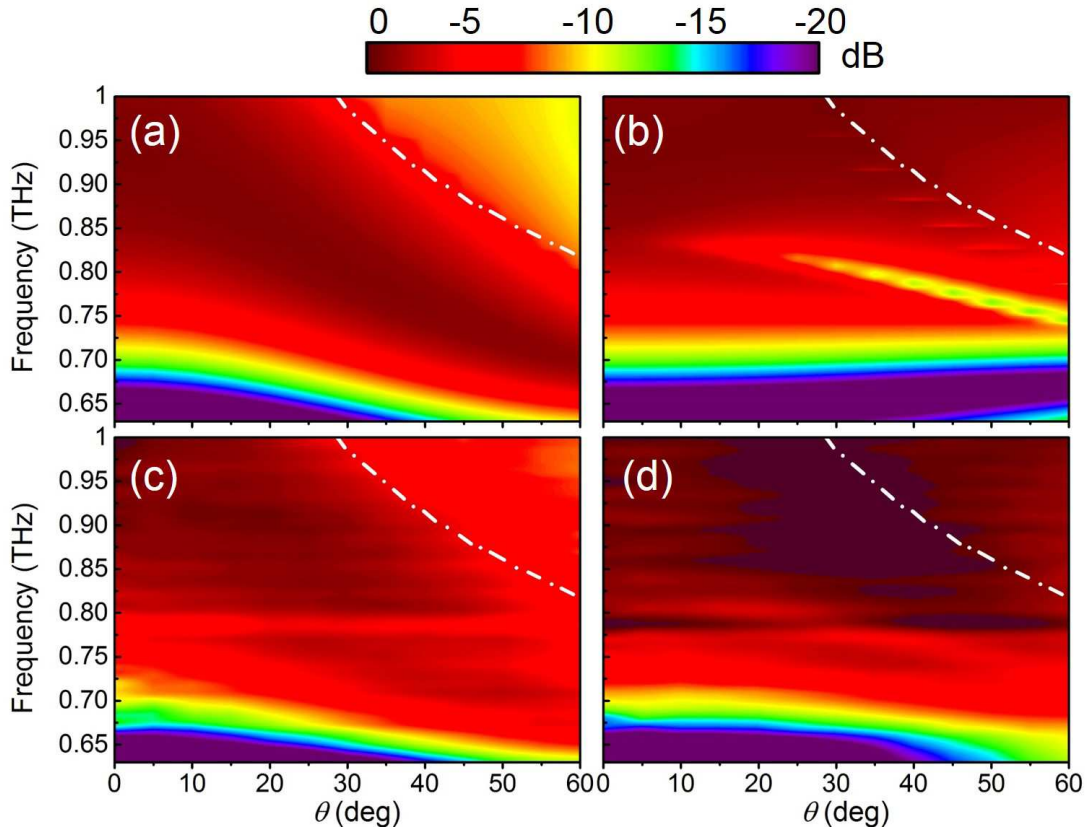

Fig. 4.5 Simulated and measured transmission for the prototype with an analyte of thickness $h_a = 20\,\mu$m at the incidence angle θ varying from 0° to 60°. (a) TM - Simulation. (b) TE-Simulation. (c) TM - Experiment. (d) TE - Experiment. Dash-dotted white contour line corresponds with the onset of the first order grating lobe

4.2.3 Enhance Sensing by means of ER

As mentioned before, the performance of a sensor based on FSS/metasurface devices can be characterized in terms of the *FoM* that relates the *S* and the spectral linewidth, i.e. FWHM.

Then one of the ways to enhance the *FoM* is to reduce the FWHM as much as possible. In other words, high Q resonances must be targeted.

Recently, ultrasensitive sensing devices have been proposed with high Q resonances resulting from Fano resonances in asymmetric resonators [Sin14]. Another option that has been lately treated is to work with absorber configurations [Yah15, Con15]. That is, to back the FSS/metasurface with a ground plane in such a way that at resonance the energy is ideally totally absorbed. From the practical point of view, the dip appearing in the reflection coefficient spectrum is the parameter used as the sensing reference.

Here, we propose an alternative which exploits the narrowband character of ET resonances. More precisely, since we are using cross-dipole FSS with stop-band character, we will make use of the extraordinary reflection (ER) phenomenon. The ER is simply the dual phenomenon of ET. As seen in Sec. 3.1, ET/ER resonances are inherently narrowband due to the fact that the required condition is extreme (in the case of periodic structures, a high order harmonic diverging to infinity). Then, by simply increasing the lattice period of the cross-dipole FSS we can create a resonance with higher Q.

Figure 4.6 shows the simulation results obtained for a cross-dipole periodic array with an analyte material deposited on top with a fixed thickness of $h_a = 20\,\mu$m. As it can be seen in the schematic in Fig. 4.6(a), the lattice period, d, is now considerably large in comparison with the cross arm length, L.

Similarly to the process followed in Sec. 4.2.2, an analyte material is placed on top of the patterned surface of the sensor. The real part of the refractive index, n, is then varied and a frequency shift of the ER resonance is obtained [see Fig. 4.6(b)]. From the transmission results the frequency shift, Δf_{res}, S and *FoM* can be easily evaluated [see Fig. 4.6(c) and (d)]. While the obtained S is lower in comparison with the results obtained in Sec. 4.2.2, the *FoM* is significantly improved. This can be explained by the high-Q factor exhibited by the ER resonances. In fact, it can be seen that when $\mathrm{Re}\{n_a\}$ approaches to 2, the resonance is widened and therefore the *FoM* is decreased.

4.3 Concluding Remarks

In this Chapter, the use of classical two-dimensional periodic structures for THz sensing applications has been studied. A cross dipole FSS based sensor has been numerically and experimentally characterized from 0.6 to 1 THz approximately. The obtained sensing performance has been found to be operative within a wide angular regime with acceptable S and *FoM* values.

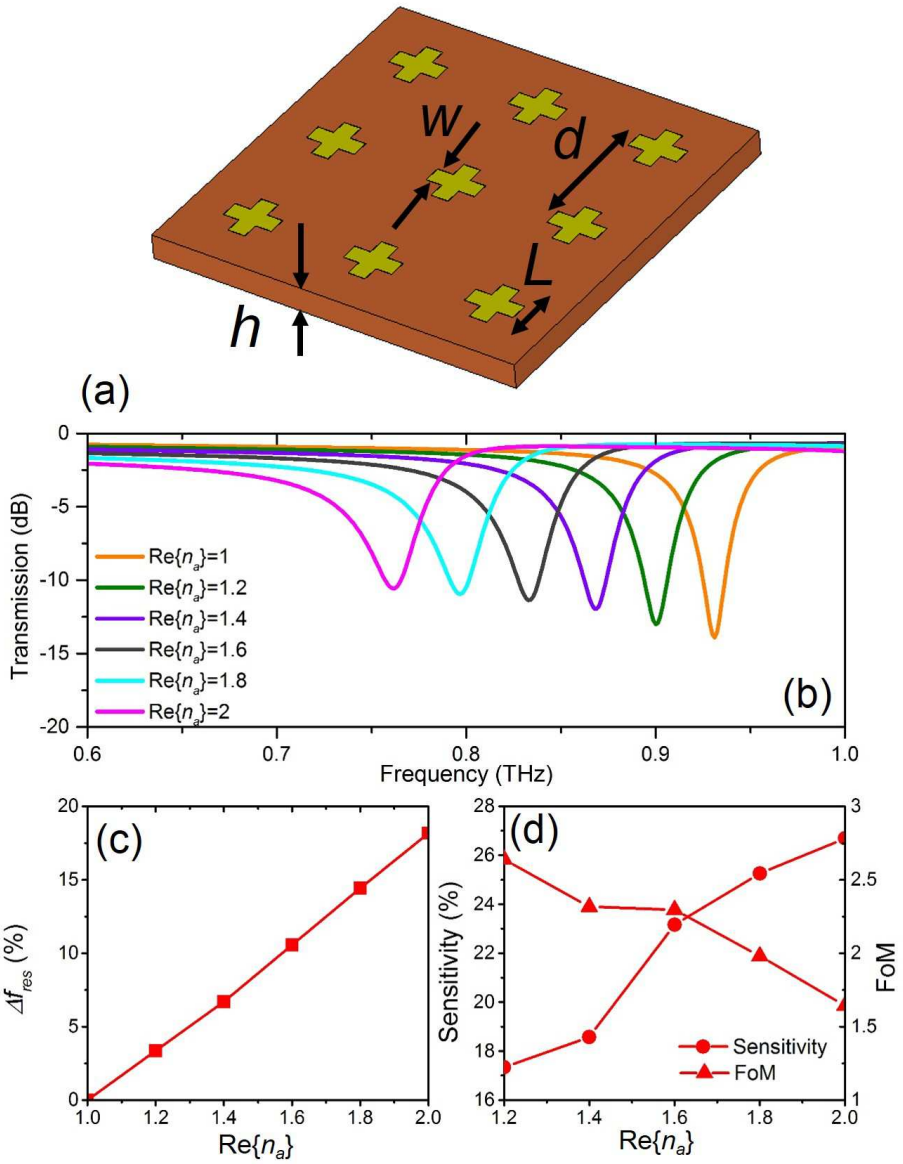

Fig. 4.6 (a) Schematic of the cross dipole design to operate at ER regime. Dimensions: cross arm length, $L = 100\,\mu$m; cross arm width, $w = 35\,\mu$m; lattice period, $d = 250\,\mu$m; substrate height, $h = 50\,\mu$m. (b) Simulated transmission results for the prototype with analyte thickness of $h_a = 20\,\mu$m and different real part of n values. (c) Δf_{res} versus Re$\{n\}$. (d) Sensitivity (left axis) and FoM (right axis) versus Re$\{n\}$.

Besides, a brief numerical study has been conducted when dealing with cross dipole periodic structures working at the ER regime. In this case, the *FoM* is significantly improved as consequence of the narrow spectral linewidth of ER resonances.

Although not reported in the Thesis, we are currently working on improving the sensing performance by enhancing the sensitivity. To this end, more complex geometries that allow a

high field confinement within larger areas are being considered. The future work is devoted to advance in this direction.

Chapter 5

Conclusions and Future Work

This final chapter summarizes the main conclusions drawn throughout this Thesis. Furthermore, guidelines and ideas for future investigations are provided. Besides proposing additional studies applicable to the topics presented in this Thesis, new ideas are briefly outlined as prospective post-doctoral research.

5.1 Conclusions

- In this Thesis several metamaterial and ET inspired devices have been proposed for the frequency regimes ranging from microwaves to terahertz waves. Theoretical, numerical and experimental results are presented for most of the reported devices.

- *En esta Tesis doctoral se han propuesto diferentes dispositivos basados en estructuras metamaterial y en el fenómeno de transmisión extaordinaria para rangos de frecuencias comprendidos entre las microondas y las ondas de terahercio. Se han presentado resultados teóricos, numéricos y experimentales para la mayoría de los dispositivos propuestos.*

- Two metamaterial-inspired radomes (metaradomes) have been designed for mitigating a blindspot in a phased-array antenna system for radar applications.

  - The blindspot origin is related with the onset of a grating lobe due to the array periodicity.
  - From an impedance point of view, the blindspot origin can be considered as an extreme impedance condition.
  - The wire medium metaradome allows to mitigate the blindspot effect by means of creating a bandgap for waves propagating along the surface of the antenna.
  - The metaradome based on Jesusalem cross metamaterial is inadequate for dealing with the blindspot effect. The blindspot represents such an extreme impedance condition that a narrowband solution as the designed metaradome results ineffective.
  - The two proposed solutions could be combined to enhance the radiation properties of the antenna. While the blindspot is mitigated by the wire medium, the Jerusalem cross based metaradome could act as a wide angle impedance matching layer provided that now the impedance profile has not extreme values.

- *Se han diseñado dos radomos inspirados en metamateriales (metaradomo) para mitigar el efecto de un ángulo ciego en un sistema de antenas para aplicaciones radar.*

  - *El origen del ángulo ciego está relacionado con la aparición de un lóbulo de difracción debida a la periodicidad de la antena.*
  - *Desde el punto de vista de la impedancia, el ángulo ciego está relacionado se puede considerar una condición de impedancia extrema.*

  - *El metaradomo basado en un medio de hilos es capaz de mitigar el efecto del ángulo ciego creando una banda prohibida para ondas que se propagan en la superficie de la antena.*
  - *El metaradomo basado en cruces de Jerusalén ha resultado inadecuado para mitigar el efecto del ángulo ciego. El ángulo ciego representa una condición de impedancia tan extrema que una solución de banda estrecha como el metaradomo propuesto resulta inefectiva.*
  - *Las dos soluciones propuestas podrían combinarse para mejorar la propiedades de radiación de la antenna. Mientras que el efecto del ángulo ciego es mitigado por el medio de hilos, el metaradomo basado en cruces de Jerusalén podría actuar como adaptador de impedancias dado que en esta situación ya no hay valores extremos de la impedancia.*

- A thorough study of two-dimensional structures composed by annular apertures drilled on metallic screens has been conducted in terms of an equivalent circuit approach (ECA) that allows setting the limits between FSS and ET regimes.
  - The ECA results have been compared with full wave numerical results obtaining a very good agreement for annular apertures with outer, b, to inner, a, radius ratio, $b/a \leq 1.5$.
  - The ECA has been tested for a wide range of scenarios obtaining very accurate results. Free-standing, dielectric backed, layered media and unit cells with two annular apertures solutions have been considered. In addition, results for obliquely incident waves have been reported.

- *Se ha realizado un estudio detallado de estructuras periódicas compuestas por aperturas anulares en pantallas metálicas en términos de técnicas de circuito equivalente (ECA) que ha permitido delimitar la frontera entre los regímenes de FSS y ET.*
  - *Los resultados obtenidos por el ECA han sido comparados con simulaciones de onda completa obteniendo un muy buen acuerdo para aperturas anulares con relación entre el radio exterior, b, y el interior, a, $b/a \leq 1.5$.*
  - *El ECA se ha testado para un amplio rango de posibles situaciones. Soluciones sin y con substrato dieléctrico (varias capas) y con celda unidad en la que se consideran dos aperturas anulares han sido estudiadas. Además, se han reportado resultados obtenidos para incidencia oblicua.*

- Theoretical and experimental demonstration of unidirectional and tunable devices working in the millimeter wave regime has been done by means of combining the dispersion behavior of a SHA and the diffraction effects of a dielectric grating.
  - A general theory has been proposed to determine the range of unidirectional and angle tunability regimes in terms of equifrequency dispersion contours.
  - Tunable devices with sign-switching capability of the output deflection angle by varying the angle of incidence and/or frequency of the impinging wave have been proposed.
  - It has been found that in the experiment the existence of air gaps related to fabrication imperfections between the adjacent layers that compose the SHA deteriorate the overall performance of the device.

- *Se han demostrado teórica y experimentalmente dispositivos con transmisión unidireccional sintonizable en el rango de las ondas milimétricas mediante la combinación de la respuesta en dispersión de un SHA y los efectos de difracción proporcionados por una rejilla dieléctrica.*
  - *Se ha propuesto una teoría general para determinar el rango de unidireccionalidad y sintonía en términos de curvas de dispersión equifrecuenciales (EFCs).*
  - *Se han propuesto dispositivos sintonizables con capacidad de cambiar el signo del ángulo de la onda de salida al variar el ángulo de incidencia y/o frecuencia de la onda incidente.*
  - *Se ha constatado experimentalmente que la existencia de capas de aire entre las placas que componen el SHA deterioran el comportamiento del dispositivo.*

- A numerical and experimental demonstration of a NB-CSRR metasurface has been performed in the millimeter wave regime.
  - It has been found that the NB-CSRR metasurface shows a very interesting angular performance for which normally incident waves are almost totally reflected and obliquely incident waves with TM polarization can be almost totally transmitted.
  - The additional transmission peak that appears in bi-layered solutions due to the coupling between layers has been found to be very sensitive to losses both in simulations and experiments.

- *Se ha demostrado numérica y experimentalmente una metasuperficie NB-CSRR en el rango de las ondas milimétricas.*

  - *Se ha constatado que la metasuperficie NB-CSRR presenta un comportamiento angular muy interesante en el cual ondas incidentes en dirección normal se reflejan casi totalmente mientras que ondas con incidencia oblicua y polarización TM puede sen transmitidas eficientemente.*
  - *Se ha comprobado que el pico de transmisión adicional que aparece en las soluciones bicapa debido al acoplo entre placas es muy sensible a las pérdidas en los materiales tanto en simulación como en medida.*

- A classical two-dimensional periodic structure has been proposed for THz sensing applications. Numerical and experimental characterization of the sensing performance of the proposed device has been conducted over a wide angular range.

  - A numerical study of a modified version of the proposed sensor to work under extraordinary reflection (ER) regime has been reported leading to an improved performance of the sensor.

- *Se ha propuesto una estructura periódica bidimensional para aplicaciones de sensado en terahercio. Se ha caracterizado la respuesta del sensor para un amplio rango angular de manera numérica y experimental.*

  - *Se ha estudiado numéricamente una versión modificada del sensor de manera que opere en el régimen de reflexión extraordinaria (ER) llegando un mejor rendimiento del sensor.*

5.2 Future Work

5.2.1 Thesis related

- Improvement of the ECA to extend its applicability range to further scenarios:
  - Annular apertures with outer/inner radius ratio $b/a \geq 1.5$.
  - Metallic screens with finite thickness.
  - Treat metals as lossy conductors.

- *Mejorar el ECA para extender su rango de aplicación a situaciones adicionales.*
  - Aperturas anulares con relación de radio exterior e interno $b/a \geq 1.5$.
  - Pantallas metálicas con grosor finito.

  - Considerar metales como materiales conductores con pérdidas.

- Improvement of the stacking process for the SHA by applying press techniques available for multilayer circuit fabrication to avoid air gaps between layers.

- *Mejorar el apilamiento de placas en el SHA aplicando técnicas de prensado comúnmente utilizadas en la fabricación de circuitos multicapa para evitar capas de aire entre las placas.*

- Conduct a deeper study of the NB-CSRR metasurface in terms of dispersion to gain more physical insight.

  - Combine the NB-CSRR metasurface with diffraction grating to propose unidirectional devices with angular selectivity.

- *Realizar un estudio más profundo de la metasuperficie NB-CSRR en términos de dispersión para obtener un mayor conocimiento de la física subyacente.*

  - *Combinar la metasuperficie NB-CSRR con una red de difracción para la propuesto de dispositivos unidireccionales con selectividad angular.*

- Conduct the experimental characterization of the sensor based on a ER structure.

- *Caracterizar experimentalmente el sensor basado en el fenómeno de ER.*

- Further investigation of more complex geometries oriented towards enhancing the sensitivity of metamaterial inspired THz sensors.

- *Investigar geometrías complejas orientadas a mejorar la sensibilidad de sensores en THz basados en metamateriales.*

5.2.2 Post-Doctoral research

- Investigate the implementation of one-way THz absorbers by using homogeneous natural materials that present a polaritonic gap (polar dielectrics) and FSS structures. To this end, ECA techniques similar to those used in this Thesis could be applied.

- *Investigar el diseño de absorbentes unidireccionales en la bamda de THz usando materiales naturales que presentan un polariton (diélectricos polares) y estructuras FSS. Para este cometido, se puede hacer uso del ECA mostrado en esta Tesis.*

- Implementation of a polarizer working in the millimeter wave regime by means of a stacked structure composed by two layers patterned with subwavelength resonators and a central layer with a subwavelength grid to obtain compact devices with relatively wide frequency and angular operation range.

- *Desarrollo de un polarizador a frecuencias milimétricas mediante apilado de dos láminas con resonadores sublambda y una lámina central con una rejilla también sublambda para conseguir soluciones compactas y con un rango frecuencial y angular relativamente amplio.*

References

[ABm] "AB Millimetre–Company Specialized in MVNA manufacturing", .

[Agu15] Aguilà, P., Zuffanelli, S., Zamora, G., Paredes, F., Martín, F., and Bonache, J., "Front-to-back ratio improvement of printed antennas based on electrically small resonators for microwave presence detectors", *Electron. Lett.*, **51**, no. 11, pp. 836–837, 2015.

[Aky14] Akyildiz, I. F., Jornet, J. M., and Han, C., "Terahertz band: Next frontier for wireless communications", *Phys. Commun.*, **12**, pp. 16–32, 2014.

[Alù07] Alù, A., Silveirinha, M. G., Salandrino, A., and Engheta, N., "Epsilon-near-zero metamaterials and electromagnetic sources: Tailoring the radiation phase pattern", *Phys. Rev. B*, **75**, no. 15, p. 155410, 2007.

[AN08] Al-Naib, I. A. I., Jansen, C., and Koch, M., "Thin-film sensing with planar asymmetric metamaterial resonators", *Appl. Phys. Lett.*, **93**, no. 8, p. 083507, 2008.

[AN13] Al-Naib, I., Jansen, C., Singh, R., Walther, M., and Koch, M., "Novel thz metamaterial designs: From near-and far-field coupling to high-q resonances", *IEEE Trans. Terahertz Sci. Technol.*, **3**, no. 6, pp. 772–782, 2013.

[Azn08] Aznabet, M., Navarro-Cía, M., Kuznetsov, S., Gelfand, A., Fedorinina, N., Goncharov, Y. G., Beruete, M., El Mrabet, O., and Sorolla, M., "Polypropylene-substrate-based srr-and csrr-metasurfaces for submillimeter waves", *Opt. Express*, **16**, no. 22, pp. 18312–18319, 2008.

[Bae05] Baena, J. D., Bonache, J., Martin, F., Sillero, R. M., Falcone, F., Lopetegi, T., Laso, M. A. G., Garcia-Garcia, J., Gil, I., Flores Portillo, M., and Sorolla, M., "Equivalent-circuit models for split-ring resonators and complementary split-ring resonators coupled to planar transmission lines", *IEEE Trans. Microw. Theory Tech.*, **53**, no. 4, pp. 1451–1461, 2005.

[Bai09] Baida, F. I., Poujet, Y., Salvi, J., Labeke, D. V., and Guizal, B., "Extraordinary transmission beyond the cut-off through sub- annular aperture arrays", *Opt. Commun.*, **282**, no. 7, pp. 1463 – 1466, Jan. 2009, ISSN 0030-4018.

[Bel06] Belov, P. A., Zhao, Y., Sudhakaran, S., Alomainy, A., and Hao, Y., "Experimental study of the subwavelength imaging by a wire medium slab", *Appl. Phys. Lett.*, **89**, no. 26, p. 262109, 2006.

[Ber04] Beruete, M., Sorolla, M., Campillo, I., Dolado, J., Martín-Moreno, L., Bravo-Abad, J., and García-Vidal, F., "Enhanced millimeter-wave transmission through subwavelength hole arrays", *Opt. Lett.*, **29**, no. 21, pp. 2500–2502, Nov. 2004.

[Ber05] Beruete, M., Sorolla, M., Campillo, I., and Dolado, J., "Increase of the transmission in cut-off metallic hole arrays", *IEEE Microw. Compon. Lett.*, **15**, no. 2, pp. 116–118, Feb. 2005.

[Ber06a] Beruete, M., Sorolla, M., and Campillo, I., "Left-handed extraordinary optical transmission through a photonic crystal of subwavelength hole arrays", *Opt. Express*, **14**, no. 12, pp. 5445–5455, 2006.

[Ber06b] Beruete, M., Sorolla, M., Marqués, R., Baena, J. D., and Freire, M., "Resonance and cross-polarization effects in conventional and complementary split ring resonator periodic screens", *Electromagnetics*, **26**, no. 3-4, pp. 247–260, 2006.

[Ber07a] Beruete, M., Campillo, I., Navarro-Cía, M., Falcone, F., and Ayza, M. S., "Molding left-or right-handed metamaterials by stacked cutoff metallic hole arrays", *IEEE Trans. Antennas Propag.*, **55**, no. 6, pp. 1514–1521, Jun. 2007.

[Ber07b] Beruete, M., Cía, M. N., Campillo, I., Goy, P., and Sorolla, M., "Quasioptical polarizer based on self-complementary sub-wavelength hole arrays", *IEEE Microw. Compon. Lett.*, **17**, no. 12, pp. 834–836, 2007.

[Ber07c] Beruete, M., Sorolla, M., and Campillo, I., "Inhibiting left-handed wave propagation by a band gap of stacked cut-off metallic hole arrays", *IEEE Microw. Compon. Lett.*, **17**, no. 1, pp. 16–18, 2007.

[Ber07d] Beruete, M., Sorolla, M., Navarro-Cía, M., Falcone, F., Campillo, I., and Lomakin, V., "Extraordinary transmission and left-handed propagation in miniaturized stacks of doubly periodic subwavelength hole arrays", *Opt. Express*, **15**, no. 3, pp. 1107–1114, Feb. 2007.

[Ber11a] Beruete, M., Navarro-Cía, M., Kuznetsov, S. A., and Sorolla, M., "Circuit approach to the minimal configuration of terahertz anomalous extraordinary transmission", *Appl. Phys. Lett.*, **98**, no. 1, p. 014106, 2011.

[Ber11b] Beruete, M., Navarro-Cía, M., and Sorolla Ayza, M., "Understanding anomalous extraordinary transmission from equivalent circuit and grounded slab concepts", *IEEE Trans. Microw. Theory Tech.*, **59**, no. 9, pp. 2180–2188, Jul. 2011.

[Ber11c] Beruete, M., Serebryannikov, A. E., Torres, V., Navarro-Cía, M., and Sorolla, M., "Toward compact millimeter-wave diode in thin stacked-hole array assisted by a dielectric grating", *Appl. Phys. Lett.*, **99**, no. 15, p. 154101, 2011.

[Bet86] Betzig, E., Lewis, A., Harootunian, A., Isaacson, M., and Kratschmer, E., "Near field scanning optical microscopy (NSOM): development and biophysical applications", *Biophys. J.*, **49**, no. 1, pp. 269–279, Jan. 1986.

[Bos98] Bose, J. C., "On the rotation of plane of polarisation of electric waves by a twisted structure", *Proceedings of the Royal Society of London*, **63**, no. 389-400, pp. 146–152, 1898.

[Bro53] Brown, J., "Artificial dielectrics having refractive indices less than unity", *Proceedings of the IEE-Part IV: Institution Monographs*, **100**, no. 5, pp. 51–62, 1953.

[Cal91] Callaghan, P., Parker, E. A., and Langley, R. J., "Influence of supporting dielectric layers on the transmission properties of frequency selective surfaces", *IEE Proceedings H-Microwaves, Antennas and Propagation*, **138**, no. 5, pp. 448–454, 1991.

[Cam16] Camacho, M., Boix, R. R., and Medina, F., "Computationally efficient analysis of extraordinary optical transmission through infinite and truncated subwavelength hole arrays", *Phys. Rev. E*, **93**, no. 6, p. 063312, 2016.

[Che04] Chen, X., Grzegorczyk, T. M., Wu, B.-I., Pacheco Jr, J., and Kong, J. A., "Robust method to retrieve the constitutive effective parameters of metamaterials", *Phys. Rev. E*, **70**, no. 1, p. 016608, 2004.

[Col60] Collin, R. E., *Field Theory of Guided Waves*, McGraw-Hill, 1960.

[Con15] Cong, L., Tan, S., Yahiaoui, R., Yan, F., Zhang, W., and Singh, R., "Experimental demonstration of ultrasensitive sensing with terahertz metamaterial absorbers: A comparison with the metasurfaces", *Appl. Phys. Lett.*, **106**, no. 3, p. 031107, 2015.

[Cos12] Costa, F., Monorchio, A., and Manara, G., "Efficient analysis of frequency-selective surfaces by a simple equivalent-circuit model", *IEEE Antennas Propagat. Mag.*, **54**, no. 4, pp. 35–48, 2012.

[Cos14] Costa, F., Monorchio, A., and Manara, G., "An overview of equivalent circuit modeling techniques of frequency selective surfaces and metasurfaces", *Appl. Comput. Electromagn. Soc. J.*, **29**, no. 12, pp. 960–976, 2014.

[Cré14] Crépin, T., Martel, C., Gabard, B., Boust, F., Martinaud, J.-P., Dousset, T., Rodriguez-Ulibarri, P., Beruete, M., Loecker, C., Bertuch, T., et al., "Blind spot mitigation in phased array antenna using metamaterials", in *Radar Conference (Radar), 2014 International*, pp. 1–4, IEEE, 2014.

[CST] "CST Microwave Studio (2017)", .

[Cui14] Cui, T. J., Smith, D. R., and Liu, R., *Metamaterials*, volume 3, Springer, 2014.

[Cun83] Cunningham, C., "Resonant grids and their use in the construction of submillimetre filters", *Infrared physics*, **23**, no. 4, pp. 207–215, 1983.

[Dav05] Davidson, D. B., *Computational electromagnetics for RF and microwave engineering*, Cambridge University Press, 2005.

[Deb07] Debus, C. and Bolivar, P. H., "Frequency selective surfaces for high sensitivity terahertz sensing", *Applied Physics Letters*, **91**, no. 18, p. 184102, 2007.

[Dri07] Driscoll, T., Andreev, G. O., Basov, D. N., Palit, S., Cho, S. Y., Jokerst, N. M., and Smith, D. R., "Tuned permeability in terahertz split-ring resonators for devices and sensors", *Appl. Phys. Lett.*, **91**, no. 6, p. 062511, 2007.

[Dub06] Dubrovka, R., Vazquez, J., Parini, C., and Moore, D., "Equivalent circuit method for analysis and synthesis of frequency selective surfaces", *IEE Proc. Microw. Antennas Propag. H*, **153**, no. 3, p. 213, Mar. 2006.

[Dub09] Dubrovka, R., Vazquez, J., Parini, C., and Moore, D., "Multi-frequency and multi-layer frequency selective surface analysis using modal decomposition equivalent circuit method", *IET Microwaves Antennas Propag.*, **3**, no. 3, pp. 492–500, Mar. 2009.

[Ebb98] Ebbesen, T. W., Lezec, H. J., Ghaemi, H., Thio, T., and Wolff, P., "Extraordinary optical transmission through sub-wavelength hole arrays", *Nature*, **391**, no. 6668, pp. 667–669, Feb. 1998.

[Ede60] Edelberg, S. and Oliner, A., "Mutual coupling effects in large antenna arrays: Part 1–slot arrays", *IRE Transactions on Antennas and Propagation*, **8**, no. 3, pp. 286–297, 1960.

[Edi12] Editorial, "Surface plasmon resurrection", *Nat. Phot.*, **6**, no. 1, p. 707, 2012.

[Edw08] Edwards, B., Alù, A., Young, M. E., Silveirinha, M., and Engheta, N., "Experimental verification of epsilon-near-zero metamaterial coupling and energy squeezing using a microwave waveguide", *Phys. Rev. Lett.*, **100**, no. 3, p. 033903, 2008.

[Eme97] Emerson, D. T., "The work of Jagadis Chandra Bose: 100 years of mm-wave research", in *Microwave Symposium Digest, 1997., IEEE MTT-S International*, volume 2, pp. 553–556, IEEE, 1997.

[Est14] Estakhri, N. M. and Alù, A., "Ultra-thin unidirectional carpet cloak and wavefront reconstruction with graded metasurfaces", *IEEE Antennas Wireless Propag. Lett.*, **13**, pp. 1775–1778, 2014.

[Fal04] Falcone, F., Lopetegi, T., Laso, M., Baena, J. D., Bonache, J., Beruete, M., Marqués, R., Martín, F., and Sorolla, M., "Babinet principle applied to the design of metasurfaces and metamaterials", *Phys. Rev. Lett.*, **93**, no. 19, p. 197401, 2004.

[Fan05] Fan, W., Zhang, S., Minhas, B., Malloy, K. J., and Brueck, S. R. J., "Enhanced infrared transmission through subwavelength coaxial metallic arrays", *Phys. Rev. Lett.*, **94**, p. 033902, Jan. 2005.

[Gai00] Gaidis, M. C., "Space-based applications of far-infrared systems", in *8th Int. Terahertz Electron. Conf.*, pp. 125–128, IEEE, 2000.

[GM11] García-Meca, C., Hurtado, J., Martí, J., Martínez, A., Dickson, W., and Zayats, A. V., "Low-loss multilayered metamaterial exhibiting a negative index of refraction at visible wavelengths", *Phys. Rev. Lett.*, **106**, no. 6, p. 067402, 2011.

[Gri15] Griffiths, D. J., *Introduction to Electrodynamics*, Pearson, 2015.

[Gug89a] Guglielmi, M. and Oliner, A. A., "Multimode network description of a planar periodic metal-strip grating at a dielectric interface-ii: small-aperture and small-obstacle solutions", *IEEE Trans. Microw. Theory Tech.*, **37**, no. 5, pp. 902–909, Mar. 1989.

[Gug89b] Guglielmi, M. and Oliner, A. A., "Multimode network description of a planar periodic metal-strip grating at a dielectric interface. iii. rigorous solution", *IEEE Trans. Microw. Theory Tech.*, **37**, no. 5, pp. 902–909, May 1989.

[GV12] Garcia-Vigueras, M., Mesa, F., Medina, F., Rodríguez-Berral, R., and Gómez-Tornero, J. L., "Simplified circuit model for arrays of metallic dipoles sandwiched between dielectric slabs under arbitrary incidence", **60**, no. 10, pp. 4637–4649, 2012.

[Han64] Hansen, R. C., *Microwave Scanning Antennas*, Academic Press, 1964.

[Han09] Hansen, R. C., *Phased Array Antennas*, volume 213, John Wiley & Sons, 2009.

[Her93] Hertz, H., *Electric Waves: being researches on the propagation of electric action with finite velocity through space*, Dover Publications, 1893.

[Hes65] Hessel, A. and Oliner, A., "A new theory of wood's anomalies on optical gratings", *Appl. Opt.*, **4**, no. 10, pp. 1275–1297, Oct. 1965.

[Hol12] Holloway, C. L., Kuester, E. F., Gordon, J. A., O'Hara, J., Booth, J., and Smith, D. R., "An overview of the theory and applications of metasurfaces: The two-dimensional equivalents of metamaterials", *IEEE Antennas Propagat. Mag.*, **54**, no. 2, pp. 10–35, 2012.

[Ish91] Ishimaru, A., *Electromagnetic Wave Propagation, Radiation, and Scattering*, Prentice-Hall, 1991.

[Jia11] Jiang, Z. H., Bossard, J. A., Wang, X., and Werner, D. H., "Synthesizing metamaterials with angularly independent effective medium properties based on an anisotropic parameter retrieval technique coupled with a genetic algorithm", *J. Appl. Phys.*, **109**, no. 1, p. 013515, 2011.

[Kai10] Kaipa, C. S., Yakovlev, A. B., Medina, F., Mesa, F., Butler, C. A., and Hibbins, A. P., "Circuit modeling of the transmissivity of stacked two-dimensional metallic meshes", *Opt. Express*, **18**, no. 13, pp. 13309–13320, 2010.

[Kia08] Kiani, G. I., Esselle, K. P., Ford, K. L., Weily, A. R., and Panagamuwa, C., "Angle and polarization-independent bandstop frequency selective surface for indoor wireless systems", *Microwave Opt. Technol. Lett.*, **50**, no. 9, pp. 2315–2317, 2008.

[Kil13] Kildishev, A. V., Boltasseva, A., and Shalaev, V. M., "Planar photonics with metasurfaces", *Science*, **339**, no. 6125, p. 1232009, 2013.

[Kin83] King, R., Thiel, D., and Park, K., "The synthesis of surface reactance using an artificial dielectric", *IEEE Trans. Antennas Propag.*, **31**, no. 3, pp. 471–476, 1983.

[Kit05] Kittel, C., *Introduction to Solid State Physics*, John Wiley and Sons, 2005.

[Kni68] Knittel, G. H., Hessel, A., and Oliner, A. A., "Element pattern nulls in phased arrays and their relation to guided waves", *Proceedings of the IEEE*, **56**, no. 11, pp. 1822–1836, 1968.

[Koc46] Kock, W. E., "Metal-lens antennas", *Proceedings of the IRE*, **34**, no. 11, pp. 828–836, 1946.

[Kuz09] Kuznetsov, S. A., Navarro-Cía, M., Kubarev, V. V., Gelfand, A. V., Beruete, M., Campillo, I., and Sorolla, M., "Regular and anomalous extraordinary optical transmission at the thz-gap", *Opt. Express*, **17**, no. 14, pp. 11730–11738, 2009.

[Lan82a] Langley, R. J. and Drinkwater, A. J., "Improved empirical model for the jerusalem cross", *IEE Proc. Microw., Optics, Antennas H*, **129**, no. 1, pp. 1–6, 1982.

[Lan82b] Langley, R. J. and Parker, E. A., "Equivalent circuit model for arrays of square loops", *Electronics Letters*, **18**, no. 7, pp. 294–296, 1982.

[Lan83] Langley, R. J. and Parker, E. A., "Double-square frequency-selective surfaces and their equivalent circuit", *Electron. Lett.*, **19**, pp. 675–677, 1983.

[Lee85] Lee, C. K. and Langley, R. J., "Equivalent-circuit models for frequency-selective surfaces at oblique angles of incidence", *IEE Proc. Microw. Antennas Propag. H*, **132**, no. 6, pp. 395–399, Oct. 1985.

[Lee09] Lee, Y.-S., *Principles of Terahertz Science and Technology*, Springer Science & Business Media, 2009.

[Li08] Li, J. and Pendry, J. B., "Hiding under the carpet: a new strategy for cloaking", *Phys. Rev. Lett.*, **101**, no. 20, p. 203901, 2008.

[Lib17] Liberal, I. and Engheta, N., "Near-zero refractive index photonics", *Nat. Phot.*, **11**, no. 3, pp. 149–158, 2017.

[Lin92] Lindell, I. V., Sihvola, A. H., and Kurkijarvi, J., "Karl F. Lindman: The last Hertzian, and a harbinger of electromagnetic chirality", *IEEE Antennas and Propagation Magazine*, **34**, no. 3, pp. 24–30, 1992.

[Liu07] Liu, H.-B., Zhong, H., Karpowicz, N., Chen, Y., and Zhang, X.-C., "Terahertz spectroscopy and imaging for defense and security applications", *Proceedings of the IEEE*, **95**, no. 8, pp. 1514–1527, 2007.

[Liu08] Liu, N., Fu, L., Kaiser, S., Schweizer, H., and Giessen, H., "Plasmonic building blocks for magnetic molecules in three-dimensional optical metamaterials", *Adv. Mater.*, **20**, no. 20, pp. 3859–3865, 2008.

[Liu09] Liu, R., Ji, C., Mock, J., Chin, J., Cui, T., and Smith, D., "Broadband ground-plane cloak", *Science*, **323**, no. 5912, pp. 366–369, 2009.

[Lom05] Lomakin, V. and Michielssen, E., "Enhanced transmission through metallic plates perforated by arrays of subwavelength holes and sandwiched between dielectric slabs", *Phys. Rev. B*, **71**, no. 23, p. 235117, 2005.

[Lue78] Luebbers, R. and Munk, B., "Some effects of dielectric loading on periodic slot arrays", *IEEE Trans. Antennas Propag.*, **26**, no. 4, pp. 536–542, 1978.

[Mac00] MacDonald, M. E., Alexanian, A., York, R. A., Popovic, Z., and Grossman, E. N., "Spectral transmittance of lossy printed resonant-grid terahertz bandpass filters", *IEEE Trans. Microw. Theory Tech.*, **48**, no. 4, pp. 712–718, 2000.

[Mag66] Magill, E. and Wheeler, H., "Wide-angle impedance matching of a planar array antenna by a dielectric sheet", *IEEE Trans. Antennas Propag.*, **14**, no. 1, pp. 49–53, 1966.

[Mai05] Mailloux, R. J., *Phased Array Antenna Handbook*, volume 2, Artech House Boston, 2005.

[Mai07] Maier, S. A., *Plasmonics: Fundamentals and Applications*, Springer Science & Business Media, 2007.

[Mar51] Marcuvitz, N., *Waveguide Handbook*, 21, Iet, 1951.

[Mar02] Marqués, R., Medina, F., and Rafii-El-Idrissi, R., "Role of bianisotropy in negative permeability and left-handed metamaterials", *Phys. Rev. B*, **65**, no. 14, p. 144440, 2002.

[Mar05] Marqués, R., Baena, J. D., Beruete, M., Falcone, F., Lopetegi, T., Sorolla, M., Martín, F., and Garcia, J., "Ab initio analysis of frequency selective surfaces based on conventional and complementary split ring resonators", **7**, no. 2, p. S38, 2005.

[Mar08] Mary, A., Rodrigo, S. G., Garcia-Vidal, F., and Martin-Moreno, L., "Theory of negative-refractive-index response of double-fishnet structures", *Phys. Rev. Lett.*, **101**, no. 10, p. 103902, 2008.

[Max81] Maxwell, J. C., *A treatise on electricity and magnetism*, volume 1, Clarendon press, 1881.

[Med08] Medina, F., Mesa, F., and Marqués, R., "Extraordinary transmission through arrays of electrically small holes from a circuit theory perspective", *IEEE Trans. Microw. Theory Tech.*, **56**, no. 12, pp. 3108–3120, Dec. 2008.

[Med10] Medina, F., Mesa, F., Ruiz-Cruz, J. A., Rebollar, J. M., and Montejo-Garai, J. R., "Study of extraordinary transmission in a circular waveguide system", *IEEE Trans. Microw. Theory Tech.*, **58**, no. 6, pp. 1532–1542, Jun. 2010.

[Mes16] Mesa, F., Rodríguez-Berral, R., García-Vigueras, M., Medina, F., and Mosig, J. R., "Simplified modal expansion to analyze frequency-selective surfaces: An equivalent circuit approach", *IEEE Trans. Antennas Propag.*, **64**, no. 3, pp. 1106–1111, Mar. 2016.

[Mit88] Mittra, R., Chan, C. H., and Cwik, T., "Techniques for analyzing frequency selective surfaces-a review", *Proceedings of the IEEE*, **76**, no. 12, pp. 1593–1615, 1988.

[Mit96] Mittleman, D. M., Jacobsen, R. H., and Nuss, M. C., "T-ray imaging", *IEEE J. Select. Topics Quantum Electron.*, **2**, no. 3, pp. 679–692, 1996.

[MM01] Martin-Moreno, L., Garcia-Vidal, F., Lezec, H., Pellerin, K., Thio, T., Pendry, J., and Ebbesen, T., "Theory of extraordinary optical transmission through subwavelength hole arrays", *Phys. Rev. Lett.*, **86**, no. 6, p. 1114, Feb. 2001.

[Möl99] Möller, K., Farmer, K., Ivanov, D., Sternberg, O., Stewart, K., and Lalanne, P., "Thin and thick cross shaped metal grids", *Infrared physics & technology*, **40**, no. 6, pp. 475–485, 1999.

[Mol14] Molero, C., Rodríguez-Berral, R., Mesa, F., and Medina, F., "Analytical circuit model for 1-d periodic t-shaped corrugated surfaces", *IEEE Trans. Antennas Propag.*, **62**, no. 2, pp. 794–803, Feb. 2014.

[Mon07] Monni, S., Gerini, G., Neto, A., and Tijhuis, A. G., "Multimode equivalent networks for the design and analysis of frequency selective surfaces", *IEEE Trans. Antennas Propag.*, **55**, no. 10, pp. 2824–2835, 2007.

[Mor06] Moreno, E., Martín-Moreno, L., and García-Vidal, F., "Extraordinary optical transmission without plasmons: the s-polarization case", *J. Opt. A*, **8**, no. 4, p. S94, 2006.

[Mun00] Munk, B. A., *Frequency Selective Surfaces: Theory and Design*, Wiley-Interscience, 2000.

[Naq13] Naqui, J., Durán-Sindreu, M., and Martín, F., "Modeling split-ring resonator (srr) and complementary split-ring resonator (csrr) loaded transmission lines exhibiting cross-polarization effects", *IEEE Antennas Wireless Propag. Lett.*, **12**, pp. 178–181, 2013.

[NC11] Navarro-Cia, M., Kuznetsov, S. A., Aznabet, M., Beruete, M., Falcone, F., and Ayza, M. S., "Route for bulk millimeter wave and terahertz metamaterial design", *IEEE J. Quantum Electron.*, **47**, no. 3, pp. 375–385, 2011.

[NC13] Navarro-Cía, M., Rodriguez-Ulibarri, P., and Beruete, M., "Hedgehog subwavelength hole arrays: control over the thz enhanced transmission", *New J. Phys.*, **15**, no. 1, p. 013003, 2013.

[O'H12] O'Hara, J. F., Withayachumnankul, W., and Al-Naib, I., "A review on thin-film sensing with terahertz waves", *J. Infrared Millimeter Waves*, **33**, no. 3, pp. 245–291, 2012.

[Oli84] Oliner, A. A., "Historical perspectives on microwave field theory", *IEEE Transactions on Microwave Theory and Techniques*, **32**, no. 9, pp. 1022–1045, 1984.

[Oli15] Oliveri, G., Viani, F., Anselmi, N., and Massa, A., "Synthesis of multilayer waim coatings for planar-phased arrays within the system-by-design framework", *IEEE Trans. Antennas Propag.*, **63**, no. 6, pp. 2482–2496, 2015.

[Ora15] Orazbayev, B., Estakhri, N. M., Beruete, M., and Alù, A., "Terahertz carpet cloak based on a ring resonator metasurface", *Phys. Rev. B*, **91**, no. 19, p. 195444, 2015.

[Ora17] Orazbayev, B., Mohammadi Estakhri, N., Alù, A., and Beruete, M., "Experimental demonstration of metasurface-based ultrathin carpet cloaks for millimeter waves", *Adv. Opt. Mater.*, **5**, no. 1, 2017.

[Orb06] Orbons, S. M. and Roberts, A., "Resonance and extraordinary transmission in annular aperture arrays", *Opt. Express*, **14**, no. 26, pp. 12623–12628, Dec. 2006.

[Ort09] Ortuño, R., García-Meca, C., Rodríguez-Fortuño, F., Martí, J., and Martínez, A., "Role of surface plasmon polaritons on optical transmission through double layer metallic hole arrays", *Phys. Rev. B*, **79**, no. 7, p. 075425, 2009.

[Ort14] Ortuño, R., García-Meca, C., and Martínez, A., "Terahertz metamaterials on flexible polypropylene substrate", *Plasmonics*, **9**, no. 5, pp. 1143–1147, 2014.

[Pal70] Palocz, I. and Oliner, A. A., "Equivalent network of a multimode planar grating", *IEEE Trans. Microw. Theory Tech.*, **18**, no. 5, pp. 244–252, 1970.

[Par14] Park, S. J., Hong, J. T., Choi, S. J., Kim, H. S., Park, W. K., Han, S. T., Park, J. Y., Lee, S., Kim, D. S., and Ahn, Y. H., "Detection of microorganisms using terahertz metamaterials", **4**, p. 4988, 2014.

[Pel79] Pelton, E. and Munk, B., "Scattering from periodic arrays of crossed dipoles", **27**, no. 3, pp. 323–330, 1979.

[Pen96] Pendry, J. B., Holden, A. J., Stewart, W. J., and Youngs, I., "Extremely low frequency plasmons in metallic mesostructures", *Phys. Rev. Lett.*, **76**, no. 25, p. 4773, 1996.

[Pen99] Pendry, J. B., Holden, A. J., Robbins, D. J., and Stewart, W. J., "Magnetism from conductors and enhanced nonlinear phenomena", *IEEE Trans. Microw. Theory Tech.*, **47**, no. 11, pp. 2075–2084, 1999.

[Pen00] Pendry, J. B., "Negative refraction makes a perfect lens", *Phys. Rev. Lett.*, **85**, no. 18, p. 3966, 2000.

[Pen04] Pendry, J., Martin-Moreno, L., and Garcia-Vidal, F., "Mimicking surface plasmons with structured surfaces", *Science*, **305**, no. 5685, pp. 847–848, 2004.

[Pfe14] Pfeiffer, C., Zhang, C., Ray, V., Guo, L. J., and Grbic, A., "High performance bianisotropic metasurfaces: asymmetric transmission of light", *Phys. Rev. Lett.*, **113**, no. 2, p. 023902, 2014.

[Pie07] Piesiewicz, R., Kleine-Ostmann, T., Krumbholz, N., Mittleman, D., Koch, M., Schoebei, J., and Kurner, T., "Short-range ultra-broadband terahertz communications: Concepts and perspectives", *IEEE Antennas Propagat. Mag.*, **49**, no. 6, pp. 24–39, 2007.

[Poz84] Pozar, D. and Schaubert, D., "Scan blindness in infinite phased arrays of printed dipoles", *IEEE Trans. Antennas Propag.*, **32**, no. 6, pp. 602–610, 1984.

[Poz09] Pozar, D. M., *Microwave Engineering*, John Wiley & Sons, 2009.

[PP14] Pacheco-Peña, V., Torres, V., Orazbayev, B., Beruete, M., Navarro-Cía, M., Sorolla, M., and Engheta, N., "Mechanical 144 ghz beam steering with all-metallic epsilon-near-zero lens antenna", *Appl. Phys. Lett.*, **105**, no. 24, p. 243503, 2014.

[Ray07] Rayleigh, L., "Note on the remarkable case of diffraction spectra (described by Prof. Wood)", *Philos. Mag.*, **14**, pp. 60–65, 1907.

[RB12] Rodriguez-Berral, R., Molero, C., Medina, F., and Mesa, F., "Analytical wideband model for strip/slit gratings loaded with dielectric slabs", *IEEE Trans. Microw. Theory Tech.*, **60**, no. 12, pp. 3908–3918, Dec. 2012.

[RB15] Rodríguez-Berral, R., Mesa, F., and Medina, F., "Analytical multimodal network approach for 2-D arrays of planar patches/apertures embedded in a layered medium", *IEEE Trans. Antennas Propag.*, **63**, no. 5, pp. 1969–1984, May 2015.

[Rot62] Rotman, W., "Plasma simulation by artificial dielectrics and parallel-plate media", *IRE Transactions on Antennas and Propagation*, **10**, no. 1, pp. 82–95, 1962.

[RU13] Rodríguez-Ulibarri, P., Beruete, M., Navarro-Cía, M., and Serebryannikov, A. E., "Wideband unidirectional transmission with tunable sign-switchable refraction and deflection in nonsymmetric structures", *Phys. Rev. B*, **88**, no. 16, p. 165137, 2013.

[RU14] Rodriguez-Ulibarri, P., Beruete, M., Falcone, F., Crépin, T., Martel, C., Boust, F., Loecker, C., Herbertz, K., Salzburg, C., Bertuch, T., et al., "Metaradome for blind spot mitigation in phased-array antennas", in *Antennas and Propagation (EuCAP), 2014 8th European Conference on*, pp. 2504–2508, IEEE, 2014.

[RU15] Rodríguez-Ulibarri, P., Pacheco-Pena, V., Navarro-Cía, M., Serebryannikov, A. E., and Beruete, M., "Experimental demonstration of deflection angle tuning in unidirectional fishnet metamaterials at millimeter-waves", *Applied Physics Letters*, **106**, no. 6, p. 061109, 2015.

[RU16] Rodríguez-Ulibarri, P., Crépin, T., Martel, C., Boust, F., Falcone, F., Loecker, C., Herbertz, K., Bertuch, T., Dousset, T., Martinaud, J.-P., et al., "Experimental demonstration of metamaterials application for mitigating scan blindness in phased array antennas", *EPJ Appl. Metamat.*, **3**, p. 9, 2016.

[RU17a] Rodríguez-Ulibarri, P. and Beruete, M., "Nonbianisotropic complementary split ring resonators as angular selective metasurfaces", *J. Opt. Soc. Am. B*, **34**, no. 7, pp. D56–D61, Jul. 2017.

[RU17b] Rodríguez-Ulibarri, P. and Beruete, M., "Sensing at terahertz frequencies", in Matías, I. R., Ikezawa, S., and Corres, J., editors, *Fiber Optic Sensors*, pp. 301–327, Springer, 2017.

[Sae13] Saeedkia, D., *Handbook of Terahertz Technology for Imaging, Sensing and Communications*, Elsevier, 2013.

[Saj10] Sajuyigbe, S., Ross, M., Geren, P., Cummer, S., Tanielian, M., and Smith, D., "Wide angle impedance matching metamaterials for waveguide-fed phased-array antennas", *IET Microwaves Antennas Propag.*, **4**, no. 8, pp. 1063–1072, 2010.

[Sav03] Savia, S. B. and Parker, E. A., "Equivalent circuit model for superdense linear dipole fss", *IEE Proceedings-Microwaves, Antennas and Propagation*, **150**, no. 1, pp. 37–42, 2003.

[Sch38] Schelkunoff, S., "The impedance concept and its application to problems of reflection, refraction, shielding and power absorption", *Bell Labs Technical Journal*, **17**, no. 1, pp. 17–48, 1938.

[Sch43] Schelkunoff, S. A., *Electromagnetic waves*, Van Nostrand, 1943.

[Sch06] Schurig, D., Mock, J., Justice, B., Cummer, S. A., Pendry, J. B., Starr, A., and Smith, D., "Metamaterial electromagnetic cloak at microwave frequencies", *Science*, **314**, no. 5801, pp. 977–980, 2006.

[Ser09a] Serebryannikov, A. and Ozbay, E., "Unidirectional transmission in non-symmetric gratings containing metallic layers", *Opt. Express*, **17**, no. 16, pp. 13335–13345, 2009.

[Ser09b] Serebryannikov, A. E., "One-way diffraction effects in photonic crystal gratings made of isotropic materials", *Phys. Rev. B*, **80**, no. 15, p. 155117, 2009.

[Sha07] Shalaev, V. M., "Optical negative-index metamaterials", *Nat. Phot.*, **1**, no. 1, pp. 41–48, 2007.

[She01] Shelby, R. A., Smith, D. R., and Schultz, S., "Experimental verification of a negative index of refraction", *Science*, **292**, no. 5514, pp. 77–79, 2001.

[Sie02] Siegel, P. H., "Terahertz technology", *IEEE Trans. Microw. Theory Tech.*, **50**, no. 3, pp. 910–928, 2002.

[Sie04] Siegel, P. H., "Terahertz technology in biology and medicine", *IEEE Trans. Microw. Theory Tech.*, **52**, no. 10, pp. 2438–2447, 2004.

[Sil06] Silveirinha, M. and Engheta, N., "Tunneling of electromagnetic energy through subwavelength channels and bends using ε-near-zero materials", *Phys. Rev. Lett.*, **97**, no. 15, p. 157403, 2006.

[Sil07] Silveirinha, M. G. and Engheta, N., "Theory of supercoupling, squeezing wave energy, and field confinement in narrow channels and tight bends using ε near-zero metamaterials", *Phys. Rev. B*, **76**, no. 24, p. 245109, 2007.

[Sil08] Silveirinha, M. G., Fernandes, C. A., and Costa, J. R., "Electromagnetic characterization of textured surfaces formed by metallic pins", *IEEE Trans. Antennas Propag.*, **56**, no. 2, pp. 405–415, 2008.

[Sil14] Silva, A., Monticone, F., Castaldi, G., Galdi, V., Alù, A., and Engheta, N., "Performing mathematical operations with metamaterials", *Science*, **343**, no. 6167, pp. 160–163, 2014.

[Sil15] Silvestri, F., Chiusolo, P., Cifola, L., Bolt, R., and Gerini, G., "Design of metamaterial based wide angle impedance matching layers for active phased arrays", in *Antennas and Propagation (EuCAP), 2015 9th European Conference on*, pp. 1–5, IEEE, 2015.

[Sin14] Singh, R., Cao, W., Al-Naib, I., Cong, L., Withayachumnankul, W., and Zhang, W., "Ultrasensitive terahertz sensing with high-q fano resonances in metasurfaces", *Appl. Phys. Lett.*, **105**, no. 17, p. 171101, 2014.

[Smi00] Smith, D. R., Padilla, W. J., Vier, D., Nemat-Nasser, S. C., and Schultz, S., "Composite medium with simultaneously negative permeability and permittivity", *Phys. Rev. Lett.*, **84**, no. 18, p. 4184, 2000.

[Smi05] Smith, D. R., Vier, D. C., Koschny, T., and Soukoulis, C. M., "Electromagnetic parameter retrieval from inhomogeneous metamaterials", *Phys. Rev. E*, **71**, no. 3, p. 036617, 2005.

[Smi06] Smith, D. R. and Pendry, J. B., "Homogenization of metamaterials by field averaging", *J. Opt. B*, **23**, no. 3, pp. 391–403, 2006.

[Sol09] Solymar, L. and Shamonina, E., *Waves in Metamaterials*, Oxford University Press, 2009.

[Sta74] Stark, L., "Microwave theory of phased-array antennas—a review", *Proceedings of the IEEE*, **62**, no. 12, pp. 1661–1701, 1974.

[Str04] Strachan, C. J., Rades, T., Newnham, D. A., Gordon, K. C., Pepper, M., and Taday, P. F., "Using terahertz pulsed spectroscopy to study crystallinity of pharmaceutical materials", *Chem. Phys. Lett.*, **390**, no. 1, pp. 20–24, 2004.

[Ter] "Teraview TPS spectra", .

[Tor12] Torres, V., Rodríguez-Ulibarri, P., Navarro-Cía, M., and Beruete, M., "Fishnet metamaterial from an equivalent circuit perspective", *Appl. Phys. Lett.*, **101**, no. 24, p. 244101, Dec. 2012.

[Tor13] Torres, V., Pacheco-Peña, V., Rodríguez-Ulibarri, P., Navarro-Cía, M., Beruete, M., Sorolla, M., and Engheta, N., "Terahertz epsilon-near-zero graded-index lens", *Optics express*, **21**, no. 7, pp. 9156–9166, 2013.

[Tor15] Torres, V., Orazbayev, B., Pacheco-Peña, V., Teniente, J., Beruete, M., Navarro-Cía, M., Ayza, M. S., and Engheta, N., "Experimental demonstration of a millimeter-wave metallic enz lens based on the energy squeezing principle", *IEEE Trans. Antennas Propag.*, **63**, no. 1, pp. 231–239, 2015.

[Tor16] Torres, V., Mesa, F., Navarro-Cía, M., Rodríguez-Berral, R., Beruete, M., and Medina, F., "Accurate circuit modeling of fishnet structures for negative-index-medium applications", *IEEE Trans. Microw. Theory Tech.*, **64**, no. 1, pp. 15–26, Jan. 2016.

[Tsa84] Tsao, C.-H. and Mittra, R., "Spectral-domain analysis of frequency selective surfaces comprised of periodic arrays of cross dipoles and jerusalem crosses", **32**, no. 5, pp. 478–486, 1984.

[Ulr67] Ulrich, R., "Far-infrared properties of metallic mesh and its complementary structure", *Infrared Physics*, **7**, no. 1, pp. 37–55, 1967.

[Val08] Valentine, J., Zhang, S., Zentgraf, T., Ulin-Avila, E., Genov, D. A., Bartal, G., and Zhang, X., "Three-dimensional optical metamaterial with a negative refractive index", *Nature*, **455**, no. 7211, pp. 376–379, 2008.

[Ves68] Veselago, V. G., "The electrodynamics of substances with simultaneously negative values of ε and μ", *Sov. Phys. Uspekhi*, **10**, no. 4, pp. 509–514, 1968.

[Wal03] Walser, R. M., "Metamaterials: An introduction", in Weiglhofer, W. S. and Lakhtakia, A., editors, *Introduction to Complex Mediums for Optics and Electromagnetics*, pp. 295–314, International Society of Optical Engineering, 2003.

[Wei77] Weiland, T., "A discretization model for the solution of maxwell's equations for six-component fields", *Archiv Elektronik und Uebertragungstechnik*, **31**, pp. 116–120, 1977.

[Whe48] Wheeler, H. A., "The radiation resistance of an antenna in an infinite array or waveguide", *Proceedings of the IRE*, **36**, no. 4, pp. 478–487, 1948.

[Woo02] Wood, R. W., "On a remarkable case of uneven distribution of light in a diffraction grating spectrum", *Philos. Mag.*, **4**, no. 21, pp. 396–402, 1902.

[Yah15] Yahiaoui, R., Tan, S., Cong, L., Singh, R., Yan, F., and Zhang, W., "Multispectral terahertz sensing with highly flexible ultrathin metamaterial absorber", *J. Appl. Phys.*, **118**, no. 8, p. 083103, 2015.

[Yak09] Yakovlev, A. B., Silveirinha, M. G., Luukkonen, O., Simovski, C. R., Nefedov, I. S., and Tretyakov, S. A., "Characterization of surface-wave and leaky-wave propagation on wire-medium slabs and mushroom structures based on local and nonlocal homogenization models", *IEEE Trans. Microw. Theory Tech.*, **57**, no. 11, pp. 2700–2714, 2009.

[Yu11] Yu, N., Genevet, P., Kats, M. A., Aieta, F., Tetienne, J.-P., Capasso, F., and Gaburro, Z., "Light propagation with phase discontinuities: generalized laws of reflection and refraction", *Science*, **334**, no. 6054, pp. 333–337, 2011.

[Yu12] Yu, N., Aieta, F., Genevet, P., Kats, M. A., Gaburro, Z., and Capasso, F., "A broadband, background-free quarter-wave plate based on plasmonic metasurfaces", *Nano Lett.*, **12**, no. 12, pp. 6328–6333, 2012.

[Yu14] Yu, N. and Capasso, F., "Flat optics with designer metasurfaces", *Nat. Mater.*, **13**, no. 2, pp. 139–150, 2014.

[Zha05] Zhang, S., Fan, W., Panoiu, N., Malloy, K., Osgood, R., and Brueck, S., "Experimental demonstration of near-infrared negative-index metamaterials", *Phys. Rev. Lett.*, **95**, no. 13, p. 137404, 2005.

[Zha08] Zhang, X. and Liu, Z., "Superlenses to overcome the diffraction limit", *Nat. Mater.*, **7**, no. 6, pp. 435–441, 2008.

[Zha10] Zhang, P., Lobet, M., and He, S., "Carpet cloaking on a dielectric half-space", *Opt. Express*, **18**, no. 17, pp. 18158–18163, 2010.

[Zha13] Zhao, Y. and Alù, A., "Tailoring the dispersion of plasmonic nanorods to realize broadband optical meta-waveplates", *Nano Lett.*, **13**, no. 3, pp. 1086–1091, 2013.

Appendix A

Methods and Techniques

In this Appendix the simulation and experiment tools used throughout the Thesis are briefly treated. First, the main features of the full wave simulation tool CST Microwave Studio® (CST MWS) are provided. The shown material is an adapted version of the contents available within the help menu of the CST MWS front-end [CST]. Furthermore, a description of the AB-Millimetre™-MVNA used for most of the experimental work reported in this Thesis is also given [ABm]. Finally, some details related to the TDS-THz system used for a part of the measurements in Chapter 4 are provided.

A.1 Simulation: CST Microwave Studio

All the available electromagnetic simulation tools deal with Maxwell's equations to solve problems at different scenarios. The main difference between the available methods and solutions relies on how they treat those well-known equations. Depending on the method chosen, the simulation is more or less accurate and/or time-efficient for a specific problem. Finite Difference Time Domain (FDTD), Method of moments (MoM) and Finite elements (FE) are three methods widely used in computational electromagnetics.

In this Thesis the chosen software package was the commercial solution CST Studio Suite®. The kernel of the software is based on the Finite Integration Technique (FIT) method [Wei77]. The CST Studio Suite pakcage includes several useful modules that allow dealing with multiphysics and particle physical problems to name a few. In this Thesis the selected module is CST Microwave Studio® (CST MWS) which it is specifically designed to deal with classical microwave components such as waveguides, antennas, filters, resonators, etc. However, its performance can be extended to infrared and optics by proper selection of the simulation settings. CST MWS provides a very powerful and intuitive graphical front end. In addition, it allows solving highly complex electromagnetic problems. For instance, regarding

periodic structures, a special boundary conditions setting which is referred to as unit cell boundary conditions, allows to apply periodicity in the transversal plane and to excite the analyze structure via Floquet/Bloch modes. This feature is very useful when designing Frequency Selective Surfaces (FSS), metamaterials and ET structures. In the next subsections some details about FIT and unit cell boundaries are provided.

A.1.1 FIT/FDTD Method

The FIT method was proposed by Weiland in 1976/77 [Wei77]. Unlike most numerical methods, FIT discretizes the integral form of Maxwell's equations instead of using the differential version. The FIT method can be represented as a standard FDTD method when using Cartesian grids. For this reason, FIT can be considered as an evolution of the FDTD method that inherits its benefits and drawbacks.

Let us now briefly give the main ideas about FIT method. When evaluating the Maxwell's equations the FIT method sets a finite calculation domain wherein the problem to be solved is enclosed. Afterwards, the resulting space-domain is split up in small elements (see Fig. A.1). Subsequently, Maxwell's equations are formulated and evaluated for each element as shown in Fig. A.2.

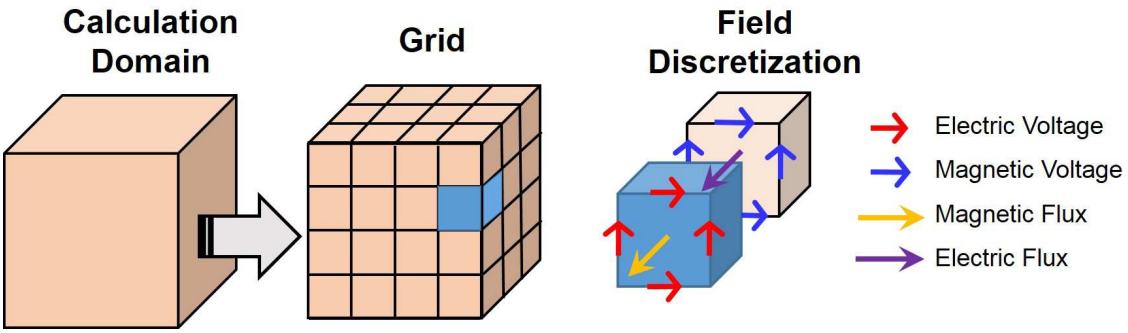

Fig. A.1 Calculation domain and grid cell in CST Microwave Studio™.

As stated above, the FIT technique belongs to FDTD family of numerical methods for solving Maxwell's equations. Therefore, its main characteristic is that works in the time-domain. Hence, from one single simulation a wide frequency range can be computed. In Fig. A.3, it is shown how CST MWS evaluates magnetic flux at a given step from electric voltage and magnetic flux from previous half-step and one-step respectively. To summarize, let us briefly enumerate the strong points of general FDTD methods [Dav05].

- Simple implementation for a full-wave solver.
- Straightforward treatment of material inhomogeneities.

- Fairly accurate geometrical modelling ability.
- Wideband data potentially available in one run (time domain method).

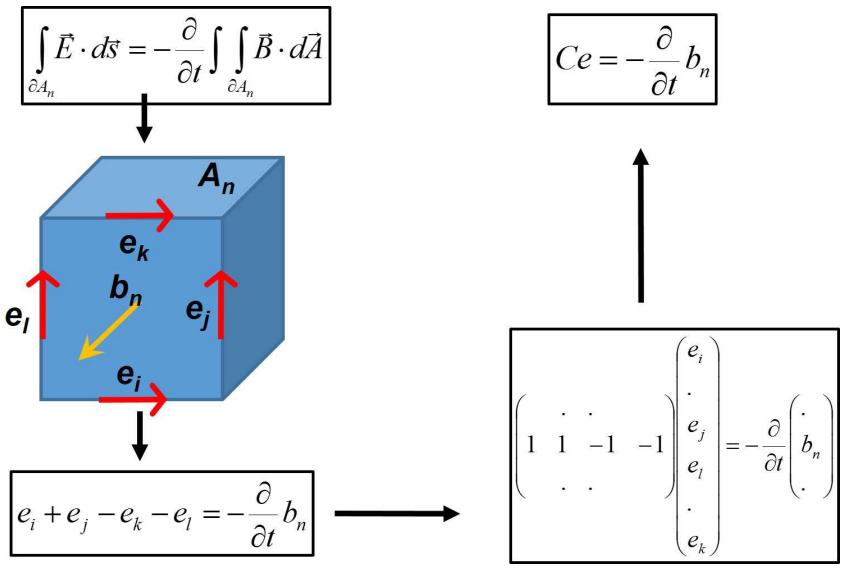

Fig. A.2 Formulation and discretization of Maxwell's equations in CST Microwave Studio™.

For a final CST MWS user, the first three FDTD strengths are transparent. On the other hand, the fourth point must be taken into account when time-domain solver simulation is applied. FDTD methods have historically suffered from the following drawbacks:

- Inflexible meshing.
- Uncertainty about the precise position of boundaries.
- A correct implementation of dispersive materials requires considerable efforts.
- Lower efficiency than Methods of Moments (MoM) for modeling entirely or highly conductive radiators.

However, the FIT method overcomes some of these weaknesses. CST MWS offers a wide range of meshing capabilities that endows it with more flexibility. Furthermore, dispersive materials can be modeled in a reasonable time and without great effort.

A.1.2 Mesh Generation

Using an appropriate mesh is crucial when solving computational electromagnetic problems. First, the mesh has to be sufficiently fine to obtain accurate results. In turn, is should not

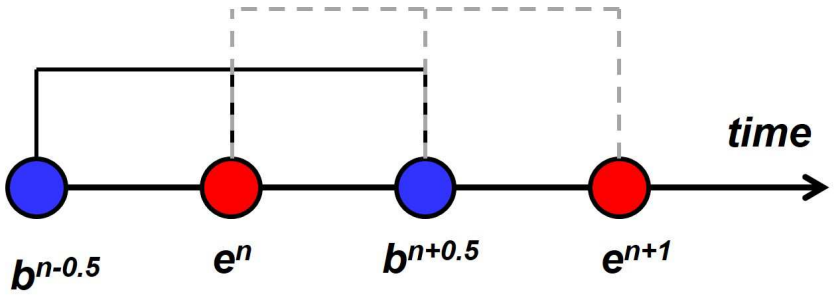

Fig. A.3 Schematic drawing of time domain sampling in CST Microwave Studio^{TM}.

be extremely dense for the sake of computational efficiency. Therefore, there is a trade-off between the accuracy of the results and the time to compute them. Obviously, the first condition is the most important.

CST MWS provides a high flexibility when building the evaluation mesh. There are two main types of mesh schemes: tetrahedral and hexahedral. The tetrahedral type can be only used in the frequency domain. Since most of the simulations presented throughout the Thesis use the tetrahedral mesh, some details about its generation and general features are provided. There are three ways of defining a mesh in CST: manually, automatically and adaptively. Additional features such as local meshing can be used to improve the mesh density in small or curved objects for instance. Generally, the most common practice is to use automatic meshing with additional settings for a good degree of accuracy in the simulation results. The basic principles of the three different ways of meshing are:

Manual: Manual meshing can be defined by user at any time without even generating the geometrical model. However, it is considered an old-fashioned way of working and requires some time to do it properly.

Automatic: It provides an efficient and quick way of working with CST MWS. The mesh generator does automatically interpret the most important features of the geometrical structure and creates an adapted mesh for each problem. In other words, the mesh generator takes into account the frequency range (the greater the upper limit, the smaller cell is taken), the dielectrics involved (a denser material delivers a finer mesh), the geometry structure (edges, corners, etc.), so on and so forth. After using the automatic mesh, one can set manually extra properties to enhance the mesh at certain locations of the structure. At a first step, it seems reasonable to generate the mesh automatically and have a glance on it to check its capability.

Adaptive: Adaptive mesh generation is an alternative for the expertise generator where the mesh is calculated iteratively by running the simulation and evaluating the S-

parameters convergence. The adaptive mesh is usually recommended when using frequency domain method unless the problem size makes its use not affordable. For each step, the mesh generator recognizes the high field concentration regions and refines the mesh. Stop criterion can be set in terms of differential quantity between consecutive S-parameters results or by limiting the number of simulation steps. In general, the first criterion is accomplished before reaching the maximum number of steps.

A.1.3 Frequency Domain Solver

The frequency-domain solver provided by CST MWS represents a powerful and useful tool for simulating electrically small to mid-size problems. In contrast with time-domain solver it is better suited for narrowband regimes. Furthermore, it allows using special boundary conditions such as periodic or unit cell.

The basics of the frequency-domain rely on the assumption of a time-harmonic dependence $\left(\frac{\partial}{\partial t} \rightarrow i\omega\right)$ of the electromagnetic fields. In such a way, Maxwell's equations can be written in terms of frequency. The fields are then described by phasors whose transient fields can be extracted by multiplying them by the time factor and taking the real part:

$$\mathbf{E}(t) = \mathrm{Re}\left(\mathbf{E}(\omega) \cdot exp(i\omega t)\right). \tag{A.1}$$

For the general purposes, frequency domain solver method evaluates the solution from Eq. A.1 for a single frequency at a time. Therefore, at each frequency sample the linear equation system must be solved increasing its computation time in comparison with the time domain method. However, it uses a special frequency sweep technique to derive the full broadband spectrum from a relatively small amount of frequency samples. Field results are not directly obtained but one might be able to evaluate them afterwards in a post-processing step. Some of the main application areas of the frequency domain solver are:

- Scattering parameter matrices.
- Electromagnetic field distributions at various frequencies.
- Antenna radiation patterns and relevant antenna parameters.
- Unit cells of infinite arrays with unit cell or periodic boundary conditions.
- Spice network extraction

Concerning the frequency sampling setting, CST MWS is quite flexible. Manual an equidistant or non-equidistant frequency sampling can be implemented. If an automatic method is selected for the frequency sampling generation, CST MWS tries to define the minimum number of frequency samples by focusing in the spectrum region where the S-parameters variation is greater. Afterwards, an interpolation to evaluate equidistantly the S-parameter in the whole spectra range is performed.

A.1.4 Unit cell boundary condition: Floquet Modes

Unit cell and periodic boundary conditions allow to model periodic infinite arrays with identical single elements (i.e. unit cells). In this Thesis, unit cell boundary conditions have been widely used (see Fig. A.4).

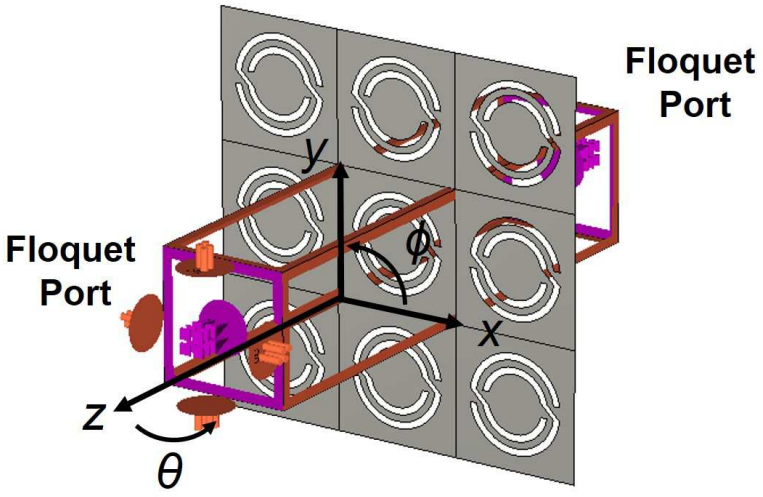

Fig. A.4 Unit cell simulation in CST Microwave Studio^{TM}.

Under unit cell boundary conditions, the fields for two opposite periodic boundary planes are solved by applying a complex factor determined by the phase shift between them. When dealing with frequency domain calculations, this phase shift can be specified by entering the constant angle of incidence corresponding to a plane wave propagating in the direction given in spherical coordinates. If unit cell boundary conditions are combined with open boundary conditions in z-direction, the open boundaries are automatically converted to Floquet ports. Otherwise, waveguide port excitation is also possible. Floquet ports permit plane wave excitation. The number of Floquet modes can be set automatically and/or manually. The automatic number of modes depends on the geometry of the problem and the frequency range. The two first modes are fundamental Floquet modes $TE_{(0,0)}$ and $TM_{(0,0)}$. Those modes are

linearly polarized and depending on the incidence plane chosen they would correspond to the commonly known TM and TE polarized waves under oblique incidence. Furthermore, they can be set up to exhibit circular polarization instead of linear.

Unit cell boundary conditions feature is then a very useful tool for simulating frequency selective surfaces (FSS), antenna arrays and, in general, infinite period structures.

A.1.5 Eigenmode Solver

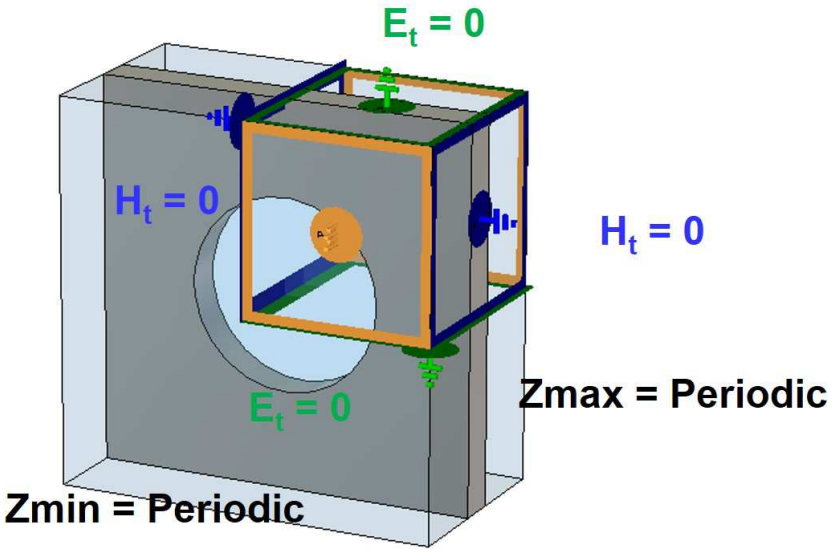

Fig. A.5 Boundary conditions for eigenmode solver in CST Microwave Studio^{TM}.

The eigenmode solver is used to calculate frequencies and their corresponding electromagnetic field patterns when no excitation is applied to the analyzed structure. These frequencies along with the associated field patterns pairs are called eigenmodes. In such a way, dispersion diagrams can be evaluated.

The eigenmode solver is based on the eigenvalue equation for non-driven and loss-free time harmonic problems that it is given as follows:

$$\nabla\mu^{-1}\nabla\mathbf{E} = \omega^2\varepsilon\mathbf{E} \Rightarrow \tilde{\mathbf{C}}\mathbf{M}_{\mu^{-1}}\mathbf{C}\mathbf{e} = \omega^2\mathbf{M}_S\mathbf{e}. \tag{A.2}$$

Lossy materials in low-loss regime can be taken into account by using the Jacobi-Davidson method (JDM) along with a perturbation method.

The eigenmode solver is very useful for the following areas:

- Scattering parameter matrices.

- Electromagnetic field distributions at various frequencies.
- Antenna radiation patterns and relevant antenna parameters.
- Unit cells of infinite arrays with unit cell or periodic boundary conditions.
- Spice network extraction

In this Thesis, the eigenmode solver has been used to evaluate the dispersion diagrams used for the design of unidirectional devices in Chapter 3. Figure A.5 shows an example of the boundary conditions set to obtain the dispersion diagram of a hole array taking the z axis as the direction of propagation. Then, the boundaries at z maximum and minimum are set to periodic and the phase between them is varied by means of parameter sweep. According to the selected boundary conditions for the x and y directions, one might be able to select a specific polarization for the eigenmode solutions. In the shown case, electric and magnetic walls are set to the y and x boundaries respectively. In this way, the electric field is forced to be oriented along y axis. In addition, in this particular case, symmetry planes can be applied due to the specific geometry and hence, the size of the problem is reduced.

A.2 Experiment

A.2.1 Quasi-Optical Vector Network Analyzer: AB-Millimetre^{TM}

The Vector Network Analyzer MVNA-8-350, is produced by AB-Millimetre^{TM} since 1990 [ABm]. It is an all-solid-state electronics millimeter- and submillimeter-waves spectrometer/network analyzer. In this way simultaneous measurements of the amplitude and the phase of the transmitted and reflected signals can be performed. The frequency range of operation can be very broad with the appropriate extensions making possible to cover from microwaves up to THz waves (from 8 to 1000 GHz, i.e from 4 cm to 300 μm in terms of wavelength). Most of the results presented in this Thesis were obtained with the AB-Millimetre VNA along with a quasi-optical bench equipped with four ellipsoidal mirrors.

The basic operation of the AB-Millimetre VNA is depicted in Fig. A.6. The first block represents the internal tunable source that has the capability to generate signals from 8 to 18 GHz. Then the output of signal is guided to the next block by coaxial cables. Afterwards, the signal is converted to upper frequencies by means of Schottky barrier diodes working at the non-linear regime enabling frequency multiplication. Next, the signal is transferred to free space by using the appropriate combination of RF components (waveguide, attenuator, antennas, etc.). Then, the output beam resulting from the TX antenna is directed by the

mirror system to the first and eventually to the detector. At the detection side, an harmonic mixing technique is performed for frequency down conversion by using again a Schottky barrier diode.

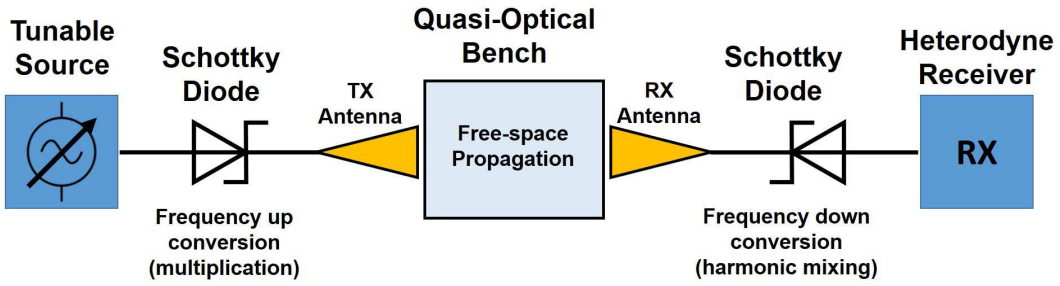

Fig. A.6 Block diagram of VNA and quasi-optical system operation.

The whole system can be divided between the central unit and the external parts. The MVNA central unit contains the generator and the receiver. The external parts are the corresponding set of diodes, waveguides, directional couplers, isolators, attenuators for each corresponding frequency band. The current equipment of the VNA enables a frequency coverage from 45 GHz to 260 GHz and from 630 to 1000 GHz. Table A.1 shows the limits for the available frequency bands. Next, the different blocks are briefly described.

Band	$f_{\min}$ (GHz)	$f_{\max}$ (GHz)	Standard
V	45	75	WR-15
W	75	110	WR-10
D	110	170	WR-6
G (partially)	170	260	WR-4
THz	630	1000	WR-2.5

Table A.1 Frequency coverage of the AB-Millimetre VNA.

Figure A.7 shows the front panel of the central unit where the receiver and transmitter modules can be distinguished Figs. A.7(a) and (b) respectively. The receiver module is a dual channel vector receiver (VR-8-350-2) which allows for simultaneous measurement of two signals (reflection and transmission for instance). The transmitter is a MP-8-350-4 with two connectors for a harmonic generator (HG) cables, and two connectors for harmonic mixer (HM) cables.

Figure A.8 shows a top view of a mounted experimental set-up for measurements in the W-band. As it can be seen the TX and RX antennas are placed at opposite sides of the quasi-optical bench. The output beam is directed towards the sample by two ellipsoidal

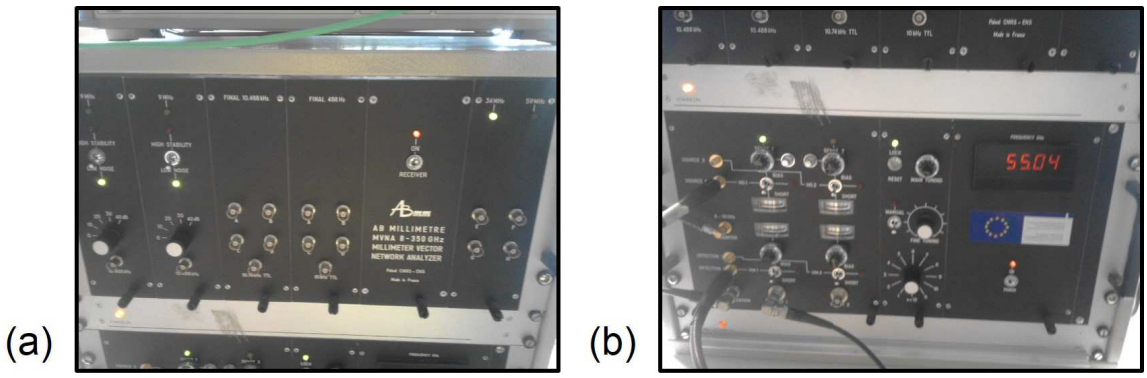

Fig. A.7 Front panel of the VNA central unit. (a) Receiver. (b) Transmitter.

mirrors. In turn, the beam travels an equivalent path from the sample position to the RX antenna by using identical mirrors. With this configuration, oblique incidence can be easily considered by mounting the sample on a rotatory platform that allows rotating around its normal axis.

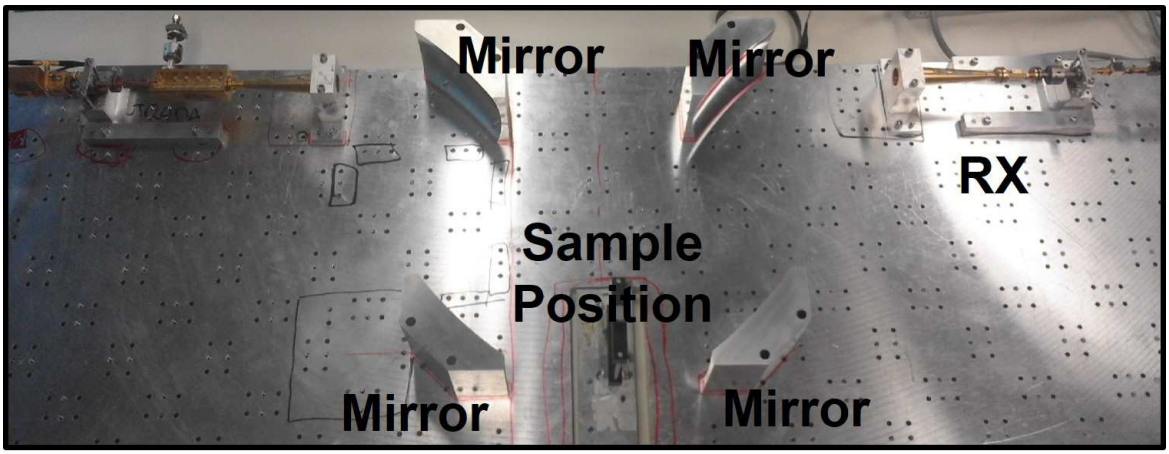

Fig. A.8 Experimental set-up for W-band measurements on the quasi-optical bench.

Finally, the complete set of components for the V-band is shown in Fig. A.9. The diodes, for both up-conversion and down conversion, are followed by isolators for protection purposes. In addition, a directional coupler can be added in the transmission chain for reflection measurements. In fact, when performing measurements on the quasi-optical bench it is highly recommended to use the directional coupler as an additional protective precaution. The antennas are corrugated horns able to emit Gaussian beams typically with about 10° half angle aperture (i.e. when the field drops $1/e$). The beam created by these antennas combined with the quasi-optical system, results in a beamwidth of about $BW \approx 0.9 D_{ant}$, with D_{ant} being the antenna diameter, at the sample location.

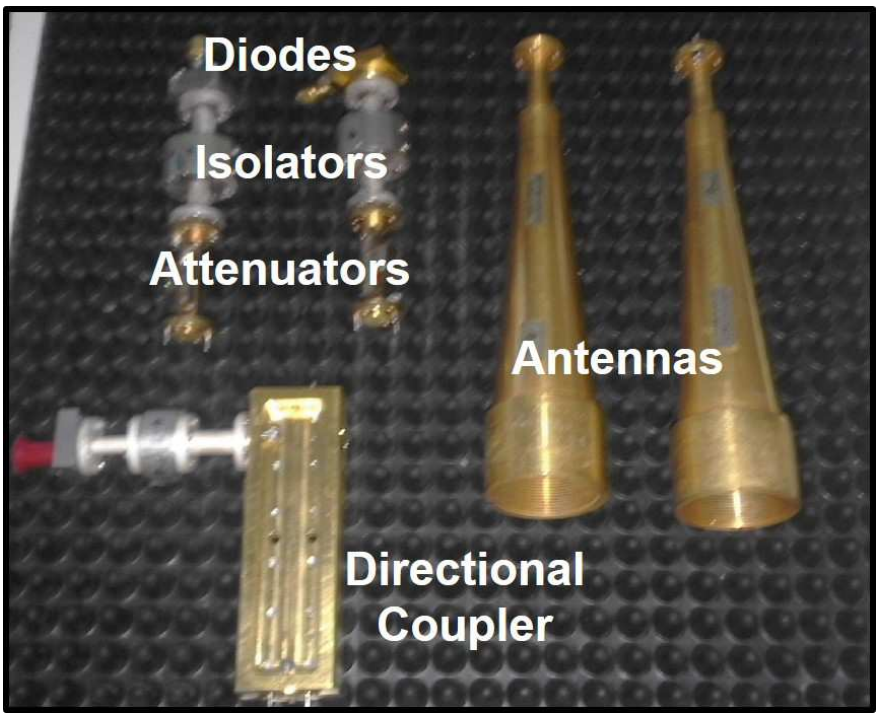

Fig. A.9 Set of components for the V-Band.

A.2.2 Time-Domain Spectroscopy System: Teraview®

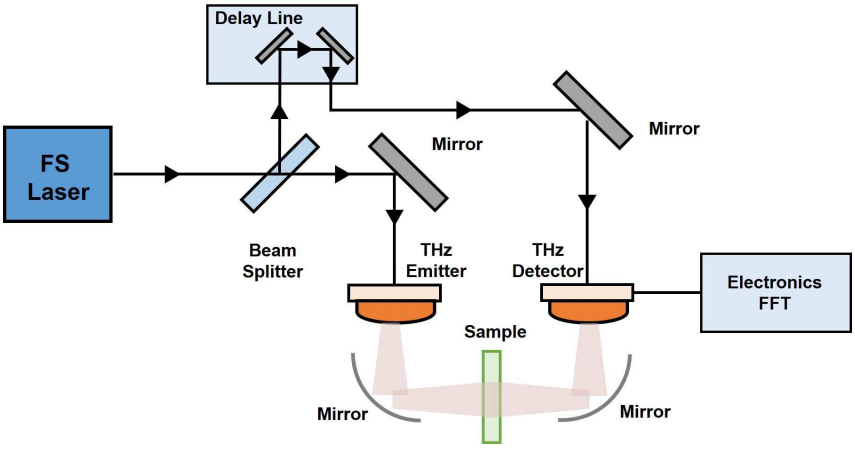

Fig. A.10 Block diagram of a TDS-THz operation principle.

In this section a brief description of the TDS-THz system used for the measurements performed in Chapter 4 is provided. The TDS-THz system used is a commercial product developed by TeraView® [Ter]. The basic operation principle of TDS-THz systems is depicted in Fig. A.10. Generally, an input pulse is generated by a femtosecond (FS) laser. The output pulse is divided in two beams by a beam-splitter (BS) creating two different paths.

One of the beams acts as the probe signal, and it is redirected to a mechanical delay line that permits controlling the optical path and hence, sampling different time steps. The other beam reaches a THz generator (which can be a photoconductive antenna or a non-linear medium) that performs the conversion from visible to THz waves. Then, the THz wave is directed by means of a mirror system towards the sample and eventually towards the detector. The THz detector is equipped with the required electronic components for converting the detected signal into voltages and currents. Generally, the Fourier transform (FT) of the detected pulse is performed to switch from time-domain to the frequency-domain and get the final THz spectrum.

Figure A.11 shows a picture of the TPS Spectra 3000 device. As it can be seen is an all-in-one TDS-THz system that enables a friendly and intuitive use. However, since all the components are transparent to the user it gives less flexibility than the AB-Millimetre case presented before. All in all, the TPS Spectra 3000 is a very complete and useful device for exploring the THz range. It covers a very wide frequency range (from 0.06 to 4 THz) without requiring liquid helium cooling or vacuum systems enabling very rapid measurements. In addition, if desired Ni gas can be injected in the sample compartment so as the measurements can get rid off the absorbance bands due to the water vapour.

Fig. A.11 Block diagram of VNA operation principle.

Appendix B

WAIM Metaradome Design Process

In this appendix a complete description of the design process of the WAIM metaradome which is studied in Chapter 2 is presented. First the optimization process for finding the homogenous anisotropic slab WAIM is described. To this end, the analytical formulation that characterizes the impedance properties of anisotropic slabs is given. Also, the stop criterion and constrains adopted for the WAIM optimization are provided. Next, the synthesis of the metamaterial structure that exhibits the constitutive parameters obtained for the optimal homogeneous WAIM is carried out. The retrieval technique used in this method is briefly discussed.

B.1 Homogenous WAIM Optimization

In this section the homogenous WAIM design steps are described. Analytical equations allow for fast optimization routines with low computational cost. Hence, the analytical impedance of an anisotropic dielectric slab under oblique incidence is extracted. Figure B.1 shows a schematic of TM and TE oblique plane wave incidence on an anisotropic dielectric slab with ε and μ as constitutive parameters along with the selected coordinate system. The equations shown next are valid for biaxial and uniaxial anisotropic slabs, i.e., ε and μ are tensors with non-diagonal elements equal to zero and diagonal elements that can be all different or two of them equal and one different.

Let us first derive the equations for the TM case. Note that the electric field vector lies within the yz plane. The impedance of a TM wave in the free-space has the next expression:

$$Z_{TM} = \eta_0 \frac{\beta_{zTM}}{k_z \varepsilon_{yy}} \tag{B.1}$$

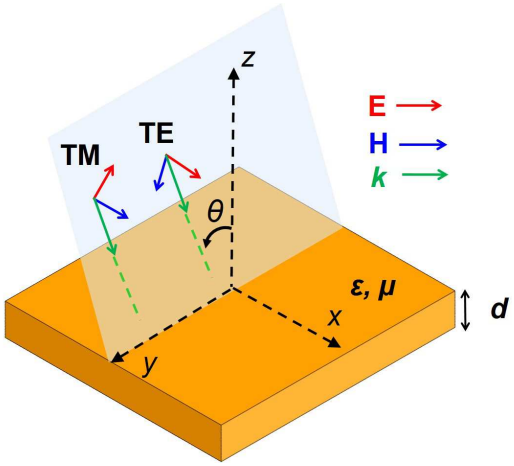

Fig. B.1 TM and TE plane wave oblique incidence on an infinite dielectric slab with finite thickness d and constitutive parameters ε and μ.

where β_{zTM} is the propagation constant, ε_{yy} is the permittivity along y axis and $k_z = k_0 \cos\theta$ is the longitudinal wave number. In addition, the dispersion relation can be written as follows:

$$\frac{\beta_{zTM}^2}{\varepsilon_{yy}} + \frac{\beta_y^2}{\varepsilon_{zz}} = k_0^2 \mu_{xx} \tag{B.2}$$

where $\beta_y = k_0 \sin\theta$ is the propagation constant along y axis, ε_{zz} is the permittivity along z axis and μ_{xx} is the permeability along x axis. After some manipulations, Eq. B.2 reads:

$$\beta_{zTM} = k_0 \sqrt{\mu_{xx}\varepsilon_{yy} - \frac{\varepsilon_{yy}}{\varepsilon_{zz}} \sin^2\theta} \tag{B.3}$$

Introducing B.3 in B.1 yields:

$$Z_{TM} = \eta_0 \sqrt{\frac{\mu_{xx}}{\varepsilon_{yy}} - \frac{\sin^2\theta}{\varepsilon_{yy}\varepsilon_{zz}}} \tag{B.4}$$

Results for TE polarization are obtained in a similar way. In this case, both the wave impedance and dispersion relation differ from the TM polarization case:

$$Z_{TE} = \frac{k_z \mu_{yy}}{\beta_{zTE}} \tag{B.5}$$

$$\frac{\beta_{zTE}^2}{\mu_{yy}} + \frac{\beta_y^2}{\mu_{zz}} = k_0^2 \varepsilon_{xx} \tag{B.6}$$

After some algebra, the characteristic wave impedance for an anisotropic dielectric slab under TE polarization is obtained as follows:

$$Z_{TE} = \eta_0 \sqrt{\frac{\mu_{yy}\mu_{zz}}{\varepsilon_{xx}\mu_{zz} - \sin^2\theta}} \tag{B.7}$$

These equations can be directly utilized in the classical transmission line formulation to obtain the scattering parameters of an anisotropic finite slab of length d (see Fig. B.1). To ensure the validity of the equations a comparison with full wave numerical simulations was conducted. An anisotropic slab with the effective parameters displayed in Tab. B.1 was considered. Figures B.2 and B.3 show the reflection and transmission coefficients (amplitude and phase) resulting from the analytical model and CST Microwave Studio simulations under TE and TM polarization respectively. The incident angle, θ, is varied from 0 to 85° with a step of 5°. A very good agreement was observed in all the cases considered.

d (mm)	ε_{xx}	ε_{yy}	ε_{zz}	μ_{xx}	μ_{yy}	μ_{zz}
2	2	5	1	3	0.2	2

Table B.1 Constitutive parameters of anisotropic slab.

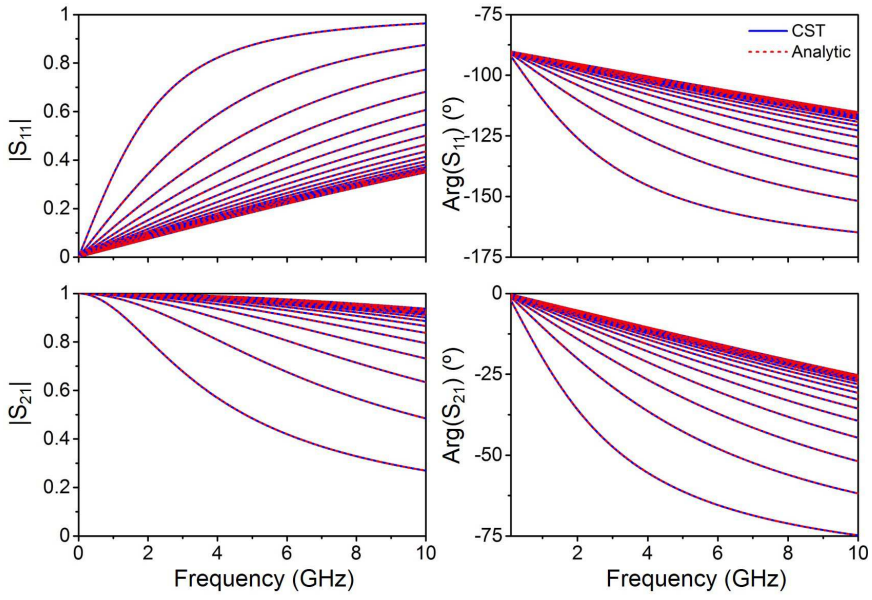

Fig. B.2 S-parameters for TE oblique plane wave incidence under different angles of incidence, θ, on an anisotropic slab with constitutive parameters and thickness shown in Tab. B.1. (a) $|S_{11}|$. (b) arg(S_{11}). (c) $|S_{21}|$. (d) arg(S_{11})

.

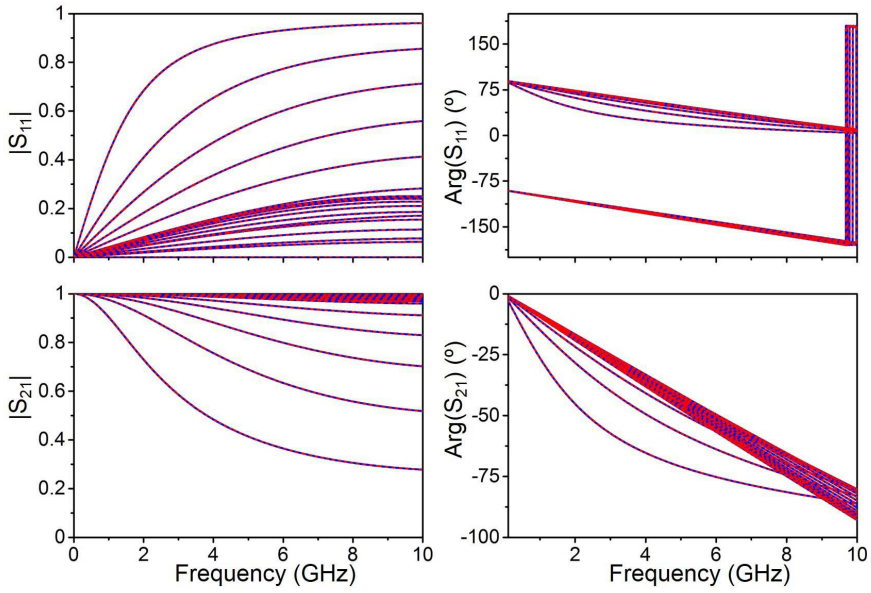

Fig. B.3 S-parameters for TM oblique plane wave incidence under different angles of incidence, θ, on an anisotropic slab with constitutive parameters and thickness shown in Tab. B.1. (a) $|S_{11}|$. (b) arg(S_{11}). (c) $|S_{21}|$. (d) arg(S_{11})

.

The results shown in Figs. B.2 and B.3 were obtained for a free-standing anisotropic WAIM slab, namely, with the free space impedance acting as the load. However, the main interest is related to the more complicated case, in which the actual load is the impedance exhibited by the antenna array. Figure B.4 shows an equivalent network where a finite WAIM slab of thickness d is designed to match the active impedance of the 50^{th} element. The matching occurs when $Z_{50^{th}\_WAIM}(f,\theta) = Z^{*}_{air}(f,\theta)$ with f and θ being the frequency and scanning angle respectively.

Next, an optimization routine was launched wherein an effective parameter search was carried out. Figure B.5 shows a block diagram of the iterative process. On one side, the antenna impedance was calculated from the active reflection coefficient which at the same time was evaluated by means of the measured coupling coefficients of the prototype antenna. Furthermore, the impedance of the homogeneous WAIM was calculated for some initial constitutive parameters with the above analytical equations. If the matching condition was not satisfied the optimization routine performed an additional iteration. To this end, the optimization toolbox of the commercial software MATLAB, which includes different optimization algorithms such as direct search (DS), genetic algorithm (GA) or simulated annealing (SA), was used for the optimization routines. For this particular problem, the SA algorithm was able to reach an optimal solution.

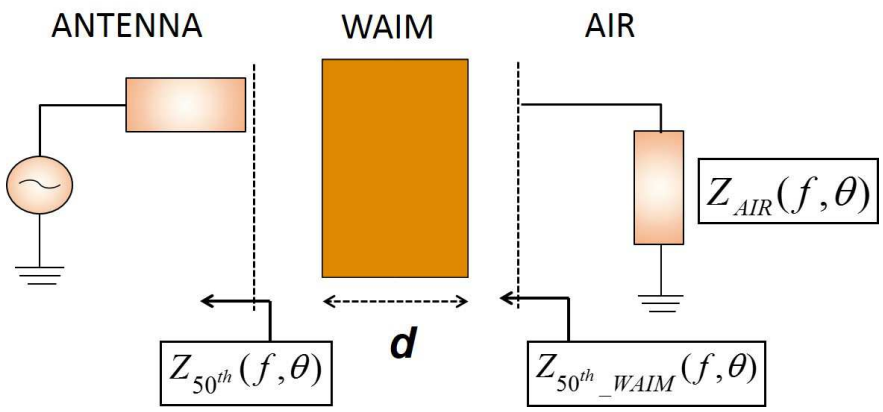

Fig. B.4 Schematic of the equivalent transmission line problem comprising the antenna and finite WAIM slab system embedded in air.

The stop criterion was set for the active reflection coefficient for the 50^{th} element, R_{50}. This quantity had to be below a reference value of $R_{Ref} = -10\,\text{dB}$ for the whole angular domain ($\theta_{max} = \pm 50°$). The cost function, $\Theta(\varepsilon,\mu,d)$ was calculated as the minimum square error between R_{Ref} and R_{50} (for the θ cases where $R_{50} > R_{Ref}$) as follows:

$$\Theta(\varepsilon,\mu,d,\theta) = \sum_{\theta=0°}^{\theta_{max}} \left(R_{ref} - R_{50}(\theta)\right)^2, \tag{B.8}$$

where ε and μ are the permittivity and permeability tensors and d is the slab thickness. Evidently the goal is perfectly achieved when $\Theta = 0$.

B.2 Metaradome Synthesis

Once the homogeneous WAIM was obtained, the next stage was to synthesize a metamaterial particle that emulated its constitutive parameters ε and μ. To this end, a homemade retrieval method was implemented for retrieving the constitutive parameters of arbitrary anisotropic slabs [Jia11]. The synthesis process is depicted in the block diagram of Fig. B.6. A metamaterial particle was simulated in CST Microwave Studio and its S-parameters were extracted. From them, the impedance, Z, and index of refraction, n, were calculated. Then, ε and μ can be directly derived. If those values were not equal to those obtained for the WAIM, the particle was physically modified. This process was iteratively run until the desired values of ε and μ were finally obtained. Next, a subsection devoted to the used retrieval method is included.

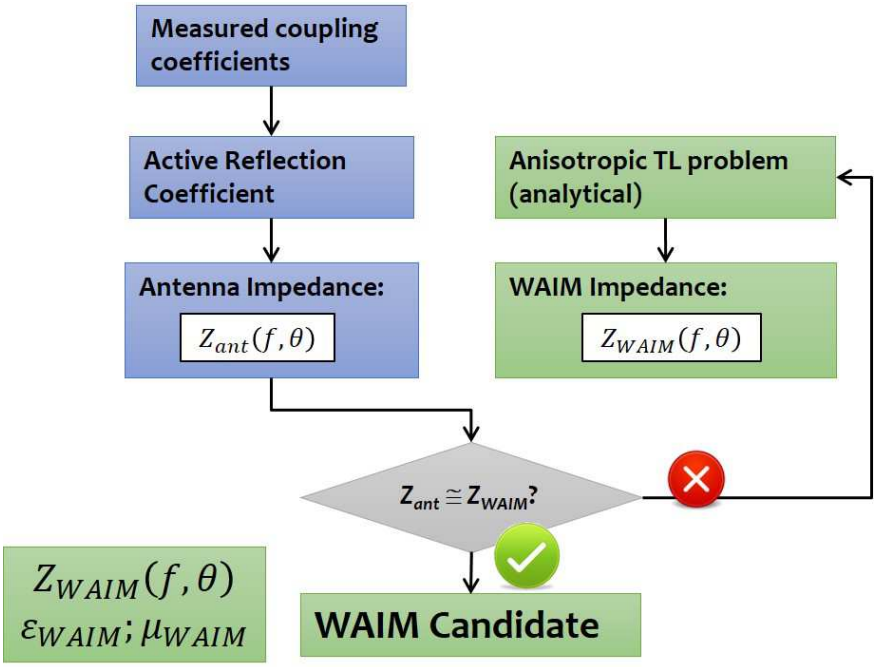

Fig. B.5 Block diagram of the WAIM optimization step.

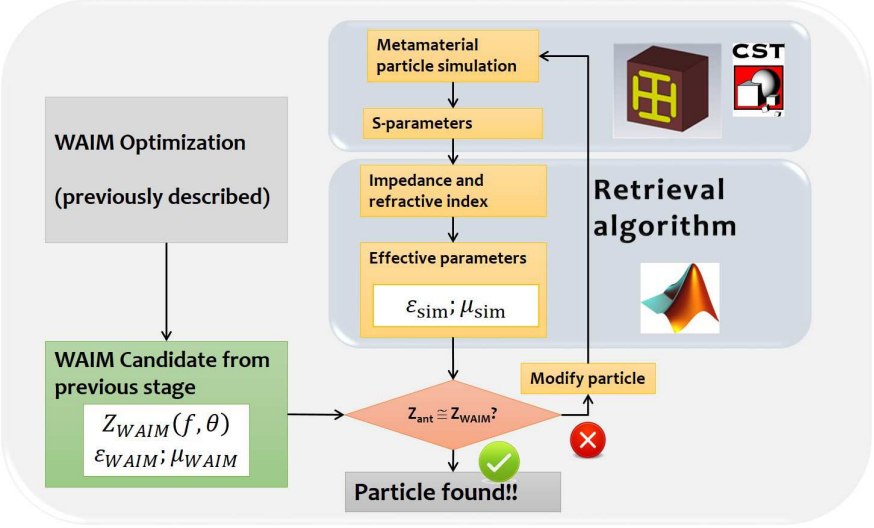

Fig. B.6 Block diagram of the WAIM optimization step.

B.2.1 S-parameter Inversion Technique: Retrieval

A retrieval is, in fact, a S-parameter inversion technique. It has been briefly described in the introduction of this Thesis. In simple words, the retrieval algorithm allows us to extract the effective constitutive parameters of an arbitrary slab from its scattering parameters. By solving Maxwell's equations numerically one can obtain the S-parameters matrix of a finite slab and, by applying some well-known inverse formulation, derive the index of refraction n and the impedance Z and from them is straightforward to obtain ε and μ.

Here, the target was to implement a retrieval algorithm which could effectively extract the constitutive parameters of an anisotropic slab. To obtain also the constitutive parameters along the longitudinal direction, oblique incidence must be considered. The analytical equations presented above in this Appendix for anisotropic slabs are applicable here. As before, the two possible polarization states TM and TE must be considered (see Fig. B.1). Hence, dispersion relations for both cases must be used (see Eqs. B.2-B.6). Furthermore, the S-parameters under TM and TE incidence can be written as:

$$\begin{aligned} S_{11} &= \frac{\Gamma_{TM(TE)}(1-e^{j2\beta_{TM(TE)}d})}{1-\Gamma^2_{TM(TE)}e^{j2\beta_{TM(TE)}d}} \\ S_{21} &= \frac{(1-\Gamma^2_{TM(TE)})e^{j2\beta_{TM(TE)}d}}{1-\Gamma^2_{TM(TE)}e^{j2\beta_{TM(TE)}d}}, \end{aligned} \tag{B.9}$$

where $\Gamma_{TM(TE)} = \frac{Z_{TM(TE)}-1}{Z_{TM(TE)}+1}$ is the reflection coefficient in the first air/medium interface and $Z_{TM(TE)}$ is the wave impedance given by

$$\begin{aligned} Z_{TM} &= \frac{\beta_{zTM}}{k_z \varepsilon_{yy}} \\ Z_{TE} &= \frac{k_z \mu_{yy}}{\beta_{zTE}} \end{aligned} \tag{B.10}$$

where $k_z = k_0 \cos\theta$. Now, the inverse formulation to obtain the index of refraction $n_{zTM(TE)}$ and the impedance $Z_{TM(TE)}$ from S_{11} and S_{21} is introduced. As previously mentioned, oblique incidence is compulsory to retrieve the effective parameters along the longitudinal axis. Additionally, to find the six unknowns, i.e., $\varepsilon_{xx}, \varepsilon_{yy}, \varepsilon_{zz}, \mu_{xx}, \mu_{yy}, \mu_{zz}$, solution of the dispersion equations, Eqs. B.2 and B.6, is required for two different angles of incidence.

Let us consider a TE polarized wave impinging with two different angles of incidence, θ_1 and θ_2. Then, four different quantities are obtained: $S_{TE11\_\theta_1}, S_{TE21\_\theta_1}, S_{TE11\_\theta_2}, S_{TE21\_\theta_2}$.

By inverting Eqs. B.9 we get

$$\begin{aligned} \cos(n_{zTE-l}k_0 d) &= \frac{1-S_{TE11-l}^2+S_{TE21-l}^2}{2S_{TE21-l}^2} \\ Z_{TE-l} &= \pm\sqrt{\frac{(1+S_{TE11-l}^2)^2-S_{TE21-l}^2}{(1-S_{TE11-l}^2)^2-S_{TE21-l}^2}} \end{aligned} \tag{B.11}$$

where $l=\theta_1,\theta_2$. Then, four different equations are available to solve the three unknowns of the dispersion relation Eq. B.6. When solving Eq. B.11 passivity of the homogeneous and continuous material must be assured. Additionally, since the index of refraction has multiple solutions, special care must be taken when selecting the solution branch. To fulfill passivity the imaginary and real part of the index of refraction n and impedance Z, respectively, must be positive:

$$\begin{aligned} n''_{zTE-\theta_1} &\geq 0 \\ n''_{zTE-\theta_2} &\geq 0 \\ Z'_{TE-\theta_1} &\geq 0 \\ Z'_{TE-\theta_2} &\geq 0 \end{aligned} \tag{B.12}$$

Once $n_{zTE-\theta_1}, n_{zTE-\theta_2}, Z_{TE-\theta_1}$ and $Z_{TE-\theta_2}$ are known, by introducing in Eq. B.6 and using Eq. B.10 the constitutive parameters can be derived as follows:

$$\begin{aligned} \varepsilon_{xx} &= \frac{n_{zTE-\theta_1}\left[\frac{\cos\theta_1}{Z_{TE-\theta_1}}\right]\sin^2\theta_2 - n_{zTE-\theta_2}\left[\frac{\cos\theta_2}{Z_{TE-\theta_2}}\right]\sin^2\theta_1}{\sin^2\theta_2-\sin^2\theta_1} \\ \mu_{yy} &= n_{zTE-\theta_l}\frac{Z_{TE-\theta_l}}{\cos\theta_l}; \quad l=1,2 \\ \mu_{zz} &= \frac{\sin^2\theta_2-\sin^2\theta_1}{n_{zTE-\theta_1}\left[\frac{\cos\theta_1}{Z_{TE-\theta_1}}\right]-n_{zTE-\theta_2}\left[\frac{\cos\theta_2}{Z_{TE-\theta_2}}\right]}. \end{aligned} \tag{B.13}$$

Following the same procedure the effective parameters under TM polarization are also obtained:

$$\begin{aligned}
\varepsilon_{yy} &= \frac{n_{zTM-\theta_l}}{Z_{TM-\theta_l}\cos\theta_l}; \quad l = 1,2 \\
\varepsilon_{zz} &= \frac{\sin^2\theta_2 - \sin^2\theta_1}{n_{zTM-\theta_1}Z_{TM-\theta_1}\cos\theta_1 - n_{zTM-\theta_2}Z_{TM-\theta_2}\cos\theta_2} \\
\mu_{xx} &= \frac{n_{zTM-\theta_1}Z_{TM-\theta_1}\cos\theta_1\sin^2\theta_2 - n_{zTM-\theta_2}Z_{TM-\theta_2}\cos\theta_2\sin^2\theta_1}{\sin^2\theta_2 - \sin^2\theta_1}.
\end{aligned} \tag{B.14}$$

These equations were implemented in a MATLAB^{TM} routine that received as input the simulated S-parameters of an arbitrary slab. To test the algorithm, an homogeneous slab with the following constitutive parameters was considered:

d (mm)	ε_{xx}	ε_{yy}	ε_{zz}	μ_{xx}	μ_{yy}	μ_{zz}
3	2	0.7	1.3	2	1	2.1

Table B.2 Constitutive parameters of anisotropic slab for retrieval test.

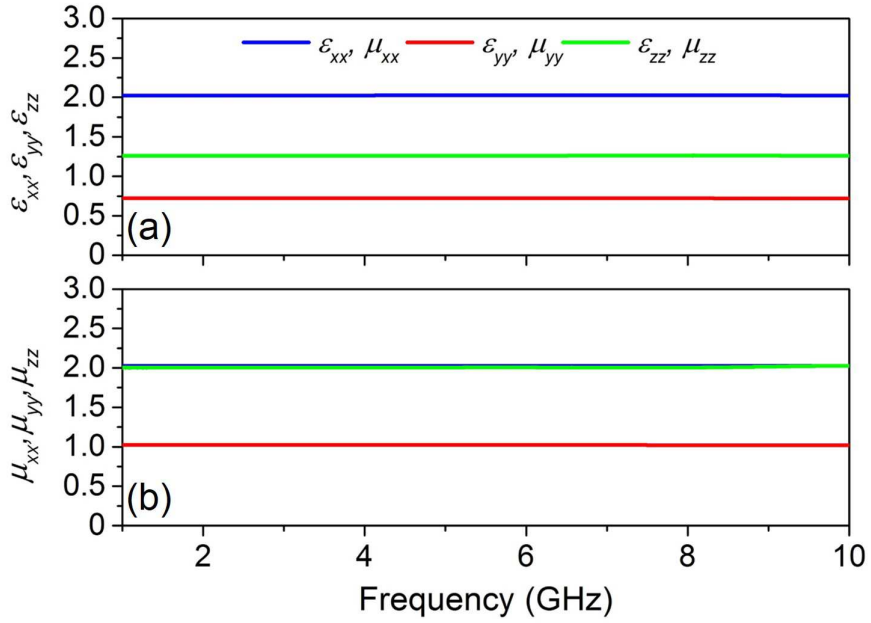

Fig. B.7 Retrieved ε and μ for an anisotropic slab exhibiting constitutive parameters shown in Tab. B.2.

A CST Microwave Studio® simulation with unit cell boundary conditions emulating an infinite slab along x and y axis and finite length in the z axis was set (see App. A). The slab material was set as anisotropic. Next, the S-parameters were exported to the Matlab routine and the effective parameters were evaluated. Figure B.7 shows the retrieved ε and μ tensors. The obtained values correspond to the effective set of parameters included in the simulation. The results shown in Fig. B.7 were obtained for angles of incidence of 10° and 30°. However, similar results (not shown here for the sake of brevity) were obtained for different pairs of impinging angles.

Appendix C

Author's Merits

C.1 Scientific production of this Thesis

C.1.1 Journal Papers

Generated by this Thesis:

- **Rodríguez-Ulibarri, P.**, Navarro-Cía, M., Rodríguez-Berral, R., Mesa F., Medina, F., and Beruete, M. "Coaxial Apertures in Metallic Screens as Extraordinary Transmission and Frequency Selective Surface Structures," submitted to *IEEE Trans. Microw. Theory Tech.*, 2017S.

- **Rodríguez-Ulibarri, P.**, and Beruete, M. "Nonbianisotropic complementary split ring resonators as angular selective metasurfaces," *J. Opt. Soc. Am. B*, 34, no. 7, pp. D56–D61, Jul. 2017.

- **Rodríguez-Ulibarri, P.**, Crépin, T., Martel, C., Boust, F., Loecker, C., ... and Beruete, M. "Experimental demonstration of metamaterials application for mitigating scan blindness in phased array antennas," *EPJ Appl. Metamaterials*, vol. 3, p. 9, Jul. 2016.

- **Rodríguez-Ulibarri, P.**, Kuznetsov S. A., and Beruete, M. "Wide angle terahertz sensing with a cross-dipole frequency selective surface," *Appl. Phys. Lett.*, vol. 108, no. 11, p. 111104, Mar. 2016.

- **Rodríguez-Ulibarri, P.**, Pacheco-Peña, V., Navarro-Cía, M., Serebryannikov, A. E., and Beruete, M. "Experimental demonstration of deflection angle tuning in unidirectional fishnet metamaterials at millimeter-waves," *Appl. Phys. Lett.*, vol. 106, no. 6, p. 061109, Feb. 2015.

- **Rodríguez-Ulibarri, P.**, Beruete, M., Navarro-Cía, and Serebryannikov, A. E. "Wide-band unidirectional transmission with tunable sign-switchable refraction and deflection in nonsymmetric structures,." *Phys. Rev. B*, vol. 88, no. 16, p. 165137, Oct. 2013.

Additional publications:

- Lozano, M., **Rodríguez-Ulibarri, P.**, Echeverría, J. C., Beruete, M., Sorolla, M., and Beriain, M. J. (2017). "Mid-Infrared Spectroscopy (MIR) for Simultaneous Determination of Fat and Protein Content in Meat of Several Animal Species". *Food Analytical Methods*, 1-9, 2017.

- **Rodríguez-Ulibarri, P.**, and Bertuch, T. "Microstrip-Fed Complementary Yagi-Uda Antenna," *IET Microwaves Antennas Propag.*, vol. 10, no. 9, pp. 926-931, Jun. 2016.

- Torres, V., Ortuño R., **Rodríguez-Ulibarri, P.**, Griol A., Martínez A., Navarro-Cía, M., Beruete, M., and Sorolla, M. "Mid-infrared plasmonic inductors: Enhancing inductance with meandering lines," *Sci. Rep.*, vol. 4, p. 3592, Jan. 2014.

- Beruete, M., **Rodríguez-Ulibarri, P.**, Pacheco-Peña, V., Navarro-Cía, and Serebryannikov, A. E. "Frozen mode from hybridized extraordinary transmission and Fabry-Perot resonances," *Phys. Rev. B*, vol. 87, no. 20, p. 205128, May. 2013.

- Torres, V., Pacheco-Peña, V., **Rodríguez-Ulibarri, P.**, Navarro-Cía, M., Beruete, M., Sorolla M., and Engheta, N. "Terahertz epsilon-near-zero graded-index lens," *Opt. Exp.*, vol. 21, no. 7, pp. 9156-9166, Apr. 2013.

- Navarro-Cía, M., **Rodríguez-Ulibarri, P.**, and Beruete, M. "Hedgehog subwave--length hole arrays: Control over the THz enhanced transmission," *New Journal Phys.*, vol. 15, no. 1, p. 013003, Jan. 2013.

- Torres, V., **Rodríguez-Ulibarri, P.**, Navarro-Cía, M., and Beruete, M. "Fishnet metamaterial from an equivalent circuit perspective," *Appl.Phys. Lett.*, vol. 101, no. 24, p. 244101, Dec. 2012.

- Iturri, P.L, Nazábal, J.A., Azpilicueta, L., **Rodríguez-Ulibarri, P.**, Beruete, M., Fernández-Valdivieso, C. and Falcone, F. "Impact of high power interference sources in planning and deployment of Wireless Sensor Networks and devices in the 2.4 GHz frequency band in heterogeneous environments," *Sensors*, vol. 12, no. 11, pp. 15689-15708, Nov. 2012.

- Navarro-Cía, M., **Rodríguez-Ulibarri, P.**, Torres, V., and Beruete, M. "Quarter-wave plate based on dielectric-enabled extraordinary resonant transmission," *IEEE Photon. Technol. Lett.* , vol. 24, no. 11, pp. 945-947, Jun. 2012.

C.1.2 Book Chapters

- **Rodríguez-Ulibarri, P.**, and Beruete, M., "Sensing at Terahertz Frequencies," in *Fiber Optics Sensors*. Springer, 2017, pp. 301-327.

C.1.3 International Conferences

Generated by this Thesis:

- **Rodríguez-Ulibarri, P.**, Jáuregui, I., and Beruete, M. "Non-Bianisotropic Complementary Split Ring Resonators Metasurfaces" submitted to *11^{th} International Congress on Advanced Electromagnetic Materials in Microwaves and Optics, METAMATERIALS 2017*, Marseille, France, 2017.

- **Rodríguez-Ulibarri, P.**, Navarro-Cía, M., Rodríguez-Berral, R., Mesa F., Medina, F., and Beruete, M. "Equivalent Circuit for Double Annular Aperture Frequency Selective Surfaces," *4^{th} International Conference on Numerical Electromagnetic and Multiphysics Modeling and Optimization for RF, Microwave, and Terahertz Applications, NEMO 2017*, Sevilla, Spain, 2017. Contribution: Written and Oral.

- **Rodríguez-Ulibarri, P.**, Kuznetsov S. A., and Beruete, M. "THz Sensing with FSS at oblique incidence" *7^{th} International Conference on Metamaterials, Photonic Crystals and Plasmonics, META 2016*, Torremolinos-Málaga, Spain, 2016. Contribution: Written and Oral.

- **Rodríguez-Ulibarri, P.**, Pacheco-Peña, V., Beruete, M., Navarro-Cía M., and Serebryannikov A.E., "Deflection angle tuning in thin structures with diffraction inspired unidirectionality" *9^{th} European Conference on Antennas and Propagation, EuCAP 2015*, Lisbon, Portugal, 2015. Contribution: Written.

- **Rodríguez-Ulibarri, P.**, Falcone F., Beruete, M., Navarro-Cía M., and Serebryannikov A.E. "Tunability and sign-switching of deflection angle in diffraction inspired unidirectional devices" *2014 14^{th} Mediterranean Microwave Symposium, MMS 2014*, Marrakech, Morocco, 2014. Contribution: Written and Oral.

- Crépin, T., Martel, C., Gabard, B., Boust, F., Martinaud, J.-P., Dousset, T., **Rodríguez-Ulibarri, P.**, Beruete, M., ... and Maci, S., "Blind spot mitigation in phased array antenna using metamaterials" *2014 International Radar Conference, Radar 2014*, Lille, France, 2014. Contribution: Written.

- **Rodríguez-Ulibarri, P.**, Beruete, M., Navarro-Cía M., and Serebryannikov A.E. "Diffraction inspired unidirectional transmission with sign-switchable refraction and deflection" *8th International Congress on Advanced Electromagnetic Materials in Microwaves and Optics, METAMATERIALS 2014*, Copenhagen, Denmark, 2014. Contribution: Written.

- **Rodríguez-Ulibarri, P.**, Beruete, M., Falcone, F., ... and Marcotegui, J.A., "Metaradome for blind spot mitigation in phased-array antennas" *8th European Conference on Antennas and Propagation, EuCAP 2014*, The Hague, Netherlands, 2014. Contribution: Written and Oral.

Additional publications:

- Torres, V., **Rodríguez-Ulibarri, P.**, Ortuño, R., Navarro-Cía, M., and Beruete, M., "Tailoring extraordinary transmission by inductance addition with meander-lines," *2013 38th International Conference on Infrared, Millimeter, and Terahertz Waves, IRMMW-THz 2013*, Mainz, Germany, 2013. Contribution: Written and Oral.

- Torres, V., **Rodríguez-Ulibarri, P.**, Falcone, F., Beruete, and Navarro-Cía, M., "Equivalent circuit of the double-fishnet metamaterial," *2013 IEEE Antennas and Propagation Society International Symposium, APSURSI 2013*, Orlando, USA, 2013. Contribution: Written.

- Navarro-Cía, M., **Rodríguez-Ulibarri, P.**, Torres, V., and Beruete, "Terahertz quarter-wave plate based on subwavelength hole arrays , " *7th European Conference on Antennas and Propagation, EuCAP 2013*, Gothenburg, Sweden, 2013. Contribution: Written and Oral.

- Torres, V., **Rodríguez-Ulibarri, P.**, Navarro-Cía, M., and Beruete, "Equivalent circuit extraction of the double-fishnet metamaterial based on its electrodynamics," *7th International Congress on Advanced Electromagnetic Materials in Microwaves and Optics, METAMATERIALS 2013*, Bordeaux, France, 2013. Contribution: Written.

- Torres, V., **Rodríguez-Ulibarri, P.**, Beruete, M., Falcone, F., Sorolla, M., and Navarro-Cía, M., "Downshifting extraordinary transmission by meander-lines in hole arrays,"

6th European Conference on Antennas and Propagation, EuCAP 2012, Prague, Czech Republic, 2012. Contribution: Written.

- Caratelli, D., Yarovoy, A. and **Rodríguez-Ulibarri, P.**, "Singularity-based modelling of antenna transient radiation processes," *2011 IEEE Antennas and Propagation Society International Symposium, APSURSI 2011*, Spokane, USA, 2011. Contribution: Written.

C.1.4 National Conferences

Generated by this Thesis:

- **Rodríguez-Ulibarri, P.**, Navarro-Cía, M., Rodríguez-Berral, R., Mesa F., Medina, F., and Beruete, M., "Equivalent Circuit Approach for Coaxial Aperture Arrays," submitted to *XXXII Symposium Nacional de la Unión Científica Nacional de Radio, URSI 2017*, Cartagena, Spain, 2017.

- **Rodríguez-Ulibarri, P.**, Jáuregui, I., and Beruete, M., "Metasuperficies basadas en anillos complementarios sin bianisotropía," submitted to *XXXII Symposium Nacional de la Unión Científica Nacional de Radio, URSI 2017*, Cartagena, Spain, 2017.

- **Rodríguez-Ulibarri, P.**, Jáuregui, I., Kuznetsov, S. A., and Beruete, M., "THz sensing structures based on classical cross-dipole FSS," *XXXI Symposium Nacional de la Unión Científica Nacional de Radio, URSI 2016*, Madrid, Spain, 2016. Contribution: Written.

- **Rodríguez-Ulibarri, P.**, Pacheco-Peña, V., Navarro-Cía M., Serebryannikov A.E., and Beruete, M., "Control del ángulo de deflexión en estructuras unidireccionales basadas en placas agujereadas terminadas en una red de difracción dieléctrica," *XXX Symposium Nacional de la Unión Científica Nacional de Radio, URSI 2015*, Pamplona, Spain, 2015. Contribution: Written and Oral.

Additional publications:

- **Rodríguez-Ulibarri, P.**, Orazbayev, B., Torres, V., Beruete, M. and Navarro-Cía, M., "Agrupamiento de Agujeros en Configuración de Erizo: Control sobre Transmisión Extraordinaria en el THz," *XXVIII Symposium Nacional de la Unión Científica Nacional de Radio, URSI 2013*, Santiago, Spain, 2013. Contribution: Written.

- **Rodríguez-Ulibarri, P.**, Torres, V., Beruete, M. and Navarro-Cía M., "Retardador de cuarto de onda basado en agrupamientos de agujeros sublambda operando en Terahercio," *XXVII Symposium Nacional de la Unión Científica Nacional de Radio, URSI 2012*, Elche, Spain, 2013. Contribution: Written and Oral.

C.2 Other Merits

C.2.1 BSc Project Cosupervision

Topic: *Design of terahertz sensors based on metasurfaces for fungal infection detection.*
Author: Irati Jáuregui López
Advisors: Miguel Beruete Díaz and **Pablo Rodríguez Ulibarri**
Public University of Navarra

C.2.2 Awards

- 2nd Yarman-Carlin Best Student Paper Contest in Microwave Mediterranean Symposium 2014, Marrakech, Morocco.
- "Disruptive Concept Award" in 2014 International Radar Conference, Lille, France.